UNIVERSIDAD DE LA LAGUNA

Tasa de formación estelar en galaxias A 0.5< z < 1.1 – un caso para el espectrógrafo infrarrojo multi-rendija liris (requerimiento técnicos)

Autor: Domínguez-Tagle Paredes, Carlos Humberto

Directores: Arturo Manchado Torres
y Francisco Prada Martínez

Departamento de Astrofísica

Resumen

Esta tesis se desarrolla en el área de investigación en instrumentación astronómica y abarca dos proyectos estrechamente relacionados, uno científico y otro instrumental. Ambos están enmarcados en la explotación científica del modo de espectroscopía multi-rendija de LIRIS (Long slit Intermediate Resolution Infrared Spectrograph). Este instrumento es un espectrógrafo multi-rendija en el infrarrojo cercano que actualmente construye el Instituto de Astrofísica de Canarias para instalarlo en el William Hershel Telescope.

El proyecto científico de esta tesis se centra en el estudio de galaxias con desplazamiento al rojo y está basado en la selección de una muestra de galaxias del Hubble Deep Field y Flanking Fields (HDF-N+FF) para su posterior estudio con LIRIS. Esta muestra incluye unas 500 galaxias, de las cuales se seleccionan 88 objetos (con amplia fotometría y medidas espectroscópicas del desplazamiento al rojo) para obtener la tasa de formación estelar en el intervalo de 0.45 a 1.1 en redshift. Las estimaciones de formación estelar se obtienen a partir de la luminosidad de la línea de emisión Hα y permitirán restringir los escenarios de formación y evolución de galaxias en el Universo. La muestra se ha seleccionado con base a las luminosidades publicadas en catálogos y su comparación con modelos de síntesis de población estelar. Como resultado de una serie de observaciones piloto con espectrógrafos del infrarrojo cercano, se ha obtenido el primer espectro de una de las galaxias de la muestra, detectando la línea de emisión Hα con una buena razón de señal a ruido. La tasa de formación estelar estimada a partir de dichas observaciones piloto, es consistente con trabajos en otras muestras de galaxias.

La parte instrumental de esta tesis se centra en las técnicas de espectroscopía infrarroja, para poder observar eficientemente la muestra de galaxias. El trabajo se lleva a cabo como parte del desarrollo del modo de espectroscopía de LIRIS e incluye el análisis de la sensibilidad del instrumento, la caracterización del detector y el diseño de las máscaras multi-rendija. Se realiza un estudio completo de las magnitudes límite en los modos de operación de imagen y espectroscopía, tanto para objetos puntuales como para extendidos. Se han estudiado las principales fuentes de ruido y se ha disminuido el ruido del detector para que las observaciones estén limitadas sólo por el ruido de la emisión del cielo (caso BLIP). Asimismo, se presenta una estimación de los tiempos de observación que se requerirán con LIRIS. Se realiza la caracterización y pruebas de los detectores HAWAII de grado de ingeniería y científico, así como de la electrónica de lectura. Dicha caracterización se realiza de una manera muy detallada en un banco de pruebas especialmente diseñado para tal efecto. Los principales parámetros analizados son: ruido de lectura, linealidad, ganancia, pixeles malos, efectos *glow* y *cross-talk*. El resultado obtenido en algunos parámetros es muy novedoso y se determina que la operación del detector es muy competitiva al compararla con los detectores de otros espectrógrafos del infrarrojo cercano. De igual manera, se presenta el diseño de las máscaras multi-rendija para las observaciones de la muestra de galaxias. Este diseño abarca el estudio de las características óptimas de las máscaras de rendija larga y multi-rendija. Finalmente, se analizan los diferentes prototipos de máscaras elaboradas con un novedoso proceso de manufactura, obteniendo resultados comparables con los mejores de otros observatorios.

Códigos UNESCO: 2101.04, 2103.03, 2203.08, 2209.16, 3311.13

Abstract

This thesis work is developed on the astronomical instrumentation research area and involves a scientific and an instrumental project tightly interrelated each other. Both projects are comprehended on the scientific exploitation of the multi-slit spectroscopy mode of LIRIS (Long slit Intermediate Resolution Infrared Spectrograph). This instrument is a near infrared multi-slit spectrograph that is being built at the Instituto de Astrofísica de Canarias to be installed at William Hershel Telescope.

The scientific project on this thesis is centered on the study of intermediate-redshift galaxies. It is based on the selection of a sample of from the Hubble Deep Field and Flanking Fields (HDF-N+FF). The sample includes 500 galaxies, from which 88 objects (with wide photometry and spectroscopically measured redshifts) have been selected to estimate the star formation of 0.45 to 1.1 redshift galaxies. The star formation is estimated from the Hα emission line luminosity and will allow us to constraint the galaxy formation and evolution scenarios. The sample of galaxies has been selected according to their luminosities, as published in catalogs, and in comparison with stellar population synthesis models. As a result of the pilot series of observations, the first spectra of one galaxy in the sample has been obtained, detecting the Hα emission line with a good signal to noise ratio. The estimated star formation is consistent with the results reported on other samples of galaxies.

The instrumental part of the thesis is centered on the infrared spectroscopy techniques to improve the observational efficiency. The work is comprehended into the LIRIS spectroscopy mode development, including the instrument sensitivity analysis, the detector characterization and the multi-slit mask design. A complete limiting magnitudes study is performed for both point and extended objects in the image and spectroscopy modes. The main noise sources have been studied and the detector readout noise has been reduced. In this manner background limited observations (BLIP) can be achieved. As well, an estimation of the observing times that will be required for LIRIS is presented. The tests and characterization of the readout electronics and the HAWAII engineering and scientific grade detectors are presented. Such characterization is deeply performed in a specially designed test bench. The main parameters under analysis are: readout noise, linearity, gain, bad pixels, glow effects and cross-talk. The results on these tests show that some parameters are novelty and it is concluded that the detector operation is very competitive when compared with the detectors in other near-infrared spectrographs. The multi-slit mask design for the sample of galaxies is presented. The design includes the study of the optimal characteristics for both long and multi-slit masks. Different prototype masks manufactured with a novel process are analyzed obtaining competitive results as the best in other observatories.

UNESCO codes: 2101.04, 2103.03, 2203.08, 2209.16, 3311.13

... por todas las noches y fines de semana
dedicados a estas páginas.

Gracias

A Arturo y Paco por apoyarme en este proyecto, a Ezequiel, José y Divakara por todo lo que me enseñaron, a todos los integrantes del proyecto LIRIS: Mary, Heidy, Roberto, Vicente, Antonio, Pablo, José Miguel, Felipe y los demás cuyos nombres escapan a mi memoria,
a Mercedes por sus interesantes comentarios sobre el trabajo,

a Victor y Rafa por echarme la mano en las buenas y en las malas y nunca dejar de discutir, a Corrado, Juan y Julio por hacer IDL más amigable,
a Bárbara, Pedro, Verónica, Mario, Denise, Silvana, Luis, Laura, Lisa, Sheila, Alicia, Verónica, Alejandra, Noemi, Angel, Eva, Mónica, Anibal,
a Isabel y Pablo, por estar ahí cuando las máquinas se negaban a trabajar,

a Soraya, Ito, Natacha, Román, Marisa, Nieves, Lourdes, Naira, Silvia, Sara, María, Toñi, Olli, Ana Patricia, Guillermo, Marina, Margot, Elva, Carlos, Virginia, Gustavo, Pedrito,
a Antonio, Eva, Ignacio, Inma, Juana, Agustin, Lourdes, Gonzalo, Cristina, Aurora, Elena, Carlos, Sergio, Dacil, Saulo, Roberto, Francisco, Tere y Sergio “alcalde de Antequera”,

a Rosalba, Carlos, Rosy, Sebastián, Ernesto y Claudia
a Mauricio, David, Alberto, Armando, Lety, Ruth, Gianna, Argelia, Marco, Leonel.

A todos ellos(as), por hacer de la amistad lo más valioso del mundo.

A la Agencia Española de Cooperación Internacional por otorgarme la beca MUTIS durante 2 años y 9 meses, lástima que decidieran terminar con ese programa de intercambio.
Al IAC por apoyarme cuando se terminó la beca MUTIS.

Contents

1 Introduction **1**
1.1 Star formation in galaxies 1
1.2 Astrophysical instrumentation development 4
1.2.1 LIRIS (Long-slit Intermediate Resolution Infrared Spectrograph) 5

I The star formation rate of intermediate redshift galaxies **9**

2 LIRIS-GAL sample of intermediate redshift galaxies **11**
2.1 Introduction 11
2.2 LIRIS-GAL sample selection: data sources 11
2.2.1 The Hubble Deep Field North and the Flanking Fields 12
2.2.2 Photometric and spectroscopic data 12
2.3 Construction of the LIRIS-GAL sample 16
2.3.1 Spectral classification of the galaxies 28
2.3.2 Color analysis of the galaxies 28
2.4 Analysis of the LIRIS-GAL sample 38
2.4.1 Spectral measurements and classification 39
2.4.2 The environment of the galaxies 40

3 Near-infrared spectroscopy of the LIRIS-GAL sample **49**
3.1 Introduction 49
3.2 Observing the galaxies from the LIRIS-GAL sample 49
3.2.1 Spectral resolving power required to separate the [NII] lines 50
3.2.2 Resolving Hα from the OH emission lines 50
3.2.3 Atmospheric transmission at the expected Hα wavelength 51
3.2.4 Instrument-dependent selection 54
3.3 Notes on some selected galaxies 54
3.3.1 BD0462-0 54
3.3.2 BD0693-1 55
3.3.3 BD0695-0 56
3.3.4 CS0819-0 56
3.3.5 BD0840-0 56

3.3.6 CS1050-0 . . . 57
3.4 The pilot study . . . 60
3.4.1 Long slit spectroscopy with Omega Cass . . . 60
3.4.2 Long slit spectroscopy with NICS . . . 66
3.4.3 BD0840-0 estimated SFR . . . 73

II LIRIS technical requirements and analysis 75

4 LIRIS estimated sensitivity 77
4.1 Introduction . . . 77
4.2 Observing at near-infrared wavelengths . . . 77
4.2.1 Thermal emission . . . 78
4.2.2 Sky background emission . . . 78
4.3 Estimating the signal of an object at the detector . . . 79
4.3.1 Image mode . . . 80
4.3.2 Spectroscopy mode . . . 81
4.4 Analysis of the signal to noise ratio . . . 82
4.4.1 Background limited performance . . . 82
4.5 Estimations for LIRIS . . . 83
4.5.1 BLIP case . . . 86
4.5.2 Limiting magnitudes . . . 89
4.5.3 Spectroscopy mode . . . 91
4.5.4 Limiting line fluxes in spectroscopy mode . . . 93
4.5.5 Estimations for the galaxies in the LIRIS-GAL sample . . . 96

5 Near-infrared detector characterization 97
5.1 Introduction . . . 97
5.1.1 Detectors for near-infrared spectrographs . . . 98
5.2 Detector description . . . 98
5.2.1 Detector control and readout electronics . . . 101
5.2.2 Noise in the detector readout . . . 102
5.2.3 Detector readout modes . . . 103
5.3 Detector test setup . . . 105
5.3.1 Data analysis . . . 107
5.4 Multiplexer tests . . . 110
5.4.1 Readout noise reduction workout . . . 110
5.5 Engineering detector tests . . . 116
5.5.1 Initial tests . . . 116
5.5.2 Engineering detector characterization . . . 116
5.5.3 Bias . . . 117
5.5.4 Gain . . . 118
5.5.5 Linearity . . . 122
5.5.6 Readout noise . . . 123
5.5.7 Dark Current . . . 125

5.5.8 Bad pixels . . . 125
5.5.9 Shift registers glow . . . 127
5.6 Scientific detector characterization . . . 130
5.6.1 Gain . . . 130
5.6.2 Linearity . . . 131
5.6.3 Readout noise . . . 134
5.6.4 Dark Current . . . 138
5.6.5 Bad pixels . . . 138
5.6.6 Shift registers glow . . . 141
5.6.7 Crosstalk . . . 143
5.6.8 Persistence . . . 144
5.7 Scientific detectors in other NIR instruments . . . 147
5.8 Discussion . . . 149

6 Multi-slit mask design **153**
6.1 Introduction . . . 153
6.2 Slit masks . . . 153
6.2.1 Requirements to the slit profile . . . 154
6.2.2 Slit width error . . . 154
6.2.3 Slit length . . . 155
6.2.4 Slit-to-slit position error . . . 155
6.3 Mask design . . . 156
6.4 Mask manufacturing . . . 157
6.5 Prototype slit-mask testing . . . 158
6.5.1 Laser-cut slit mask . . . 158
6.5.2 EDM-cut slit mask . . . 159
6.6 Mask design for the LIRIS-GAL sample of galaxies . . . 162

7 Conclusions **165**

1

Introduction

The observational research on astrophysics has been always related to the development of telescopes and scientific instrumentation (e.g. photometers, cameras, spectrographs, etc). As instruments get more sensitive the fainter, or deeper, objects in the Universe can be studied. Nowadays, the advent of specialized and very sensitive instruments in the optical wavelengths has allowed the identification of numerous distant galaxies. The emission of these galaxies is redshifted as a function of their distance. Therefore the systematic analysis of their properties depends on the availability of instruments observing on wavelengths redder than the optical range (i.e. infrared wavelengths). The development of a modern near-infrared (NIR) instrument opens new possibilities to the research on star formation in intermediate-redshift galaxies. The thesis work presented here describes both, the research on intermediate-redshift galaxies and the instrument development.

1.1 Star formation in galaxies

One of the most intriguing questions in modern cosmology is the epoch at which the galaxies are formed. The standard theory is that galaxies created the bulk of their stars in a single early episode as a consequence of a monolithic collapse (Sandage 1961, Eggen, Lynden-Bell, & Sandage 1962). In contrast, recent cosmological theories (e.g. White & Frenk 1991; Kauffmann, White, & Guiderdoni 1993; Cole et al. 1994) depicts an Universe dominated by cold dark matter (CDM), where the galaxies are formed from small fluctuations following a hierarchical clustering. These theories assume that massive galaxies form at all redshifts from the merger of smaller galaxies, and suggest that the bulk of the stars in the current galaxies was formed at a median redshift of z $\approx$ 1. The basic cosmological models predict the structure of the dark matter halos without giving detailed information on the gas and stars formed. That is why, a new approach is based on modeling the properties of galaxies into the hierarchical clustering models; this novel technique is called semianalytic modeling (Cole et al. 1994; Baugh, Cole, & Frenk 1996; Baugh et al. 1998). Some of the main parameters used as inputs in these models, as described by Baugh et al., are: the epoch of star formation and its timescale, the Initial Mass Function (IMF) and the merger timescale for galaxies.

Now, the models can predict properties that are observed in the galaxies, such is the case of the star formation rate (SFR). The observations establish constraints to the models while the latter

allows depicting the evolutionary stage of the galaxies in the evolution of the Universe. The observational estimation of the star formation for individual galaxies gives important clues about their stage of evolution, and to the global galaxy evolution if studied for large samples of galaxies. The most remarkable examples of these constraints are the series of observations at the Canada France Hawaii Redshift Survey (CFRS; Lilly et al. 1995), the observations of star-forming galaxies at z $\sim$ 3 by Steidel et al. (1996), the work in the "cosmic star formation history" of Madau et al. (1996) and the recent observations of Tresse et al. (2002). The *cosmic star formation history* is built from the variation of the SFR per comoving volume as a function of redshift and it allows to review the star formation activity at different ages of the Universe (e.g. see Figure 9 in Madau et al. (1996) and Figure 16 in Baugh et al. (1998)).

The methods to estimate the SFR at individual star-forming galaxies are based on: ultraviolet luminosities, Balmer-series emission lines, oxygen forbidden emission lines, far infrared luminosities and radio measurements. The first two methods are the most widely used, because they are direct estimators of the SFR. The oxygen forbidden-line-doublets, [OII] (3726, 3729 Å), are star formation indicators rather than good SFR estimators (Kennicutt, Tamblyn, & Congdon 1994). The SFR determination from ultraviolet luminosities is based on the assumption that the continuum at these wavelengths is dominated by the emission of young stars and that the star formation has remained constant over the UV-emitting population timescale. The wavelength range where the SFR scales linearly with luminosity is from 1250 to 2500 Å, where the continuum can be considered flat (i.e. not affected by the Lyα forest) for a Salpeter's (1955) IMF. The calibration of the SFR derived from ultraviolet luminosities is based on population synthesis models. Some of the latest published calibrations can be found at Cowie et al. (1997) or Madau, Pozzetti, & Dickinson (1998). The main drawback of this method is that the ultraviolet luminosities are extremely affected by dust absorption, going up to 3 mag of extinction (Buat & Xu 1996). Moreover, such extinction has a non homogeneous distribution, thus, its correction becomes highly complex (Calzetti, Kinney, & Storchi-Bergmann 1994).

The determination of the instantaneous SFR using the Balmer-series emission lines is based on the assumption that the interstellar gas is ionized by all the massive star formation. The ionizing radiation produced by hot stars excites the hydrogen atoms in the gas, which is assumed to be in thermodynamic equilibrium at 10^4 K. The recombination of all of these ionized atoms (Case B; Osterbrock 1974) produce the hydrogen Lyman, Balmer and Pashen series. The Balmer series emission lines are: Hα (6563 Å), Hβ (4861 Å), Hγ (4340 Å) and Hδ (4100 Å). Only Hα is frequently used to estimate the SFR because of the drawbacks from the other lines: Hβ is diminished by dust extinction, Hγ and Hδ are more affected by extinction and stellar absorption. The main drawbacks of Hα as a SFR tracer are the uncertainties due to extinction and the dependence on the assumed IMF (i.e. which is common to all of the direct methods). A mean extinction of A(Hα)= 0.8 to 1 mag is reported by Kennicutt, Tamblyn, & Congdon (1994) and Niklas, Klein, & Wielebinski (1997).

The diagram in Figure 1.1 shows a compilation of SFR measurements derived with Hα and ultraviolet luminosities. The diagram is a representation of the *cosmic star formation history* and contrasts both models and observations. The filled symbols are the measurements derived from Hα luminosities and the open ones are the estimations obtained from ultraviolet luminosities. The dashed line is the model "C" of Baugh et al. (1998), based on a standard CDM theory and assuming a Salpeter IMF. The data derived from the Hα luminosity are: the filled triangle is from Gallego et al. (1995) at z$\sim$0; the filled diamond is from Tresse & Maddox (1998) at z$\sim$0.2; the filled circle is from Glazebrook et al. (1999) at z$\sim$1; the filled star is from Yan et al. (1999) at $0.7 \leq z < 1.9$;

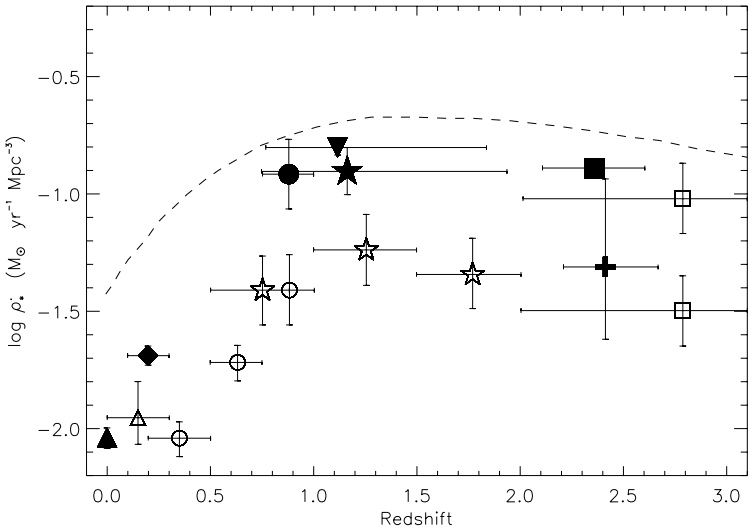

Figure 1.1: SFR per comoving volume as a function of redshift. The SFR is obtained from Hα luminosities (filled symbols) and from ultraviolet luminosities (open symbols). The dashed line is a model prediction. See text for data references.

the filled inverted triangle is from Hopkins, Connolly, & Szalay (2000) at $0.7 \leq z < 1.8$; the filled square is from Moorwood et al. (2000) at z=2.2; the filled cross is based in narrow band imaging at z=2.2 from Iwamuro et al. (2000). The data derived from UV luminosities are: the open triangle is from Treyer et al. (1998) at $0 < z < 0.25$; the open circles are from Lilly et al. (1996); the open stars are from Connolly et al. (1997); the open squares, are the point of Madau et al. (1996, 1998) at z=2.8, with and without extinction correction of Pettini et al. (1998).

Figure 1.1 shows that a peak of activity seems to have occurred at a redshift $z \approx 1$, although the SFR does not differs by more than one order of magnitude for different redshifts. However, the problems in the determination of the extinction in the measurements introduce significant uncertainties in the estimation of the SFR. According to Yan et al. (1999), the ratio from the UV (2800 Å) estimated SFR to the one estimated with Hα, goes from 2 to 3 for no correction and dust correction cases, respectively. Therefore, the analysis must be done separately for each SFR-estimation method. For that reason, the data points in Figure 1.1 have different notation: filled symbols for Hα luminosities and open symbols for UV luminosities. The numerous measurements with the latter method, could depict better the SFR profile , however this analysis depends sensitively on the correction applied for the extinction (see the large difference between the open squares values, which are given with and without correction).

In the case of Hα estimations, it is not easy to define the SFR profile due to the lack of measurements at redshift ranges of $0.3 \leq z < 0.9$ and at $z > 1$. Moreover, the horizontal error bar represents the redshift range of the sample used for the SFR estimation and, as it can be seen in the figure, some points include very large ranges. For redshift values $z > 0.4$, the Hα emission-line falls out of the optical-spectrographs range and goes into the near infrared. In fact, the measurements of Glazebrook et al. (1999) were obtained with CGS4, one of the first NIR spectrographs with a 2D

array. This point comes from the measurement of 12 galaxies which were observed individually with 1000 to 4000 s exposures. The points of Yan et al. (1999) and Hopkins, Connolly, & Szalay (2000) were obtained with NICMOS (on-board of the Hubble Space Telescope) using slit-less spectroscopy. These observations include 33 and 37 galaxies respectively with $\sim$1000 s exposures per field. The points at z $>$ 2, are: a) Moorwood et al. (2000) with 6 galaxies individually observed employing 3600 s exposures with the recently commissioned NIR spectrograph ISAAC; and b) Iwamuro et al. (2000) with narrow band imaging at the H2 filter (2.1 μm).

To understand the peak of star formation activity it is extremely important to map the redshift gaps using Hα estimations. Such a project requires to observe large samples of galaxies with NIR spectrographs. Part I of this thesis describes the construction of a sample of a hundred star-forming galaxies. It includes the study the sample selection parameters, the analysis of the sample (Chapter 2) and a series of pilot observations directed to measure their Hα luminosities (Chapter 3). If the NIR instrumentation nowadays available were used, the complete spectroscopic follow up of the sample of galaxies would require one observing night per each two galaxies (according to the experience of these pilot observations and that of Glazebrook et al.). Therefore the employment of a new NIR spectrograph that improves the observational efficiency is crucial to the project.

1.2 Astrophysical instrumentation development

The advancement of infrared technology over the past few years, especially in the fields of optical materials, detectors and cryogenics, has promoted the development of NIR spectrographs. In the past decade, these instruments have evolved in order to achieve similar characteristics (i.e. array size, resolution, slit length, sensitivity) than the optical spectrographs. Table 1.1 shows a list with some of the NIR instruments that exemplify such evolution. The list starts with those developed in the early 90's: CGS4 (Ramsay 1993) and MAGIC (Herbst et al. 1993), which are some of the first NIR spectrographs with a 2D array. They are followed by SOFI (Moorwood, Cuby, & Lidman 1998) and Omega Cass (Lenzen et al. 1998), which incorporate large-format arrays (i.e. with more than a million of pixels). After the success of these instruments, it started the development of spectrographs for 8-10 m class telescopes: Nirspec (McLean et al. 1998), ISAAC (Moorwood et al. 1998), NIRI (Hodapp et al. 2000), GNIRS (Elias et al. 1998), and NIRMOS (Le Fevre et al. 2000). Simultaneously, some instruments have been designed for 4 m-class telescopes incorporating new observing modes: NICS (Lisi et al. 1999), Flamingos (Elston 1998) and LIRIS (see Section 1.2.1). The improvements on these instruments makes them to be highly competitive, such is the case of the low resolution mode (R $\sim$ 50) in NICS, and the multi-slit spectroscopy mode in LIRIS and Flamingos.

The observational requirements to detect the Hα emission-line of intermediate redshift galaxies take some of these instruments to the limit. The series of observations cited in Chapter 3 describes the experience with some of the instrument parameters: resolution, sensitivity, spatial coverage (i.e. slit length), instrument flexures, etc. The analysis of these instrumental requirements, conjugated with the observational experience are applied to the development of LIRIS (see below for its description), in order to guarantee the success with the Hα measurements. Part II of the thesis presents my contribution to the project with the following objectives: a) the study of the instrument sensibility, b) the detector characterization and its effect on sensibility, and c) the requirements of the design of the masks used in the multi-slit mode, which represents the observing efficiency improvement.

Table 1.1: Main characteristics of near-infrared spectrographs.

Instrument	Tel. (m)	Slit length (arcmin)	J-band Resolution (0.5 or 0.6" slit)	Multi-slit?	Observing modes
CGS4	3.5	1.5	1000, 5800	no	image & spec.
MAGIC	3.5	1.4	700	no	image & spec.
SOFI[e]	3.6	4.7	1000, 1400	no	image & spec.
Omega Cass	3.5	2.4	1100	no	image & spec.
ISAAC[e]	8.0	2.0	860, 5200	no	image & spec.
Nirspec	10	0.7	2000	no	spectroscopy
NICS	3.5	4.3	1000, 2400	no	image & spec.
NIRI[a]	8.0	0.8	600	no	image & spec.
Flamingos[ac]	8.0	2.6	350, 2400[d]	11 masks	image & spec.
LIRIS[b]	4.2	4.2	1000, 3000[d]	10 masks	image & spec.
GNIRS[be]	8.0	0.8	400, 1200, 3600	no	spectroscopy
NIRMOS[ef]	8.0	8.0	5000	yes	image & spec.

Notes: *a*) Currently under commissioning. *b*) Currently under integration (estimated to be on telescope next year). *c*) Portable instrument (currently in 8m Gemini South). *d*) Upgrade. *e*) South-hemisphere instruments. *f*) Design stage.

1.2.1 LIRIS (Long-slit Intermediate Resolution Infrared Spectrograph)

LIRIS[1] is a NIR camera and spectrograph, whose design started at the IAC in 1996. This instrument will be installed at the cassegrain focus of the William Hershel Telescope (hereafter WHT) at the Observatory Roque de los Muchachos (hereafter ORM) in La Palma. LIRIS will have imaging, long-slit and multi-slit spectroscopy observing modes (Manchado et al. 1998; Manchado et al. 2000). Table 1.2 summarizes the main characteristics of LIRIS. It works in the range of 0.9 to 2.5 μm to cover the z, J, H and Ks bands. For that reason the whole instrument is cooled down inside a cryostat to a temperature of 65 K to reduce the internal thermal emission. The main cooling system is a two-stage closed-cycle refrigerator and it is precooled with LN_2.

Figure 1.2 shows the optical design of LIRIS. It is based on a classical collimator-pupil-camera concept. The entrance of the instrument is designed to match the f/11 focal ratio of the WHT Cassegrain focus. A window in the cryostat constitutes the entrance for the beam to the instrument. The *slit wheel* (also called *entrance wheel*) is located behind the window, at the telescope focal plane. This wheel includes 1 open position, 5 long slits masks (see Table 1.2 for the widths) and up to 10 multi-slit masks. The open position is employed for the imaging mode, while the long slits and the multi-slits are for the spectroscopy mode. Due to the fact that each multi-slit mask is manufactured specially for a determined observational project the cryostat includes a special removable cover to exchange the masks (the multi-slit mask characteristics are described in Chapter 6).

Following the optical path, the next element is the collimator, which is composed of three lenses and a folding mirror. This mirror redirects the optical path and allows to reduce the instrument size, as it is evident from Figure 1.2. All the elements in the figure are represented in proportional sizes. The collimator and all its components were acquired as a modular set, assembled and aligned.

[1]The description presented here is a summary of the work carried out by the LIRIS project team.

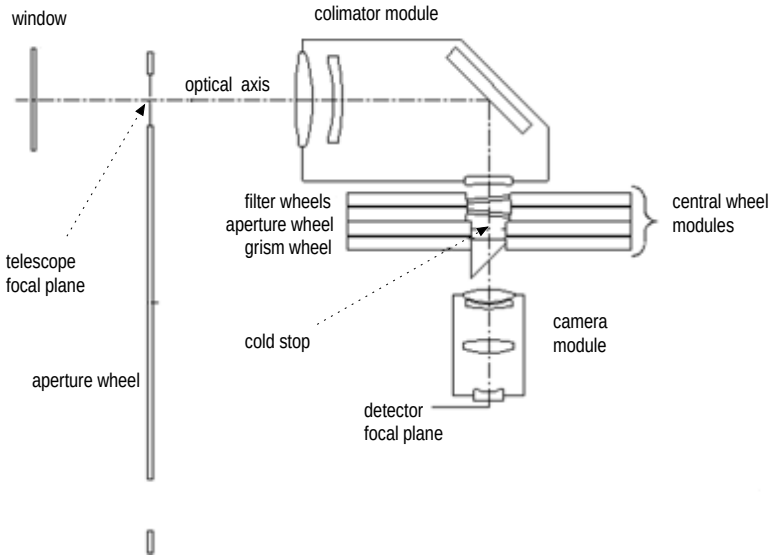

Figure 1.2: LIRIS optical design

In this manner the optical alignment is simplified. The central wheel assembly is placed in the collimated beam and it is formed by: two filter wheels, a pupil wheel and a grism wheel. The *filter wheels* hold up to 11 filters each. Table 1.3 lists the standard broad-band and narrow-band filters that have been already acquired. There are also two positions reserved for the Wollaston prisms (i.e. for polarimetry). The *pupil wheel* has place for different-size pupil masks and one apodization mask. The pupil mask is, in fact, the "pupil" of the optical design. It is basically a cold stop element that eliminates the thermal emission from the WHT-primary-mirror border[2]. The wheel contains pupil masks with different sizes in order to experimentally determine the one that produce the best thermal emission reduction. The *grims wheel* holds up to 9 grisms, which are the dispersion elements in the spectroscopy mode. Table 1.4 lists the grisms already acquired, their respective spectral ranges and resolving powers. The latter parameter is given for 2 pixel slit widths.

The next element is the camera, which is placed on the *camera wheel*. This wheel switches between the camera and the "optics" to reimage the pupil onto the detector plane (i.e. useful to align LIRIS to the telescope). It also has an aperture and a black cover. The camera consists of four lenses and, as in the case of the collimator, it was acquired assembled and aligned. The camera produces an f/3.65 beam onto the detector, which is mounted on a focussing mechanism to compensate for non-achromaticity along the observing spectral range. The detector is a 1024×1024 array that allows to image a 4.2×4.2 arcmin^2 field of view (F.O.V.). The characteristics of the detector and its control system, which has been developed under an agreement between the IAC and the Isaac Newton Group (ING), are described in Chapter 5.

The optical design of LIRIS, based on BaF2 and Silica materials, is optimized to achieve high efficiencies (Atad-Ettedgui 1999): 67% and 40.2% in image and spectroscopy modes respectively (see Chapter 4 for a complete description). The detailed optical design and the conceptual mechanical design were subcontracted to the Royal Observatory of Edinburgh. The mechanical design is

[2]In contrast to IR telescopes, the WHT has an oversized secondary mirror that introduces the primary-mirror border and structure thermal emissions into the beam.

Table 1.2: LIRIS Characteristics

Parameter	**Value**
Detector	Rockwell Hawaii HgCdTe 1024×1024 pixel
Scale	0.25 arcsec / pixel
Imaging F.O.V.	4.2×4.2 arcmin^2
Observing modes	Imaging, long-slit spectroscopy, multi-object spectroscopy, Coronography[a] and polarimetry[a]
Slits	Long slit: 0.5, 0.75, 1, 2.5, and 5 arcsec × 4.2 arcmin Multi-object: 10 multislit masks available.
Resolving power	R≈1000 and R≈3000

Note. *a*) Modes that will be added after commissioning

Table 1.3: LIRIS Filters

Filter Name	**Cut-on (μm)**	**Cut-off (μm)**
z	0.996	1.069
J	1.170	1.330
H	1.490	1.780
K_s	1.990	2.310
Br-gamma	2.150	2.182
K-continuum	2.253	2.287
H-continuum	1.558	1.582
[FeII]	1.632	1.656
H2 v=1-0	2.106	2.138
H2 v=2-1	2.231	2.265
CH4	1.640	1.740
He I	2.043	2.073

Table 1.4: Grisms spectral range

Resolving power	**Bands**	**Spectral range (μm)**
R≈1000	*z J*	0.887 - 1.531
	H K	1.388 - 2.419
R≈3000	*z*	0.997 - 1.185
	J	1.178 - 1.403
	H	1.451 - 1.733
	K	2.005 - 2.371

directed to reduce the instrument flexures. All the internal structure and mechanisms are manufactured in aluminum to minimize the total weight. All the mechanisms use cryogenic motors.

The software system will be fully integrated in the observer environment system available at the WHT and it will provide pipeline data reduction.

Some of the LIRIS characteristics that make it very competitive are:

- The imaging mode provides a wide field NIR camera (4.2×4.2 arcmin^2) and allows very easy target positioning in the slit for the spectroscopy mode. The change from imaging to spectroscopy mode simply consists on placing a grism into the optical path (i.e. the use of a filter is also necessary). Therefore, the same detector is used to image and center the object, as well as to record the spectra. In this manner, faint objects can be observed without any risk of loosing the object position at the slit.

- The multi-slit spectroscopy mode allows to observe up to 30 objects simultaneously (i.e. the recommended maximum number of slits). With such observing efficiency, several projects can be performed in a few nights.

- The polarization and spectro-polarization modes can be added as an upgrade with the inclusion of the Wollaston prisms and the calibration plates.

Part I

The star formation rate of intermediate redshift galaxies

2

Construction and analysis of the LIRIS-GAL sample of intermediate redshift galaxies

2.1 Introduction

As it was discussed in Chapter 1, large samples of galaxies are needed to fill the redshift gaps in the cosmic star formation history. These samples must be homogeneous data sets. The $0.3 < z < 0.9$ gap in the SFR measurements based on Hα luminosities can be filled with spectroscopic observations from 0.996 to 1.378 μm covering $0.46 \leq z < 1.1$ galaxies. This range includes the *z* and *J* bands. With this idea in mind, I have studied the main selection parameters to obtain a sample of star-forming galaxies to measure their Hα luminosities and determine their SFR. The spectroscopy of this sample will take advantage of the multi-slit mode of LIRIS due to the relatively high density of galaxies, as presented in chapter 6.

2.2 LIRIS-GAL sample selection: data sources

The criteria to select the sample of galaxies and study the SFR history have the following outline: to identify the galaxies that show evidence of star formation activity (see section 2.3). Several parameters can play a role in the selection and I have identified some of the most important: a) the spatial distribution of the sample, b) the precise determination of the galaxies redshifts, c) the observed evidence of star formation activity and, d) the possibility to observe of Hα emission in a OH sky-clear region of the spectrum.

The observations on the Hubble Deep Field North (HDF-N; Williams et al. 1996) derived in one of the largest data bases on galaxies as they have been extensively studied. Its depth, as well as the number of identified galaxies on it, makes the HDF-N an excellent source of galaxies with broad photometry and optical-spectroscopy data. Even more, most of these data are of public access. In spite of the high number of observations, up to date, there is not any published near-infrared spectrum for these galaxies at medium redshift (i.e. $0.4 < z < 1.1$). The SFR data estimated by Madau

Table 2.1: HDF-N Magnitude limits

Filter	AB mag limit (10 σ)
F300W	26.98
F450W	27.86
F606W	28.21
F814W	27.60

et al. (1996) and shown in Figure 1.1, was determined at the HDF-N with the 1500 Å luminosity, rather than Balmer line fluxes. The lack of near-infrared observations may be justified by the limited number of spectrographs in the northern hemisphere that work at these wavelengths. As explained in section 1.2 these instruments have been made available only in the past few years.

2.2.1 The Hubble Deep Field North and the Flanking Fields

The HDF-N and its surrounding area, known as the Flanking Fields (FF), have been observed from ground in the optical (Hogg et al. 2000; Barger et al. 1999) and in the near-infrared (Thompson, Weymann, & Storrie-Lombardi 1999, Connolly et al. 1997 and Hogg et al. 2000). Moreover, several groups have taken optical spectra from a huge number of galaxies in the region of the HDF-N (see Cohen 2001; DEEP[1]). These groups have elaborated catalogs to access the data (see Barger et al.; DEEP; Hogg et al.). The catalogs provide some reduced images, broad band photometry, morphological classification for some galaxies and redshift estimations. Recently, Fernández-Soto, Lanzetta, & Yahil (1999), DEEP and Cohen (2001) have published three new data compilations extending the photometric data and improving the redshift estimations (i.e. incorporating the spectroscopically measured values).

The HDF-N and the FF cover a region of approximately 8×8 arcmin^2. The FF are not as deep as the HDF-N, thus they have been less exploited and observed in a lower number of bands than the HDF-N. However they are deep enough to identify high redshift galaxies and, with the available spectroscopic-redshift values, these fields are a very reliable source of galaxies.

2.2.2 Photometric and spectroscopic data

The HDF-N was originally observed using the Wide Field Planetary Camera 2 (WFPC2) with the filters: F300W, F450W, F606W and F814W, whose central wavelengths are 0.294, 0.452, 0.594 and 0.792 μm respectively. The limiting magnitudes are described in Table 2.1. The FF were observed only at the WFPC2 F814W filter.

The major observation programs of these fields are shown in Figure 2.1 with the following identification: the red area is the HDF-N as observed by Williams et al. (1996); The blue area contains the FF, also observed by Williams et al.; the yellow area includes the near-infrared observations of Connolly et al. (1997); the brown area includes the optical observations of Hogg et al. (2000) and Cohen (2001); the gold area is the K_s-band observations of Hogg et al.; finally, the green area identifies the optical observations of Barger et al. (1999).

[1]DEEP is the Deep Extragalactic Probe program (Koo 1995)

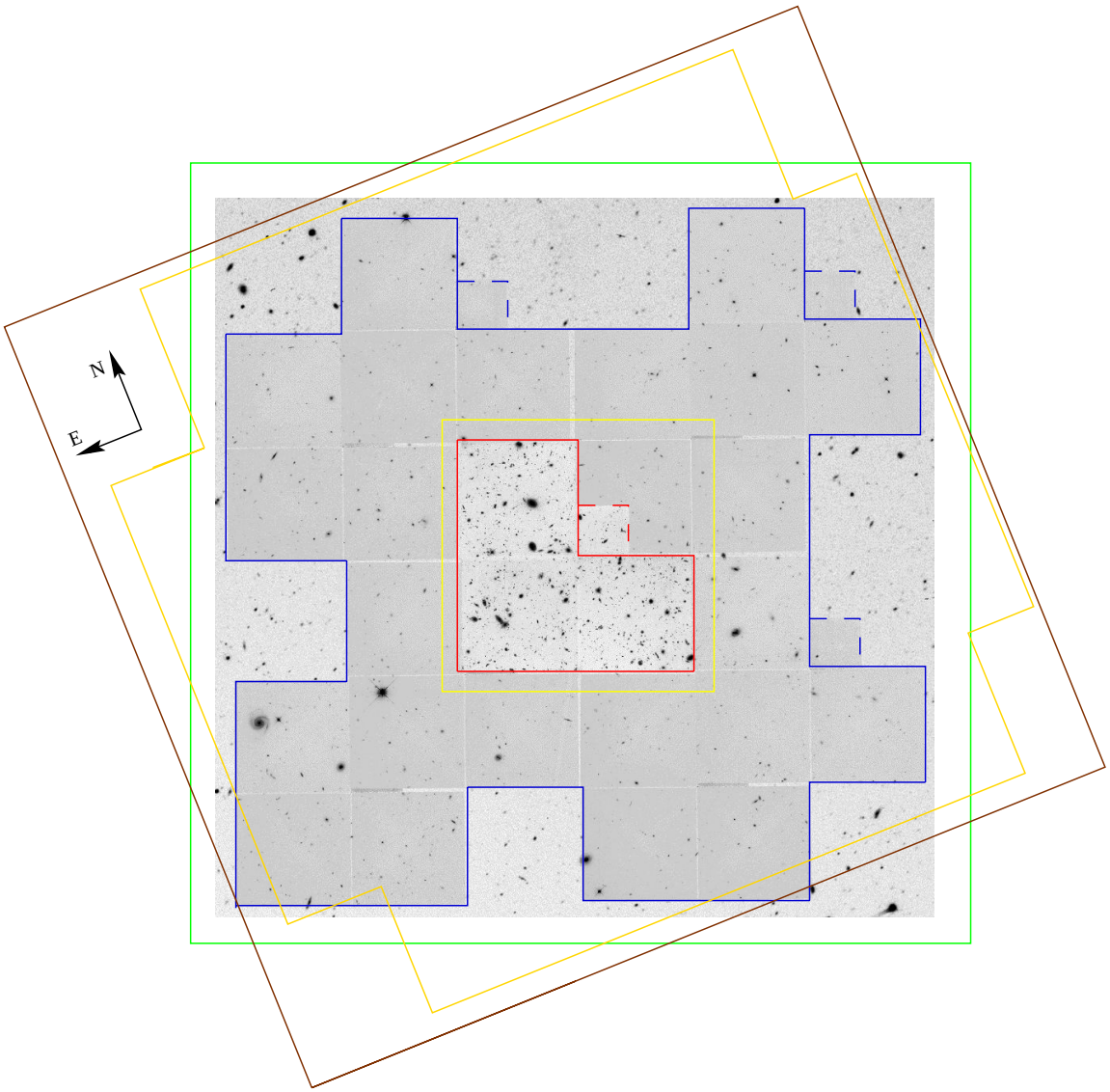

Figure 2.1: HDF-N and FF observations. See the text for the identification of the colors

Table 2.2: Data sources for the Hubble Deep Field North and the Flanking Fields

Catalog	**Fields**	**Main data**
Williams et al. (1996)	HDF-N	F300W, F450W, F606W & F814W
Hogg et al. (2000)	HDF-N + FF	U_n, G & R' & K_s
Cohen (2001)	HDF-N + FF	spectroscopic redshifts
Barger et al. (1999)	HDF-N	F300W[a], F450W[a], F606W[a], F814W[a] & HK'
Barger et al. (1999)	FF	B, V, I, HK'
DEEP	HDF-N	F606W[a], F814W[a] & spectroscopic redshifts
DEEP	FF	V(606), I(814) & spectroscopic redshifts
Connolly et al. (1997)	HDF-N	J, H & K_s
Fernández-Soto et al.	HDF-N	F300W[a], F450W[a], F606W[a], F814W[a], J^b, H^b, K_s^b

Notes: *a*) Measured from Williams et al. (1996) images, *b*) Measured from Connolly et al. (1997) images.

Several catalogs with observations at the HDF-N and FF have been published, as those listed in Table 2.2. The combined observations, from the catalogs, constitute one of the deepest sources of galaxy data. Figure 2.2 shows a representation of all the galaxies at all redshifts, identified in the fields, and published on these catalogs. It can be seen that, even the region with higher density of galaxies lies in the HDF-N itself, the surface density for the FF is as high as 53 galaxies per arcmin^2.

The largest catalog with ground observations is the one of Hogg et al. (2000). This catalog is made with observations at all the fields in the U_n, G and R' bands. The data limiting magnitudes are roughly U_n=25 mag, G=26 mag and R'=25.5 mag. The catalog in R'-band contains 3607 objects and covers an area of 8.6 $\times$ 8.7 arcmin^2 centered at the HDF-N. The area covered by this catalog is represented by a green box in Figure 2.1. The observations are from the COSMIC camera (Kells et al. 1998) at the prime focus of the Hale Telescope (Palomar Observatory). The definitions of the U_n, G and R' filters with effective wavelengths of 0.357, 0.483 and 0.693 μm respectively, can be found in Steidel & Hamilton (1993). The FWHM bandpasses of U_n, G and R' are 0.070, 0.120 and 0.150 μm respectively.

The catalog of Hogg et al. (2000) in K_s-band consists on 488 sources to a limit of K_s=20 mag. This catalog is based on near-infrared observations of a region of roughly 8 $\times$ 8 arcmin^2, centered on the HDF-N (gold area at Figure 2.1). The observations were done with the NIR camera (Jarrett 1994) mounted at prime focus of the Hale Telescope.

As part of the same group of Hogg et al., the catalog of Cohen et al. (2000) and Cohen (2001) contributes with the spectroscopic redshifts of 151 objects in the HDF-N and 554 objects in the FF to a limit of $R' \approx$24 mag and $R' \approx$23 mag respectively. The redshifts are estimated from optical spectra taken at Keck telescope with the Low Resolution Imaging Spectrograph (LRIS; Oke et al. 1995) using the multi-slit mode.

The "Hawaii Catalog Of The Hubble Deep Field" (Barger et al. 1999) covers the HDF-N and the FF. For the HDF-N, 184 objects are included with measurements at the WFPC2 bands and HK' band photometry taken with QUIRC (University of Hawaii Quick Infrared Camera; Hodapp et al. 1996) at CFHT (Canada-France-Hawaii telescope of 3.6 m) and UH (University of Hawaii 2.2 m telescope).

For the Flanking Fields, there are 2579 objects with photometry in Johnson V and Cousins I

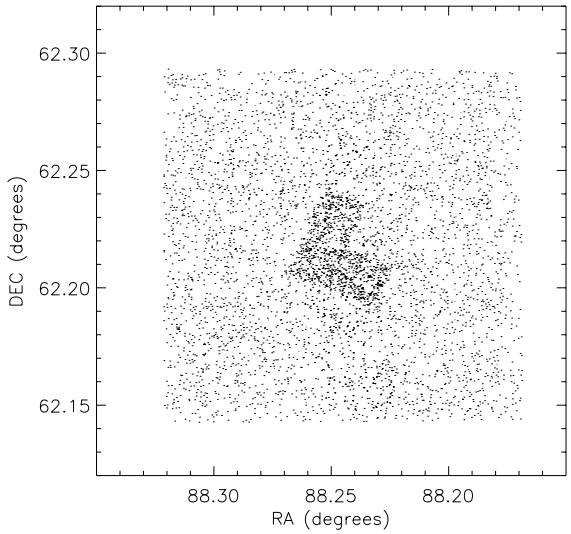

Figure 2.2: HDF-N and FF identified galaxies. Each point represents one galaxy in the catalog. The region with higher density of galaxies is the HDF-N.

bands with the UH 8K CCD Mosaic Camera at CFHT. The data limits at 2 σ are: I=24.8 mag and V=25.8 mag. B band, observed with LRIS, is also included for about half of the galaxies in the catalog. This catalog[2] includes a compilation of spectroscopic redshifts for 330 objects in the FF and 70 objects in the HDF-N. It also includes photometric redshifts for the HDF-N. The global area covered by this catalog is represented by a green box in Figure 2.1.

Connolly et al. (1997) observed the HDF-N in the near-infrared bands with the Infrared Imager (IRIM) at the KPNO Mayall 4m Telescope. The observations are in the bands J, H and K_s with limiting magnitudes of 23.4, 22.3 and 21.9 respectively. The field of view is less than 3×3 arcmin^2, covering the HDF-N (the yellow area in Figure 2.1).

The compilation of DEEP[3] contains the HDF-N and the FF with spectroscopic redshifts. For the FF, it includes 984 objects with ground-based V-band image, obtained using LRIS on Keck. The area covered by this catalog is the same than that, defined by Williams et al. (1996) for the HDF-N and the FF. As part of this catalog, Guzman et al. (1997) published optical spectra of 51 "compact" galaxies and 84 galaxies of diverse types. All the spectra were taken with the multi-slit spectrograph LRIS (Oke et al. 1995) with 3000 s exposure times and a dispersion of 1.26 Å per pixel (Phillips et al. 1997).

Finally, the most recent compilation of photometric redshifts is the one of Fernández-Soto, Lanzetta, & Yahil (1999). It only covers the HDF-N but includes the luminosity estimations for 1067 objects at all the bands observed with WFPC2 (F300W, F450W, F606W and F814W) and the NIR bands (J, H and K_s) observed by Connolly et al. (1997). The luminosity measurements are given in the AB-magnitude system (Oke & Gunn 1983). The optical limiting magnitudes of this catalog are those from the original observations. This compilation also provides the photometric

[2]The catalog is available at: www.ifa.hawaii.edu/čowie/hdf.html
[3]The catalog is available at: saci.ucolick.org/verdi/public/index.html

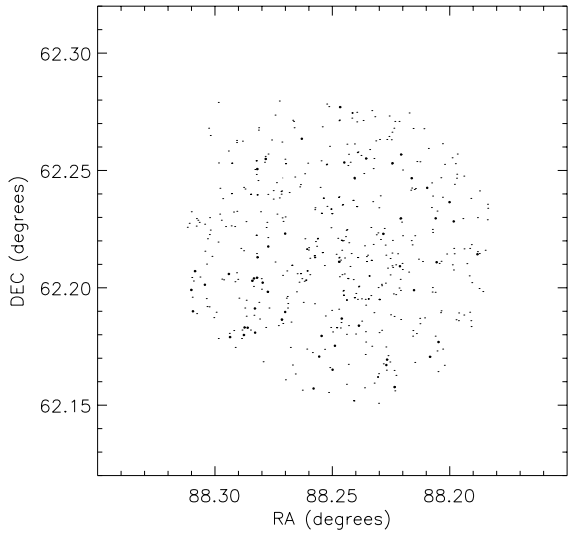

Figure 2.3: HDF-N and FF galaxies with spectroscopic redshifts. The field of view and orientation are the same than Figure 2.2

redshifts for all the identified galaxies in the HDF-N, as well as some spectroscopic redshifts.

2.3 Construction of the LIRIS-GAL sample

Based on the published HDF-N and FF data, I have constructed the sample of galaxies whose redshifted Hα emission would fall in the *z* and *J* bands. I have written a program to select the galaxies from the catalogs described before, making a correlation among the different sources of data; the objective of the program was to gather all the observations for each galaxy, including luminosities, redshifts and spectral types (or identified spectral features). The correlation technique uses the galaxies' coordinates, matching those that are closer than 2 arcsec to each other; it also includes a discrimination algorithm to match the correct galaxy when more than one match is found. The correlation among the 9 catalogs was not trivial due to the differences in the astrometry among some objects, requiring visual inspection to discriminate between two candidates in a catalog matching the same reference galaxy.

I have included only galaxies with redshifts measured spectroscopically, since those determined photometrically present large uncertainties (see Figure 2.4). This is to be able to estimate with high precision the observed wavelength of Hα for each galaxy and to determine how close it would fall respect to strong OH sky emission lines, as detailed in section 3.2.2.

The final redshift-selected sample contains 513 galaxies at $0.46 \leq z < 1.1$, and its spatial distribution is represented in Figure 2.3. It can be seen that, although the spectroscopic sample could be incomplete (i.e. due to the lack of observations), the surface density is around 13 galaxies per arcmin^2. This number gives an idea of the power of the multiobject spectroscopy, as discussed in chapter 6. The large dots in the figure, represent the HII region-like galaxies described in section 2.3.1.

Table 2.3 summarizes the redshift and luminosity correlated data for all the galaxies. The first column is the J2000 coordinate; column 2 is the spectroscopic redshift. The redshifts estimations have an error of $\sigma(z) \leq 0.002$ (Cohen et al. 1999). The rest of the columns are the photometric data detailed in the previous section, with the following order: columns 4 to 6 are from Hogg et al. (2000); columns 7 to 9 are from Barger et al. (1999); columns 10 and 11 are from DEEP and, columns 12 to 19 are from Fernández-Soto, Lanzetta, & Yahil (1999). The latter luminosities are only for the galaxies in the HDF-N. The redshift distribution of the sample of galaxies has a median of 30 galaxies at each bin (z=0.05), as it can be seen in Figure 2.5, with a peak at low redshifts.

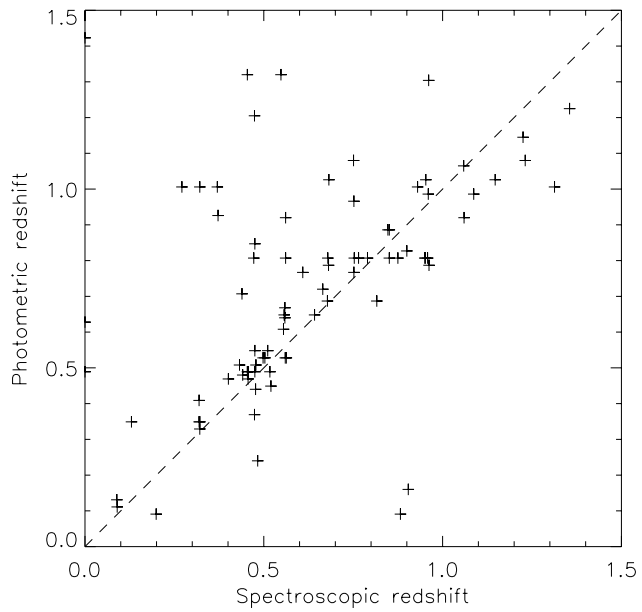

Figure 2.4: Comparison between the spectroscopic and photometric redshifts for the sample of galaxies.

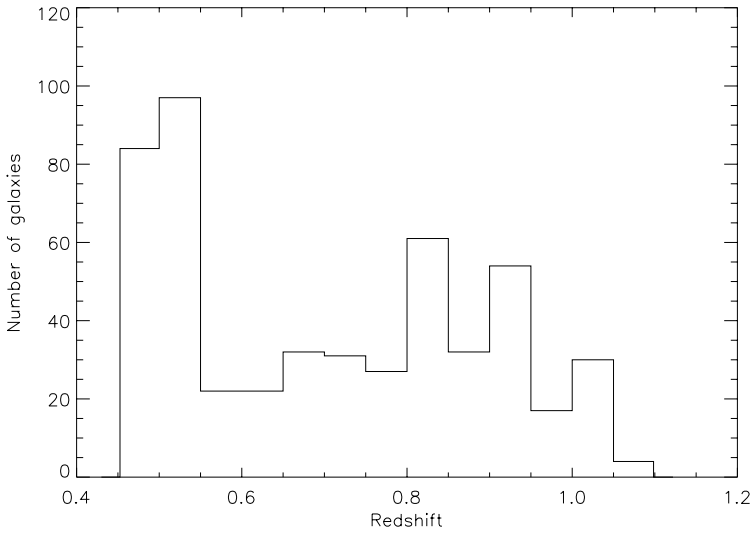

Figure 2.5: Distribution of the redshift-selected galaxies. The bin size is z=0.05

Table 2.3: Galaxies at $0.46 < z < 1.1$

J RA+DEC	zsp	zph	Un[a]	G[a]	R^a	Ks[a]	B[b]	V[b]	I[b]	J[b]	V[c]	I[c]	UAB^d	BAB^d	VAB^d	IAB^d	JAB^d	HAB^d	KAB^d
J123617.60+621402.2	0.818							22.6	21.3			21.5							
J123617.69+621344.3	0.534			23.5	20.9	17.2		22.8	20.2			20.4							
J123617.65+621408.1	0.848		22.9	23.4	22.5	18.9													
J123618.16+621257.6	0.473		24.0	24.7	23.5			24.5	23.1										
J123618.70+621154.1	0.766		23.7	23.9	22.3	18.5		24.1	22.0										
J123619.41+621428.7	0.798		23.4	23.8	22.6	19.4		23.6	21.8			21.8							
J123619.47+621252.5	0.474		22.4	22.2	20.0	16.6		22.0	19.9										
J123619.50+621158.9	0.938		22.7	23.4	22.4	19.8		23.5	22.0										
J123619.89+621347.8	0.535		21.8	22.1	20.7	17.9		22.1	20.4			20.7							
J123619.85+621255.3	0.695		23.5	24.4	23.5														
J123619.89+621251.5	0.695		20.6	21.2	20.3	18.2													
J123621.12+621207.9	0.841		23.3	23.4	21.8	18.2		23.8	21.5										
J123621.20+621306.4	0.474		23.7	23.7	21.9	19.1		23.4	21.6										
J123621.33+621417.1	0.520		23.3	22.9	20.7	16.8		22.5	20.1			20.3							
J123621.27+621100.5	0.635		23.8	24.3	22.8	20.4		24.3	22.5										
J123621.33+621109.7	1.014			25.8	23.5	18.8		25.1	21.8										
J123621.59+621300.3	0.688		22.4	22.7	21.1	17.9		22.9	20.8										
J123621.59+621122.4	0.639		23.4	24.2	22.8			24.1	22.5										
J123621.69+621218.2	1.008		23.8	24.5	23.3	20.6		24.3	22.5										
J123622.21+621237.2	0.630		23.3	23.7	21.8	18.4		24.0	21.7										
J123622.85+621451.3	0.652		24.5	24.7	23.5	20.5		24.3	22.6			22.9							
J123622.82+621259.7	0.472		23.4	22.6	20.3	17.1		22.2	20.0										
J123622.86+621118.4	0.895		24.6	24.9	23.7			24.9	23.0										
J123623.06+621346.3	0.485		22.1	22.2	20.7	17.5		21.9	20.2			20.4							
J123623.98+621121.6	0.842		23.7	24.5	23.5		24.4	24.6	22.9										
J123624.02+621109.6	0.766		23.5	23.9	22.4	19.3	24.2	23.9	22.0										
J123624.31+621525.3	0.682			24.9	22.7	18.8	25.5	24.4	21.8			22.0							
J123624.41+621454.1	0.628		24.2	23.0	20.3	16.5	24.0	22.5	19.6			19.9							
J123624.44+621448.0	0.582		24.7	24.4	22.4	18.8	25.4	24.3	21.9			22.1							
J123624.55+621111.2	0.748		24.1	24.1	22.0	18.2	24.5	23.8	21.3										
J123624.71+621510.4	0.641		22.6	22.5	20.4	16.9	23.2	22.4	19.8			20.1							
J123624.91+621438.7	0.642		25.1	24.2	21.5	17.6	25.0	23.4	20.6			20.8							
J123624.95+621252.1	0.631		24.4	24.4	22.7	20.0	25.0	24.3	22.3		23.7	22.9							
J123625.08+621300.5	0.518		24.4	23.2	20.7	17.2	23.7	22.9	20.3		21.9	20.3							
J123625.07+621341.8	0.654		24.7	25.2	24.3		25.0	24.7	23.4			23.6							
J123625.14+621227.5	1.091		24.7	25.2	23.6		25.1	24.7	23.2										
J123625.36+621235.2	0.526		24.8	24.8	22.8	19.7	25.2	24.5	22.3										
J123625.45+621519.6	0.642		22.4	23.0	21.8	19.4	23.1	22.9	21.3			21.5							
J123625.99+621411.4	0.528		24.2	24.9	23.5	20.5	24.9	24.5	23.0			23.3							
J123626.63+621252.0	0.557		21.6	22.1	20.6	17.9	22.5	22.3	20.6		21.7	20.7							
J123627.07+621509.4	0.794			24.7	21.6	17.2	25.3	23.7	20.4			20.7							
J123627.10+621001.1	0.842		22.0	22.6	21.5	19.3		23.0	21.4										
J123627.50+621026.0	0.763			25.4	23.4	20.2		25.0	22.6			22.4							
J123627.53+621541.2	0.487		23.3	23.6	21.9	19.4	23.7	23.1	21.5										
J123627.55+621418.8	0.751		23.0	23.1	22.3		23.5	23.2	22.0		23.2	22.3							
J123627.82+621240.6	0.519		24.8	23.7	21.3	18.1	24.3	23.5	20.8		22.3	20.8							
J123627.83+621124.6	0.519		23.3	23.7	22.1	19.3	23.4	23.2	21.3										
J123627.89+621449.0	0.680			24.2	21.6	17.3	25.1	23.7	20.7			21.0							
J123627.97+621122.0	0.925		22.9	23.7	22.7														
J123628.26+621237.5	0.518		22.6	22.9	21.3	18.6	23.2	23.0	21.1		22.1	21.0							
J123628.43+621037.0	0.760		23.2	23.9	22.7	20.6		23.9	22.3			22.1							
J123628.53+620951.4	1.016																		
J123628.73+621357.8	0.639		24.3	25.1	23.0	20.4	25.0	24.4	22.5		23.7	22.6							
J123628.72+621023.3	0.936		22.4	23.1	22.1	18.8		23.6	21.7			21.8							
J123628.80+621239.3	0.880		23.6	24.5	24.0		24.1	24.5	23.7		23.9	23.3							
J123629.01+621346.6	0.693		23.7	24.2	23.0	20.3	24.1	23.9	22.2		23.4	22.3							
J123629.13+621153.0	0.530		23.0	23.7	22.6	20.4	23.7	23.9	22.5		23.3	22.4							
J123629.14+621046.0	1.013		25.1	25.3	23.5	18.3	26.0	25.4	22.4										
J123629.68+621420.6	1.055		24.3	23.7	22.5	20.3	23.6	22.9	21.6		22.5	21.8							
J123629.70+621325.0	0.758		23.3	24.1	23.2		24.0	24.0	22.6		23.5	22.5							

J RA+DEC	zsp	zph	Un[d]	G[d]	R[d]	Ks[d]	B[b]	V[b]	I[b]	J[b]	V[c]	I[c]	UAB[d]	BAB[d]	VAB[d]	IAB[d]	JAB[d]	HAB[d]	KAB[d]
J123629.75+621200.3	1.016		22.7	23.6	23.1		23.6	23.8	22.6		23.3	22.6							
J123629.77+621329.7	0.748		23.4	23.9	23.0		23.6	23.5	22.0		23.1	22.1							
J123629.82+621153.4	0.529		23.7	24.3	23.1		24.3	24.3	22.8		23.5	22.7							
J123629.91+621440.9	0.762		24.1	24.4	22.8	19.1	24.4	23.8	21.7		23.1	22.0							
J123629.98+621403.1	0.793		23.0	23.3	21.9	18.2	23.6	23.1	21.1		22.5	21.3							
J123630.24+621014.0	0.482		23.2	23.5	22.0	20.2		23.4	21.8			21.7							
J123630.62+621533.7	0.530		22.9	23.5	22.0	19.8	23.7	23.3	21.7										
J123631.47+621113.9	1.013		22.4	23.2	22.0	18.8	23.4	23.3	21.5			21.5							
J123631.62+621604.0	0.784		22.6	22.8	21.3	18.2		22.6	20.7										
J123631.90+621240.4	0.528		22.2	22.8	21.5	19.6	22.9	22.9	21.3		22.1	21.2							
J123632.47+621105.1	0.518		23.5	22.1	19.6	16.2	23.3	22.4	19.7			19.8							
J123632.55+621113.3	0.518			24.9	22.5	19.7	25.6	24.6	22.1			22.0							
J123632.47+621513.2	0.684		23.7	23.8	21.9	18.2	24.3	23.7	21.3										
J123632.77+621243.8	0.562		23.8	23.6	21.4	17.7	24.2	23.7	21.2		22.8	21.3							
J123633.16+621513.8	0.521		23.1	23.4	21.9	19.1	23.7	23.3	21.6										
J123633.23+621049.9	1.006		23.5	24.3	23.3	20.2	24.4	24.3	22.4			22.3							
J123633.44+621432.3	0.748		23.8	24.5	23.0	20.2					23.2	22.2							
J123633.60+621319.8	0.845		22.8	23.2	21.7	17.9	23.4	23.0	20.9		22.4	21.1							
J123633.62+621005.6	1.015		22.7	23.4	22.1	18.1		23.6	21.5			21.6							
J123633.70+621431.0	0.519		23.8	23.2	20.8	16.8	24.0	23.0	20.5		22.4	20.8							
J123634.00+621054.4	0.762		22.0	22.7	21.5	19.0	22.8	22.9	21.2			21.2							
J123633.99+621604.6	0.835		22.9	23.5	22.6	19.8		23.5	22.0										
J123634.06+621045.8	1.011		23.3	24.2	23.2	20.0	24.1	24.2	22.6			22.6							
J123634.17+621305.8	0.847		25.3	25.6	24.2	20.1	25.5	25.5	23.2										
J123634.26+621448.3	0.507		23.0	23.7	22.5		23.7	23.6	22.3		23.2	22.3							
J123634.36+621312.5	0.845		23.8	24.4	23.1	19.7	24.5	24.2	22.2		23.5	22.3							
J123634.28+621433.0	0.520		23.9	22.7	20.2	16.9													
J123634.50+621429.7	0.519		23.8	24.1	22.5	20.4	24.5	24.0	22.1		23.4	22.2							
J123634.84+621628.3	0.847		24.5	24.7	22.7	18.3		24.2	21.7										
J123634.97+621224.1	0.562		21.8	21.6	19.6	16.1	22.3	21.9	19.5		21.4	20.5							
J123636.28+621319.8	0.680										22.9	22.0							
J123636.29+621500.7	0.559		23.4	24.3	23.0		24.1	24.0	22.4		23.5	22.6							
J123636.35+621228.2	0.486		23.0	23.1	21.4	18.5	23.5	23.2	21.2		22.8	22.4							
J123636.40+621237.3	0.961																		
J123636.50+621340.7	0.558			24.1	21.5	17.5	24.6	23.7	21.0		22.9	21.3							
J123636.65+621346.6	0.960		20.6	21.2	20.3	17.6	22.3	22.0	20.7		21.6	20.9							
J123636.59+621524.5	0.744		22.6	23.5	22.8		23.4	23.6	22.3										
J123636.69+621111.3	0.846		23.5	24.1	23.2		24.0	24.1	22.7			22.4							
J123636.76+621156.0	0.557		23.3	23.5	21.8	18.6	23.8	23.5	21.4		22.5	21.3							
J123636.79+621213.1	0.846		22.4	22.6	20.8	16.7	23.3	23.0	20.6		22.2	20.7							
J123636.74+621346.2	0.846		20.9	21.6	20.7	18.0					22.2	21.2							
J123636.88+621345.7	0.846		21.3	22.1	21.2	18.3													
J123637.04+621159.5	0.779		22.2	22.8	21.5	18.7	23.3	23.3	21.4		22.6	21.4							
J123637.07+621615.1	0.852		24.1	24.7	23.5	20.5		24.5	22.8										
J123637.36+621252.3	0.485		24.3	23.4	21.1	17.8	24.1	23.2	20.8		22.2	20.8							
J123637.72+620945.8	0.513		23.9	24.4	23.3			24.4	23.0			22.3							
J123637.77+621235.1	0.485		24.0	25.0	23.8		25.1	25.4	23.6										
J123637.80+621149.4	0.838		23.9	24.2	22.7	18.4	24.7	24.3	22.1		23.4	22.1							
J123637.97+620922.0	0.767		23.0	23.0	21.4	17.9		23.2	21.0			21.0							
J123638.03+620927.7	0.513		24.6	24.7	23.2							22.5							
J123637.97+621615.2	0.531		25.0	23.8	21.3	18.2		23.2	20.7										
J123638.13+621116.2	1.018		22.3	23.0	22.2	19.0	23.3	23.4	21.8		22.7	21.8							
J123638.11+620927.9	0.513							24.3	22.7										
J123638.14+620953.3	0.512		21.8	22.3	21.0	18.9						20.7							
J123638.20+621604.9	0.855			25.2	22.2	17.5		24.5	20.9										
J123638.29+621150.8	0.842		24.5	24.5	22.7	18.7	24.9	24.2	21.9		23.3	21.8							
J123638.43+621231.2	0.944			25.0	22.8	19.2	25.5	24.6	22.3				26.2	25.2	23.7	22.7	21.7	21.4	21.0
J123638.48+621312.9	0.635		22.7	23.4	22.2	20.0	23.5	23.5	21.9		22.8	22.0							
J123638.51+621511.1	0.462										23.6	22.7							
J123638.60+621253.3	0.960		23.9	24.7	23.4		24.8	24.5	23.2		23.8	23.1							

J RA+DEC	zsp	zph	Un[a]	G[a]	*R*[a]	Ks[a]	B[b]	V[b]	I[b]	J[b]	V[c]	I[c]	U*AB*[d]	B*AB*[d]	V*AB*[d]	I*AB*[d]	J*AB*[d]	H*AB*[d]	K*AB*[d]
J123638.60+621558.6	0.478		24.2	24.4	22.9														
J123638.61+621233.8	0.904	0.160	25.3	25.0	24.0								27.4	25.0	24.4	24.0	23.7	23.7	23.3
J123638.67+621510.1	0.462		24.5	25.1	23.6	20.2	24.5	24.2	22.2			22.7							
J123638.76+621547.1	0.904		22.6	23.3	22.2	19.7	23.3	23.1	21.4										
J123638.90+621118.6	0.934		22.2	23.1	22.5	20.1	23.2	23.6	22.4		23.0	22.2							
J123639.00+621245.0	0.487		24.6	24.3	22.5	19.7	24.6	24.3	22.2		23.1	21.8							
J123638.99+621219.7	0.609		22.9	23.5	22.1	19.7	23.6	23.7	21.9				24.0	23.6	22.9	22.2	21.7	21.6	21.5
J123639.06+621006.1	0.635		22.1	22.5	21.2	18.4		23.0	21.2			21.1							
J123639.22+621623.4	0.850		25.7	25.6	23.2	18.7		24.1	21.1										
J123639.28+621552.1	0.521		24.7	24.9	23.2		24.9	24.4	22.5										
J123639.47+621016.0	0.485		24.0	24.5	23.3			24.4	23.1			23.0							
J123639.60+621230.2	0.943	3.400		25.2	23.8								29.4	27.7	26.2	25.5	25.7	24.5	23.3
J123639.68+621009.7	0.509		23.7	23.4	21.5	18.7		23.3	21.2			21.0							
J123639.75+621547.7	0.848			25.1	22.0	17.6	25.9	24.2	20.8										
J123639.82+620953.7	0.748			26.3	25.0														
J123639.92+621250.0	0.848		22.8	23.1	21.5	17.9	23.4	23.1	20.9		22.2	20.9							
J123639.95+621029.2	0.935		24.2	24.4	22.5	18.6		24.3	21.6			21.5							
J123640.02+621207.3	1.015		24.9	24.5	22.7	18.9	24.8	24.3	21.8				26.5	24.7	23.6	22.2	21.0	20.8	20.5
J123640.12+621305.5	0.488			23.0	20.6	17.3	23.7	22.8	20.1		21.7	20.1							
J123640.32+621331.0	0.484			24.7	22.5	18.6	25.4	24.1	21.7		23.2	21.8							
J123640.49+621322.9	0.485		25.1	25.5	23.8		25.3	24.6	23.2		24.2	23.3							
J123640.50+621003.3	0.749		23.7	23.9	22.3	19.0						22.0							
J123640.88+621054.7	0.875											21.9							
J123640.85+621203.1	1.010		23.3	24.1	23.4	20.4	23.9	24.1	22.7				24.7	24.2	24.1	23.4	22.7	22.7	22.7
J123640.94+621205.3	0.882	0.091	23.4	23.6	22.9		23.4	23.8	22.4	20.9									
J123641.13+621314.3	1.017		23.4	24.2	23.0	19.5	24.1	24.1	22.2		23.3	22.2							
J123641.17+621421.0	0.519		22.9	23.1	21.4	18.4	23.2	22.8	20.9		22.2	21.1							
J123641.33+621547.6	0.472		24.2	24.3	22.8	20.2	24.5	23.9	22.3										
J123641.37+621141.5	0.585		23.9	23.9	22.3	18.3	24.4	24.3	22.0				26.2	24.8	23.6	22.5	21.4	21.0	20.7
J123641.43+621142.5	0.585		24.5	24.5	23.5	19.2													
J123641.42+621051.2	0.937		24.5	24.8	23.3	19.7	25.1	24.6	22.3			22.3							
J123641.43+621142.5	0.548	1.320											25.4	24.4	24.1	23.3	21.7	21.2	20.7
J123641.47+621402.7	0.557		24.4	23.3	20.8	17.5	24.1	22.8	20.3		22.1	20.5							
J123641.53+620902.9	0.713		22.7	23.1	22.3	19.6						22.7							
J123641.56+620948.1	0.518		23.3	22.8	20.4	16.5													
J123641.62+621200.5	0.483	0.240		26.3	25.0								27.3	26.3	25.6	25.2	24.8	24.5	25.1
J123641.74+620943.3	0.845			24.9	22.5	18.2						21.6							
J123641.68+621324.2	0.488		23.8	24.4	22.8	20.3													
J123641.80+620943.2	0.845							24.4	21.6										
J123642.04+621321.2	0.846		24.0	24.9	23.9		24.7	24.5	23.2		24.1	23.1		24.3	24.6	23.6	23.6	23.3	23.5
J123642.16+621545.2	0.857		23.7	23.5	21.6	17.3	24.1	23.3	20.8										
J123642.34+621622.3	0.855		25.3	24.8	23.3	20.6		24.4	22.4										
J123642.55+621121.9	0.845		23.1	23.9	23.0	20.2	23.9	24.0	22.4		23.2	22.2							
J123642.53+620933.8	0.530		22.8	22.5	20.7	17.4						20.3							
J123642.55+621518.4	0.533		22.6	23.1	21.7	20.0	23.3	23.0	21.4										
J123642.71+621306.7	0.485		24.1	24.0	22.0	18.4	24.7	23.9	21.6				25.6	25.6	24.9	24.0	22.5	22.2	21.5
J123642.73+621502.7	0.698		24.0	24.5	23.1	20.2													
J123642.84+621412.1	0.586		23.7	24.6	23.4		24.4	24.4	22.9		23.7	22.7							
J123643.01+621030.2	0.551		22.6	23.1	21.8	19.4		23.2	21.5			21.5							
J123643.03+621631.9	0.870		22.8	23.4	22.4	20.3		23.4	21.8										
J123643.15+621242.2	0.847	0.886					23.4	25.3	21.1	19.4			26.9	25.3	23.4	21.7	20.5	20.2	19.8
J123643.16+621242.2	0.849			25.1	22.3	18.0	25.5	24.3	21.2										
J123643.21+621148.1	1.010		24.5	24.9	23.1	18.5	24.9	24.9	22.1				26.0	24.9	23.9	22.5	21.0	20.7	20.2
J123643.24+621332.5	0.905		23.5	24.5	23.4		24.4	24.3	22.6		23.8	22.8							
J123643.50+621532.2	0.847		23.5	24.0	22.8	20.5	23.9	23.8	21.9		23.2	22.1							
J123643.61+621218.1	0.752	0.767	23.1	23.8	22.5		23.5	24.1	22.0	20.8			24.4	24.1	23.5	22.7	22.2	22.3	22.1
J123643.63+621218.3	0.748						23.9	24.0	22.2										
J123643.81+621142.9	0.765	0.807		24.1	21.2	17.3	22.5	24.6	20.3	18.7			26.3	24.4	22.4	20.8	19.8	19.5	19.1
J123643.82+621142.7	0.764						24.9	23.4	20.4										
J123643.97+621250.1	0.557		22.3	22.5	20.8	17.7	22.8	22.6	20.5				23.6	22.8	21.8	21.0	20.2	19.9	19.6

J RA+DEC	zsp	zph	Un[a]	G[a]	*R*[a]	Ks[a]	B[b]	V[b]	I[b]	J[b]	V[c]	I[c]	U*AB*[d]	B*AB*[d]	V*AB*[d]	I*AB*[d]	J*AB*[d]	H*AB*[d]	K*AB*[d]
J123644.19+621240.3	0.875	0.807					24.0	24.3	22.6	21.4			24.5	24.3	24.1	23.3	23.0	23.3	23.1
J123644.20+621247.8	0.555	0.608	21.8	22.5	21.4	19.3	22.1	22.7	21.0	20.0			22.9	22.6	22.1	21.6	21.4	21.3	21.3
J123644.27+621518.2	0.570						23.9	23.8	21.9		22.9	22.0							
J123644.19+621240.3	0.873		23.3	24.3	23.3		24.2	24.4	22.8										
J123644.38+621036.7	0.890		22.9	23.6	22.7			24.0	22.2			22.2							
J123644.42+621052.8	0.937		23.7	24.3	23.5							22.9							
J123644.38+621133.2	1.050			25.0	21.9	16.9	25.6	24.7	21.0				25.5	25.2	23.2	21.3	19.6	19.2	18.7
J123644.48+621017.9	0.518		24.4	24.5	22.9	20.0		24.3	22.4			22.2							
J123644.49+621142.3	1.020		24.0	24.8	24.3		24.0	24.2	22.6				23.9	23.6	23.5	22.8	22.2	22.4	22.1
J123644.61+620926.6	0.518		22.8	23.0	21.4	18.3						21.3							
J123644.61+621304.6	0.485		23.4	23.1	21.1	17.6													
J123644.80+621455.2	0.845		23.6	24.1	22.9	20.6	24.0	23.9	22.1										
J123644.94+621616.6	0.748		22.3	23.1	21.8	19.0		23.4	21.6										
J123645.24+621108.7	0.513		23.4	24.4	23.4		24.3	24.2	23.0		23.8	22.9							
J123645.30+621142.9	0.558		24.2	25.0	24.0		25.0	24.9	23.5				25.1	24.9	24.5	23.9	23.6	24.4	23.4
J123645.42+621523.0	0.683		22.2	23.0	22.0	19.7	23.0	23.0	21.6										
J123645.84+621102.0	0.936										23.9	21.8							
J123645.86+621202.4	0.679	0.807					24.4	25.0	23.0	21.8									
J123645.96+621201.3	0.679		24.4	25.2	23.8	20.8	25.0	25.0	23.3				25.3	25.0	24.5	23.7	23.2	23.3	23.2
J123645.97+621101.2	0.936		25.1	25.6	22.7	18.2	26.0	25.0	21.7		24.7	21.8							
J123646.13+621246.5	0.900	0.827	25.2	25.2	22.8	19.0	23.9	25.2	21.7	20.1			27.1	25.1	23.9	22.3	21.3	21.1	20.9
J123646.06+621528.3	0.851										22.8	21.6							
J123646.12+621246.4	0.901						25.3	24.5	21.7										
J123646.17+621142.2	1.013		21.9	22.6	21.5	17.3	23.0	22.8	20.9				23.3	22.8	22.3	21.3	20.1	19.8	19.3
J123646.22+621527.3	0.851		22.9	23.6	22.1	18.0	23.8	23.3	21.4										
J123646.34+621404.6	0.962	0.787					22.6	23.8	20.7	19.0									
J123646.31+621614.5	0.504		23.1	23.4	21.7	18.8		23.1	21.2										
J123646.32+621629.2	0.502		24.2	22.8	20.4	17.2		22.7	20.1										
J123646.34+621404.6	0.960		23.0	23.2	21.6	17.8	23.6	22.8	20.7				25.0	23.6	22.5	21.3	20.1	20.0	19.6
J123646.51+621151.3	0.503	0.528	25.2	24.3	22.0	19.1	23.0	24.6	21.3	19.9			27.2	24.6	23.0	21.9	21.1	20.9	20.7
J123646.56+621049.1	0.857		25.1	25.3	23.7	19.0	26.1	24.8	22.4										
J123646.80+621144.9	1.060	0.920	23.8	24.8	24.2								29.1	29.8	29.5	28.6			
J123646.84+621540.6	0.912		23.1	23.6	22.2	18.8					22.7	21.6							
J123646.76+621448.4	0.558										22.2	20.6							
J123646.86+621144.8	1.059	1.065					24.0	24.2	22.7	21.3			24.3	24.1	24.0	23.3	22.7	22.7	22.5
J123646.94+620906.6	0.905		24.5	25.1	23.8	19.9						22.7							
J123646.86+621447.1	0.558		23.3	23.3	21.0	17.7	23.9	22.8	20.4										
J123646.87+621144.7	1.059						24.2	24.2	22.8										
J123647.03+620906.9	0.905							24.8	22.9										
J123647.10+621212.5	0.677		24.6	25.6	24.6		25.3	25.4	24.0				25.7	25.7	25.4	24.8	24.9	25.0	24.2
J123647.16+621414.4	0.609	0.767	25.6	25.6	23.9	20.2	24.6	25.8	22.9	21.1			26.8	25.7	24.6	23.5	22.7	22.3	21.9
J123647.17+621414.0	0.609						25.2	24.9	22.8										
J123647.28+621628.3	0.873		24.5	24.2	21.6	17.7					23.0	20.9							
J123647.38+621620.3	0.502		23.2	23.4	21.7	19.2		23.2	21.4										
J123647.39+621628.1	0.873							23.8	20.7										
J123647.55+621252.7	0.681	0.787	24.5	25.3	24.2		24.6	25.3	23.2	22.4			25.5	25.2	24.7	24.0	23.7	23.8	24.2
J123647.53+621252.5	0.681						25.1	25.0	23.4										
J123647.76+621512.7	0.534		22.4	22.9	21.4	18.9					22.4	21.5							
J123647.79+621232.9	0.960	0.986	24.0	24.8	23.8	20.6	24.2	24.8	22.7	21.1			25.2	24.7	24.3	23.3	22.6	22.6	22.3
J123647.80+621232.8	0.958						24.6	24.5	22.8										
J123648.12+621102.2	0.650		24.1	24.2	22.5	19.3					23.3	22.1							
J123648.07+621309.0	0.476		23.9	22.8	20.4	17.2	23.4	22.5	20.0				25.1	23.1	21.4	20.4	19.7	19.4	19.2
J123648.18+621002.5	0.682		22.5	23.1	21.9	19.7		23.3	21.7			21.7							
J123648.15+621524.9	0.535		23.4	24.0	23.0		24.1	23.8	22.5										
J123648.25+621213.9	0.960						23.8	23.8	22.1				24.2	23.9	23.6	22.7	21.7	21.8	21.6
J123648.28+621507.4	0.890		25.2	25.0	22.3	17.9	25.5	24.5	21.2										
J123648.33+621214.3	0.962		23.9	24.6	23.8	20.9													
J123648.48+621540.4	0.506		23.1	23.6	22.2	20.0	23.8	23.5	21.9		23.0	22.1							
J123648.50+621329.2	0.958	0.807					23.8	24.1	22.2	20.9									
J123648.58+620932.1	0.518		22.3	22.6	21.0	18.0						21.1							

J RA+DEC	zsp	zph	Un[a]	G[a]	*R*[a]	Ks[a]	B[b]	V[b]	I[b]	J[b]	V[c]	I[c]	U*AB*[d]	B*AB*[d]	V*AB*[d]	I*AB*[d]	J*AB*[d]	H*AB*[d]	K*AB*[d]
J123648.61+621141.1	0.962										23.7	21.6							
J123648.62+621328.1	0.958		23.3	24.1	23.1		24.3	24.0	22.3				24.7	24.0	23.7	22.8	22.1	22.3	22.1
J123648.57+621048.8	0.940		23.4	24.2	23.3		24.4	24.4	22.7										
J123648.61+621141.1	0.962			25.0	22.2	17.7	25.5	24.5	21.2										
J123648.77+621318.4	0.753	0.807	23.3	24.0	22.8		23.5	24.0	22.2	21.1			24.3	23.9	23.5	22.8	22.5	22.4	22.3
J123648.77+621318.3	0.749						24.0	24.0	22.4										
J123648.98+621245.8	0.512		24.4	24.8	23.4		24.8	24.6	23.2				25.3	24.9	24.2	23.7	23.4	23.5	23.5
J123649.05+621221.1	0.953	1.026	22.6	23.3	22.5	20.0	23.2	23.5	21.8	20.5			23.9	23.5	23.2	22.4	21.8	21.9	21.7
J123649.05+621221.1	0.953						23.4	23.5	21.9										
J123649.24+621148.8	0.961	1.760	23.9	24.5	23.2	19.1							28.7	26.4	25.9	25.5	23.8	23.9	23.6
J123649.24+621156.0	0.961	1.304					23.9	23.9	22.8	21.7									
J123649.24+621148.5	0.961						24.5	24.5	22.3				25.4	24.9	24.2	23.0	21.8	21.5	21.1
J123649.28+621312.2	0.478	0.508					22.7	23.6	21.5	20.5									
J123649.34+621155.1	0.961		22.8	23.8	23.3		23.5	23.9	22.7				23.9	23.8	23.8	23.4	23.0	23.0	22.9
J123649.36+621311.2	0.477	0.440	22.8	23.3	21.9	19.4							24.1	23.4	22.7	22.1	21.7	21.5	21.4
J123649.41+621407.7	0.752	0.966					22.8	23.6	21.1	19.7									
J123649.49+621406.6	0.752		22.9	23.4	21.9	18.5	23.5	23.1	21.2				24.1	23.5	22.8	21.8	21.0	20.7	20.3
J123649.57+621220.0	0.961		24.7	24.9	24.4		24.7	24.8	23.5				25.8	25.4	25.2	24.4	23.9	25.8	23.6
J123649.62+621112.8	0.475		22.0	22.6	21.4	19.4					22.2	21.4							
J123649.63+621257.6	0.475	0.847	23.3	23.5	21.9	18.7	22.7	23.7	21.4	20.0			24.4	23.6	22.7	21.9	21.2	20.9	20.5
J123649.62+621257.5	0.477						23.6	23.2	21.4										
J123649.70+621313.0	0.475	0.489	23.1	23.3	21.4	18.0	22.4	23.7	21.0	19.7			24.9	23.5	22.3	21.5	20.7	20.3	19.9
J123649.67+621112.9	0.475						22.9	22.6	21.4										
J123649.72+621312.9	0.475						23.7	23.0	21.1										
J123649.75+621106.7	1.018		23.0	23.9	23.3	20.1	23.8	23.9	22.6										
J123649.93+621058.6	0.684		23.4	24.0	22.6	20.1					23.2	22.1							
J123649.86+621242.3	0.751	1.080	24.3	25.2	24.3								25.5	25.4	25.1	24.6	25.6	24.7	25.1
J123649.95+621637.1	0.504		22.7	22.9	21.3	18.7					22.1	21.1							
J123649.99+621637.2	0.504							22.6	20.9										
J123650.15+621216.9	0.905	1.720	24.9	25.0	23.0	18.8							29.2	28.2	28.1	28.2	25.5	25.7	23.5
J123650.14+621617.3	0.503										23.3	22.0							
J123650.19+621239.8	0.474	0.369	21.2	21.7	20.4	18.1	21.3	22.2	20.1	19.2			22.6	22.0	21.2	20.6	20.2	20.1	19.9
J123650.18+621246.9	0.678	0.687					23.0	24.7	20.8	19.4									
J123650.23+621616.2	0.503			25.0	22.6	19.7		24.2	21.9										
J123650.23+621239.7	0.474						22.1	21.8	20.3										
J123650.25+621419.7	0.816	0.687					23.9	24.3	22.5	21.4									
J123650.26+621245.7	0.680		24.7	24.2	21.7	18.0	25.2	23.8	20.9				26.7	24.7	22.9	21.4	20.5	20.1	19.9
J123650.27+621127.4	0.954		22.8	23.7	22.8	20.3	23.8	23.8	22.2										
J123650.34+621418.5	0.819		23.5	24.4	23.4		24.3	24.2	22.6				24.6	24.3	23.9	23.1	23.1	23.0	22.5
J123650.48+621316.1	0.851	0.886	24.5	24.7	23.0	19.2	24.0	25.1	22.2	20.5			25.4	24.6	23.8	22.7	21.7	21.3	20.8
J123650.71+621058.8	0.474		21.9	22.4	21.1	19.0					21.8	21.0							
J123650.74+621058.7	0.474						22.7	22.3	20.9										
J123650.83+621251.5	0.485		24.0	24.4	23.1		24.5	24.1	22.8				25.0	24.4	23.8	23.2	22.9	23.0	22.9
J123651.64+621052.3	0.518		23.1	24.0	23.0						23.5	22.7							
J123651.77+621353.7	0.557	0.648	22.6	22.7	21.0	17.7	22.0	23.1	20.5	19.2			23.9	22.9	21.9	21.1	20.3	19.9	19.6
J123651.84+621125.4	0.919		22.2	22.2	21.6						22.4	21.8							
J123651.79+621353.8	0.557						23.1	22.5	20.5										
J123651.96+621332.1	1.087	0.986	24.0	24.6	23.5	19.8	24.1	24.6	22.4	20.9									
J123651.96+621400.7	0.559	0.668	24.3	24.5	23.0	20.6	23.7	24.5	22.4	21.2									
J123651.98+621400.8	0.557						24.6	24.2	22.5				25.2	24.5	23.7	23.0	22.6	22.4	22.1
J123652.03+621059.1	0.955		24.0	24.6	23.6		24.6	24.4	22.6										
J123652.24+620957.6	0.750		24.3	24.6	23.0	19.6						22.2							
J123652.30+621537.0	0.936			25.7	22.7	18.2	25.9	24.6	21.5										
J123652.49+620919.6	0.954			25.5	22.8	18.4						21.6							
J123652.43+621637.8	0.515		23.4	24.1	22.7			23.9	22.3										
J123652.80+611405.9	0.498	0.528					24.0	24.8	22.6	21.6									
J123652.84+621404.8	0.498		24.2	24.9	23.4	20.6	25.0	24.4	22.6				25.5	24.9	24.1	23.3	22.8	22.6	22.3
J123652.90+621509.6	0.942										23.8	21.7							
J123652.93+621642.0	0.558		25.0	25.4	24.0			24.8	23.4										
J123652.99+621508.6	0.942			25.4	22.8	18.4	25.9	24.8	21.5										

J RA+DEC	zsp	zph	Un[a]	G[a]	R[a]	Ks[a]	B[b]	V[b]	I[b]	J[b]	V[c]	I[c]	UAB[d]	BAB[d]	VAB[d]	IAB[d]	JAB[d]	HAB[d]	KAB[d]
J123653.20+621116.9	0.942		23.1	23.5	22.0	18.0	23.8	23.4	21.2			22.2							
J123653.36+621025.8	0.973		23.2	24.0	23.2														
J123653.43+621234.3	0.560	0.528	23.9	24.2	22.7	20.2	23.5	24.3	22.2	21.0									
J123653.45+621234.3	0.559						24.2	24.0	22.3				25.0	24.2	23.5	22.8	22.3	22.1	22.0
J123653.65+621417.6	0.517	0.489	24.4	24.8	23.3		23.8	24.7	22.7	21.3			25.5	24.9	24.1	23.5	23.0	22.8	23.2
J123653.66+621417.4	0.517						24.8	24.3	22.8										
J123653.88+621254.0	0.642	0.648	22.4	22.6	20.9	17.6	22.0	22.9	20.3	19.1			23.6	22.8	21.9	20.9	20.1	19.7	19.4
J123653.90+621606.9	0.851		23.0	23.7	22.8	20.3		23.5	22.0		22.9	22.0							
J123653.89+621253.9	0.642						22.9	22.5	20.4										
J123654.02+621046.3	0.594		22.8	23.6	22.6		23.7	23.7	22.3		23.2	22.4							
J123654.07+621354.2	0.851	0.807	23.2	23.8	22.7	19.8	23.4	23.8	21.8	20.7			24.4	23.8	23.4	22.4	21.8	21.6	21.4
J123654.13+621514.9	0.849		22.7	23.6	22.8		23.4	23.4	22.1		23.1	22.1							
J123654.08+621354.3	0.849						24.0	23.5	21.8										
J123654.36+621434.2	0.577		22.7	23.4	22.1	19.6	23.5	23.2	21.6		22.6	21.6							
J123654.96+621314.8	0.511		24.8	24.9	23.8		24.2	24.1	23.0				25.2	25.0	24.4	23.8	23.7	23.9	23.4
J123654.90+621315.9	0.511	0.548					24.3	25.1	23.1	22.1									
J123655.14+621303.7	0.952				24.2	19.9	26.9	26.3	22.9				28.2	27.2	25.2	23.5	22.2	21.9	21.6
J123655.39+621311.0	0.968	2.680	25.0	25.4	22.8	18.2							28.1	27.4	26.7	26.3	24.9	24.8	24.1
J123655.47+621246.7	0.790	0.807					23.0	23.6	21.4	20.1									
J123655.49+621402.6	0.564		24.6	24.9	23.0	19.9	25.3	24.6	22.5				25.5	24.7	23.9	23.0	22.4	21.9	21.9
J123655.57+621135.6	0.559		22.8	23.4	22.3	19.9					22.9	22.0							
J123655.55+621359.8	0.559	0.640	24.1	25.0	23.7								25.2	25.0	24.4	23.8	23.9	23.2	23.3
J123655.59+621246.2	0.790		23.8	24.4	23.0	19.8	23.6	23.4	21.4				24.1	23.6	22.9	21.9	21.2	21.0	20.7
J123655.59+621249.3	0.950	0.807	23.3	24.3	23.5		24.0	24.3	22.6	21.7			24.3	24.1	23.9	23.1	22.7	22.7	22.7
J123655.67+621249.0	0.950						24.3	24.5	22.8										
J123656.03+621020.7	0.938		24.0	24.8	23.6	20.5		24.4	22.6			22.5							
J123656.61+621220.1	0.930	1.006	25.1	25.2	23.1	18.7	24.1	25.1	21.9	19.9									
J123656.62+621245.5	0.518		23.0	22.5	20.0	16.6	23.6	22.6	20.0				23.9	22.4	21.0	20.0	19.0	18.8	18.5
J123656.89+621301.5	0.474	1.205	23.9	24.8	23.6	19.2	24.2	24.7	22.4	20.4			25.2	24.7	24.3	23.1	21.5	21.2	20.8
J123656.90+621258.0	0.520	0.449	25.4	25.3	23.8	20.7	24.3	25.5	22.8	21.5			26.4	25.5	24.4	23.7	23.1	23.0	22.9
J123657.07+621511.2	0.849		23.8	24.5	23.5	20.5	24.5	24.3	22.6		23.7	22.8							
J123657.18+621225.9	0.561	0.807	22.8	23.6	22.3	20.3	23.1	23.7	21.9	20.7			23.8	23.6	23.0	22.4	22.1	22.1	22.0
J123657.27+621259.5	0.475	0.548	21.6	22.3	21.0	19.1	22.0	22.7	20.9	20.0			22.7	22.4	21.8	21.3	21.1	21.0	21.0
J123657.23+621225.8	0.561						23.6	23.4	22.0										
J123657.30+621026.1	0.847		24.1	24.9	23.2	19.6	22.6	24.6	22.2										
J123657.32+621259.5	0.473							22.3	21.0										
J123657.49+621211.0	0.665	0.720											26.9	24.3	23.1	21.2	20.1	19.8	19.5
J123657.51+621212.1	0.561	0.920											25.0	24.4	24.1	23.2	22.6	22.7	22.6
J123657.69+621315.3	0.952	0.807	23.1	23.8	22.9	19.8	23.6	24.0	22.2	20.9			26.8	26.2	25.6	25.2	25.3	24.9	
J123657.72+621315.2	0.952						23.9	23.8	22.3				24.4	24.1	23.8	23.0	22.5	22.3	22.3
J123657.76+621454.8	0.849		24.3	24.4	22.4	18.4	24.9	23.9	21.4										
J123657.83+621210.1	0.971		23.1	24.1	22.9						23.3	22.5							
J123658.06+621137.8	0.681		23.1	23.9	23.0		23.7	23.9	22.6										
J123658.26+620923.1	0.530		23.4	23.4	22.0	19.7		23.4	21.8										
J123658.35+621214.1	1.020		23.4	24.3	23.7		23.7	23.9	22.6				24.4	24.0	23.9	23.2	22.8	22.9	23.0
J123658.63+621221.8	0.682	1.026	23.7	24.5	23.4		24.0	24.5	22.7	21.4			24.7	24.5	24.0	23.3	23.0	22.9	22.9
J123658.70+621438.3	0.512		23.1	23.7	22.3						23.1	22.1							
J123658.66+621221.6	0.681						24.4	24.5	22.8										
J123658.82+621434.8	0.678		22.6	22.6	20.8	17.3	23.0	22.5	20.1		21.8	20.4							
J123658.96+621208.8	0.853		23.9	24.1	22.3	17.9	24.6	23.8	21.3		23.1	21.5							
J123659.41+621221.5	0.472	0.807	23.8	24.9	23.5		24.2	24.8	23.0	21.8			25.3	25.1	24.5	24.1	23.6	23.5	24.6
J123659.54+621153.9	1.021		22.5	23.4	22.5	19.4	23.4	23.5	21.9		23.0	22.1							
J123659.89+621449.8	0.762		23.1	23.2	21.6	18.0	23.5	22.9	20.9		22.3	21.1							
J123659.83+620947.9	0.679		22.8	23.6	23.0			23.7	22.5										
J123700.04+621605.7	1.013		22.5	23.3	22.4	19.7		23.2	21.6		22.7	21.7							
J123700.16+621615.1	0.914		23.1	23.8	22.8	20.1					23.2	22.0							
J123700.36+621616.9	0.913		23.0	23.6	22.3	18.8		23.4	21.6		23.0	21.7							
J123700.42+621001.6	0.791		23.4	24.1	23.2			24.2	22.7										
J123700.53+621234.7	0.563	0.528	24.7	23.8	21.4	18.2	22.5	24.2	20.8	19.5			26.5	24.1	22.5	21.3	20.6	20.3	20.1
J123700.55+621234.5	0.562						24.3	23.4	20.8										

J RA+DEC	zsp	zph	Un[a]	G[a]	R[a]	Ks[a]	B[b]	V[b]	I[b]	J[b]	V[c]	I[c]	UAB[d]	BAB[d]	VAB[d]	IAB[d]	JAB[d]	HAB[d]	KAB[d]
J123700.73+621107.3	0.801		23.3	24.0	22.9	20.2	23.9	23.9	22.3		23.3	22.3							
J123700.90+621028.4	0.563		23.5	23.7	22.2	19.4		23.6	21.9										
J123701.11+621426.0	0.901		23.6	24.3	23.4	20.6	24.4	24.0	22.6		23.8	22.8							
J123701.44+621135.7	0.594		23.2	23.5	22.0	19.1	23.7	23.4	21.6		22.7	21.7							
J123701.51+621129.0	0.779		22.5	22.9	21.4	18.0	23.2	22.9	20.9		22.2	21.1							
J123701.57+621146.6	0.884										22.6	21.9							
J123701.67+621226.0	0.973		23.6	24.5	23.9		24.4	24.6	23.3										
J123701.77+621144.0	0.744		23.1	22.9	22.1	20.5	23.1	22.9	21.8										
J123701.92+621510.3	0.938		22.3	23.1	22.2	19.4					22.5	21.6							
J123701.93+620939.0	0.750		22.9	23.5	22.4	20.2		23.6	22.0										
J123701.94+621510.3	0.938						23.2	23.0	21.4										
J123702.07+621517.3	0.744		24.5	24.9	23.5	20.3	24.8	24.5	22.7		23.7	22.6							
J123702.03+621348.8	0.511		22.7	23.5	22.3		23.7	23.4	22.0										
J123702.49+621342.0	0.559		21.7	22.4	21.2	18.9	22.7	22.6	21.1		22.2	21.3							
J123702.53+621105.3	1.014		23.1	23.8	23.4		23.7	24.0	22.9		23.5	22.8							
J123702.54+621448.4	0.558		23.9	24.1	22.3	19.8	24.6	23.9	21.8		23.2	21.9							
J123702.56+621219.2	1.073		24.8	25.4	24.9		25.1	25.2	22.8		24.7	23.0							
J123702.67+621347.2	0.513		23.4	24.3	23.1	20.7	24.2	24.0	22.7		23.9	23.5							
J123702.71+621543.5	0.514		20.2	20.7	19.4	16.4	21.2	20.9	19.2		20.5	19.4							
J123702.71+621111.5	0.560										22.3	21.0							
J123702.80+621428.8	0.898										24.0	22.7							
J123702.81+621110.4	0.560		23.6	23.5	21.6	18.0	23.8	23.3	21.0										
J123702.89+621423.7	0.512		22.2	22.3	20.2	17.1	22.9	22.2	20.0										
J123702.92+621427.6	0.898		24.3	24.9	23.6		25.1	24.6	22.7										
J123703.27+621417.8	0.512		24.2	23.0	20.9	17.7	23.8	22.8	20.4		22.1	20.6							
J123703.29+621646.6	0.744		22.8	23.3	22.2	19.9		23.2	21.7										
J123703.50+621102.0	0.518		24.6	23.6	21.4	18.3	24.0	23.2	20.9										
J123703.80+621353.1	0.745		21.7	22.5	21.6	19.2	22.8	22.8	21.4		23.1	21.9							
J123703.90+621441.1	0.475		22.3	22.8	21.4	19.2	23.1	22.6	21.1		22.2	21.4							
J123704.20+621239.6	0.861		23.4	23.7	23.1	20.4					23.2	22.8							
J123704.24+621624.8	0.474		22.9	23.0	21.4	18.3		23.0	21.3			21.5							
J123704.61+621416.0	1.050		23.7	24.5	23.9		24.4	24.3	23.1		24.0	23.3							
J123704.62+621429.1	0.561		23.0	22.9	20.9	17.4	23.3	22.6	20.4		21.9	20.6							
J123705.02+621546.9	0.532		23.8	24.3	22.7	20.7	24.3	23.9	22.2		23.3	22.5							
J123705.57+621129.2	1.001		23.3	23.3	22.3	20.1	23.7	23.3	22.2		23.0	22.2							
J123705.75+621525.1	0.503		22.9	23.3	21.8	19.3	23.5	23.1	21.4		22.6	21.6							
J123705.81+621317.2	0.753		22.4	23.1	21.9	19.5	23.4	23.3	21.6		22.9	21.8							
J123705.83+621423.4	0.970		23.4	23.9	22.4	18.1					22.9	21.6							
J123705.84+621153.8	0.904		22.3	22.6	21.2	17.5					22.0	20.7							
J123705.87+621153.6	0.902						23.0	22.6	20.5										
J123706.04+621340.4	0.672		24.0	24.0	23.2		24.1	23.8	22.9		23.5	23.0							
J123706.19+621332.7	0.753		22.7	23.3	21.8	18.7	23.6	23.4	21.4		22.8	21.6							
J123706.27+621517.7	0.840		22.0	22.9	22.2	20.2	22.5	22.5	21.2		22.2	21.4							
J123706.26+621059.1	0.906		24.6	25.4	24.0		24.4	24.1	22.8										
J123706.41+621521.5	0.513		23.5	23.9	22.3	19.7	24.2	23.8	22.0		23.2	22.1							
J123706.54+621512.5	0.840		23.1	24.0	22.9		24.4	24.0	22.4		24.0	22.4							
J123706.83+621006.6	0.938		23.1	23.7	22.8	19.9		23.7	22.2										
J123706.93+621208.0	0.693		24.2	24.9	24.1		24.8	24.8	23.1		24.3	23.3							
J123707.23+621157.8	0.593		23.0	23.6	22.4	20.3	23.6	23.7	22.1		23.0	22.1							
J123707.25+621214.1	0.655			24.8	22.1	18.5	25.1	23.9	21.2		23.1	21.3							
J123707.42+621356.7	0.752		24.0	24.7	23.6	20.5	24.6	24.5	22.7		23.7	22.7							
J123707.62+621112.1	0.472		23.4	22.5	20.7	17.7	23.1	22.5	20.4		21.8	20.5							
J123707.75+621137.7	0.557		22.7	23.4	22.4		23.4	23.4	22.0		22.9	22.0							
J123707.84+621605.7	0.936		22.9	23.3	21.8	17.7		23.1	20.9			21.2							
J123707.87+621602.0	0.514		23.2	24.0	22.6			23.8	22.2			22.4							
J123708.00+621444.5	0.570		24.2	24.2	22.2	19.3	24.6	24.0	21.7		23.2	21.9							
J123708.08+621246.8	0.654		22.4	23.0	21.8	19.8					22.7	21.7							
J123708.12+621422.6	0.563		22.7	22.4	19.9	16.5					21.6	19.9							
J123708.16+621215.3	0.594		22.8	23.4	22.0	19.7	23.4	23.4	21.7		22.7	21.7							
J123708.13+621502.0	0.570		25.1	24.9	22.6	19.6					24.1	22.2							

J RA+DEC	zsp	zph	Un[a]	G[a]	R[a]	Ks[a]	B[b]	V[b]	I[b]	J[b]	V[c]	I[c]	UAB[d]	BAB[d]	VAB[d]	IAB[d]	JAB[d]	HAB[d]	KAB[d]
J123708.10+621246.7	0.654						23.3	23.3	21.7										
J123708.16+621422.5	0.563						23.2	22.3	19.6										
J123708.34+621453.9	0.564		22.4	23.1	21.8	20.0	23.2	23.1	21.5		22.6	21.7							
J123708.31+621252.5	0.838		22.8	23.4	22.2	19.1	23.6	23.4	21.6		22.7	21.7							
J123708.33+621320.8	0.785		23.1	23.8	22.8						23.2	22.3							
J123708.36+621514.6	0.839		22.0	22.7	21.6	18.9					22.1	21.1							
J123708.37+621320.6	0.785						23.7	23.7	22.3										
J123708.38+621514.7	0.839						22.8	22.6	20.9										
J123708.65+621501.4	0.570		24.8	24.0	21.6	18.5	24.7	23.6	21.1		22.9	21.3							
J123708.66+621128.5	0.907		22.0	22.8	22.2	20.4	22.7	23.0	21.8		22.5	21.8							
J123708.83+621214.4	0.788		24.3	24.9	23.9		24.8	24.9	23.4		24.2	23.4							
J123708.88+621117.9	0.639		24.8	24.9	23.0	19.6	24.9	24.4	22.3		23.5	22.2							
J123708.95+621202.2	0.855		23.0	23.8	22.9		23.8	23.8	22.3		23.2	22.4							
J123709.20+621210.9	0.476		24.0	24.4	23.0		24.4	24.4	22.7		23.7	22.8							
J123709.56+621423.4	0.476		24.8	23.4	21.1	18.1					22.0	20.5							
J123709.61+621055.2	0.858		23.3	24.0	23.1		24.0	24.0	22.6		23.3	22.5							
J123709.59+621423.5	0.476						23.9	22.9	20.4										
J123710.24+621058.9	0.475		23.6	23.8	22.3	20.3	24.0	23.7	22.1		23.0	22.1							
J123710.56+621141.0	0.789		22.1	22.6	21.2	17.8	23.2	23.0	21.1		22.5	21.3							
J123710.54+621116.3	0.841		23.7	24.6	23.6		24.4	24.4	22.8		23.9	22.9							
J123710.58+621341.6	0.747		23.2	23.7	22.4	19.8	23.8	23.6	21.8										
J123710.79+621431.5	0.677		25.0	24.7	22.3	19.1					23.4	21.6							
J123710.91+621059.0	0.747		24.6	25.6	24.2		24.8	24.8	23.0		24.6	23.2							
J123710.86+621129.1	0.475		23.7	24.2	22.8		24.3	24.0	22.5		23.6	22.8							
J123710.91+621059.0	0.747																		
J123711.08+621047.6	0.483		25.1	25.2	23.9		24.4	24.2	22.8		23.6	22.8							
J123711.13+621433.9	0.677		22.7	22.7	21.8		23.4	23.3	21.8										
J123711.14+621257.0	0.484		23.7	24.5	23.2		24.3	24.1	22.8		23.6	22.7							
J123711.36+621545.1	0.692		22.6	23.5	22.4	20.2	23.7	23.7	22.2		23.4	22.4							
J123711.46+621055.3	0.855		22.9	23.5	22.4	19.7	23.8	23.7	21.9		23.1	22.0							
J123711.59+621042.4	0.778		22.3	22.9	21.9	19.9	23.1	23.1	21.6		22.5	21.6							
J123711.75+621300.5	0.485		23.2	24.0	23.0		24.0	23.8	22.7										
J123712.15+621144.2	0.909		23.8	24.4	23.1	20.2	24.4	24.1	22.7										
J123712.38+621213.1	0.476		24.9	25.7	24.4		25.9	26.0	23.9										
J123712.68+621223.0	0.557		23.3	23.8	22.3	19.9	23.9	23.7	21.9		23.1	22.0							
J123712.68+621546.1	0.937		22.6	23.2	22.0	18.6					22.5	21.5							
J123712.68+621542.8	0.533		22.6	22.8	21.3	18.6	23.1	22.8	21.0		22.3	21.2							
J123712.63+621357.3	0.850		23.3	24.1	23.1		24.1	24.0	22.3										
J123713.00+621209.5	0.559		23.5	24.2	22.9	20.4	24.3	24.1	22.5		23.6	22.6							
J123712.96+621028.6	0.858		23.5	23.9	22.6	19.3		23.8	22.0		23.1	22.0							
J123713.10+621333.9	0.842		22.6	23.2	22.1	19.6	23.3	23.2	21.6										
J123713.30+621054.3	0.936		21.9	22.6	21.8	19.3	22.7	22.6	21.3		22.2	21.3							
J123713.31+621356.4	1.014		22.0	22.9	22.4	20.3	22.7	22.9	21.8										
J123713.70+621511.3	0.524		23.0	23.0	21.2	18.0					22.0	20.9							
J123713.79+621424.5	0.475		23.9	23.7	21.5	18.2					22.4	21.1							
J123713.73+621511.3	0.524						23.3	22.7	20.6										
J123713.81+621424.6	0.475						24.0	23.2	20.9										
J123713.85+621335.2	0.779		22.3	22.9	21.6	18.9	23.1	22.9	21.1										
J123714.12+621044.4	0.821		22.4	23.1	22.3		23.2	23.2	21.9		22.7	21.9							
J123714.25+621050.0	0.525		23.0	23.0	22.2		23.3	23.0	22.0		22.9	22.1							
J123714.38+621221.2	1.084		25.5	25.2	24.1	19.9	25.5	24.8	22.8		23.9	22.7							
J123714.48+621529.8	0.857			25.7	22.8	18.4	26.6	24.6	21.4										
J123715.07+621334.1	0.898		23.1	23.8	23.0	20.4	23.9	23.8	22.2										
J123715.49+621212.2	1.014			25.3	23.2	18.6	26.2	26.0	22.3		24.2	22.3							
J123715.71+621416.7	0.760		22.6	23.3	22.0	19.3	23.5	23.2	21.5										
J123715.91+621213.3	1.020			25.2	23.2	18.3	25.4	24.8	22.2		24.0	22.5							
J123716.02+621343.5	0.681		23.2	23.8	22.2	19.3	23.9	23.5	21.6										
J123716.34+621432.8	0.635		22.8	23.4	22.5														
J123716.37+621353.1	0.476		22.3	22.9	21.4	19.4	23.3	22.9	21.4										
J123716.63+621511.4	0.559																		

J RA+DEC	zsp	zph	Un[a]	G[a]	R[a]	Ks[a]	B[b]	V[b]	I[b]	J[b]	V[c]	I[c]	UAB[d]	BAB[d]	VAB[d]	IAB[d]	JAB[d]	HAB[d]	KAB[d]
J123716.67+621644.4	0.557		22.7	23.2	21.9	18.4		23.1	21.6										
J123716.70+621042.2	0.821		21.9	22.5	21.5	19.7					22.4	21.5							
J123716.72+621310.3	0.898		23.2	23.8	22.7	19.9	23.7	23.6	21.8										
J123717.15+621122.6	0.676			25.7	22.9	19.1	26.3	24.6	21.9		23.7	22.1							
J123717.65+621114.2	0.906			24.7	22.0	17.3	25.6	24.1	20.8		23.0	21.0							
J123718.05+621248.3	0.912		24.3	24.6	22.8	18.8	25.2	24.5	22.1		23.5	21.9							
J123718.45+621553.7	0.476		22.2	22.4	20.6			22.2	20.3										
J123718.43+621328.7	0.476		24.5	24.7	22.7	19.7	24.6	24.1	22.2										
J123718.66+621131.0	0.555		24.7	25.2	23.9						24.4	23.1							
J123718.58+621347.8	0.480		23.2	23.9	22.5		23.8	23.4	22.1										
J123718.65+621321.7	0.475		24.0	23.2	21.0	17.7	23.7	22.8	20.4										
J123718.78+621604.8	0.558		23.0	23.3	21.7			23.0	21.2										
J123719.04+621315.4	1.005		22.8	23.7	23.1		23.6	23.7	22.5										
J123719.13+621131.1	0.556		21.8	21.8	20.0	16.8	22.5	22.0	19.9		21.4	20.1							
J123719.23+621236.3	0.484		23.7	24.1	22.5	19.7	24.0	23.6	21.9		22.8	21.8							
J123719.28+621143.5	0.784		23.1	23.8	22.8	20.1	23.8	23.7	22.1		23.1	22.2							
J123719.60+621256.2	0.909		24.9	25.0	23.3	19.7	25.5	24.7	22.2		23.5	22.1							
J123719.64+621337.6	0.479		22.8	22.7	20.5	16.9	23.5	22.7	20.4										
J123720.68+621216.7	0.476		24.6	24.7	23.9		25.1	24.8	23.3		24.3	23.8							
J123720.87+621340.5	1.020		23.2	23.9	23.0		23.8	23.9	22.2										
J123721.15+621343.7	1.022		21.9	22.7	22.2	20.3	22.6	22.7	21.5										
J123721.40+621120.3	0.656		22.6	23.4	22.2	20.1	23.7	23.5	21.9		22.9	21.9							
J123721.47+621346.2	1.019		23.7	24.2	23.1	19.2	24.4	24.2	22.1										
J123721.53+621334.8	0.477		23.7	22.0	19.6	16.5	22.9	21.8	19.3										
J123721.78+621225.4	0.480		22.8	22.9	21.4	18.8	23.3	22.7	21.0		22.1	21.0							
J123722.11+621210.4	0.928		23.8	24.3	23.0	19.2					22.9	21.7							
J123722.24+621124.1	0.784		22.9	23.5	22.3	19.6	23.9	23.5	21.7		22.9	21.7							
J123722.38+621145.5	0.530		22.3	22.9	21.7	19.5					22.5	21.6							
J123722.48+621216.0	0.963		23.4	24.0	22.2	18.0	24.3	23.8	21.5		23.2	21.7							
J123722.61+621356.7	1.022		22.3	23.1	22.0	18.5	23.2	23.1	21.3										
J123722.59+621156.7	0.487		22.6	22.9	21.6	18.9	23.5	23.2	21.4		22.7	21.7							
J123723.05+621339.0	1.020		23.2	24.0	23.2		23.9	23.7	22.4										
J123723.46+621333.0	0.480		23.6	23.6	21.5	18.7		23.4	21.1										

2.3.1 Spectral classification of the galaxies

A large number galaxies in the redshift selected sample have a general spectral classification (i.e. from the catalog of Cohen 2001): *emission-line* and *absorption-line* galaxies as well as objects with both, emission and absorption lines. The classification of *emission-line* includes broad and narrow -emission-line galaxies. Moreover, the latter type includes HII region-like galaxies and narrow-emission-line AGNs (Active Galactic Nuclei). The main difference between them is the mechanism by which the emission lines are produced. In the HII region-like galaxies the gas is photoionized by hot OB stars. While in the AGNs (i.e. the Seyfert 2 galaxies and the Low-Ionization Nuclear Emission-Line Regions (LINERs)), the photoionization is due to a non-thermal or "power law" continuum (Veilleux & Osterbrock 1987). It is also possible that both types of photoionization mechanisms could be present (Dessauges-Zavadsky et al. 2000). Since the LIRIS-GAL sample is thought to be constituted with star-forming galaxies, such sample has to be centered on the HII region-like galaxies, which are populated by young stars and therefore, are undergoing star formation episodes. The most luminous objects of this type are called *starburst* galaxies.

A broad discussion between HII region-like galaxies, Seyfert 2 and LINERs is presented in Section 2.4.1. Figure 2.6 shows the color distribution of the galaxies. They are represented by their general spectral type: emission-line galaxies are represented by *crosses* and *asterisks*; the latter symbol indicates that the galaxy shows strong Balmer-series emission-lines; the *diamonds* represent galaxies with absorption lines; the *dots* represent galaxies of intermediate type (i.e. with emission and absorption lines); finally, the galaxies with no published spectral characteristics are represented by $\times$.

Galaxies with strong Balmer emission-lines detected

A total of 41 emission-line galaxies shows strong emission in the Balmer-series lines; these galaxies are represented as filled dots in Figure 2.3. Some galaxies are classified by the detection of Hβ, Hγ and Hδ; however, for others, Hβ falls out from the observed spectral range. There are also some cases in which Hγ and Hδ are not detected because the low S/N ratio. I have identified these objects as HII region-like galaxies for the color-color analysis described below in advance to the spectral type analysis of section 2.4.1. Moreover, such identification is affected by the limited availability of the published spectral data.

2.3.2 Color analysis of the galaxies

I have also analyzed the properties of the stellar population in the sample of galaxies from their integrated luminosities. This analysis is based on the observed colors and theoretical continuum distribution, establishing a set of characteristics to classify the galaxies.

Colors from published luminosities

Table 2.3 shows the compilation of luminosities for all the galaxies. It can be seen that the bands with greater coverage in the sample of galaxies, are U_n, G, R' and K_s (from Hogg et al. 2000), and B, V and I (from Barger et al. 1999); B-band observations are not as complete as for the other bands. With these luminosities, I have constructed color-color diagrams to study the typical colors of the galaxies as function of their spectral type. Figure 2.6 shows the $G-R'$ vs $V-I$ color distribution

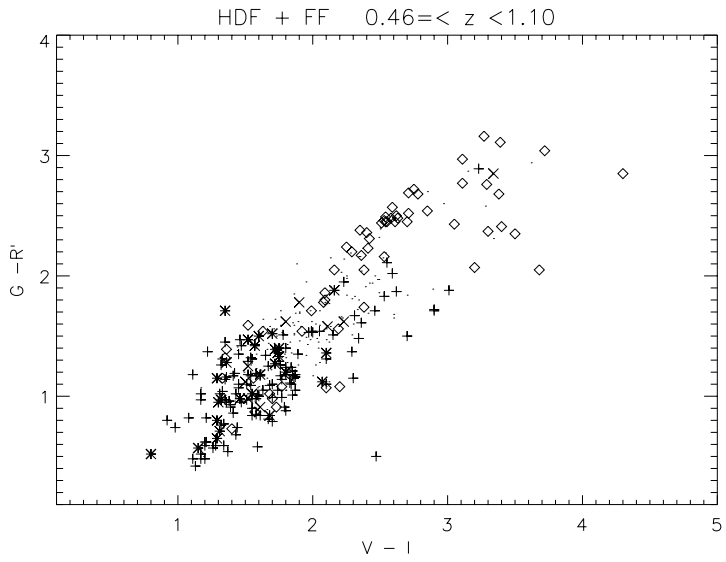

Figure 2.6: $G-R'$ vs $V-I$ diagram of galaxies at $0.46 \leq z < 1.1$. The spectral types are: emission-line galaxies *crosses* and *asterisks* (see text), absorption-line galaxies *diamond*, intermediate cases *dots* and galaxies with no published spectral characteristics ($\times$).

of the galaxies of the sample. This figure includes all the galaxies from the redshift selected sample (i.e. except those that are not observed in any of the bands).

As it can be seen in Figure 2.6, the majority of the emission-line galaxies are bluer than those with absorption lines. The galaxies with strong Balmer series emission lines are even bluer. Such color implies that the galaxy integrated luminosity is dominated by a young stellar population. This color classification agrees with the work of Cohen (2001), who make the analysis with U_n, G, R' and K_s -bands on her catalog of galaxies.

Colors from models

The theoretical continuum distributions are constructed by a synthesis model developed by Mayya (1994), which is similar to the known models of Bruzual A. & Charlot (1993) and Leitherer et al. (1999). The code is a combination of a population synthesis model and a spectral evolution model. It works on a basis of: a) the initial distribution of the stars with an assumed initial mass function (IMF), b) the luminosity and the effective temperature as a function of time and derived by an evolutionary model and, c) the spectrum of each star for different positions in the H-R diagram. The photoionization algorithm is based on the "Case B" of recombination. The input parameters of the model are the IMF, the metallicity and the star formation scenario. The model assumes a Salpeter initial mass function (IMF) with a power law of exponent α=2.35 and cutoff masses of 0.1 and 100 $M_\odot$. The source of the stellar parameters ($T_{\rm eff}$ & g) are the Geneva tracks and the library of spectral types is derived form the atmosphere models of Kurucz (1992).

I have extended the models of Mayya (1994) to synthesize colors within the passbands of *B*, *G*, *V*, *R*‘ and *I* filters. I have also implemented the redshift corrections of all the modeled quantities such as spectra, magnitudes and emission-line fluxes.

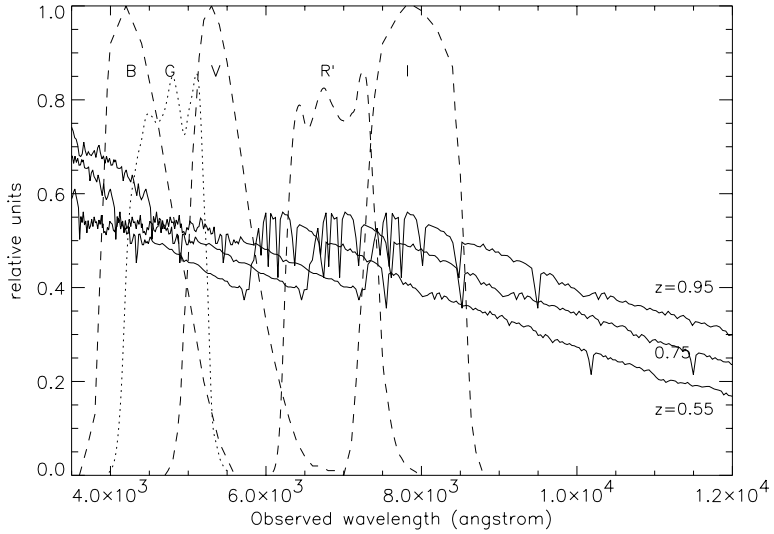

Figure 2.7: Theoretical spectrum of a galaxy at a redshift of 0.55 (thick line), 0.75 and 0.95. The bandpasses of the filters: *B*, *G*, *V*, *R*‘ and *I*, are also plotted.

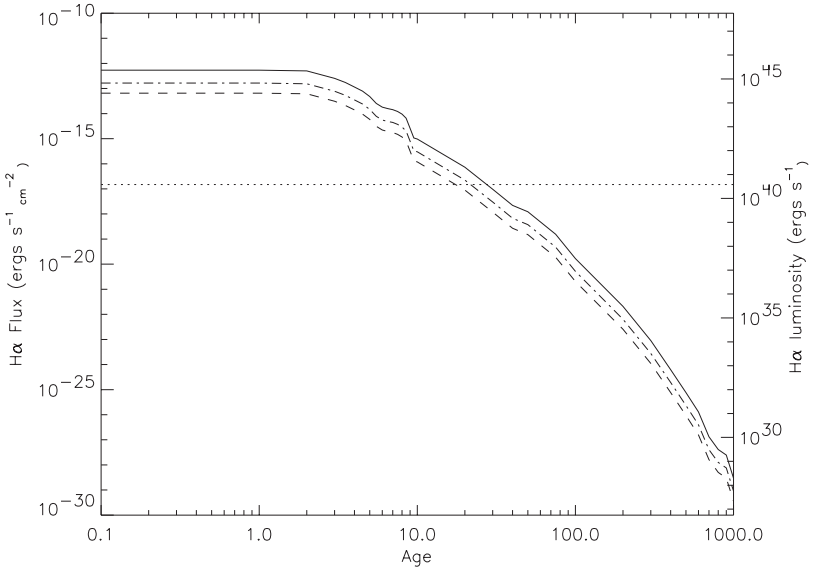

Figure 2.8: Prediction for the integrated flux of the Hα emission line in a galaxy at z=0.46 (solid line), z=0.75 (dash-dotted line) and z=1.1 (dashed line). The flux is represented as a function of the time (in Myr) since the burst of star formation. The luminosity, at the right axis, represents the z=0.46 galaxy flux only. The horizontal line represents the theoretical flux limit of LIRIS (see text)

The analysis of the results from the model must consider the following assumptions: a) no extinction is applied and, b) it is assumed an instantaneous burst of star formation c) starburst models older than 10^9 years are not considered, as such regions would be too faint to detect.

Figure 2.7 shows the theoretical spectra (described below) for three different redshifts. It can be seen that the color obtained from observed luminosities in a selected couple of bands, depends greatly on the redshift. For the color analysis purposes, I have considered three main redshift ranges: $0.46 \leq z < 0.65$; $0.65 \leq z < 0.85$ and $0.85 \leq z < 1.1$.

The results from the model on the Hα emission line luminosity are shown in Figure 2.8. Three redshifts are represented for the flux estimation: z=0.46 (solid line), z=0.75 (dash-dotted line) and z=1.1 (dashed line). The flux is obtained from the luminosity, computing the luminosity distance with the cosmology constants: H_0=100 h km s^{-1} Mpc^{-1}, h=0.7 and q_0=0.2. It is also assumed a burst mass of 10^9 $M_\odot$. It can be seen that the flux of the line diminishes as a function of the age, as expected from the instantaneous burst scenario; the horizontal dotted line represents the theoretical flux limit of LIRIS spectroscopy (R=1000), which determine a maximum age limit at 18 or 25 Myr, depending on redshift. The limiting flux estimation is set for a S/N=3 at J-band with 3 h exposure time, as described in chapter 4.

The distribution of the galaxies in the color-color diagrams is analyzed by comparison to the predictions from the model. Figures 2.9 to 2.11 (for the three redshift ranges) show that the model follows very well the observed colors. The model is computed for the following ages: 0.1, 1, 2, 3, 3.5, 4, 4.5, 5, 5.5, 6, 6.5, 7, 7.5, 8, 8.5, 9, 10, 15, 20, 30, 40, 50, 75, 100, 200, 300, 400, 500, 600, 700, 800, 900 and 1000 Myr. Each age step is marked by a box. The model is plotted as a solid line for solar metallicity, Z=0.02 and, as a dashed line for Z=0.04. The modeled redshift tracks go from the lowest to the highest value of redshift in the specified range. They are marked by the thin solid lines that start at the age points. The arrow represents the extinction, based on values from Rieke & Lebofsky (1985). These diagrams are used to select the galaxies that show colors corresponding to a young population, as described in the following section. The diagrams for the redshift ranges $0.46 \leq z < 0.65$ and $0.65 \leq z < 0.85$ are formed with the colors $G - R'$ vs $B - I$, whereas the diagram at $0.85 \leq z < 1.1$ is formed with $G - R'$ vs $V - I$. The use of different colors is due that redder colors are more indicated for higher redshifts, as described before.

Selection of galaxies by the color criteria

The criteria to select the galaxies from the color-color diagrams in figures 2.9, 2.10 and 2.11, are based on: a) the analysis of the model, b) the behaviour of the galaxies with detected Balmer lines, and c) the instrumental limits. The modeled evolution shows how the galaxies become redder with the increase of age; in al diagrams the model is plotted for the two boundary values of the redshift range.

Using the age limit derived from the instrumental limit (20 Myr; see Figure 2.8), a box (marked with dashed lines) is constructed in the diagram (figures 2.12, 2.13 and 2.14). The maximum color is estimated including the extinctioneffect, represented in the figure by the arrow.

Then, the emission line galaxies that fall inside the color box are selected; it can be seen that there are more than 15 galaxies at each redshift range. The selected galaxies are listed on tables 2.4 to 2.6 together with those showing Balmer emission lines; the first column is the name assigned to the galaxies, where “BD” means that this galaxy has strong Balmer emission lines, and “CS”, that the galaxy was selected by the color criteria. The second column is the spectroscopic redshift,

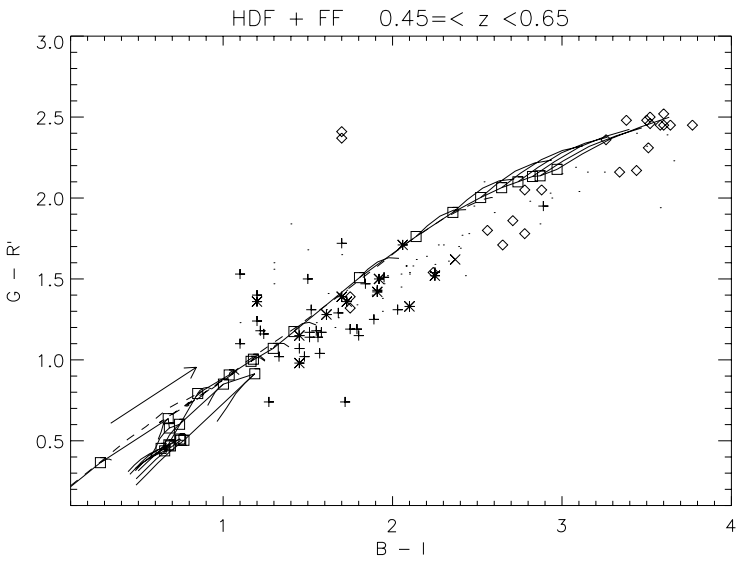

Figure 2.9: $G-R'$ vs $B-I$ diagram of galaxies at $0.46 \leq z < 0.65$. The symbols are the same than in Figure 2.6. The solid line represents the modeled evolution of the colors of a galaxy at z=0.46 with solar metallicity. The age range is from 1 to 1000 Myr. The thin solid lines are the redshift tracks going from z=0.46 to z = 0.65. The dashed line represents the same model computed for a metallicity Z=0.008.

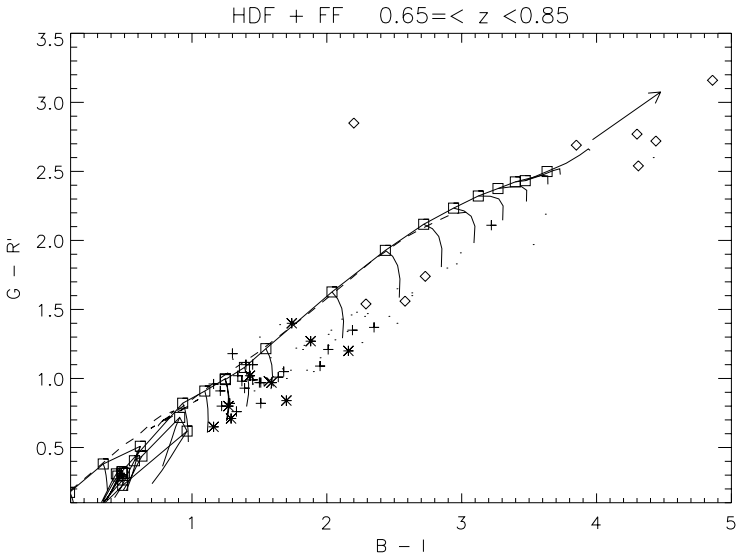

Figure 2.10: $G-R'$ vs $B-I$ diagram of galaxies at $0.65 \leq z < 0.85$. The symbols are the same than in Figures 2.6 and 2.9. The solid line represents the modeled evolution of the colors of a galaxy at z=0.65. The thin solid lines are the redshift tracks going from z=0.65 to z = 0.85.

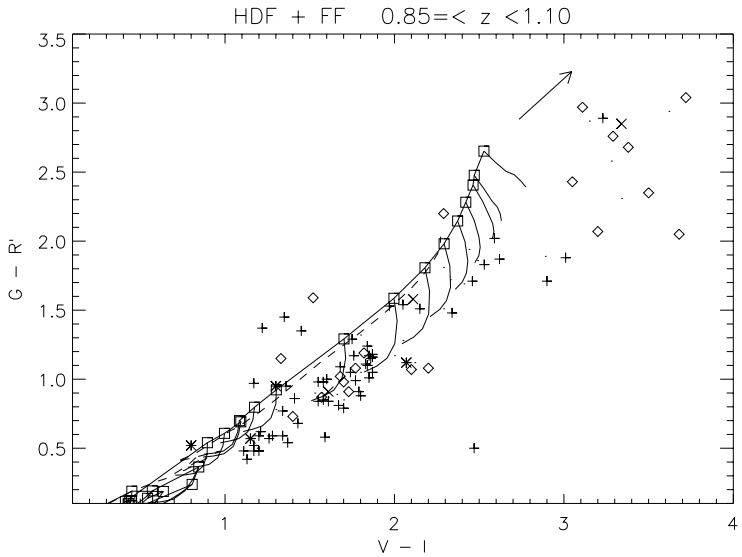

Figure 2.11: $G - R'$ vs $V - I$ diagram of galaxies at $0.85 \leq z < 1.1$. The symbols are the same than in Figures 2.6 and 2.9. The solid line represents the modeled evolution of the colors of a galaxy at z=0.85. The thin solid lines are the redshift tracks going from z=0.85 to z = 1.1.

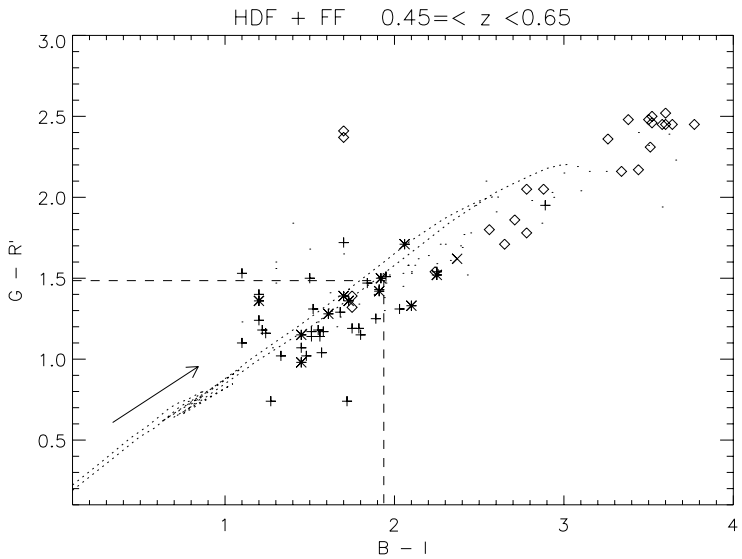

Figure 2.12: Color selection diagram of galaxies at $0.46 \leq z < 0.65$. The dashed lines are the delimiters for the selection of galaxies according to the modeled color-color criteria. The models shown are for z = 0.46 and z = 0.64. The symbols are the same than in Figure 2.6.

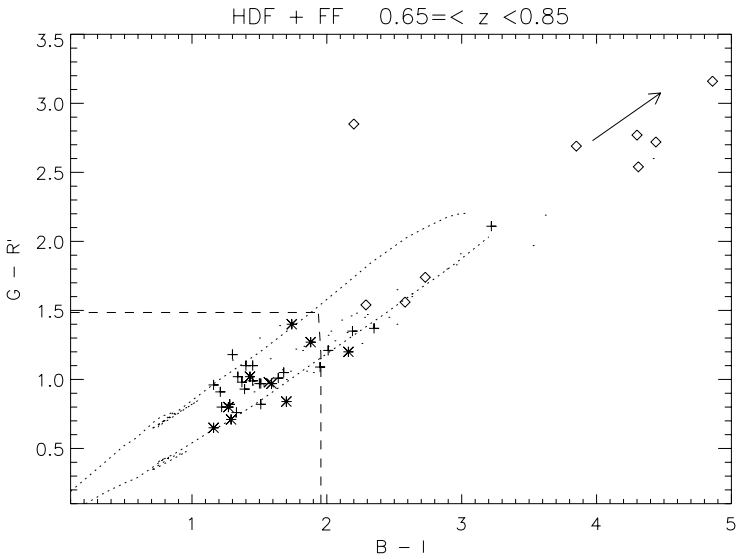

Figure 2.13: Color selection diagram of galaxies at $0.65 \leq z < 0.85$. The models shown are for z = 0.65 and z = 0.84. The symbols are the same than in Figures 2.6 and 2.12.

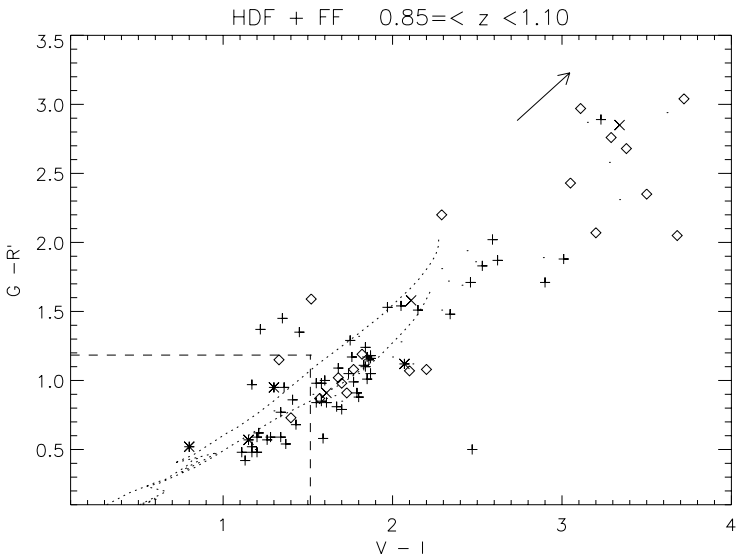

Figure 2.14: Color selection diagram of galaxies at $0.85 \leq z < 1.1$. The models shown are for z = 0.85 and z = 1.09. The symbols are the same than in Figures 2.14 and 2.12.

Table 2.4: LIRIS-GAL sample at $0.46 \leq z < 0.65$

Name	z_{sp}	$B-I$	$G-R'$
BD0462-0	0.462	—	—
CS0472-0	0.472	1.20	1.40
BD0474-0	0.474	1.20	1.36
BD0475-0	0.475	—	1.22
BD0475-1	0.475	1.92	1.50
BD0476-0	0.476	1.70	1.39
BD0480-0	0.480	2.25	1.52
BD0482-0	0.482	—	1.47
BD0483-0	0.483	1.61	1.28
CS0484-0	0.484	1.52	1.31
BD0485-0	0.485	2.06	1.71
CS0485-0	0.485	1.33	1.02
CS0485-1	0.485	1.51	1.14
BD0487-0	0.487	2.10	1.33
BD0504-0	0.504	—	1.59
BD0507-0	0.507	1.45	1.15
BD0509-0	0.509	—	1.88
CS0511-0	0.511	1.22	1.18
BD0513-0	0.513	—	1.53
CS0513-0	0.513	1.56	1.14
CS0520-0	0.520	1.50	1.50
CS0525-0	0.525	1.27	0.74
BD0528-0	0.528	1.91	1.42
CS0529-0	0.529	1.55	1.18
CS0535-0	0.535	1.57	1.04
CS0555-0	0.555	1.10	1.10
CS0557-0	0.557	1.45	1.07
BD0558-0	0.558	—	—
CS0558-0	0.558	1.48	1.02
CS0559-0	0.559	1.68	1.29
BD0560-0	0.560	—	—
CS0561-0	0.561	1.20	1.24
BD0570-0	0.570	1.99	—
BD0570-1	0.570	—	2.25
CS0586-0	0.586	1.51	1.17
BD0594-0	0.594	1.45	0.98
BD0594-1	0.594	1.73	1.36
CS0635-0	0.635	1.58	1.17

Table 2.5: LIRIS-GAL sample at $0.65 \leq z < 0.85$

Name	z_{sp}	$B-I$	$G-R'$
BD0654-0	0.654	1.59	0.97
BD0654-1	0.654	—	1.25
CS0672-0	0.672	1.22	0.79
CS0677-0	0.677	1.34	1.02
CS0681-0	0.681	1.40	1.10
CS0681-1	0.681	1.16	0.95
CS0682-0	0.682	1.30	1.18
CS0683-0	0.683	1.37	0.98
CS0692-0	0.692	1.45	1.10
BD0693-0	0.693	1.88	1.27
BD0693-1	0.693	1.70	0.84
BD0695-0	0.695	—	0.94
BD0744-0	0.744	1.16	0.65
CS0744-0	0.744	1.28	0.82
BD0747-0	0.747	1.74	1.40
CS0751-0	0.751	1.51	0.82
CS0758-0	0.758	1.39	0.93
BD0760-0	0.760	—	1.18
CS0778-0	0.778	1.50	0.97
BD0784-0	0.784	2.16	1.20
BD0788-0	0.788	1.43	1.02
CS0819-0	0.819	1.68	1.05
BD0821-0	0.821	1.27	0.80
BD0840-0	0.840	1.29	0.71
CS0841-0	0.841	1.64	1.01
CS0842-0	0.842	1.45	0.99
CS0846-0	0.846	1.21	0.91
CS0846-1	0.846	1.51	0.96
CS0849-0	0.849	1.33	0.76

Table 2.6: LIRIS-GAL sample at $0.85 \leq z < 1.1$

Name	z_{sp}	$V-I$	$G-R'$
CS0858-0	0.858	1.41	0.86
BD0880-0	0.880	0.80	0.52
CS0901-0	0.901	1.36	0.95
BD0904-0	0.904	—	1.44
BD0907-0	0.907	1.15	0.57
CS0934-0	0.934	1.20	0.59
BD0936-0	0.936	—	—
BD0960-0	0.960	1.30	0.95
CS0961-0	0.961	1.17	0.48
CS0961-1	0.961	1.26	0.57
CS0973-0	0.973	1.28	0.59
CS1001-0	1.001	1.17	0.96
CS1005-0	1.005	1.17	0.52
CS1010-0	1.010	1.43	0.68
CS1014-0	1.014	1.13	0.42
CS1014-1	1.014	1.11	0.48
CS1018-0	1.018	1.34	0.58
CS1020-0	1.020	1.37	0.53
CS1020-1	1.020	1.34	0.76
CS1022-0	1.022	1.20	0.48
CS1050-0	1.050	1.21	0.62
BD1084-0	1.084	2.07	1.12

the third and fourth columns are the observed color. The galaxies listed on these tables form the LIRIS-GAL sample and are candidates to the spectroscopic observations described in Chapter 3.

2.4 Analysis of the LIRIS-GAL sample

The final sample presents different selection effects, due to various circumstances: the availability of data, the spatial distribution of the galaxies and the selection process itself.

The main catalogs, used to gather galaxy data (see section 2.2.2), are complete to a certain magnitude as shown in the diagrams of Figure 2.15. The R' and V -band diagrams represent the distribution of the HDF-N and FF galaxies (solid line). The limited availability of spectroscopic data is reflected by the low and high-magnitude cutoffs in the distribution (dashed line). Finally, the color-criteria selection has a slight effect on the distribution profile, as it can be seen for the LIRIS-GAL sample (dotted line).

The limited number of galaxies with spectroscopy data also produces selection effects on the redshift distribution, as it was seen in the distribution of the redshift-selected galaxies (Figure 2.5). The LIRIS-GAL sample, represented in Figure 2.16 also shows a peak at low values in the redshift distribution. The median is 6 galaxies at each bin (z=0.05).

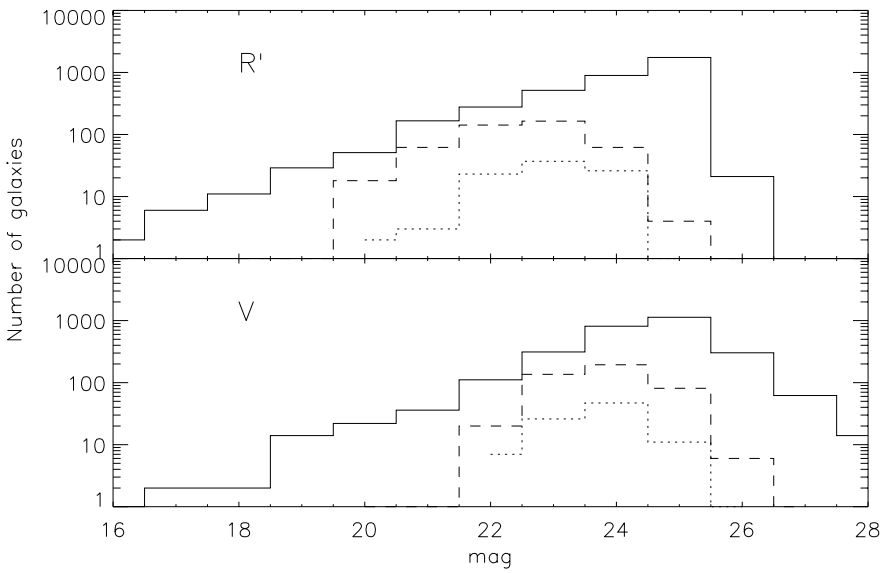

Figure 2.15: Distribution of galaxies in the R' and V -bands. The solid line represents the objects from the HDF-N and FF, the dashed line represents the galaxies with spectroscopic data and the dotted line represents the LIRIS-GAL sample.

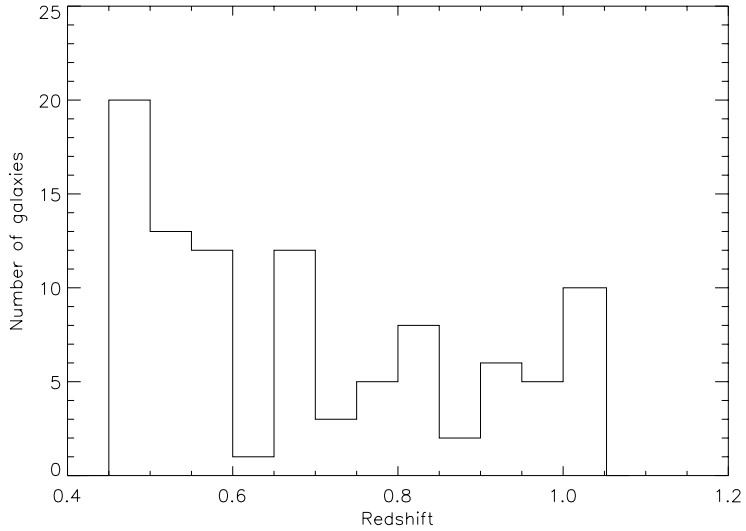

Figure 2.16: Redshift distribution of the LIRIS-GAL sample. The bin size is z=0.05

2.4.1 Spectral measurements and classification

As it was described in Section 2.3.1 the spectral classification is essential to identify among HII region-like galaxies, Seyfert 2 and LINERs. Unfortunately, there are no absolute nor unique criteria to perform such classification. Even more, the diagnostic methods have evolved, for example the [OIII] (5007 Å) / Hβ $>$ 3 ratio of Shuder & Osterbrock (1981) to identify Seyfert 2 galaxies, has been later referred as only useful to separate between Seyfert 2 and LINERs (see Veilleux & Osterbrock 1987; Filippenko & Terlevich 1992). As well, the [OII] (3727 Å) / Hβ versus [OI] (6300 Å) / Hα intensity ratios diagram is suggested by Veilleux & Osterbrock (1987) to discriminate between HII region-like galaxies and AGNs. However, at intermediate redshift (z $>$ 0.4) both, [OI] (6300Å) and Hα emission-lines fall out of the optical-spectrographs range. In addition, the study of intermediate redshift galaxies comes from their integrated light, so that the whole galaxy is classified within the same spectral type (i.e. excluding the possibility of combined types). For these cases, a set of new diagnostic methods have been studied by Rola, Terlevich, & Terlevich (1997), employing the lines: [OII] (3727 Å)[4], [Ne III] (3869 Å), [OIII] (5007 Å) and Hβ.

I have measured the relative intensities and equivalent widths (hereafter EW) of these emission-lines in the galaxies of the LIRIS-GAL sample with the optical-spectra published by DEEP. These data are used to construct two emission-line ratio diagrams. The line ratios are selected on the basis of the consistency of the spectral data and the shortest wavelength separation between the lines, in order to reduce reddening effects.

The EW([OII] (3727 Å)) / EW(Hβ) versus EW([OII]) diagram, shown in Figure 2.17, allows to identify the HII region-like galaxies from the LINERs (*asteriks*, taken from the work of Rola, Terlevich, & Terlevich (1997)). The LINERs show values of EW([OII] (3727 Å)) / EW(Hβ) $\approx$ 10. The dashed line represents the place in the diagram of the HII region-like galaxies from Rola et al. and

[4][OII] (3727 Å) represents the sum of the lines [OII] (3727 and 3729 Å)

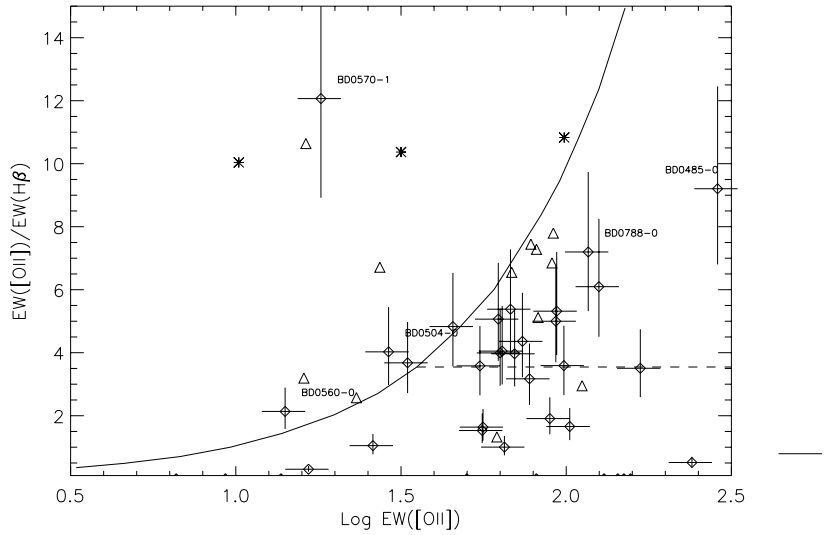

Figure 2.17: [OII] (3727 Å) / Hβ equivalent-width ratio versus [OII] equivalent width. The *diamonds* (i.e. with error bars) represent the galaxies in the LIRIS-GAL sample, the *asterisks* are LINERs and the *triangles* are Seyfert 2, both from Rola et al. (1997). The curve represents the points with EW(Hβ) = 10 Å.

the curve represents what they define as an upper limit to HII region-like galaxies: EW(Hβ) = 10Å. It can be seen that most of the galaxies from the LIRIS-GAL sample fall in the region of the dashed line. The galaxy BD0570-1 presents an equivalent-width ratio consistent with the LINERs, so that, it shall be excluded from the SFR analysis. BD0788-0 and BD0485-0 should also be classified carefully, as well as BD0560-0 and BD0504-0 which are out of the EW(Hβ) = 10 Å limit. In this diagram the separation between HII region-like galaxies and Seyfert 2 (*triangles*, also from the work of Rola et al.) is rather clear. Such separation is easier to detect in the [OIII] (5007Å) / Hβ versus [OII] (3727 Å) / [NeIII] (3869 Å) intensity-ratios diagram, shown in Figure 2.18. Here the separation between HII region-like galaxies and Seyfert 2 is notorious and none of the galaxies in the LIRIS-GAL sample fall in the Seyfert 2 region. The horizontal line represents an empirical upper limit to the HII region-like galaxies in the Figure 1 of Rola et al. Further analysis will be performed (i.e. compare with the diagrams of Veilleux & Osterbrock 1987) when the measurements of: Hα (6563 Å), [NII] (6583 Å) and [SII] (6725 Å) become available from NIR spectroscopy.

2.4.2 The environment of the galaxies

As it was seen in Figures 2.2 and 2.3, the galaxies in the HDF-N and FF appear to be in high density environments. Numerous studies have provided evidence that galaxy-galaxy interactions and cluster environments alter the star formation properties (e.g. Dressler 1984; Moss & Whittle 1993; Kennicutt 1998; Iglesias-Páramo & Vilchez 1999; Noeske et al. 2001). The effects on the star formation, being quite complex and highly dependent on the type of interactions, are controversial. Therefore, the environment conditions have to be considered for SFR analysis.

I have performed an environmental study for each galaxy in the LIRIS-GAL sample to identify

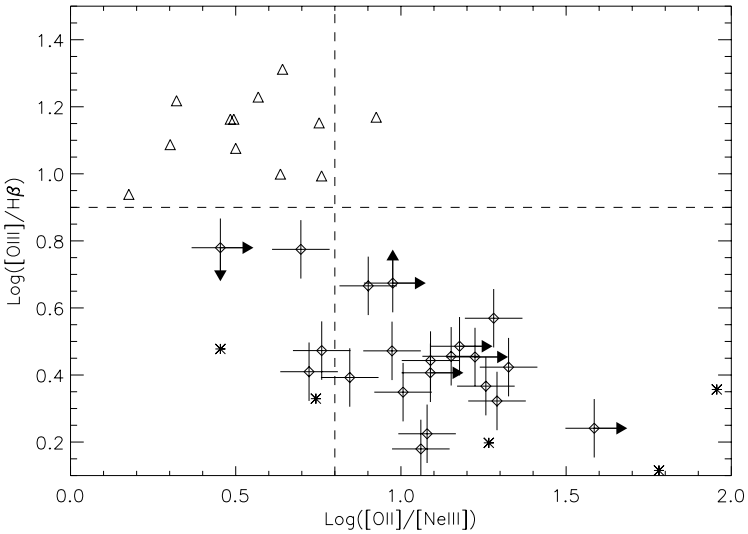

Figure 2.18: [OIII] (5007 Å) / Hβ versus [OII] (3727 Å) / [NeIII] (3869 Å) intensity ratios. The symbols are the same than in Figure 2.17. Arrows on data points indicate lower or upper limits. The horizontal dashed line represents a minimum for the Seyfert 2 (see text). The vertical dashed line represents the empirical separation between Seyfert 2 and LINERs reported in Rola et al. (1997).

companion galaxies and clusters. This study is more reliable for strong evidence that a galaxy belongs to a cluster than for the contrary case, where the assumptions are limited by the available spectroscopic data (i.e. redshifts) of the galaxies.

The criterion adopted for the size of a cluster of galaxies is based on the typical radius from 0.5 to 1 h^{-1} Mpc found in different clusters at $0 \leq z < 1.2$ (e.g. Girardi et al. 1998 and Lubin & Postman 1996). The search region in the spatial direction (α, δ), around the galaxy is set from a circle of 1 h^{-1} Mpc radius, which is projected at the distance of the galaxy. The radius r, given in arcseconds, is determined by:

$$r = \frac{\theta Dl}{(1+z)^2} \tag{2.1}$$

where, θ is the solid angle that forms the search circle at a luminosity distance Dl, which is given by:

$$Dl = \frac{cz}{H_0}\left(1 + \frac{z(1-q_0)}{\sqrt{1+2zq_0}+1+zq_0}\right) \tag{2.2}$$

where the cosmological constants adopted are: H_0=100 h km s^{-1} Mpc^{-1}, h=0.7 and q_0=0.2.

In the direction of redshift (i.e. velocity) the environment analysis is done in terms of the typical velocities for galaxies in clusters. The Virgo cluster is used as a reference, which has galaxies with apparent velocities Δv = 1500 km s^{-1}. The redshift range represented is given by:

$$\Delta z = \sqrt{\frac{c+\Delta v}{c-\Delta v}} - 1 \tag{2.3}$$

The environment diagrams shown in Figure 2.19 are built for each galaxy in the LIRIS-GAL sample. The galaxy under analysis is represented by a black filled circle and it is placed at the center of each diagram. A dashed circle of 1 h^{-1} Mpc radius is drawn around it. The near galaxies that deviate Δz = 0.005 are represented by open circles. The size of these circles is function of the absolute R' magnitude. The crosses represent the galaxies that are not observed in that band. Is then, possible to conclude from the diagrams, that there are four mayor clusters of galaxies at redshifts: 0.474, 0.484, 0.558 and 0.681. In contrast, there are galaxies that are good candidates to be isolated objects. Such is the case of: BD0570-0, CS0692-0, BD0693-1, CS0819-0, CS1001-0, CS1005-0, and BD1084-0. However, this is a preliminary conclusion due to the limited availability of spectroscopic redshifts (i.e. there are galaxies that fall inside the 1 h^{-1} Mpc circle proyection, but their lack of a precise redshift makes impossible to place them in the diagram). The rest of galaxies are ambiguous cases.

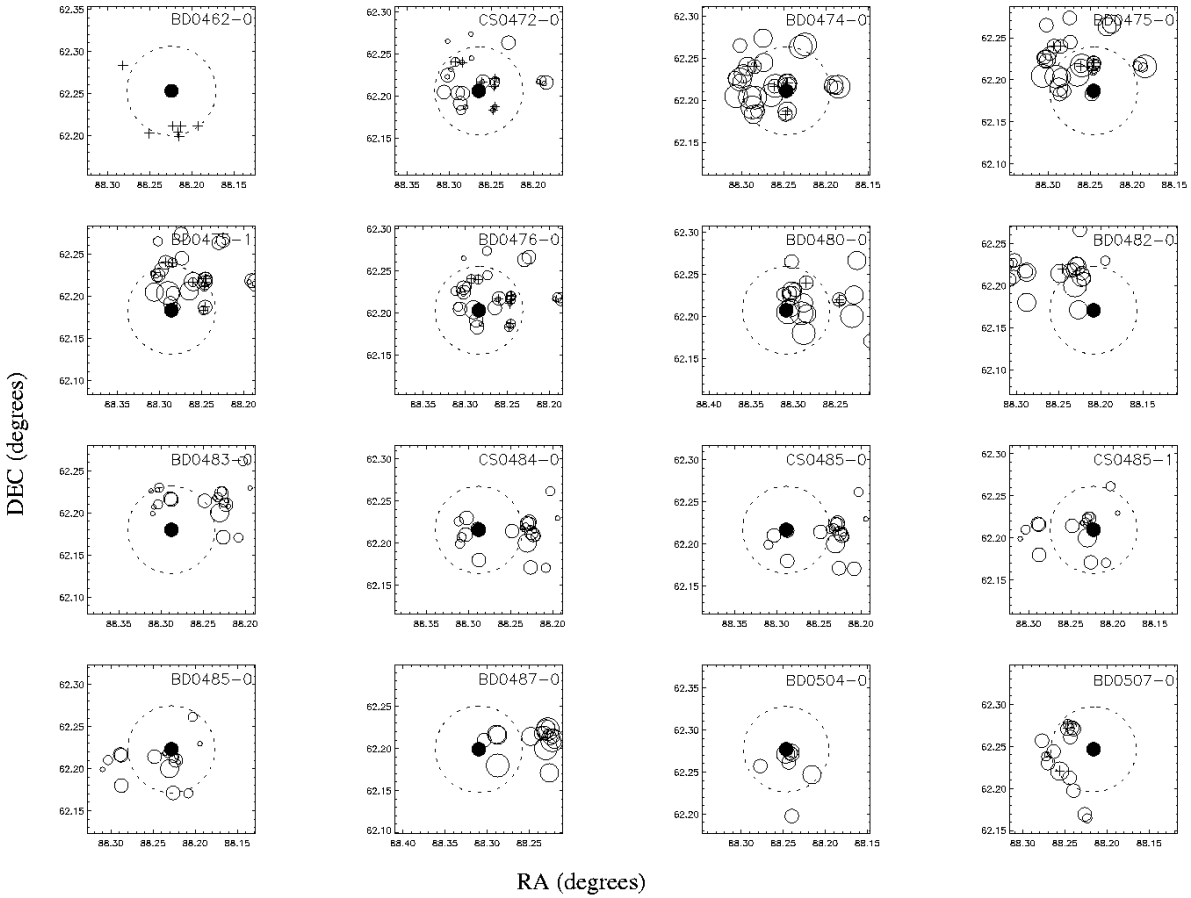

Figure 2.19: Representation of each galaxy environment. The galaxy cited is represented by the black filled circle. The dashed circle has a radius of 1 h^{-1} Mpc. The small circles represent the galaxies and their size are function of their absolute magnitudes. The crosses represent the galaxies with no photometric data.

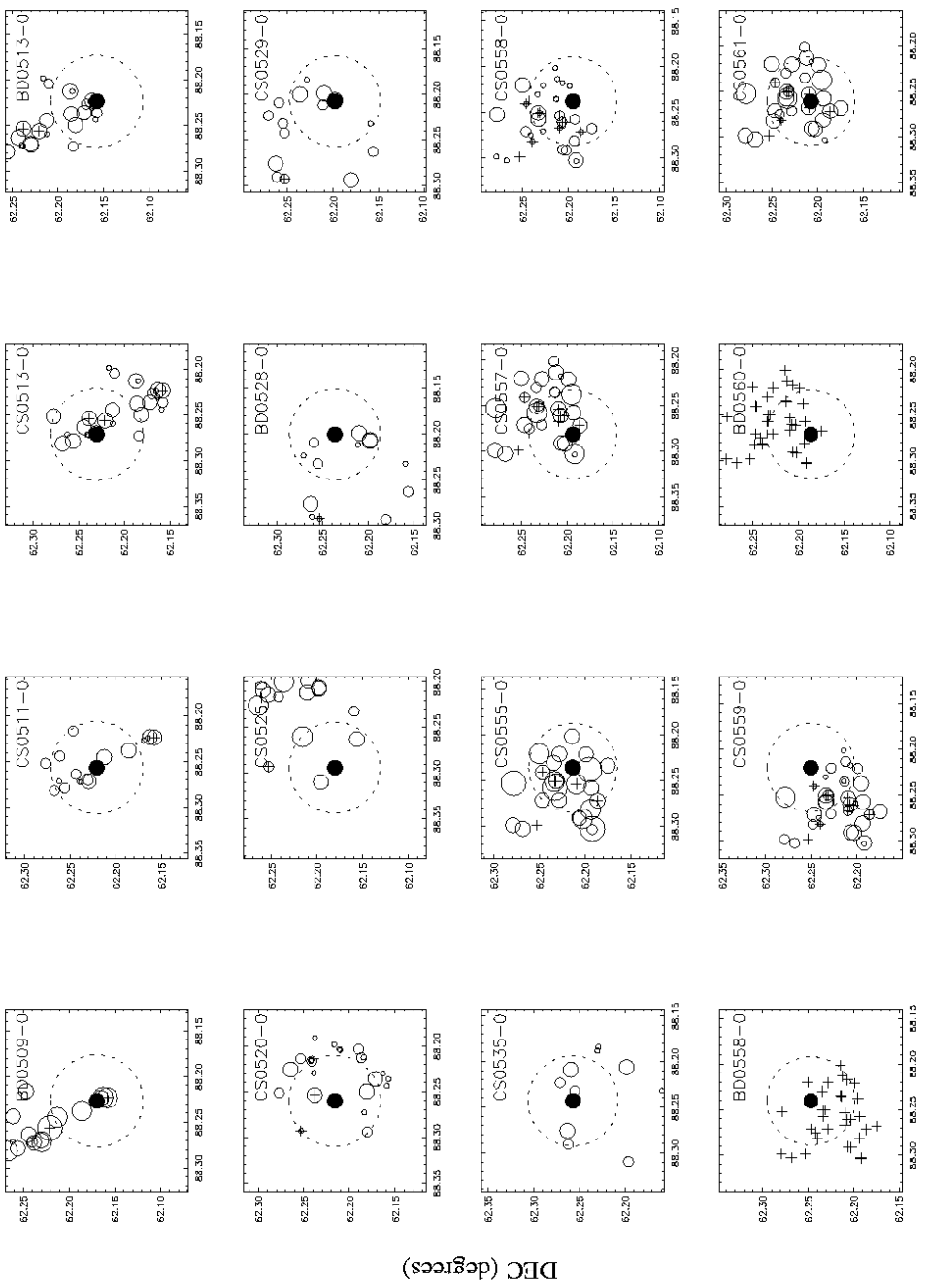

Figure 2.19: Continued

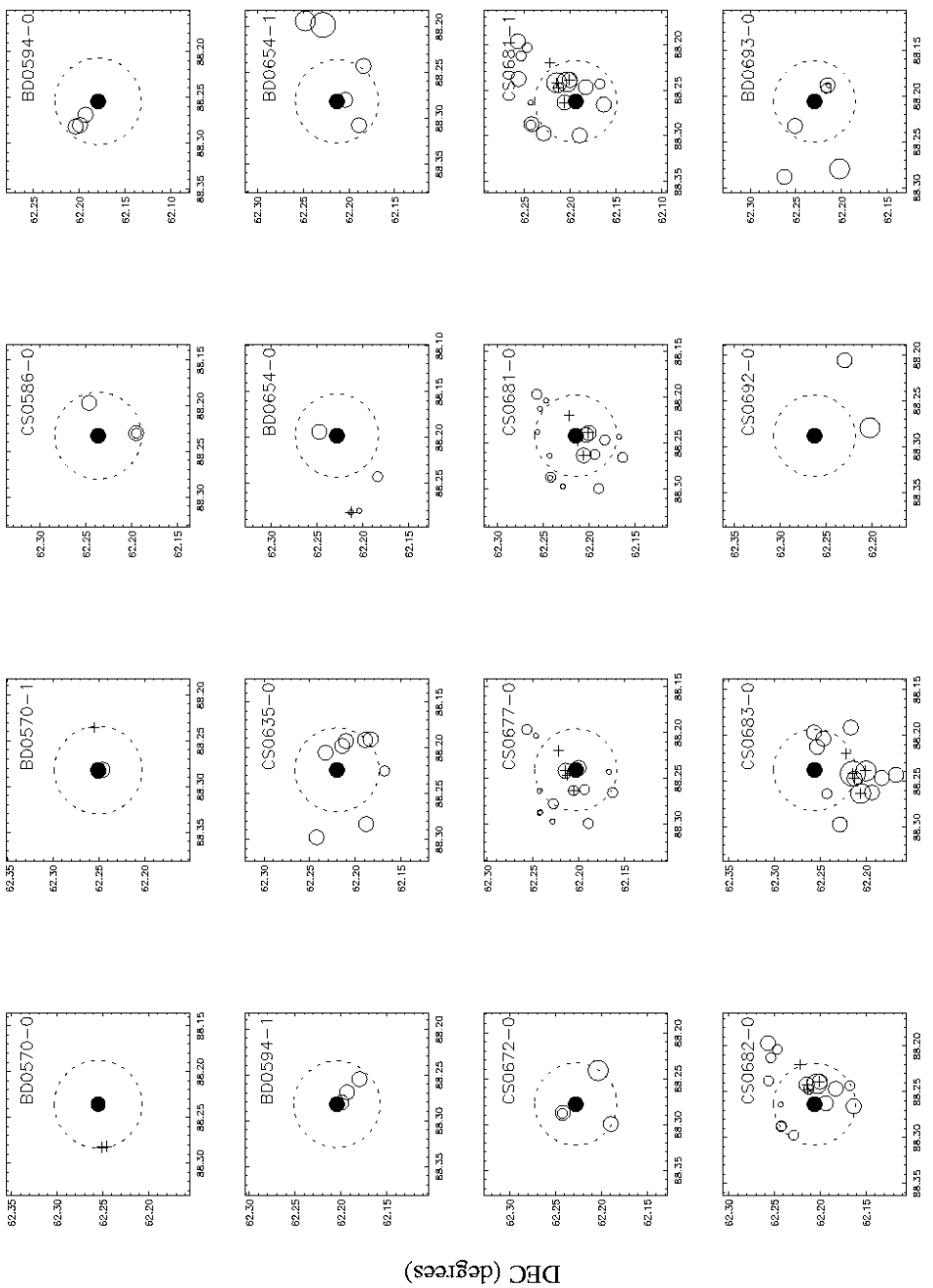

Figure 2.19: Continued

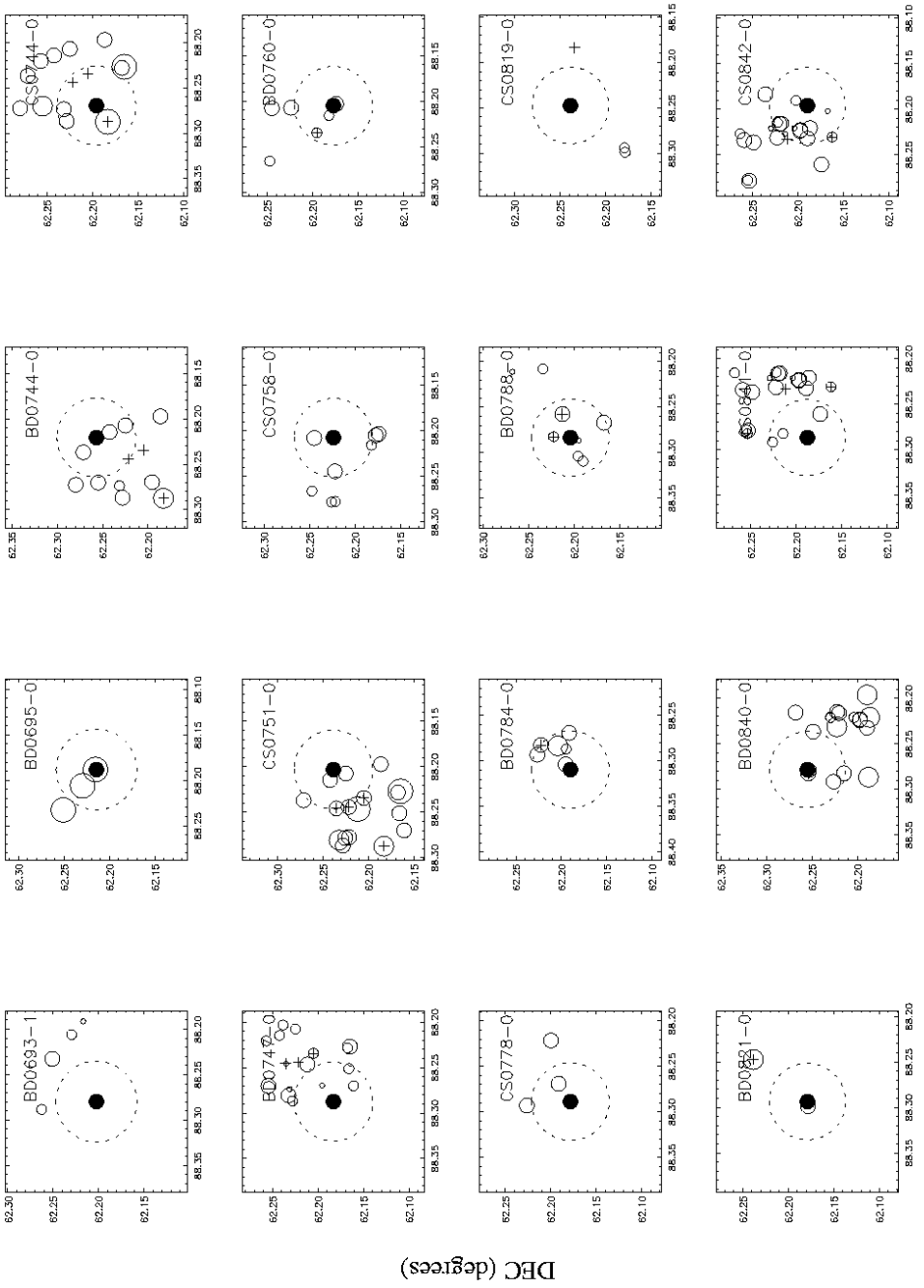

Figure 2.19: Continued

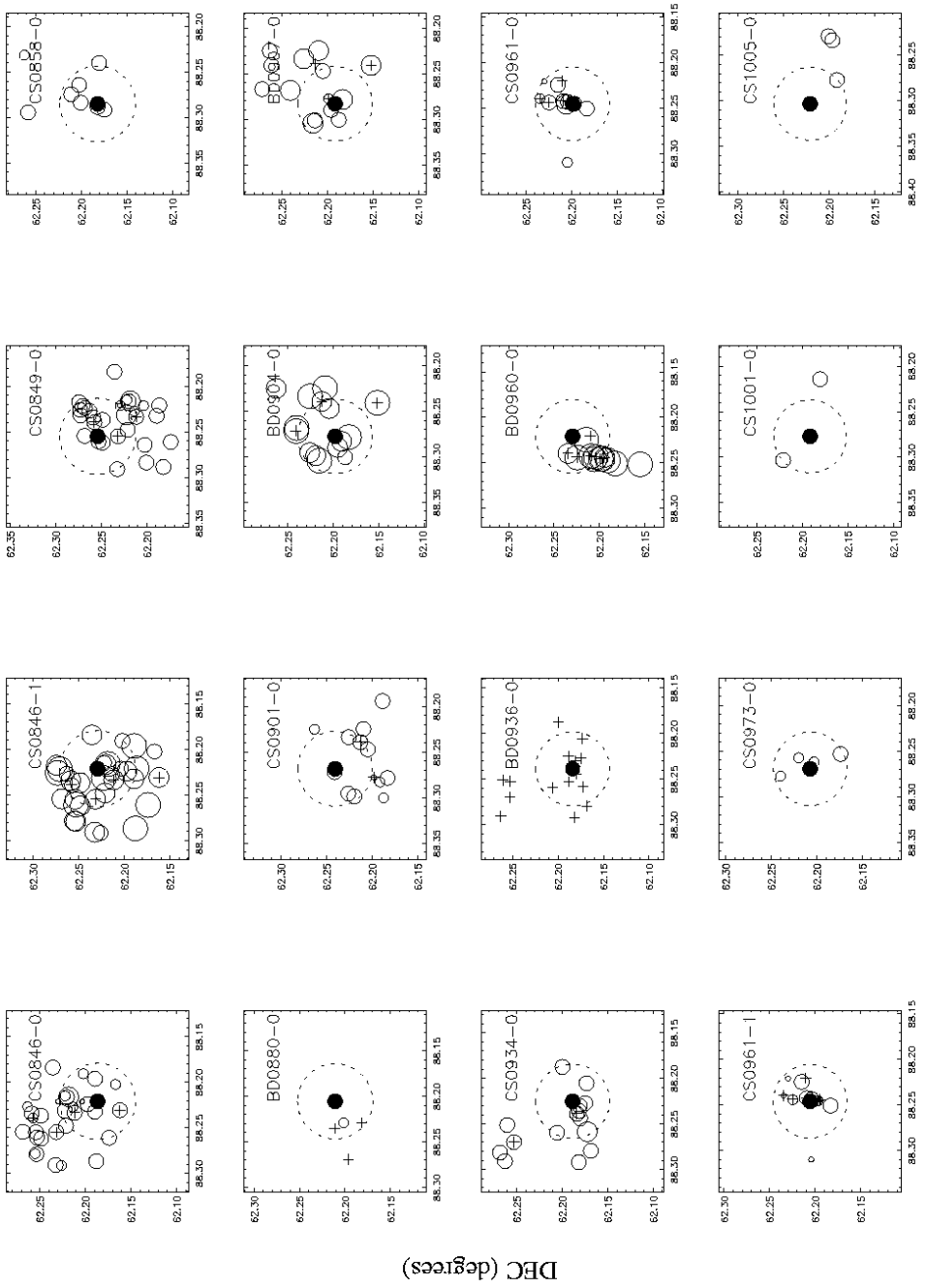

Figure 2.19: Continued

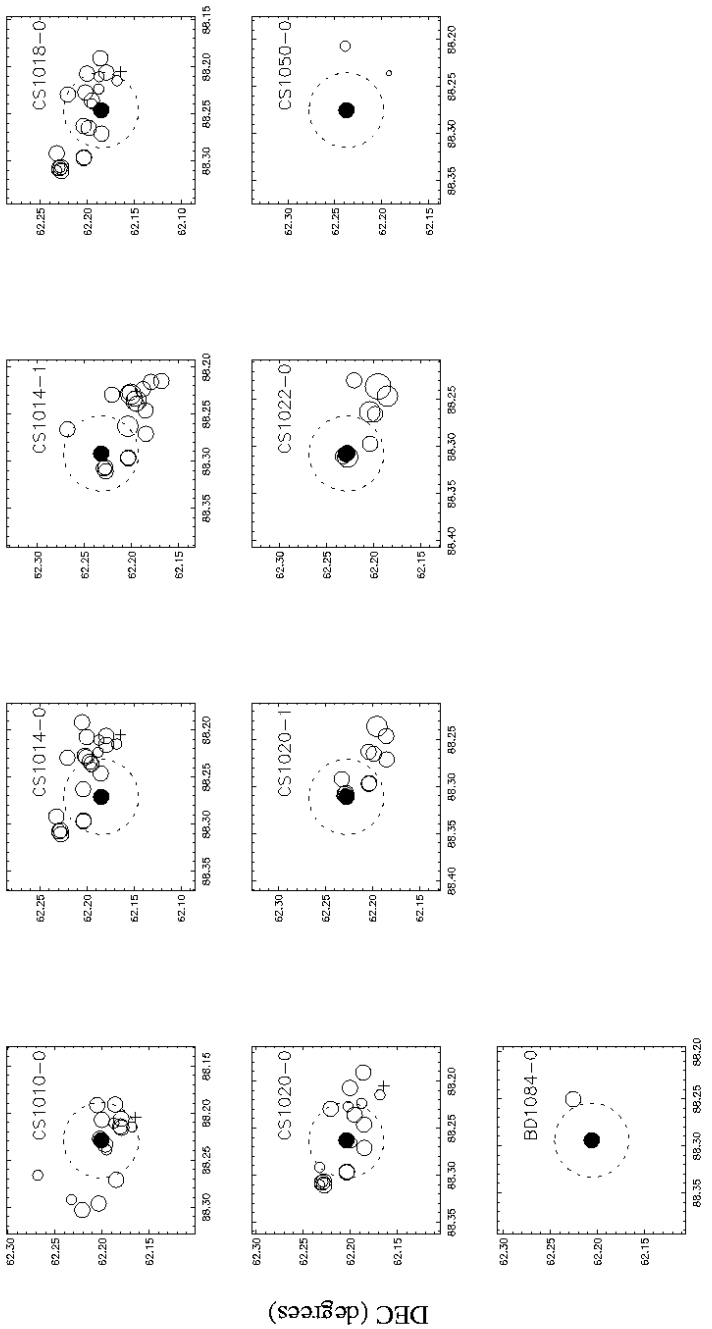

Figure 2.19: Continued

3

Near-infrared spectroscopy of the LIRIS-GAL sample of galaxies: a pilot study

3.1 Introduction

In the previous chapter I discussed the selection and analysis of the LIRIS-GAL sample of galaxies at a redshift range of $0.46 < z < 1.1$. The result of such selection is a set of 88 galaxies, which are expected to be undergoing star forming episodes. These galaxies shall have strong emission of the Hα (6563 Å) line at *z* and *J*-bands (i.e. depending on redshift). The Hα flux measurement of these galaxies has to be carried out with intermediate-resolution near-infrared spectrographs (as described below). Moreover, the surface density of the sample of galaxies (1.6 arcmin^{-2}) represents that from 5 to 6 galaxies could be observed simultaneously with the multi-object spectroscopy mode of LIRIS (see chapter 6). In advance to the availability of this instrument, I have prepared the observation strategy taking into account all the parameters that would affect the emission line detection. Then, I performed the observation of three galaxies employing the long-slit near-infrared spectrographs Omega Cass and NICS, as a pilot study to asses the selection and observational strategies. The SFR estimation as a result from the observation of BD0840-0 is discussed in the final section.

3.2 Observing the galaxies from the LIRIS-GAL sample

All the galaxies in the LIRIS-GAL sample are from the Hubble Deep Field North and Flanking Fields, which have their central coordinates at J2000 12h 36m 49.4s +62° 12' 58". Therefore, the best time for the observations is from January to June, in order to have an airmass $x < 2$ if observed from the ORM. Several other parameters affect the detection and measurement of the Hα emission line. The most important parameters are: a) the spectral resolving power required to separate the [NII](6548, 6583 Å) lines, b) that to resolve Hα from the OH emission lines and, c) the atmospheric transmission. The galaxies are then, classified from the analysis of these parameters, as it will be seen in the following sections. Other parameters concerning previous observations will also be

discussed for some selected galaxies.

3.2.1 Spectral resolving power required to separate the [NII] lines

The collisionally excited emission lines [NII](6548, 6583Å) are close, in wavelength to Hα(6563 Å). The distance is so small that the flux of Hα is commonly measured as the blend of Hα and [NII], (i.e., when they are not resolved). Some authors (e.g. Kennicutt 1992; Gallego et al. 1997; Yan et al. 1999) apply the empirical ratio: Hα/[NII] = 2.3, which is obtained from star-forming galaxies observations, to correct the Hα flux. The SFR can be calculated with the flux extracted in this way, however, the uncertainties on the assumed ratio will affect the SFR estimation. The best results are obtained if the three lines were resolved, which implies to observe the galaxy with a minimum spectral resolving power. Such minimum depends on the galaxy redshift, since the difference in wavelength increases directly as a function of 1+z. The spectral resolving power, R is defined by $\frac{\lambda}{\delta\lambda}$, where the *limit of resolution*, $\delta\lambda$ is the wavelength difference between two emission lines (i.e. monochromatic sources) for which the separation between their images, projected on the detector, is equal to the slit width (e.g. Hutley 1982; Schroeder 1987). Such definition is based on the Rayleigh criterion of two images with the same intensity. Therefore, this definition can only be applied to lines with similar fluxes. In the case of Hα and [NII] emission lines, the relatively small difference between the fluxes and the fact that for all the star-forming galaxies, Hα is stronger than [NII] (Veilleux & Osterbrock 1987), the *limit of resolution* applies well. Therefore, a spectra with $R > 450$ allows to resolve these lines for galaxies at redshifts $0.4 < z < 1.1$.

3.2.2 Resolving Hα from the OH emission lines

As it is described in section 4.2.2 the OH lines limits the observations at near-infrared wavelengths. This is specially important for the observation of the LIRIS-GAL sample of galaxies because the flux of most OH emission lines is stronger than that expected for Hα. Although the OH lines can be subtracted, the photon shot noise produced by these lines remains in the spectra, affecting the measurement of Hα. Such noise goes as the square root of the line flux (see section 4.4). Therefore it is preferred not to have an OH line close to Hα. As in the case of the [NII] lines, the minimum recommended separation between the observed Hα wavelength and that of any OH emission line, depends on the spectrograph resolving power. However, since most OH emission lines are much more stronger than Hα, the definition of *limit of resolution*, stated in the previous section, does not guarantee that the lines will be resolved. In this particular case, a separation between the line images, projected on the detector, of two times to the projected slit width will be considered as the minimum recommendable.

Table 3.2.2 lists the LIRIS-GAL sample galaxies indicating the expected Hα emission line wavelength in column 3 and, the strongest OH line that is close to Hα. The OH line flux, relative to the flux of the OH line at 12122 Å (i.e. the strongest one in the *J*-band, according to the catalog of Rousselot et al. 2000) is given in column 5. The wavelength separation to Hα are given in column 6. From this value, I estimated the minimum spectral resolving power and compared it with that required to resolve the [NII] lines (described in the previous section). The resultant minimum resolving power is given in column 7. Some notes are added in order to identify such galaxies where the presence of very weak OH lines closer than the strong line (i.e. that cited in columns 5 and 6) could produce a *noisy* spectrum. As well, no value is given if the minimum is greater than

R=10000.

It is concluded from Table 3.2.2, that 28 galaxies can be observed with R$\leq$1000 and 38 galaxies can be observed with 1000$<$R$\leq$3000, from which 11 are *noisy*. There are also 13 galaxies that require 3000$<$R$\leq$10000 spectroscopy and 9 galaxies that are not recommended to be observed in Hα because they require an extremely high resolving power.

3.2.3 Atmospheric transmission at the expected Hα wavelength

The atmospheric transmission is not uniform along the near infrared spectral range. The global shape of such transmission is followed by the standard *J*,*H* and *K*-bands. However, considering that the spectroscopy is not limited to the standard filters, I performed a basic analysis of the atmospheric transmission at each possible wavelength of Hα of the LIRIS-GAL sample of galaxies. An example of the atmospheric transmission[1] is shown in Figure 3.1; it goes from 0.9 to 1.4 μm and is given normalized to 1. The same figure shows the cut-edges of the standard *z* and *J*-band filters as well as the NICS special bands called *1mic* and *Js*.

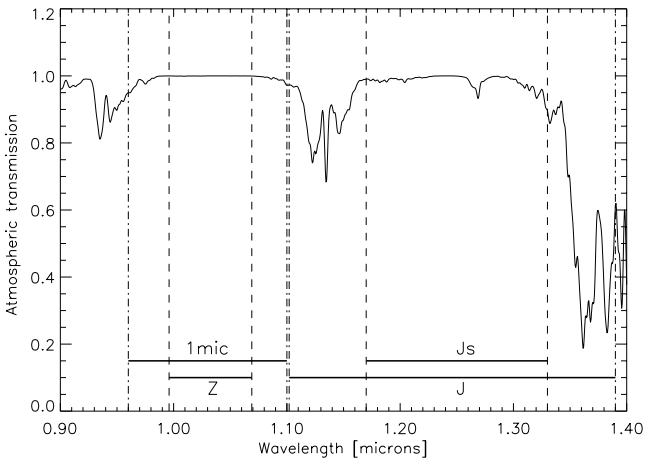

Figure 3.1: Atmospheric transmission from 0.9 to 1.4 μm normalized to 1 (solid line). The dashed vertical lines indicate the cut-on and cut-off wavelengths of the standard *z* and *J*-bands and for 1*mic* and *Js*-bands from NICS.

The analysis of the atmospheric transmission at the expected Hα wavelength, allows to identify those galaxies whose emission line are affected, and those that fall in a region of good transmission. Column 4 in Table 3.2.2 lists the transmission approximated value estimated for each galaxy; it can be seen that all but 5 galaxies have Hα falling in regions with atmospheric transmission better than 90%.

[1]These data, produced using the program IRTRANS4, were obtained from www.jach.hawaii.edu/JACpublic/UKIRT/astronomy/ext-menu.html

Table 3.1: Observational parameters for the LIRIS sample of galaxies

Name	z_{sp}	Hα λ_{obs} [Å]	Atm. %	Closest OH line rel. intensity[a]	at [Å]	R (minimum)
BD0462-0	0.462	9595	95	0.04	25	767
CS0472-0	0.472	9661	97	0.05	40	483
BD0474-0	0.474	9674	97	0.03	10	1934[b]
BD0475-0	0.475	9680	97	0.04	20	968[b]
BD0475-1	0.475	9680	97	0.04	20	968[b]
BD0476-0	0.476	9687	98	0.05	15	1291[b]
BD0480-0	0.480	9713	98	0.02	1	—[c]
BD0482-0	0.482	9726	100	0.06	4	4863
BD0483-0	0.483	9733	98	0.06	10	1946[b]
CS0484-0	0.484	9739	98	0.06	17	1145[b]
BD0485-0	0.485	9569	92	0.04	2	9569
CS0485-0	0.485	9569	92	0.04	2	9569
BD0487-0	0.487	9759	98	0.15	35	557
BD0504-0	0.504	9871	100	0.02	4	4935
BD0507-0	0.507	9890	100	0.15	15	1318
BD0509-0	0.509	9904	100	0.12	13	1523
CS0511-0	0.511	9917	100	0.13	0	—[c]
BD0513-0	0.513	9930	100	0.30	15	1324
CS0513-0	0.513	9930	100	0.30	15	1324
CS0520-0	0.520	9976	100	0.12	40	498
CS0525-0	0.525	10009	100	0.13	7	2859
BD0528-0	0.528	10028	100	0.10	12	1671
CS0529-0	0.529	10035	100	0.10	20	1003
CS0535-0	0.535	10074	100	0.09	10	2014[b]
CS0555-0	0.555	10205	100	0.17	9	2267[b]
CS0557-0	0.557	10219	100	0.18	5	4087
BD0558-0	0.558	10225	100	0.20	11	1859[b]
CS0558-0	0.558	10225	100	0.20	11	1859[b]
CS0559-0	0.559	10232	100	0.20	16	1279[b]
BD0560-0	0.560	10238	100	0.20	25	819
CS0561-0	0.561	10245	100	0.45	45	455
BD0570-0	0.570	10304	100	0.45	14	1472
CS0586-0	0.586	10409	100	0.35	12	1734
BD0594-0	0.594	10461	100	0.25	10	2092
BD0594-1	0.594	10461	100	0.25	10	2092
CS0635-0	0.635	10730	100	0.21	1	—[c]
BD0654-0	0.654	10855	100	0.25	10	2171
BD0654-1	0.654	10855	100	0.70	20	1085
CS0672-0	0.672	10973	98	0.55	2	—[c]
CS0677-0	0.677	10006	96	0.35	23	870
CS0681-0	0.681	11032	97	0.35	2	—[c]
CS0681-1	0.681	11032	97	0.35	2	—[c]
CS0682-0	0.682	11039	97	0.35	10	2207
CS0683-0	0.683	11045	97	0.35	16	1380

Name	z_{sp}	Hα λ_{obs} [Å]	Atm. %	Closest OH line rel. intensity[a]	at [Å]	R (minimum)
CS0692-0	0.692	11105	96	0.20	15	1480
BD0693-0	0.693	11111	94	0.20	20	1111
BD0693-1	0.693	11111	94	0.20	20	1111
BD0695-0	0.695	11124	94	0.20	33	674
BD0744-0	0.744	11446	85	0.80	6	3815
CS0744-0	0.744	11446	85	0.80	6	3815
BD0747-0	0.747	11466	82	0.10	3	3822[b]
CS0751-0	0.751	11492	86	0.60	48	478
CS0758-0	0.758	11538	90	0.60	1	—[c]
BD0760-0	0.760	11551	90	0.60	10	2310
CS0778-0	0.778	11669	99	0.45	19	1228
BD0784-0	0.784	11708	98	0.25	7	3345
BD0788-0	0.788	11735	98	0.25	19	1235
CS0819-0	0.819	11938	100	0.20	50	477
BD0821-0	0.821	11951	100	0.20	37	646[b]
BD0840-0	0.840	12076	100	0.95	48	503
CS0841-0	0.841	12082	99	0.95	45	536
CS0842-0	0.842	12089	99	0.95	32	755
CS0846-0	0.846	12115	100	0.10	5	4846
CS0846-1	0.846	12115	100	0.10	5	4846
CS0849-0	0.849	12135	100	0.35	1	—[c]
CS0858-0	0.858	12194	100	0.20	3	4065
BD0880-0	0.880	12338	100	0.55	12	2056
CS0901-0	0.901	12476	100	0.13	26	959
BD0904-0	0.904	12496	100	0.15	7	3570
BD0907-0	0.907	12516	100	0.15	13	1925
CS0934-0	0.934	12693	94	0.10	60	437
BD0936-0	0.936	12706	97	0.10	40	635
BD0960-0	0.960	12863	100	1.00	42	612
CS0961-0	0.961	12870	100	1.00	35	735
CS0961-1	0.961	12870	100	1.00	35	735
CS0973-0	0.973	12949	99	0.40	28	924
CS1001-0	1.001	13133	96	0.62	25	1050
CS1005-0	1.005	13159	97	0.62	2	—[c]
CS1010-0	1.010	13192	95	0.62	35	753
CS1014-0	1.014	13218	95	0.35	18	1468
CS1014-1	1.014	13218	95	0.35	18	1468
CS1018-0	1.018	13244	96	0.35	8	3311
CS1020-0	1.020	13257	95	0.35	20	1325
CS1020-1	1.020	13257	95	0.35	20	1325
CS1022-0	1.022	13270	94	0.35	33	804
CS1050-0	1.050	13454	85	0.06	33	815
BD1084-0	1.084	13677	25	0.25	3	4559

Notes: *a*) The flux values are relative to that of the OH line at 12122 Å *b*)Risk of *noisy* spectra (i.e. even if the strong OH lines are resolved there is one or more very weak OH lines closer) *c*) No value is given for R>10000.

3.2.4 Instrument-dependent selection

The spectrograph selected for the observations plays an important role in terms of its throughput as a function of wavelength. Besides, the available grisms/gratings and filters, have to be considered to select those galaxies that can be observed with the best performance of the instrument.

The spectral resolving power is the main-driving parameter on the selection criterion because, as reviewed before, the success of the detection of the emission line depends highly on the proximity of the OH lines. The selection of the spectrographs that fulfils the resolving power requirement comes from their characteristics (see Table 1.1), when compared to the last column of Table 3.2.2. It can be seen that the R$\sim$3000 spectroscopy mode of LIRIS is adequate for most galaxies in the sample. The resolving power and the desired S/N ratio depend on each other (see section 4.5). Therefore, the best trade off between both parameters must be pursued for the observation.

3.3 Notes on some selected galaxies

As it was discussed before, several parameters have to be taken into account to observe a galaxy at intermediate redshifts. Up to here, it has been summarized the selection of the sample, the presence of strong OH emission lines close to the wavelength of Hα and the required resolving power. These parameters are summarized in Table 3.2.2. There are also, other parameters that have to be considered, such as: morphology, observed spectral properties, environment, Hα estimated flux, etc. The published data does not provide these parameters for all the galaxies, then I will present these data for some galaxies as examples of objects that can be observed with low resolving power (according to the criteria given in section 3.2.2) and that are found in low-density environments (from the analysis described in section 2.4.2). All the distance estimations and other calculus assume a cosmology of H_0=100 h^{-1} Km s^{-1} Mpc^{-1}, h=0.7 and q_0=0.2.

3.3.1 BD0462-0

BD0462-0 is the galaxy with the lowest redshift at the LIRIS-GAL sample; it is at z=0.462. Figure 3.2 shows the FW814-band image, where three galaxies can be seen. That one in the center is BD0462-0. There is another galaxy at the same redshift and at a distance of 1.71 arcsec (9 kpc). The small distance between them suggests that they have interaction on each other. It also makes the observation very difficult. The third galaxy does not have the redshift measurement. Guzman et al. (1997) report the detection of [OII], [OIII] and Hβ emission lines from optical spectroscopy. The optical spectrum of Hβ is shown in Figure 3.3, where it can be seen that the emission is very strong. The measured line ratios [OIII](5007 Å) / Hβ = 2.7$\pm$0.3, [OII] (3727 Å) / [NeIII] (3869 Å) = 12.2$\pm$1 and EW([OII] (3727 Å)) / EW(Hβ) = 3.5$\pm$0.7 identify this object as a HII region-like galaxy (see Section 2.4.1).

The Hα emission line is expected at 9595 Å, where the atmospheric transmission is 95%. Practically, there is only one weak OH emission line close to this wavelength, which sets the required resolving power in R $\geq$ 767.

Figure 3.2: WFPC2 8 arcsec image of BD0462-0 in the FW814 filter.

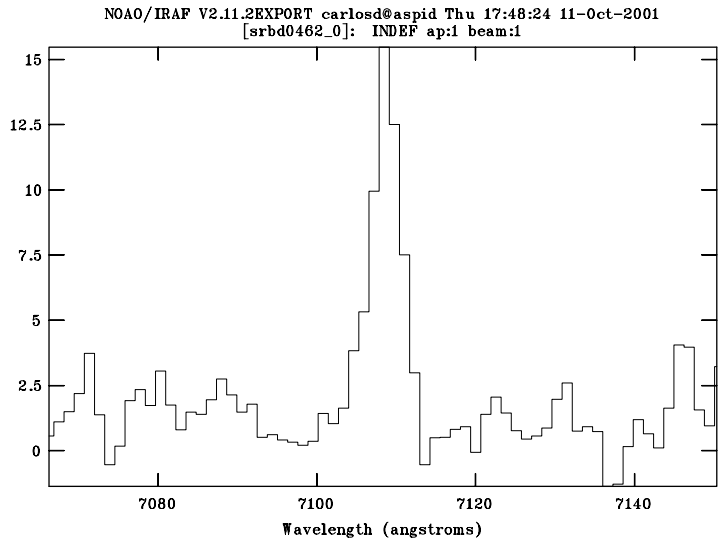

Figure 3.3: Hβ emission line detection in the optical spectrum of BD0462-0. Observed wavelength.

3.3.2 BD0693-1

The F814W-band image of this galaxy at z=0.693 is shown in Figure 3.4. It can be seen that there are no companion galaxies closer than 1 Mpc, as discussed in the environment analysis (see section 2.4.2).

The optical spectrum from Guzman et al. is shown in Figure 3.5. The spectrum reveals the [OII], [OIII], Hβ and Hγ emission lines with the ratios [OIII](5007 Å) / Hβ = 5.9±0.5, [OII] (3727 Å) / [NeIII] (3869 Å) = 4.9±0.5 and EW([OII] (3727 Å)) / EW(Hβ) = 0.5±0.1. From these values and, according to the analysis described in Section 2.4.1, this object can be identified as a HII region-like galaxy.

Hα is expected to fall at 11111 Å, where the atmospheric transmission is about 94%. Close to this wavelength, there are two OH emission lines, one strong line at 20 Å and one very weak line at 33 Å. To resolve the strong OH line, the spectral resolving power must be $R > 1111$.

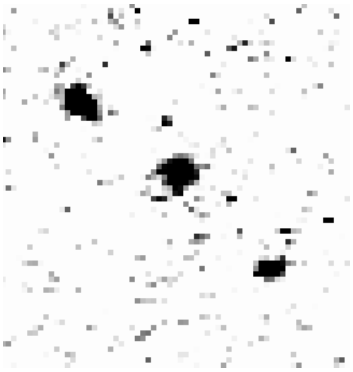

Figure 3.4: WFPC2 8 arcsec image of BD0693-1 in the FW814 filter.

3.3.3 BD0695-0

The galaxy BD0695-0 is not detected at the catalog of DEEP, therefore there is no spectral information about it. However, it is classified by Cohen (2001) as a *Balmer-emission-line* galaxy at redshift z=0.695. The FW814-band image in Figure 3.6 shows two galaxies, one at z=0.286 and the other at z=0.535. BD0695-0 is not detected on the image between these two galaxies.

The expected wavelength of Hα is 11124 Å, where the atmospheric transmission is about 94%. The closest OH emission line is very weak and it is at 15 Å , which relaxes the required spectral resolving power at R $>$ 674.

3.3.4 CS0819-0

The galaxy CS0819-0 is also selected on the fact of having colors that indicate the galaxy is undergoing a star formation episode. This galaxy, at redshift z=0.819, is included in the HDFN, thus its FW814-band image (see Figure 3.7) has very high S/N.

There is no evidence of companions closer than 1 Mpc to CS0819-0, according to the environment analysis, described on section 2.4.2. The Hα emission line is expected at 11398 Å, where the atmospheric transmission is 100% and the closest OH emission line is at 37 Å. Therefore, the required spectral resolving power is R $>$ 477, which is very similar to that required by the [NII] emission lines.

3.3.5 BD0840-0

The galaxy BD0840-0 is at redshift z=0.84. The F814W-band image can be seen Figure 3.8. The optical spectra from Guzman et al. shows the emission of the lines: [OII], Hδ and Hγ. The latter line is shown in Figure 3.9. Hβ is not observed because it falls at 0.894 μm, outside from the spectral range covered by the observations. Guzman et al. measure the ratios [OII]/Hδ $\approx$ 6.4 and [OII]/Hγ $\approx$ 4.6. The ratio [OII] (3727 Å) / [NeIII] (3869 Å) = 10.4$\pm$1 is also derived from the spectrum and suggests that this object is a HII region-like galaxy. As it will be discussed in section 3.4.3, Guzman et al. estimate a high value for the SFR based on [OII]. The strength of the Hδ and Hγ emission lines indicates that Hα must be very strong, unfortunately no flux estimation can be performed since the published spectra is not flux calibrated.

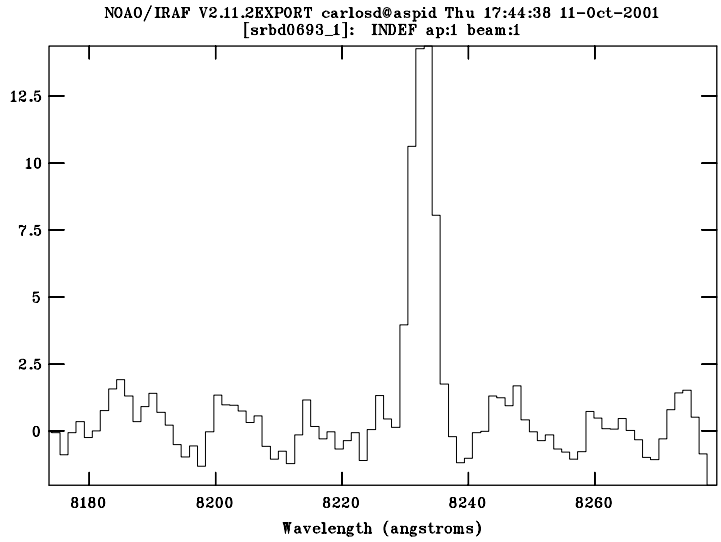

Figure 3.5: Optical spectrum of BD0693-1. The Hβ emission line is detected at 8229 Å (observed wavelength).

The environment analysis, discussed in section 2.4.2, revealed that this galaxy belongs to a group of a least 3 galaxies , being the closest one at the same redshift and at a distance of 5.1 arcsec (34 kpc).

The Hα emission line of this galaxy is expected at 12075 Å, where there is one strong OH emission line 20 Å apart (see Table 3.2.2). The required resolving power for the spectroscopy of this galaxy must be $R > 503$. Such dispersion was employed in the NICS spectroscopy of this object, in which Hα was successfully detected (see section 3.4.2).

3.3.6 CS1050-0

The galaxy CS1050-0 is at redshift z=1.050. It is also selected from the fact of having colors that indicate the galaxy is undergoing a star formation episode. The FW814-band image is shown in Figure 3.10. It can be see that there are no companion galaxies closer than 1 Mpc, according to the environment analysis (see section 2.4.2). The Hα emission line is expected at 13454 Å, where the atmospheric transmission is only 85%. Therefore a large extinction is expected for the observation of CS1050-0. On the other hand, the closest OH emission line is at 33 Å, which sets the required spectral resolving power in $R < 815$.

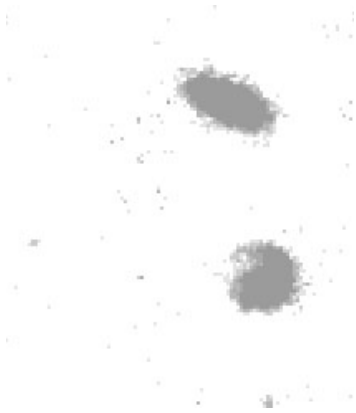

Figure 3.6: WFPC2 8 arcsec image of BD0695-0 in the FW814 filter.

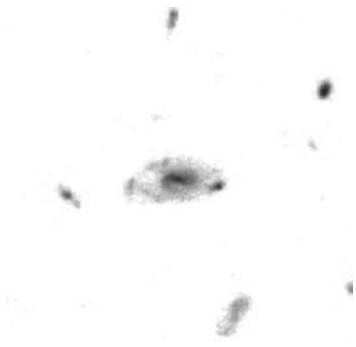

Figure 3.7: WFPC2 8 arcsec image of CS0819-0 in the FW814 filter.

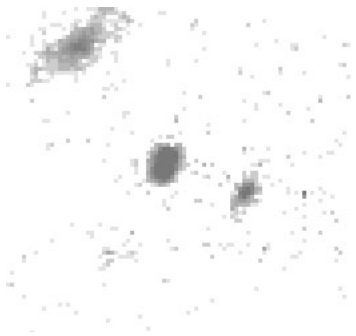

Figure 3.8: WFPC2 8 arcsec image of BD0840-0 in the FW814 filter.

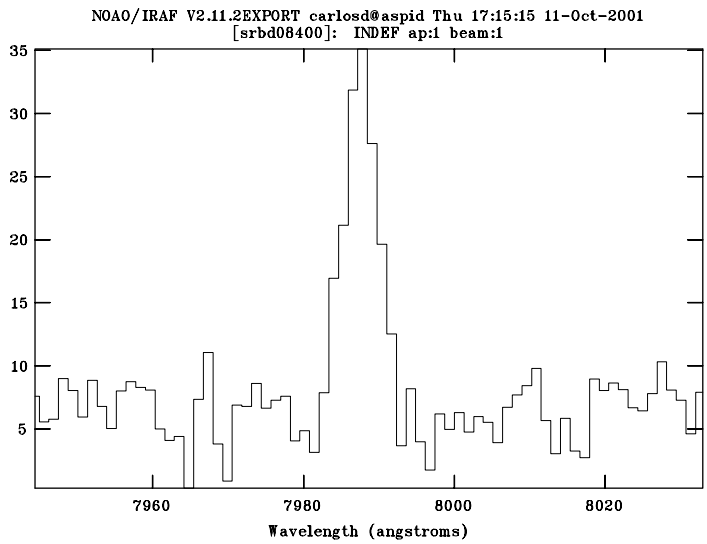

Figure 3.9: Optical spectrum of BD0840-0 (observed wavelength). The Hγ emission lines is detected with high S/N

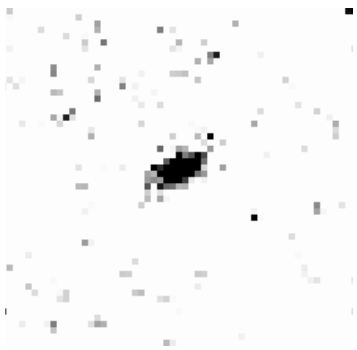

Figure 3.10: WFPC2 8 arcsec image of CS1050-0 in the FW814 filter.

3.4 The pilot study

I have conducted a series of pilot observations to assess the strategy in the near infrared spectroscopy of the sample of galaxies and to test the S/N estimations (described in section 4.4). Three galaxies were observed in two different runs. The first observations were done with Omega Cass at the observatory of the "Centro Astronomico Hispano Aleman" (hereafter, CAHA) and the second one with NICS at the Telescopio Nacionale Galileo (hereafter, TNG). Both instruments are long-slit near infrared spectrographs, being necessary to observe each galaxy independently.

3.4.1 Long slit spectroscopy with Omega Cass

The galaxies BD0907-0 and BD0693-1 were observed at the 3.5 m telescope in the CAHA observatory. The observations were performed on April 4^{th} 2001, during a Discretionary Director's Time run. We used Omega Cass (Lenzen et al. 1998), the near-infrared long slit spectrograph, which has a Hawaii 1024 $\times$ 1024 detector. The spectrograph setup included the "grism 3" and a slit of 0.9 arcsec width. This combination allowed to achieve a spectral resolving power of R=740 (in 4.5 pixels, which is the slit width). The mean seeing along the observations was slightly better than 0.9 arcsec.

Observations strategy

Figure 3.11 represents the observed field with the galaxies, the reference star and the position of the slits. The slits are not to scale and, even though, they are drawn together, the observations were carried out separately. The figure is intended only to represent the slit alignment. For both observations the slit was aligned north-south to ensure precise movements along the slit during the *nodding* technique (described below). This angle was preferred over the paralactic angle, since the worst cassegrain-flange angle-error was larger than the estimated displacement by differential refraction ($\sim$0.1 arcsec, for the observing altitude and wavelength, according to Filippenko 1982). The reference star, marked in the figure, is used because the galaxy is too faint to be centered by itself into the slit employing short time image exposures. Instead, the reference star is imaged during a few seconds and then, it is centered into the slit; a spectra of the star is acquired and after that, an offset is applied to the telescope to move it toward the galaxy centering it. This technique is called "blind offset" because the galaxy is never imaged. It requires a very good astrometry in order to compute the offset with minimum errors. In practice, such technique would not be "blind" if the galaxy were imaged when it is at the center of the slit. However, this approach would require almost half of the time estimated for the spectra (i.e. the process would require to image of the galaxy, move the telescope to acquire a sky image and to subtract both). Therefore, I preferred to use the "blind offset" technique, being confident on the fact that the astrometry to compute the offsets had errors less than 0.2 arcsec. Such precision is possible because the astrometry is based on images from the WFPC2, which has a pixel size of 0.099 arcsec. It should be noted that, a relative astrometry between the galaxy and the reference star is more important than an absolute astrometry. The reference star is imaged at the moment of centering the slit, so that, the offset is the only that has to be computed with high precision.

The *nodding* technique consists on taking an exposure and to offset the telescope, in such manner that the galaxy moves along the slit to a different position, where a second exposure is taken.

With this technique, the sky background emission and the OH emission lines can be almost eliminated from the spectra by subtracting two consecutive exposures with the galaxy in different positions. The *nodding* technique saves observing time for point objects (such is the case of most high redshift galaxies), because the object is acquired at both exposures with simultaneous acquisition of the "sky". The main restriction of this technique is the fluctuation of the sky background emission as a function of time.

The observation strategy consisted on a *nodding* technique at 3 different positions along the slit. The reason of using three positions instead of two, is that the detector of Omega Cass has a high number of bad pixels. Therefore, there is a high probability that the galaxy would fall close to a bad pixel in any of the *nodding* positions; if the latter would be the case, two of the positions could still be used to reduce the spectra.

The *nodding* was done in four steps: A, B, C and D, where A and C represent the same position along the slit. B and D are positions at both sides of the central position with offsets of 15 arcsec. The exposure time was 200 s at each position. After each two "ABCD" series, the reference star was imaged and re-centered into the slit attempting to prevent any misalignments. A total of 10 series were acquired representing a total integration time of 8000 s.

I estimated the required exposure time to achieve a good S/N for the Hα emission line of these galaxies. The base of the calculation is described in section 4.4, using the Hα typical fluxes from the references given in section 3.4.3.

Photometric and *telluric* standard stars were acquired at the beginning and at the end of the galaxy observations. These stars are used to calibrate the flux of the spectra, the telluric standard star is used to correct from the atmospheric transmission, and the photometric standard star is used to calibrate the flux respect to an absolute reference. The standard stars were selected on a basis to have the same airmasses than the galaxy, minimizing the errors when correcting for atmospheric extinction. They were acquired using the *nodding* technique, and the same positions in the slit, than the galaxy. Bright and gray sky flat-fields where also acquired with the same "grism 3".

Data reduction

The reduction of the spectra was performed using the IRAF[2] packages NOAO.TWODSPEC in the following sequence:

1. The flat-field exposures were combined by the median using IMCOMBINE. The bright and the gray flat-fields were reduced in groups, obtaining one flat-field for each group: FFon and FFoff. The gray flat was subtracted from the bright to eliminate the thermal contribution. The result from the subtraction was linearized at the dispersion direction using RESPONSE. No correction was needed at the spatial direction, since the resultant flat-field showed to be linear. All the images were, then "flat-fielded", dividing them by the result from RESPONSE.

2. The sky emission was eliminated by subtracting A1 - B1 and C1 - D1, where the number indicates that the four images containing the spectra were from the series "1". The resultant images (AB1 and CD1) contained, each, a positive and a negative spectrum. Then, two consecutive series were averaged, obtaining: (AB1 + AB2)/2 and (CD1 + CD2)/2. The same procedure was performed for all the series, in pairs; the series "3" were averaged with "4",

[2]IRAF: Image Reduction and Analysis Facility developed at NOAO

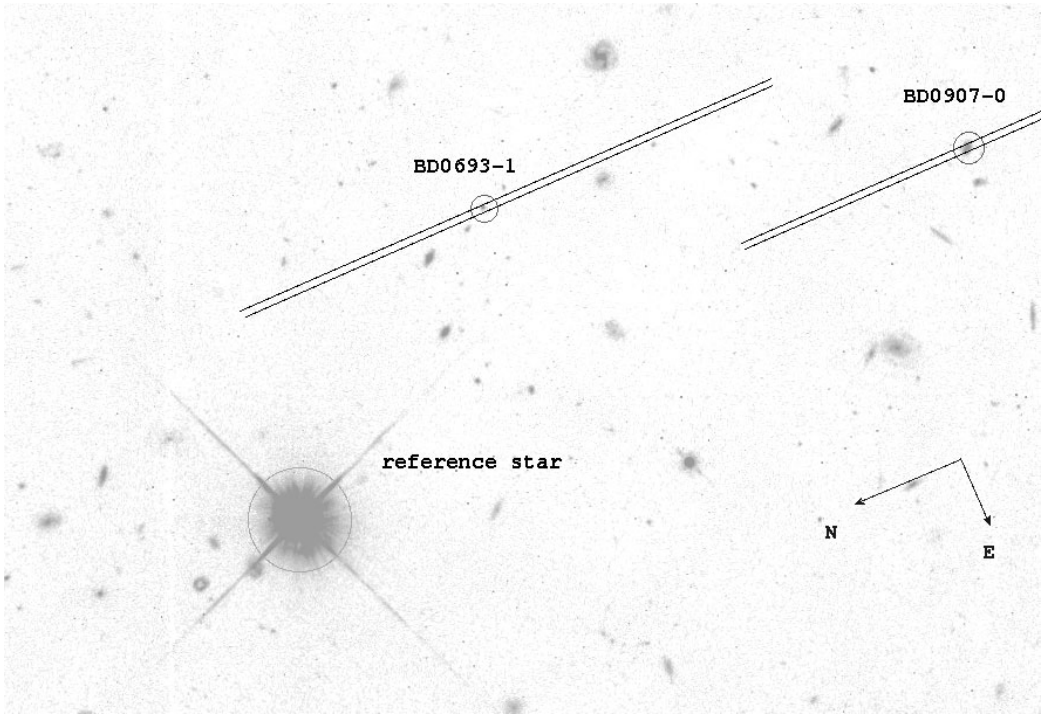

Figure 3.11: Representation of the position of the galaxies and the bright reference star observed with Omega Cass; the slit was parallel to north-south axis.

"5" with "6", etc. Bad pixels and cosmic rays were eliminated from the images using FIXPIX and bad pixel masks created with IDL[3] programs.

3. From visual inspection to the standard stars spectra, I tryed to determine the center of the aperture at each position to combine them. The determination of the exact position became complicated due to the fact that each series of the standard stars presented significant errors in their positions along the slit (i.e. the slit is parallel to the detector pixel columns and the position is measured at the rows of the detector). The first error found was, that the star does not return to the same point after moving all the offset of one series; the error is approximately 2 pixels, as it can be seen in Figure 3.12. Another problem was found when reviewing the reference star: the spatial position has an error respect to the previous spectra of the same star, each time that it was acquired (i.e. each two "ABCD"series). As it can be seen in Figure 3.13, the error in the position of the star, the spatial direction is approximately 5 pixels per hour. The figure shows a cut along the spatial direction to identify the center of the aperture of the reference star. The dashed and dotted lines are the apertures for the same star taken 1 and 2 h after the solid one, respectively. It seems that these errors could be related to instrument flexures or to telescope misalignment after the series offset movements.

   Following the visual inspection, I reviewed the dispersion direction, in order to estimate the errors at this direction. Although any shift in the spectral direction can be solved with the

[3]IDL is the acronym of Interactive Data Language, by Research Systems, Inc

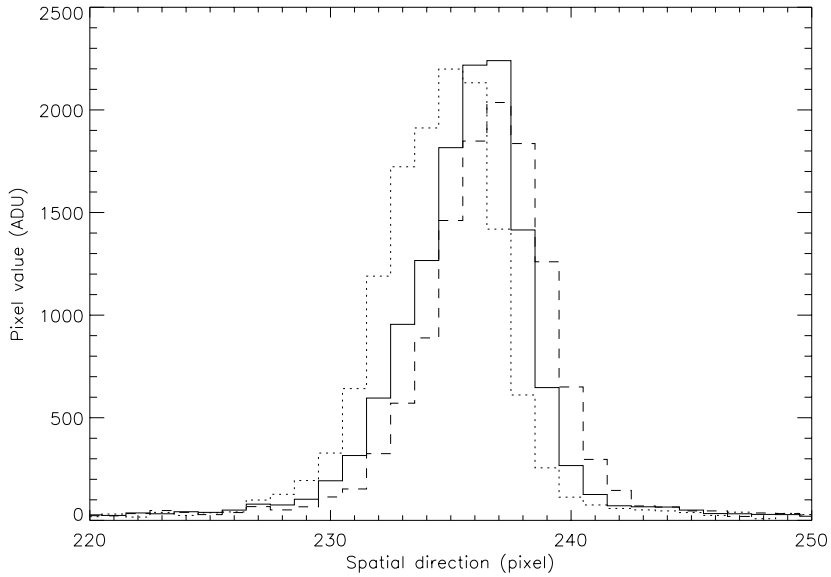

Figure 3.12: Error in the aperture positioning in the Omega Cass spectra. The different lines represent the position B before the offset (solid line), after 1 series of offsets (dashed line) and after 2 series (dotted line)

wavelength calibration (described below), the presence of shifts as function of time, would confirm if the instrument flexures were the main effect. The spatial direction shifts could be attributed either, to the error in the telescope offsets, or an instrument flexure that changes the optical path from the slit to the detector. However, the shifts in the spectral direction, shown in Figure 3.14 confirms the latter case, since this effect can not be attributed to the telescope. The OH emission line spectra, shown in the figure were taken at three different times; the time between the solid line spectra and the dashed line one is 1 h, and from the first to the dotted line spectra is more than 2 h. The shifts are from 2 to 3 pixels per hour.

Unfortunately, the effect of the flexures complicated the reduction process because the galaxy is so faint that, no continuum, nor any emission line could be detected from a single exposure. Therefore, the galaxy aperture determination depended entirely on the assumption that the shifts of the galaxy spectra, respect to the reference star, taken each two series, were minimum. I decided then, to work with the apertures as “images”, rather than extracting the spectra to one dimension (i.e. as normal in spectra reduction) to reduce the uncertainties in the exact aperture determination. Moreover, the wavelength calibration had to be performed each two “ABCD” series.

4. Keeping in mind that the misalignments were present, I determined the center of the apertures “in an empirical way”, using the reference star and adding or subtracting the equivalent offset in pixels for the different positions in the slit. The offsets were 15 arcsec equal to 79 pixels, according to the mean positions in the series of the standard stars. The offset computed in this way, was used to cut the images, saving only a section of 30 pixel at both sides of the theoretical position of the aperture.

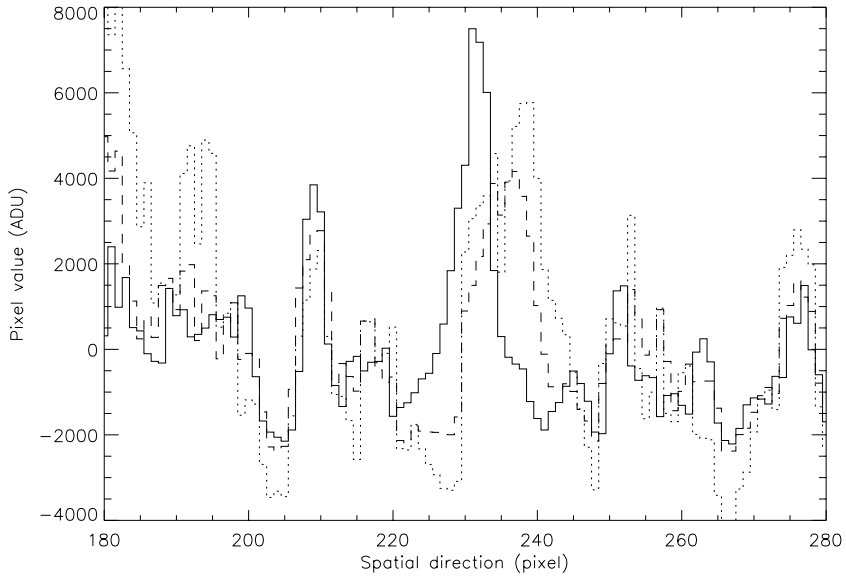

Figure 3.13: Spatial shift in the Omega Cass standard-star spectra due to instrument flexures or beam-switch movement errors. The dashed and dotted lines are for spectra taken around 1 h and 2 h latter, respectively.

5. I performed the wavelength calibration to determine the spectral dispersion for different regions of the spectra along the spatial directions. The procedure IDENTIFY allows to fit the wavelengths of the lines in the spectra (from a calibration lamp, or from the sky using the well know OH emission lines). I used a calibration lamp only for a rough determination of the spectral range, since the calibration based on the OH emission lines would provide higher precision. Moreover, taking into account the observed shifts in the spectral direction, the entire calibration had to be based on the OH emission lines. The package IDENTIFY allows to integrate several rows to improve the S/N ratio of the OH emission lines and, to facilitate the identification; in fact, the spectra of Figure 3.14 is the integration of the 1024 rows in in the spatial direction. The problem arose at the moment to run REIDENTIFY (i.e. this package corrects the inclination of the lines) because only a small amount of rows can be used to integrate the emission lines, therefore, the S/N is extremely low to intend any line identification. The main reason of the low signal of the OH emission lines is the high readout noise (R = 25 e^-) and the short exposure time used (200 s). To achieve higher signal, I combined all the eight images containing the spectra of the two consecutive series. The resultant image was calibrated with REIDENTIFY obtaining a higher level of confidence.

6. Once the images, centered at the apertures, were calibrated in wavelength and, the negative spectra was converted to positive, the four aperture images were averaged to obtain a reduced aperture image representing two series. Then, all the resulting images of each couple of series were averaged to produce a final image containing the spectra, ready to be extracted.

7. The aperture was extracted, in a first approach using SPLOT and combining the central rows

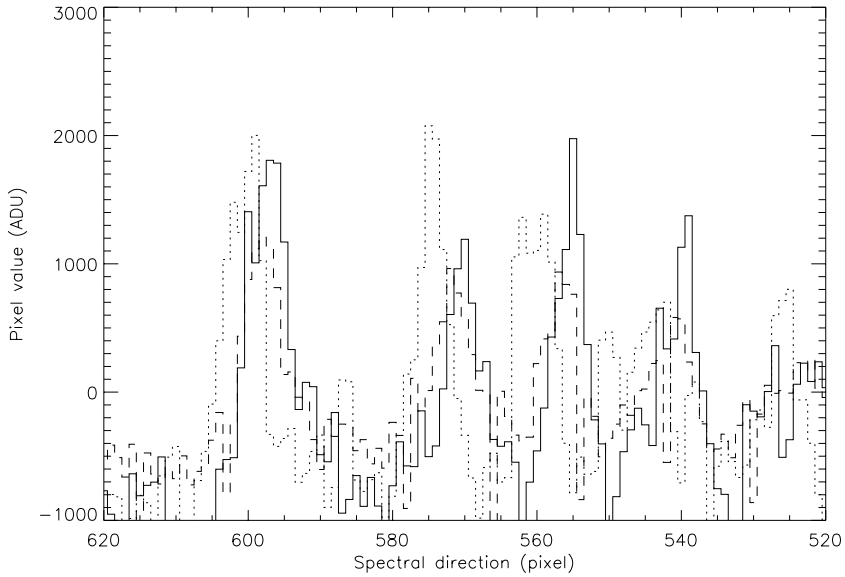

Figure 3.14: Wavelength shift in the OH emission lines spectra due to Omega Cass flexures. The dashed and dotted lines are for spectra taken around 1 h and 2 h latter, respectively.

for the pixel line corresponding to the wavelength where the Hα emission line was expected. The resultant spectra neither showed continuum nor special features that could be associated to the emission line; different rows were also combined with no improvement on the results. The spectra showed a large amount of bad pixels. Therefore, I tryed to go back in the reduction process doing again the combination of the apertures from the different positions and from the different series, following three different algorithms trying to achieve higher performance: a) simple addition, b) an average, eliminating the bad pixels using a threshold and, c) a median combination from three position in the slit ABD or BCD, for a complete elimination of the bad pixels. Although the bad pixels were removed from the final spectra, and the noise was slightly reduced, none of these approaches showed the expected spectrum.

The reduction process was performed to the second galaxy spectra with the same bad results. As reviewed in section 3.3, both galaxies show strong Hβ emission lines, assessing the emission of Hα. Therefore, I think that there are three possible reasons for the non detection of this emission line: a) the instrument flexures in the spatial direction, that could have shifted the aperture more than what it was estimated; b) the short exposures and low signal to noise ratio and, c) errors in the astrometry, due the fact that the reference star reaches the saturation level in the WFPC2 image. The last option is less probable than the others, because the error would be less than 4 pixels (0.4”).

As described in the previous sections, the most probable reason is that the instrument flexures shifted the spectrum in both directions spectral and spatial. For bright objects, these shifts can be identified and corrected, but for faint objects, such as intermediate redshift galaxies, the flexures become a restriction for the use of this instrument for such project. The origin of the flexures is related to the mechanical structure of the instrument and to the fact that it is mounted on the cassegrain focus of the telescope.

3.4.2 Long slit spectroscopy with NICS

A second opportunity to take the infrared spectra was available thanks to the collaboration of Dr. Victor Sánchez and Dr. Rafael Rebolo. The observations were carried out at the Telescopio Nacionale Galileo on June 5^{th} 2001, using the long-slit spectrograph: Near Infrared Camera Spectrometer (NICS; Oliva et al. 2001). The main difference between this spectrograph and Omega Cass is that NICS is mounted on the Naysmith focus of the telescope, thus the instrument flexures should be minimized. The reason is that the only movement applied to the instrument is the field derotation.

For this observation I selected the galaxy BD0840-0, which is described in section 3.3.5. It shows very strong Hγ and Hδ emission lines, being evidence of a strong Hα line and a high star formation activity. Besides, as it will be described below, there is a reference star close to this galaxy and this helps in the observation technique. The required resolving power was fulfilled by the spectrograph.

Observation strategy

NICS has a 1024 x 1024 Hawaii detector and the selected setup was to use the 0.25"/pixel camera, the medium resolution grism (IJ, with a resolving power of R$\sim$500) and a 1" slit.

Due to the low signal to noise ratio of the spectra in the previous observations with Omega Cass the exposure time was increased; the telescope offset in the *nodding* technique was limited to $\pm$10 arcsec along the slit and the sequence was reduced to "A-B-B-A".

To avoid the uncertainty in the aperture position, due to flexure problems (as experienced in the observations with Omega Cass), I selected a reference star close to the galaxy in order to place both objects in the slit observing them simultaneously. In this manner, measuring the spatial shift in the star continuum could solve any flexures in the spatial direction. This was not an easy solution, because, the lack of bright stars in the HDF+FF. As can be seeing in Figure 3.15 the closest bright star is at 0.55 arcmin from the galaxy.

This reference star has a I=19.7 mag and a V-I= 2.0 mag, from which a M1V spectral type can be assigned; then a J=18.5 mag is estimated. With this magnitude, even the acquirement of the reference star spectra, was a challenge by itself. With this in mind I selected an exposure time of 900 s to obtain a S/N $>$ 2 in the continuum of the star. Although the signal to noise ratio is minimum, it is just enough to trace the aperture; no longer exposure times were considered due to the variation in the sky emission.

I calculated the relative astrometry from the reference star to the galaxy and the slit angle to put both objects into the slit; the result was 17.17 degrees north to east. This slit angle has the disadvantage of not observing at parallactic angle. According to the work of Filippenko (1982), the differential refraction estimated for the observation airmasses goes from 0.10 to 0.17 arcsec, so that, its effect can be neglected.

The galaxy observations proceeded by, first pointing to the reference star and centering it at the slit by 2 minutes images. Then, the spectra was acquired at the A–B–B–A positions. A total integration time of 5400 s was performed.

Two standard stars were acquired at similar airmasses to minimize the errors in the flux calibration due to extinction. One standard star is used to correct the telluric features (HD107582) and the other to calibrate in flux (SAO105832). The last star is a photometric standard, instead of a

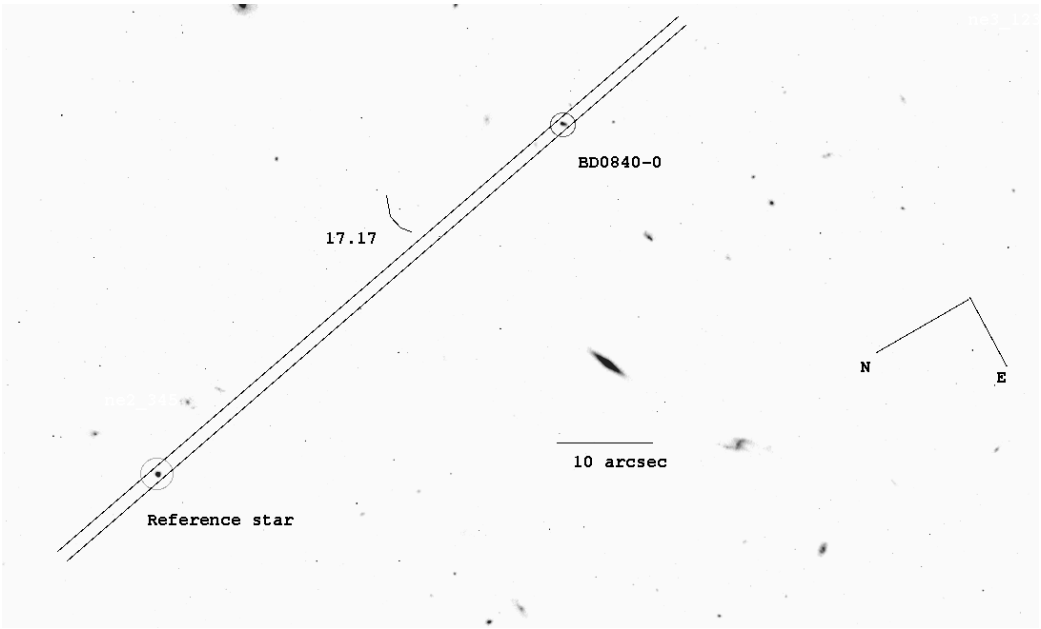

Figure 3.15: Representation of the position of the galaxy (at the top of the figure), the reference star and the slit angle used for the NICS observations.

spectrophotometric one, because of the lack of the latter kind of standards at infrared wavelengths. Although it seems to be quite rare, this limitation is present in infrared spectroscopy; this is an example that the infrared spectrographs have become available very recently. The solution to the flux calibration is to use an early type standard star with available photometric data. Such star is assumed to behave as a black body at the respective temperature. Then, the flux per unit of wavelength is derived from the integration of the spectra at any of the bands with photometric measurements. The whole procedure can be performed with the IRAF package NOAO.ONEDSPEC.STANDARD.

Spectra reduction

During the observations, I carried out an *on line* spectra reduction subtracting the sky by computing A-B. The apertures were determined with the reference star and the offsets between the positive and negative spectra were measured. All the individual spectra were averaged using IMCOMBINE. The wavelength calibration was performed using the OH emission lines. For this purpose the ONEDSPEC package was preferred since the galaxy spectra was analyzed only in the region where the Hα emission line was expected. Finally, I added all the individual spectra and inspected it using SPLOT. Hα was found at the expected wavelength, showing a S/N ratio of $\sigma > 3$, thus confirming the success of the observations.

The complete reduction was done in a similar way than that described for Omega Cass observations; nevertheless, the details and the flux calibration that was not done before, are described in the following sections:

1. The first step was to correct the images from the *electronic cross-talk*, because all the images showed a high pattern; each image was corrected using a program written by Dr. Oliva at

TNG[4].

2. The bright and gray flat–field exposures were combined in groups using IMCOMBINE. The combination of the gray flat–fields was subtracted to the to bright one, in order to eliminate the thermal contribution of the telescope. The result from the subtraction was linearized at the dispersion direction using RESPONSE. No correction at the spatial direction was needed since the flat-field showed to be linear. All the images containing the spectra were flat-fielded using the normalized flat image obtained with RESPONSE.

3. The sky emission was subtracted to images in the form of A1-B1, B1-A1, A2-B2, B2-A2, etc., to obtain all the sky subtracted images in positive values. All of them, except for one, showed acceptable OH lines elimination.

4. From the visual inspection at the photometric and the telluric standard star spectra, I found that the observations of these stars presented a problem. The star fell slightly out of the slit for the exposures after the first one of the series, producing a diminished star continuum flux for the last exposures. This problem could be caused by the stop of the telescope *auto-guiding*. Therefore, only one spectra of each calibration star is available for flux calibration purposes. Fortunately the galaxy spectra does not present such problem, because a different observing macro was used for the long exposures. In any case, I inspected the galaxy spectra using the reference star; the result is that the continuum of the star shows similar levels for all the exposures. This inspection revealed also, that no flexure shifts are noticeable at the images of the spectra, as it can be seen in Figure 3.16.

   The galaxy spectra were averaged in groups according to their position along the slit. The A1, A2 and A3 groups were averaged obtaining one “A” 900 s average exposure. The same was done for the “B” group.

5. The wavelength calibration was done for each one of the positions of the object in the slit. There are two positions for the galaxy and one for the standard stars. A section in the spatial direction of the image with 100 pixels was cut centered on the aperture. Each section was calibrated independently, using the OH emission lines as a reference. The image with the OH lines, obtained from an *off-object* exposure, was cut from the same region. The calibration was performed using the package NOAO.TWODSPEC.LONGSLIT. The first step was to identify the OH lines from the center of the image section (i.e. line 50) using as database of Rousselot et al. (2000) and running IDENTIFY. The spectral dispersion solution was determined with an error of ~ 1.5 Å r.m.s. The second step was to apply the same dispersion solution to 10 pixel intervals along the spatial direction using REIDENTIFY. The solution here was determined with the residuals going from 1 to 1.5 Å r.m.s. This procedure corrected the inclination of the lines in the spectral direction.

   The dispersion solution in 2D was determined with FITCOORDS, using the result from REIDENTIFY. The final residuals were from 2 to 3 Å for the three regions of the slit. The estimated spectral solutions were applied to all the spectra of the same region using TRANSFORM. This calibration procedure was performed for the spectra on the standard stars and for the galaxy. The wavelength calibration was applied to the averaged spectra groups “A” and

[4]The program, written in fortran, is available at: www.tng.iac.es/instruments/nics/nics.html

"B". I reviewed them with SPLOT confirming that both groups showed the Hα emission line at the expected wavelength.

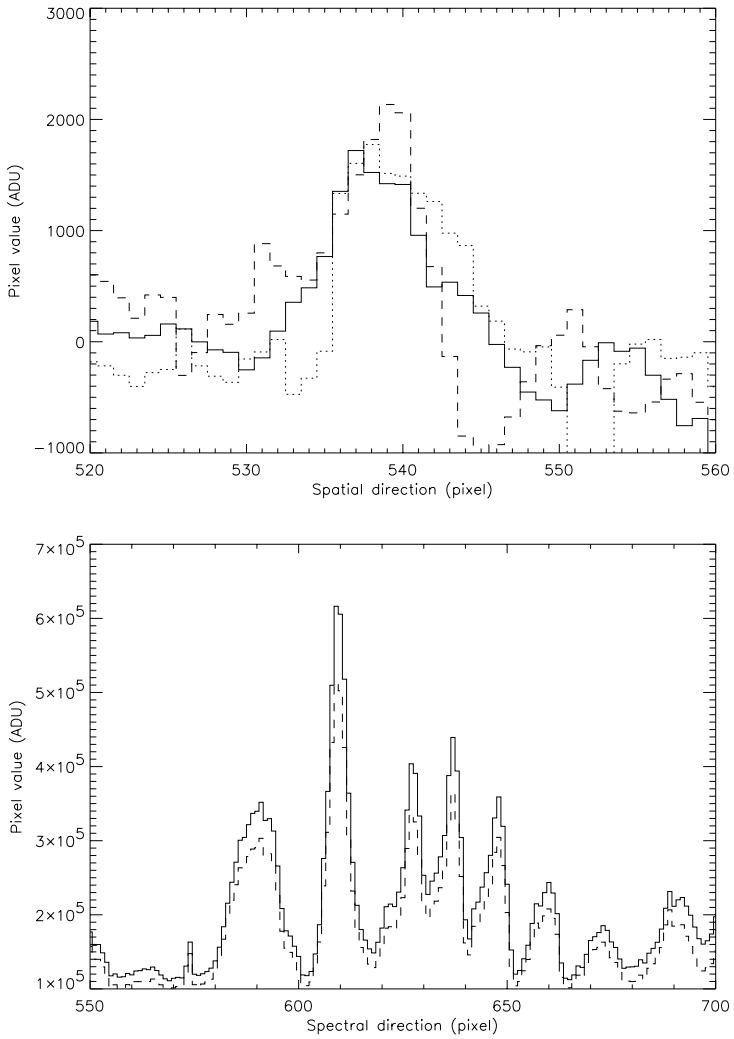

Figure 3.16: Visual inspection of the NICS spectra in spatial direction (top) and dispersion direction (bottom). The notation is the same than in Figures 3.13 and 3.14. It can be seen that no shifts are detected.

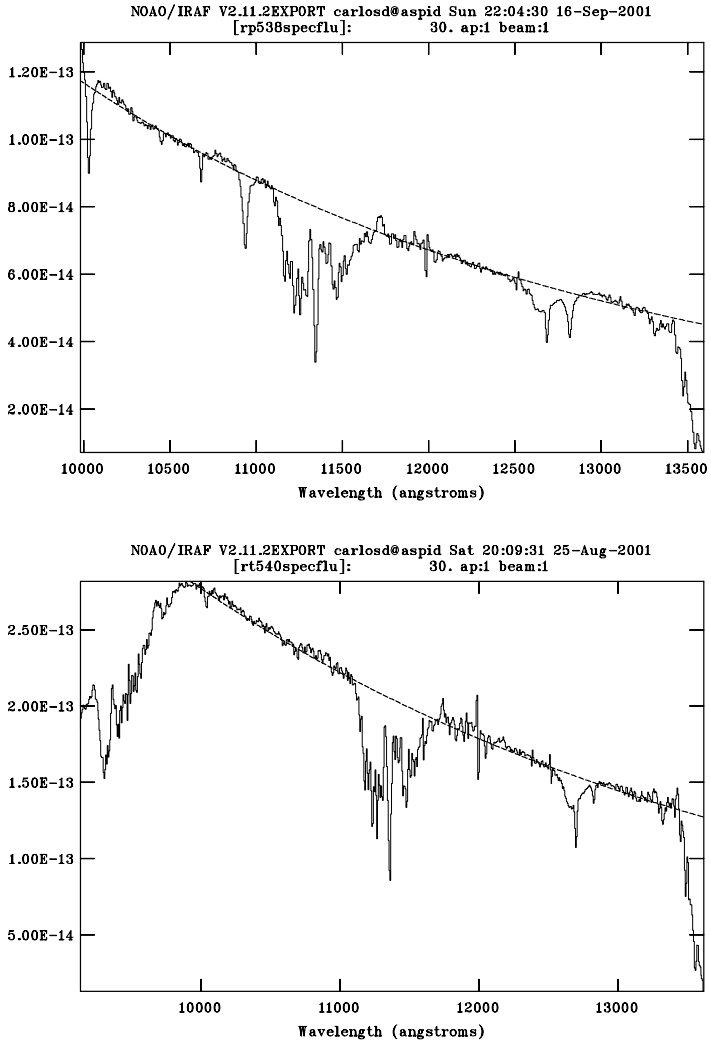

Figure 3.17: Flux calibrated spectra of the photometric (top) and telluric (bottom) standards. The flux units are: ergs s^{-1} cm^{-2} $Å^{-1}$. The dashed line represents the black body fit to the continuum.

6. The extraction of the standard stars spectra was done with the package NOAO. TWODSPEC. APEXTRACT, running APALL. Since these stars show a strong continuum, the extraction was relatively easy. The apertures were found to be around 10 pixel width and the curvature of the spectra was corrected with a 2^{nd} order function. The spectra of the standard stars is shown in Figure 3.17, with the telluric standard star HD107582 (top) and the photometric standard SAO105832 (bottom). The procedure to extract the spectra of the galaxies was more complex than that for the standard stars. The first approach was to extract the spectra of the standard stars observed at the same positions as the galaxy. Although, these standards could not be used for the flux calibration due to the misalignment explained before, they are good tracers of the curvature of the continuum at the points where the galaxy was observed. The importance of these stars rely on the fact that the galaxy shows almost no continuum, and therefore, the

extraction can not be done with the galaxy by itself. The standard stars were extracted and the curvature of the spectra was estimated; the solution was, then, applied to the spectra of the galaxy. Only the size of the aperture was estimated from the spectra of the galaxy; for that purpose, the region to define the aperture was fixed to the spectral region of the Hα emission line. The size of the aperture was 5 pixels. Once the spectra at both slit positions were extracted, they were summed using SARITH. This package was selected, rather than a simple addition or average, to match the two wavelength calibrated spectra of the galaxy.

7. Once the spectrum was extracted and the Hα emission line was detected at the expected wavelength, I performed the flux calibration. The calibration procedure was done using the IRAF package NOAO.ONEDSPEC. The telluric standard star (HD107582) is a "G1V" spectral type. This star must have minimum absorption features, so that it can be assumed that it has an homogeneous continuum with all the absorption bands being produced by the atmosphere. Nevertheless, since the galaxy spectra does not show continuum and flux calibration is focused only on the emission line, which falls away from any atmospheric absorption feature, the telluric correction does not affect the result. The photometric standard star was the SAO015832, which has precise photometry in the J, H and K-bands. The effective temperature of this star is estimated in 8545 K. and using STANDARD[5] it was calibrated by the fit to a black body, as it can be seen in Figure 3.17.

   The second step in the flux calibration was to estimate the instrument sensitivity ratio, using the standard star and the package SENSFUNC. Here, the sensitivity is adjusted as function of wavelength. The final step is to apply such sensitivity ratio to the galaxy spectrum using CALIBRATE.

[5]It is worth to mention that STANDARD in the package NOAO.TWODSPEC can not be used for these purposes, due to the lack of the black body parameters; probably, a bug in the program.

Calibrated spectrum

The resultant spectrum is shown in Figure 3.18. It can be seen that the Hα emission line is detected with a S/N >4; it falls at 12080 Å, which allows to make my own redshift estimation for the galaxy of: z=0.8406 (remember that this galaxy is has a measurement of z=0.840 with optical spectroscopy). In fact, the difference between both estimations lies below the spectral dispersion value. Therefore, there is no doubt that the line detected is Hα. The OH emission lines are indicated in the figure by the dotted lines at: 11988.6, 12007.1, 12030.9, 12055.9, 12122.6, 12196.4 and 12222.3 Å.

The Hα emission-line flux is estimated using a gaussian-profile fit to the line. It is also assumed that the continuum lies below the noise level. The flux estimation is:

$$\mathrm{F(H\alpha)} = 15.4 \pm 3 \times 10^{-17} \mathrm{ergs\ s^{-1} cm^{-2}}$$

It is also evident in the figure that the [NII] emission lines (indicated in the spectrum by the dashed lines) are not detected, due primarily by their coincidence with two strong OH emission lines (indicated by the dotted lines). This fact inhibits the possibility of any reliable estimation of the [NII] emission-line fluxes.

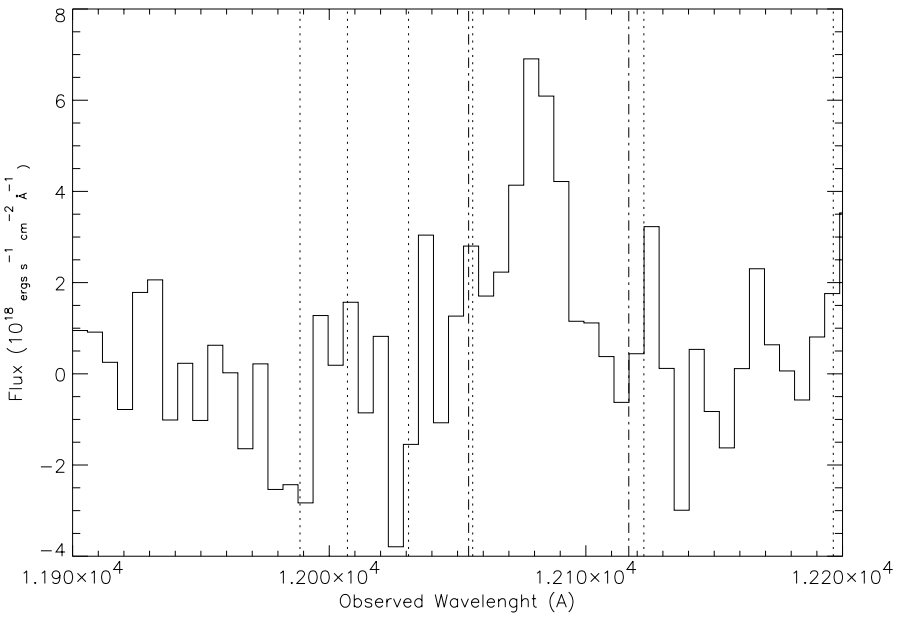

Figure 3.18: Hα emission line at observed wavelength. The dotted lines represent the wavelengths of the OH emission lines; the dash-dotted lines represent the redshifted wavelengths of the [NII] (6583, 6548 Å) lines.

3.4.3 BD0840-0 estimated SFR

The detection of the Hα emission line in the galaxy BD0840-0 allows to estimate its star formation rate. I employed the calibration of Kennicutt, Tamblyn, & Congdon (1994) to estimate the SFR from the integrated luminosity of Hα. This calibration, which is based on the observation of a sample of nearby galaxies, is:

$$\text{SFR } [\text{M}_\odot \text{yr}^{-1}] = 7.9 \times 10^{-42} L(H\alpha) [\text{ergs s}^{-1}] \tag{3.1}$$

The luminosity is estimated from the measured flux and the luminosity distance, *Dl* of the galaxy at a redshift of z=0.84, as given by the equation 2.2 in Chapter 2 and assuming the cosmological constants: H_0=100 h^{-1} km s^{-1} Mpc^{-1}, h=0.7 and q_0=0.2.

The resultant luminosity is $L_{H\alpha}$= 3.98 $\pm$0.7 $\times 10^{41}$ ergs s^{-1}. Comparing this value with the spectral evolution models it suggest that for a instantaneous burst scenario, the mass is around 10^{11} solar masses. This estimation comes from the burst age determined with the models in the color-color diagrams. The modeled Hα luminosity, represented in Figure 2.8 allows to estimate the mass of the burst. Employing the Hα luminosity and the calibration of Kennicutt et al., the derived SFR is:

$$3.1 \pm 0.6 \text{M}_\odot \text{yr}^{-1} \tag{3.2}$$

Guzman et al. (1997) gives a SFR estimation for BD0840-0 based on optical spectroscopy using the equivalent width of [OII](5007 Å) ($EW_{[OII]}$). The value that they derive is 11.0 $M_\odot$ yr^{-1} with errors about 15%. Guzman et al. uses the $EW_{[OII]}$ to estimate the SFR based on a calibration that was determined from a local sample of emission-line galaxies. With this method, they first calibrate the sample [OII] luminosity from Hα and then, they calibrate the $EW_{[OII]}$ from the [OII] luminosity. According to the authors, such calibration is $\sim$3 times smaller than the one derived by Kennicutt (1992). Guzman et al. also present the discrepancy for the measurements for another galaxy at z=0.137. They estimate SFR's of 0.2 and 1.2 $M_\odot$ yr^{-1} for $EW_{[OII]}$ and Hα, respectively. Such discrepancy shows the large uncertainty in the estimation of the SFR from the $EW_{[OII]}$. In the case of BD0840-0, the difference between the SFR values using the two different methods must be considered as another example of the inconsistency in others estimators rather than the Hα luminosity.

Table 3.2: Hα SFR measurements in local galaxies.

Galaxy	SFR ($M_\odot$ yr^{-1})	reference
NGC 3034 (M82)	0.3	*a*
NGC 4038 ("Antennae")	2.1	*b*
NGC 4039 ("Antennae")	1.7	*b*
NGC 4038/39 ("Antennae")	5.0	*b*
NGC 4676A ("Mice")	0.8	*b*
NGC 4676B ("Mice")	1.7	*b*

Notes: *a*) from Oconnell & Mangano (1978) measurements,
b) from Mihos, Bothun, & Richstone (1993)

The measured SFR for BD0840-0 is comparable to several measurements from local to intermediate redshift galaxies. The values of Table 3.2 has been derived from Hα luminosities, employing the same calibration (i.e. from Kennicutt et al.) for all of them. The table includes the "typical" starburst galaxy, M82, as well as other two interacting galaxies. It can be seen that the SFR values span from $\sim$1 to $\sim$2 $M_\odot$ yr^{-1} and that they are higher at the closest region to the interaction between the two galaxies (i.e. the case of the overlap region between NGC 4038 and NGC 4039, called NGC 4038/39). It can be concluded that the SFR measured for BD0840-0 is in the range of the local starburst galaxies typical rates. However, as it was discussed on section 2.4.2 the star formation rate could be affected by the interaction of a companion galaxy that, in this case, is at a distance of 34 kpc (see section 3.3.5).

Table 3.3: Hα SFR measurements in galaxies at different redshifts.

Observations	redshift	SFR ($M_\odot$ yr^{-1})
Gallego et al. (1995) (138)	$\sim$0.04	0.3 to 31.4
Tresse & Maddox (1998) (138)	$\sim$0.20	0.02 to 5.0
Glazebrook et al. (1999) (2)	$\sim$0.79	5.6 and 19.5
Glazebrook et al. (3)	$\sim$0.82	12.1, 12.2 and 23.5
BD0840-0 (this work) (1)	0.84	3.1$\pm$0.6
Glazebrook et al. (1)	1.04	54.6$\pm$9

Notes: *a*) the number of galaxies from the estimation is given in parentheses

A final comparison is performed with other intermediate redshift galaxies, whose estimations are listed on Table 3.2. The data come from the works of Gallego et al. (1995), Tresse & Maddox (1998) and Glazebrook et al. (1999), and it is the same as the one used to estimate the SFR density in the diagram of Figure 1.1. For the two former works, the SFR values span from two limits due to the large number of galaxies (given in parentheses). For the latter work, the SFR value is given for each galaxy. BD0840-0 shows a small rate if compared with the estimations of the three galaxies at a similar redshift. Glazebrook et al. refer to one of these galaxies (i.e. that with SFR = 12.2 $M_\odot$ yr^{-1}) as undergoing a "merger", that could be associated with the high SFR's estimated.

Part II

LIRIS technical requirements and analysis

4

LIRIS estimated sensitivity

4.1 Introduction

As it was seen on Chapter 3, the success of the near-infrared spectroscopy depends on several instrumental parameters. Many of these parameters are related to the telescope and instrument efficiencies, to the sources of noise, and to the special observing requirements for the near-infrared. The observations of the project of near-infrared spectroscopy of intermediate redshift galaxies takes the spectrograph close to their limits, as it was concluded from the Omega Cass and NICS observations (see sections 3.4.1 and 3.4.2, respectively). To asses the success of the future observations with LIRIS in such scientific project (i.e. and/or any other where very faint objects are targeted), it is necessary to study the parameters that affect the near-infrared observations efficiency. This chapter presents my analysis of all these parameters and an estimation of the sensitivity of LIRIS, as well as the prediction of its limiting magnitudes.

4.2 Observing at near-infrared wavelengths

The infrared observations make the observer to face with the "background emission", a signal at the detector that increments with wavelength and saturates the pixel full well in a few seconds. Moreover, most of the time it will hide the emission of the object under study if its flux is less than that of the background. This background emission is formed by sky and thermal components. The former one comes from the radiation of excited molecules in the upper atmosphere and the latter is the contribution from the telescope (and surroundings) thermal radiation. Figure 4.1 shows both components; the former one is the series of emission lines and, the thermal emission is presented as the exponential curves; a full description is given below.

The background emission limits the observations, thus several techniques are employed to observe at near-infrared wavelengths; the most used is the *nodding*, which consist on the acquisition of two consecutive images, one with the object and the other with only the background emission (see section 3.4.1). In this manner the background emission can be eliminated from the images by subtracting them. However, the photon shot noise from the emission is not removed. Therefore, the background emission always limits the near-infrared observations, mainly in spectroscopy mode. As it will be seen on section 4.5.1, the background emission noise has been established as a

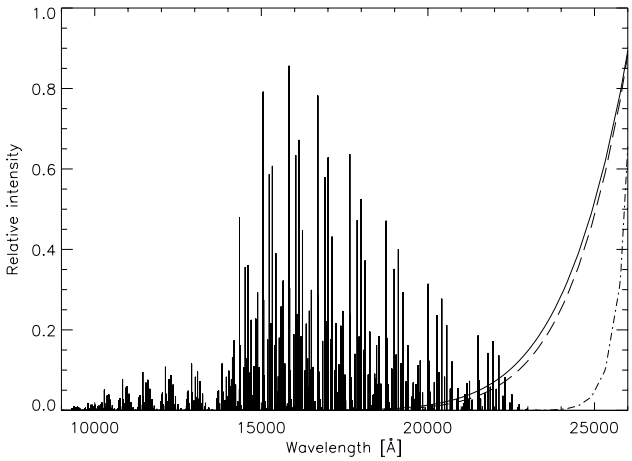

Figure 4.1: OH sky emission lines and thermal emission for three different temperatures: 290 K (solid line), 270 K (dashed line) and 65 K (dot-dashed line).

reference in the near-infrared observation to determine the impact of the other limiting factors.

4.2.1 Thermal emission

As shown in the Figure 4.1, the thermal emission starts to be a limitation at *K*-band (for wavelengths longer than 22000 Å). Three thermal emission components are represented: the telescope at 290 K, the atmosphere (represented with a slightly lower temperature) and the instrument itself, cooled to 65 K. All of them are assumed to have a black body radiation behavior. The telescope mirrors have, emissivities from 4 to 20%, depending on whether their design is optimized, or not, for the infrared (McLean 1989). The thermal emission from the instrument comes from the optical components and all the mechanical parts that are in the detector field of view. Such emission can be reduced cooling the whole instrument. Although, the entrance window is always at room temperature, its emission can be neglected, according to Vincent (1989), who concludes that the window transmission is too high to have any considerable emission. In other words, the window emission is very low because reflectivity, rather than absorption cause the transmission losses (i.e. for most of the window materials).

4.2.2 Sky background emission

The sky background emission has three main components: a) the OH vibration-rotation bands, b) the oxygen atmospheric bands and, c) the non-thermal continuum. The former presents in a form of spectral emission lines as shown in Figure 4.1. The OH lines in this figure are from the catalog of Rousselot et al. (2000) and are represented in relative fluxes. As it can be seen, although they are emitted along all the near-infrared range, the highest fluxes are over 14000 Å. The emission of these lines comes from vibrational-rotational transitions of the hydroxyl radical (OH), which occurs at high atmospheric altitudes (85-100 km). This radical is produced by the reaction (Bates & Nicolet 1950; Llewellyn, Long, & Solheim 1978): $H + O_3 \rightarrow OH^* + O_2$. This reaction occurs

mainly through a radiative cascade. The relaxation of the excited states of this molecule can cause the excitation of the oxygen molecule (Llewellyn & Solheim 1978): $OH^* + O \rightarrow H + O_2$. The oxygen emission, considered as the second component of the sky background, is found mainly in the form of two emission lines at 12690 and 15800 Å. The observations of these lines, as well as for the OH lines are published in several catalogs (e.g. Steed & Baker 1979; Oliva & Origlia 1992; Rousselot et al. 2000).

The flux of the OH emission has temporal and spatial variations. Taylor et al. (1991), Ramsay, Mountain, & Geballe (1992) and Adams (1997) have measured temporal flux variations be up to 15%. The period of these variations is from 10 to 15 minutes and is attributed to temperature and pressure perturbations in the upper atmosphere in the form of gravity waves changes (Taylor et al. 1991). Content (1996) also report an almost linear decrease of the OH emission during the night, with a ratio going from 2-3 from the beginning to the end of the night. Adams (1997) report spatial variations from 5 to 10%, measured[1] in a scan scale of ~ 6 degrees. All these variations limits the lenght of the exposure times, in other words, the time between the *on-object* and the *off-object* images in the *nodding* technique must be lower than the period of the temporal variations to guarantee that the OH emission will be subtracted efficiently.

The other main component in the sky background emission is the airglow (i.e. also called *nightglow*), which, is the remaining non-thermal background intensity between the OH lines. According to Content (1996) and Maihara et al. (1993) the origin of this emission is not yet very well understood. They assume an airglow contribution of about 2% of the background flux.

The overall background emission (i.e. continuum and emission lines) is, then, the combination of many factors that depends on the observatory and on the instrument. Some examples of the background magnitudes are given in Table 4.1, with measurements from the WHT using WHIRCAM[2] (Hughes 1996); from TCS using CAIN (Hammersley 1998) and from WHT using INGRID[3].

Table 4.1: Background magnitudes (Mag/arcsec^2) measured at different observatories (see text)

Band	WHIRCAM (WHT) (02/1995)	WHIRCAM (WHT) (06/1995; full Moon)	CAIN (TCS)	INGRID (WHT)
J	16.6	15.6	15.5	16.1
H	14.4	13.9	13.5	14.7
K	11.0	11.4	12.5	12.1
Ks	12.0	12.0	—	12.7

4.3 Estimating the signal of an object at the detector

The signal of an object at the detector is the number of electrons generated proportionally to the incident object flux. This flux is affected by several factors, such as: the atmospheric extinction, the seeing, the telescope efficiency, the detector efficiency, the instrument optics and filter throughputs.

[1] At 2MASS www: pegasus.phast.umass.edu/adams/airglowpage.html

[2] WHIRCAM manual at www.ing.iac.es/∼manuals/html_manuals/WHT_instr/WHIRCAM/node26.htm

[3] At INGRID manual: www.ing.iac.es/Astronomy/instruments/ingrid/ingrid_throughput.html

In the following sections, I review how the flux from an object produces a signal on the detector in two observing modes: image and spectroscopy.

4.3.1 Image mode

The flux from an object with an apparent magnitude, m_{obj} and observed at the Earth's ground can be represented as:

$$F(\lambda) = F(\lambda_0) \cdot 10^{-0.4(m_{obj}+m_{ext})} \tag{4.1}$$

where the flux is given in W cm^{-2} μm^{-1}; m_{ext} is the atmospheric extinction. The typical extinction values are given in Table 4.3. $F(\lambda_0)$ is the flux for the magnitude zero standard star: Vega (see Table 4.2).

Table 4.2: Standard fluxes of Vega

Band	F(λ_0) [W/cm^2 μm]
z	8.32×10^{-13}
J	3.21×10^{-13}
H	1.08×10^{-13}
K	3.84×10^{-14}

The flux collected by a telescope of effective area A, and diminished by the telescope efficiency (τ_{tel}), is:

$$F_{tel} = \tau_{tel} \cdot A \cdot F(\lambda) \tag{4.2}$$

Table 4.3: Extinction values

Band	m_{ext} [mag/airmass]
z	0.1
J	0.1
H	0.11
K	0.07

The flux that reaches the detector, F_{det} is the flux integrated all over the filter bandwidth $\Delta\lambda$ (in μm). As it can be seen in equation 4.3, it is affected by the instrument optics and filter throughputs (τ_{inst}).

$$F_{det} = \tau_{inst} \cdot \Delta\lambda \cdot F_{tel} \tag{4.3}$$

Finally, the signal at the detector, given in electrons per second, is the object flux that reaches the detector times its quantum efficiency (η_{det}). This signal, according to McLean (1989), is:

$$S_{im} = \eta_{det} \cdot (hc)^{-1} \cdot \lambda \cdot F_{det} \tag{4.4}$$

where hc, given in J μm is the product of the Planck constant and the speed of light. λ is the band central wavelength. Combining equations 4.1 to 4.4, the signal at the detector for imaging mode, given in electrons per second is:

$$S_{im} = \eta_{det} \cdot (hc)^{-1} \cdot \lambda \cdot \tau_{inst} \cdot \Delta\lambda \cdot \tau_{tel} \cdot A \cdot F(\lambda_0) \cdot 10^{-0.4(m_{obj}+m_{ext})} \tag{4.5}$$

The signal, S_{im} is calculated for a point object that fits in the seeing disc. It means that the area, into which the object is imaged at the detector, is a circle with a diameter equal to the FWMH. Such area, given in square pixels is:

$$area_{im} = \pi \cdot \left(\frac{seeing}{2 \cdot scale} \right)^2 \tag{4.6}$$

where $scale$ is the detector scale given in arcsec/pixel.

In the case of extended objects, the signal, S_{im} is calculated per pixel, considering that the magnitude of the object is given per unit of area. Therefore, the $area = 1 pixel$. Such is the case of the signal from the sky background emission (S_{sky}), which is given in electrons per second per pixel.

$$S_{sky} = \eta_{det} \cdot (hc)^{-1} \cdot \lambda \cdot \tau_{inst} \cdot \Delta\lambda \cdot \tau_{tel} \cdot A \cdot scale^2 \cdot F(\lambda_0) \cdot 10^{-0.4(m_{sky})} \tag{4.7}$$

where no atmospheric extinction is calculated since the sky emission comes from the atmosphere itself. In the case of extended objects, the extinction must be included

4.3.2 Spectroscopy mode

For spectroscopy mode the signal estimation is similar to that in the image mode, except for two factors that must be taken into account: a) the efficiency (τ_{inst}) is affected by the grisms throughputs; and, b) the bandwidth ($\Delta\lambda$) depends on the spectral resolution (R) (usually given for 2 pixels):

$$\Delta\lambda = \frac{\lambda}{R} \tag{4.8}$$

Then, the signal integrated over 2 pixels of the detector and given in electrons per second, is:

$$S_{sp} = \eta_{det} \cdot (hc)^{-1} \cdot \lambda \cdot \tau_{inst} \cdot \frac{\lambda}{R} \cdot \tau_{tel} \cdot A \cdot scale^2 \cdot F(\lambda_0) \cdot 10^{-0.4(m_{obj}+m_{ext})} \tag{4.9}$$

4.4 Analysis of the signal to noise ratio

Once the signal of the object has been estimated, the signal to noise ratio (S/N) can be determined giving a measurement of how high is the signal level, in respect to the noise level. Four main noise sources have to be considered: the noise from the incident flux of the observed object, the noise from the the sky background emission, the dark-current noise and the detector readout noise. The former two comes from the photon shot noise from the fluxes of the object (S) and the background (S_{back}). The dark-current noise is produced by the detector dark current (D), which is described in section 5.5.7. Assuming that these three sources of noise behave according to Poisson statistics, they can be calculated as the square root of their respective signals. The readout noise (N) is consequence of reading the detector and varies as a function of the readout mode, as described in section 5.2.3. The ideal near-infrared instrument is that, whose observations are only limited by the sky background emission noise (see below).

Assuming that the noise sources are independent from each other, the total noise (N_{total}) for one pixel is obtained from the quadratic addition of all of them:

$$N_{total} = \sqrt{\left(\sqrt{S \cdot t}\right)^2 + \left(\sqrt{S_{sky} \cdot t}\right)^2 + \left(\sqrt{D \cdot t}\right)^2 + \left(\frac{\sqrt{(2)}N}{\sqrt{m}}\right)^2} \tag{4.10}$$

The S/N for a signal integrated during a time (t) and calculated for all the object *area* over the detector is:

$$\frac{S \cdot t}{\sqrt{(S \cdot t + area \cdot \left(S_{sky} \cdot t + D \cdot t + \frac{2N^2}{m}\right)}} \tag{4.11}$$

where, *area* is the object area, in pixels, at the detector, D is the dark current given in electrons per second, and N is the readout given in electrons.

4.4.1 Background limited performance

At near-infrared observations, the optimum exposure time is reached at background limited performance (BLIP), in other words, when all other noise sources are much less than the background noise:

$$S_{sky} \cdot t \quad \gg \quad D \cdot t + \frac{2N^2}{m} \tag{4.12}$$

Therefore, it can be supossed that the only noise contribution is the background noise (McLean 1989). A ratio of 10, between the background noise and the other sources is the minimum to consider the BLIP case (I will use this value in the further estimations).

Table 4.4: Filter passbands

Band	λ [μm]	$\Delta\lambda$
z	1.033	0.073
J	1.25	1.60
H	1.635	0.29
K	2.2	0.34
Ks	2.15	0.32

4.5 Estimations for LIRIS

The values that are used for the estimations with LIRIS are, the readout noise that, according measurements described in section 5.6.3, is N=16.5 e^-; the dark current value for the detector at a temperature of 65 K is lower than 0.07 e^-/s and the detector quantum efficiency given by RSC (Table 4.5). On the other hand, the LIRIS optics transmissions are summarized in Table 4.6, where the throughput of each component is from specifications (Atad-Ettedgui 1999) or from measurements. Figures 4.2 to 4.4 show the J, H, Ks-band filter transmissions, measured by Roberto López in the laboratory at room temperature. The filter bandpasses are given in Table 4.4.

Table 4.5: Detector quantum efficiency

Band	η_{det}
z	0.50
J	0.58
H	0.56
K	0.60

The values concerning the telescope (i.e. the WHT) are the primary collection area (A = 124767.6 cm^2) and the primary and secondary mirrors combined reflectivity (τ_{el} = 72%). The latter value comes from an annual median visual reflectivity of $\sim$85% for the primary mirror. It is aluminized each once a year and cleaned with CO_2 snow every couple of months[4].

[4]Benn, Chris, WHT mirror reflectivity, Feb99, http://www.ing.iac.es/$\sim$crb/WHT/ mirror.html

Table 4.6: LIRIS throughput in image and spectroscopy modes.

Element	Material	Throughput [%]
Entrance window	Fused Silica	96
$Colimator_1$	BaF2	98
$Colimator_2$	Silica	96
Mirror	Gold plated	98
$Colimator_3$	BaF2	98
Filters[a]		82
$Cammera_1$	BaF2	98
$Cammera_2$	SF6	98
$Cammera_3$	BaF2	98
$Cammera_4$	BaF2	98
Total in image		**67**
Grisms		60
Total in spectroscopy		**40.2**

Notes: *a*) Mean value for the broad band filters (see Figures 4.2 to 4.4)

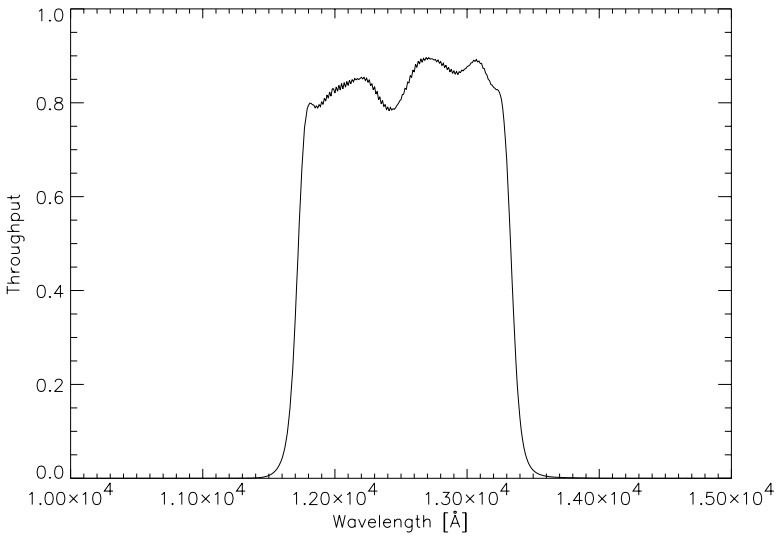

Figure 4.2: LIRIS *J*-band filter throughput measured in warm conditions.

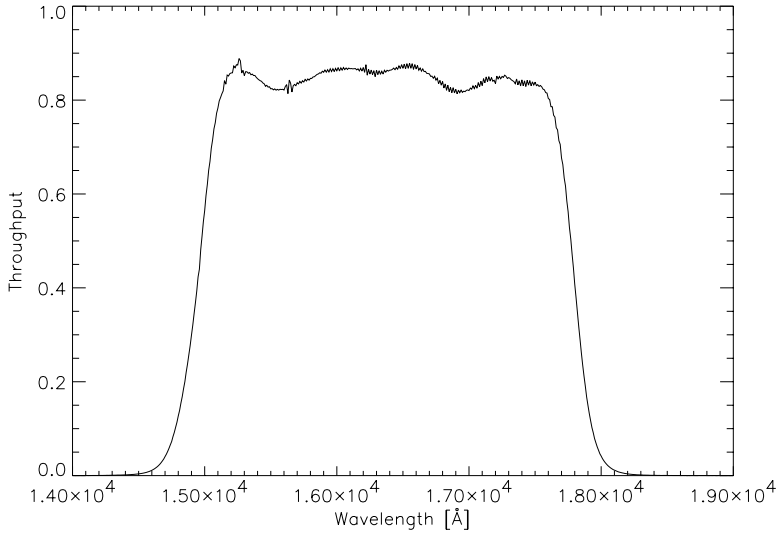

Figure 4.3: LIRIS *H*-band filter throughput measured in warm conditions.

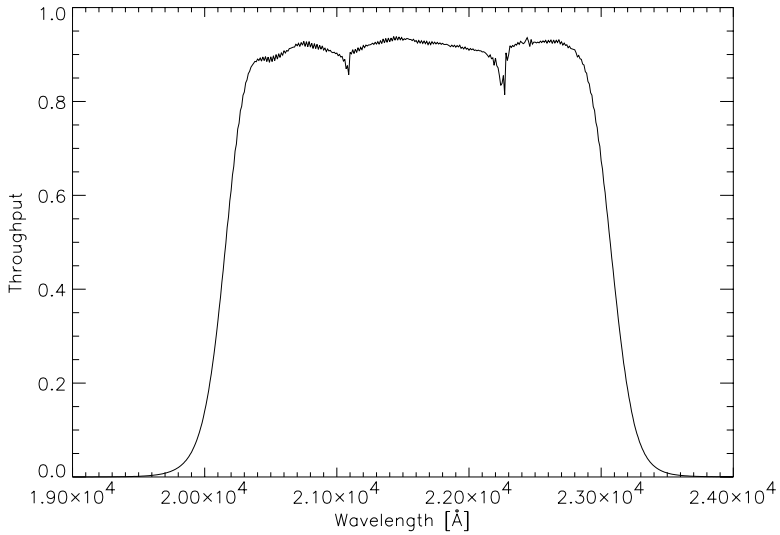

Figure 4.4: LIRIS *Ks*-band filter throughput measured in warm conditions.

4.5.1 BLIP case

Image mode

In image mode, the background signal saturates the detector (100,000 e^-; depending on the detector, as seen on section 5.6.2) in a few seconds. As it can be seen in Figure 4.5, for *Ks*-band, the saturation level is reached in $\sim$20 s (the background noise is only plotted for values less than the saturation level). The readout noise is plotted for the MNDR mode with $m = 1$ (the upper dotted line) and, for the MNDR mode with $m = 16$ (the lower dotted line). 16 is the maximum number of reads supported by the SDSU controller software. Both noise lines are plotted with a minimum possible time considering that the detector readout time is approximately 0.8 s. It can also be noticed that the dark current noise is negligible for image mode.

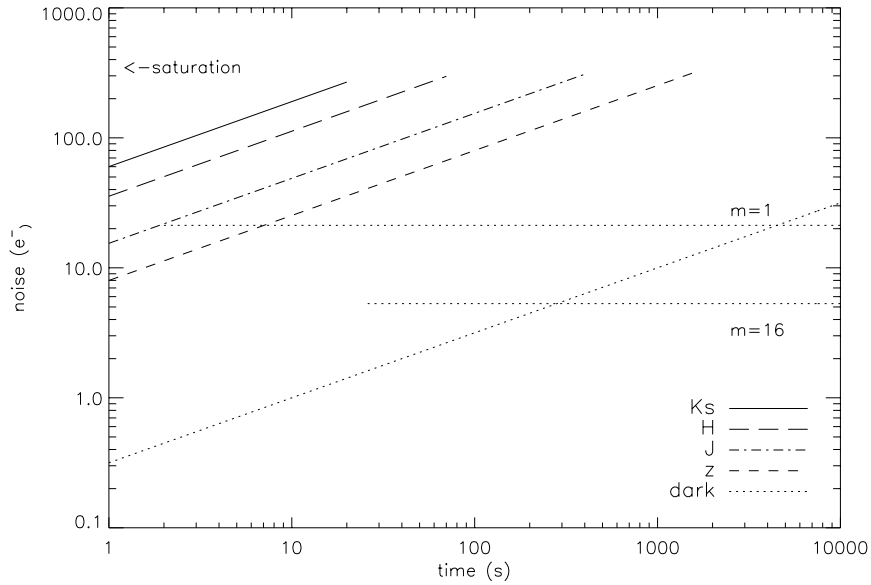

Figure 4.5: Sources of noise in image mode. The background noise is represented for the z, J, H, Ks-bands up to the limit where the emission saturates the detector. The dark current noise and the readout noise are also plotted. The latter one is represented by the horizontal dotted lines for m=1 and m=16 in *MNDR* mode.

It can be seen that, in image mode the background noise is the dominating source at all bands and at all integration times. This means that, the signal is most of the times background-noise limited in image mode, as it can be concluded from the estimated integration times for BLIP given in Table 4.7. From these values arises that the optima exposure times must be longer than the one required for BLIP, and lower than that for the saturation limit. For example, at *J*-band, the minimum time should be 277 s, and the maximum time is specified by the saturation level, which is reached by the addition of the object signal and the background emission. In any case, it must not be longer than 691.6 s (i.e. the time for the backgound saturation). Therefore, for *J*-band 300 s is a good exposure time to reach BLIP and to sample the sky background emission variations (with a 600 s period, see section 4.2.2).

Table 4.7: Estimated minimum integration times for BLIP in image mode.

Band	S_{back} [e^-/s]	Time for background saturation [s]	Time for BLIP[a] [s] m=1	m=16
z	63.9	1565.0	626.0	39.1
J	144.6	691.6	277.0	always
H	1314.5	76.0	30.4	always
K	8043.6	12.4	4.9	always
Ks	3608.8	27.7	11.0	always

Notes: *a*) "always" means that it is background limited.

Spectroscopy mode

In spectroscopy mode, the background emission flux over each pixel is less than that in image mode. This is due to the dispersion of the spectra. It is even less for higher resolution values, as it can be concluded from the comparison of Figures 4.6 and 4.7. In the former figure, the *Ks*-band background emission saturates the detector at $\sim$ 6000 s. This only a hypothetical case, because, due to the OH emission temporal variations (section 4.2.2), such a long integration time will never be set to a single exposure. Instead, the coaddition of multiple short exposures is better. Figure 4.7 shows that *z* and *J*-bands are readout-noise limited for integration times less than 1000 s, even in MNDR mode with 16 read. A single band representation of this figure can be seen at Figure 4.8, where the dashed lines represent the total noise (i.e. the quadratic addition of all the components).

Table 4.8: Estimated minimum integration times for BLIP in spectroscopy mode (R=1000).

Band	R=1000 s_B [e^-/s]	Time for BLIP[a] [s] (m=1)	(m=16)
z	0.5	—	—
J	0.7	—	—
H	4.4	—	568
K	31.2	1282	80
Ks	17.3	2312	144

Notes: *a*) No values are given if it is reached over 10000 s.

Although the goal at near-infrared observations is to be background-noise limited and not instrumental-noise limited, for intermediate resolution spectroscopy it is not always possible. The background noise is so low at short exposure times that its value is below any possible readout noise. Therefore, the spectrograph is readout-noise limited for the short exposure times and background-noise limited for the long ones (see Figure 4.8).

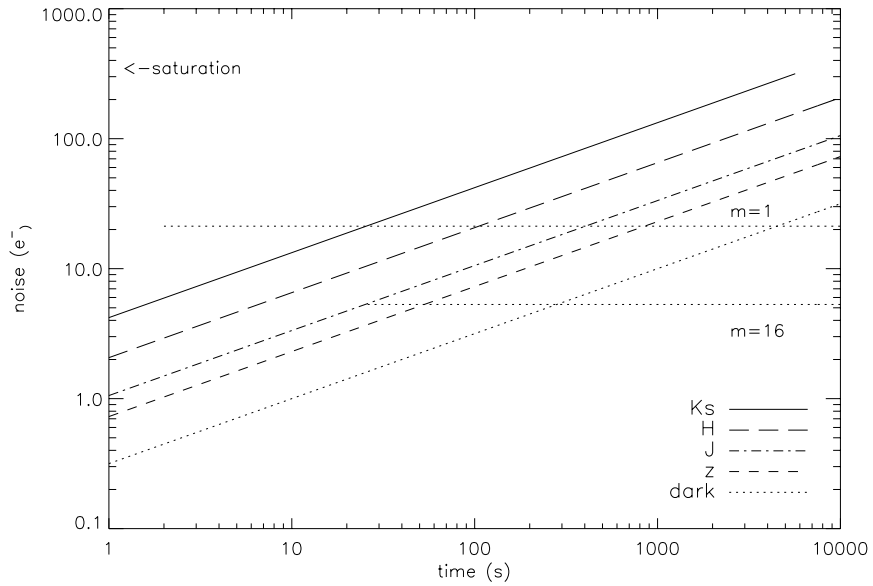

Figure 4.6: Sources of noise in spectroscopy mode. The resolution is R=1000. z, J, H, Ks-band background noise are plotted up to the limit where the emission saturates the detector. The dark current noise and the readout noise are also plotted. The latter one is represented by the horizontal dotted lines for m=1 and m=16 in *MNDR* mode.

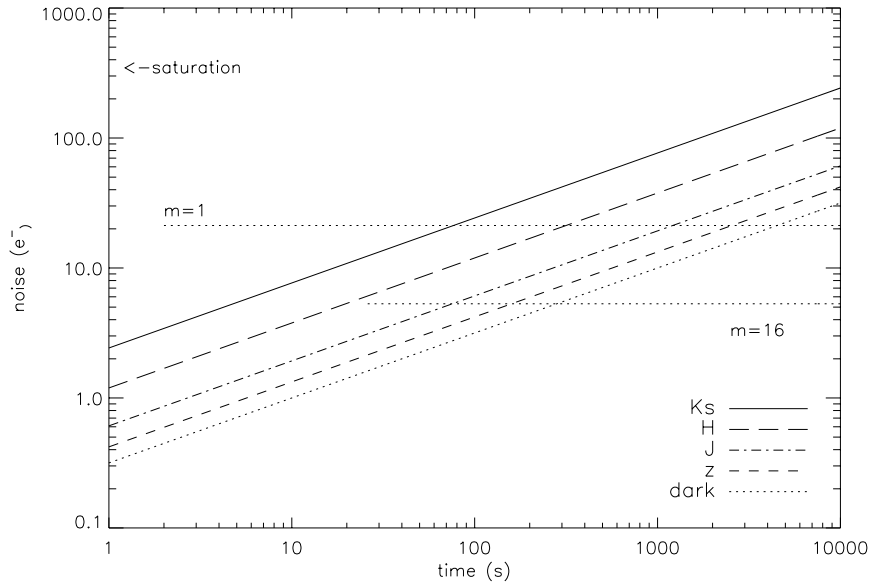

Figure 4.7: Sources of noise in spectroscopy mode. The resolution is R=3000. Symbols are the same than in Figure 4.6.

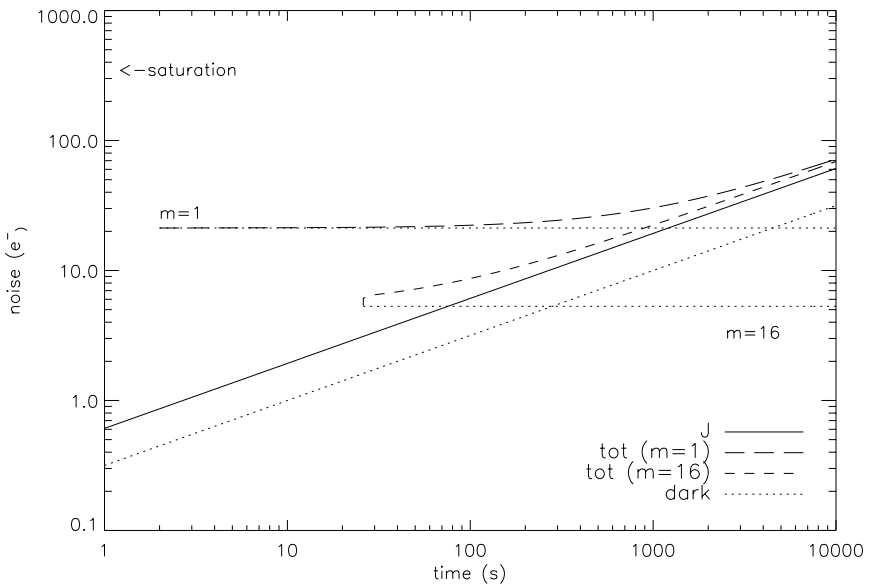

Figure 4.8: Quadratic addition of the sources of noise in spectroscopy mode for *J*-band. The resolution is R=3000. Two total noise values are presented (dashed lines) for m=1 and for m=16 in the *MNDR* mode.

4.5.2 Limiting magnitudes

The sensitivity of the instrument+telescope can be estimated from the signal to noise ratio (equation 4.11), seeking for the faintest object that can be detected. This estimation gives the limiting magnitudes for different criteria and for both observing modes, image and spectroscopy. The standard criterion is to estimate the magnitude of an object that can be detected with a S/N=3 (also called the 3σ level) and an exposure time of 1 h. Such magnitude will depend on the band, the type of object, the observing mode, and the seeing conditions.

Image mode

As it was seen before, the image mode is mainly limited by the background noise. However, *z* and *J*-bands are readout noise limited for short exposure times, as can be concluded from Figure 4.9, which represents the 3σ limiting magnitudes for a point object observed with a seeing of 0.5 arcsec. Table 4.9 summarizes two values of limiting magnitudes: for 1 minute and for 1 hour of exposure time. The rest of the parameters are the same than those at the figure. The case of extended objects is also summarized in Table 4.9, which gives the limiting magnitudes per square arcmin.

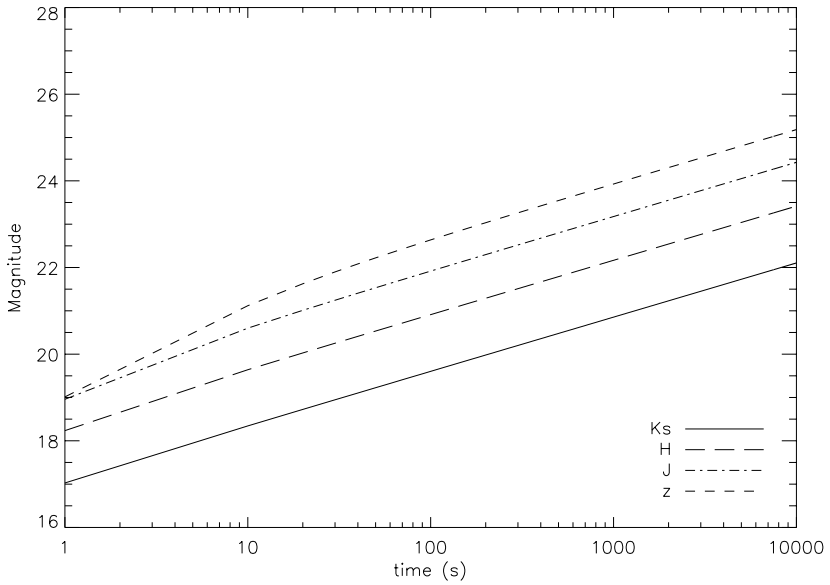

Figure 4.9: Limiting magnitudes in imaging mode at 3 σ. A seeing of 0.5 arcsec is assumed. Notice the limitation at *z*-band for short exposure times.

Table 4.9: 3 σ limiting magnitudes for point and extended objects imaging.

Band	point objects [mag]		extended objects [mag/arcsec^2]	
	1 min	1 h	1 min	1 h
z	22.3	24.6	19.9	22.2
J	20.6	24.3	19.7	21.9
H	20.6	22.8	18.2	20.5
K	19.1	21.4	16.8	19.0
Ks	19.3	21.5	16.9	19.2

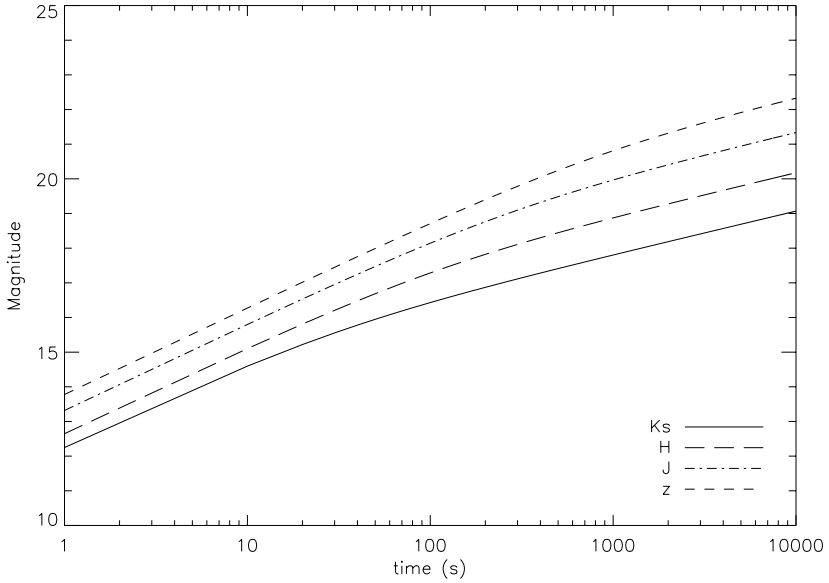

Figure 4.10: Limiting magnitudes in spectroscopy mode. The resolution is R= 1000. The limit is set at 3 σ and the seeing is assumed to be 0.5 arcsec. The magnitudes are estimated for the CDS mode. Notice the limitation at all the bands for short exposure times.

4.5.3 Spectroscopy mode

In contrast to the image case, at spectroscopy mode all the bands are limited by the readout noise at short exposure times. Such limitation is higher if the resolution is increased, as it can be concluded from Figures 4.10 and 4.11 for resolutions R=1000 and R=3000 respectively. Both estimations are computed for the integrated continuum along each band and considering a slit width of 0.5 arcsec and a seeing of the same value. Table 4.10 summarizes the limiting magnitudes for a point object at both resolutions with 1 minute and 1 hour exposure times. It is noticed that the difference between two resolution values goes up to 1 mag. The case for extended objects is given in Table 4.11.

Table 4.10: 3 σ limiting magnitude [mag] for 1 hour spectroscopy of point objects.

Band	R=1000		R=3000	
	1 min	1 h	1 min	1 h
z	18.2	21.7	17.0	20.8
J	17.7	21.2	16.5	20.3
H	16.8	19.6	15.8	19.0
K	15.9	18.2	15.1	17.6
Ks	17.3	18.5	15.2	17.9

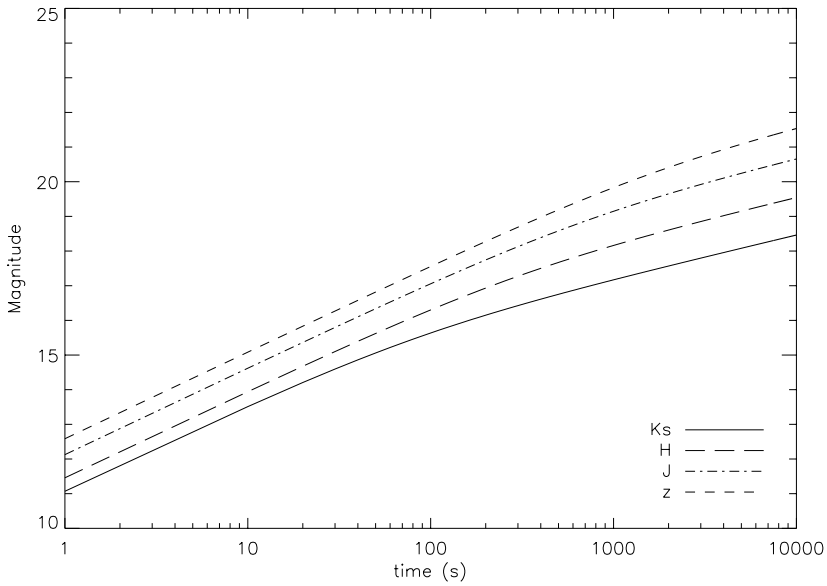

Figure 4.11: Limiting magnitudes in spectroscopy mode. The resolution is R= 3000. The limit is set at 3 σ and the seeing is assumed to be 0.5 arcsec. The magnitudes are estimated for the CDS mode. Notice the stronger limitation at all the bands for short exposure times.

Table 4.11: 3 σ limiting magnitude [mag/arcsec^2] for 1 hour spectroscopy of extended objects.

Band	R=1000		R=3000	
	1 min	1 h	1 min	1 h
z	15.2	18.7	14.0	17.8
J	14.7	18.2	13.5	17.3
H	13.8	16.6	12.8	15.9
K	12.9	15.2	12.1	14.6
Ks	13.1	15.5	12.2	14.9

4.5.4 Limiting line fluxes in spectroscopy mode

At spectroscopy mode, it is more useful to estimate the S/N of an emission line rather than the continuum. This is the case of projects as the LIRIS-GAL sample of galaxies (see Chapter 3). For such galaxies, the continuum is extremely faint. Thus, the estimation of the exposure times must be based on the expected emission line flux. Figure 4.12 shows the 3 σ limiting fluxes in a similar manner than that for the limiting magnitudes. The flux is computed integrating over 2 pixels at the spectral direction (i.e. the instrumental line profile) and over 2 pixels in the spatial direction, considering a point object and a seeing of 0.5 arcsec. For practical purposes, the wavelength of the line is assumed to be the central wavelength of the band. Figure 4.12 shows the case for a resolution of R=1000. It is interesting to notice that, with short exposure times, fainter line fluxes can be detected at *Ks*-band than at *z* band, due to the readout noise limitation. At long exposure times, the case is almost the opposite, being the line fluxes at *J*-band the faintest that can be detected. The *z*-band is more limited that *J*-band due to the dark current noise, as it was seen on section 4.5.1. The cases for R=3000 and R=8000 are shown in Figures 4.13 and 4.14, respectively. The latter represents only the line flux at *Ks*-band, since the high resolution grism only covers a small wavelength range at that band. The flux estimations for 1 hour exposure times are given in Table 4.12.

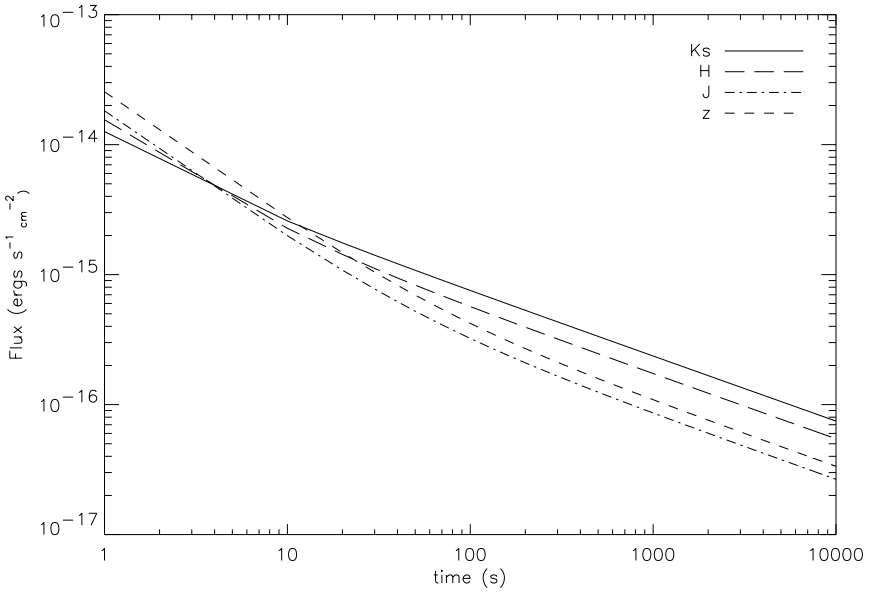

Figure 4.12: Limiting line fluxes in spectroscopy mode. The resolution is R= 1000. The limit is computed for the 3 σ integrated flux of the line. A seeing of 0.5 arcsec is assumed. The CDS mode is used for the estimations. Notice the that *z* and *J*-bands are more limited than *H* and *Ks* for short exposure times, while for long ones the case is the opposite.

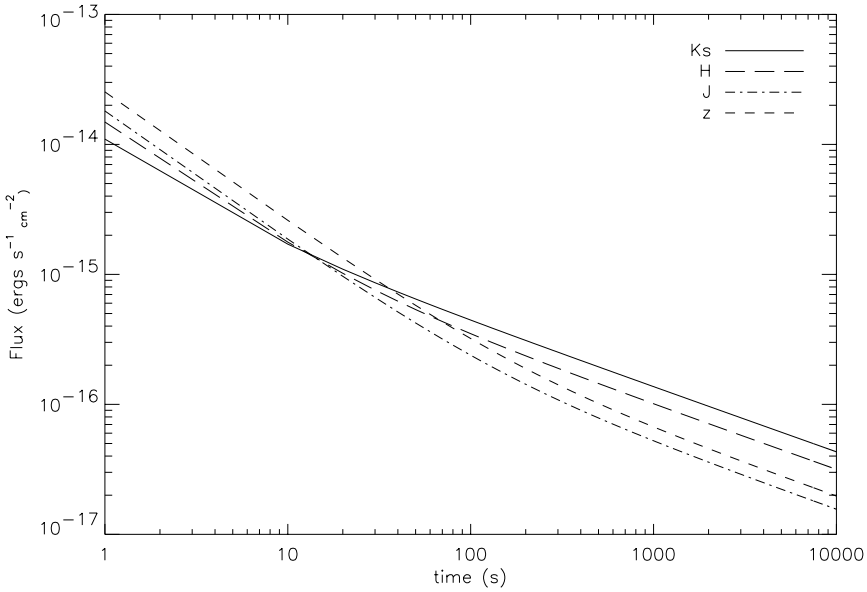

Figure 4.13: Limiting line fluxes in spectroscopy mode. The resolution is R= 3000. The limit is computed for the 3 σ integrated flux of the line. A seeing of 0.5 arcsec is assumed. The CDS mode is used for the estimations. Notice the that *z* and *J*-bands are more limited than *H* and *Ks* for short exposure times, while for long ones the case is the opposite.

Table 4.12: 3 σ limiting line fluxes [ergs s^{-1} cm^{-2}] for 1 hour spectroscopy.

Band	R=1000	R=3000	R=8000[a]
z	5.6×10^{-17}	3.3×10^{-17}	—
J	4.4×10^{-17}	2.6×10^{-17}	—
H	9.1×10^{-17}	5.3×10^{-17}	—
K	1.6×10^{-16}	9.4×10^{-17}	—
Ks	1.2×10^{-16}	7.2×10^{-17}	4.4×10^{-17}

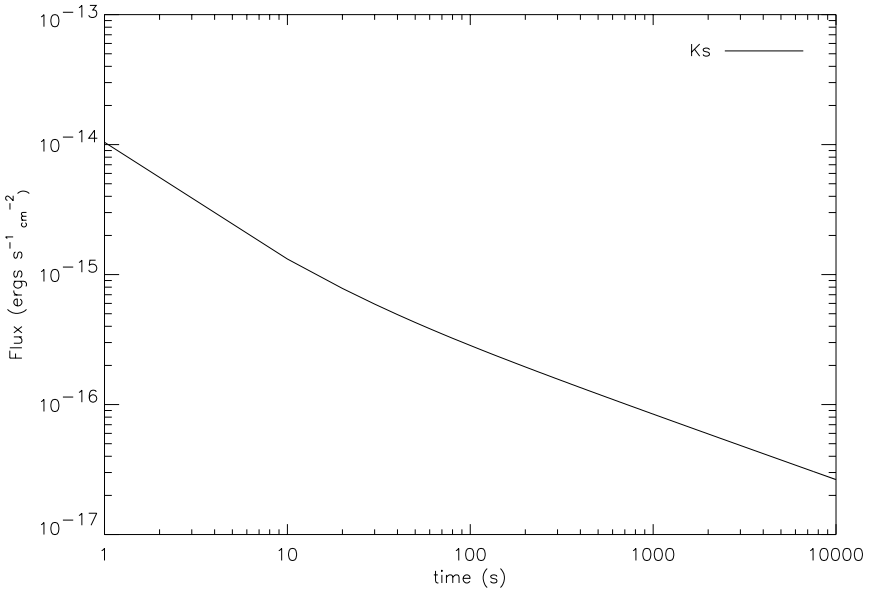

Figure 4.14: *K*-band limiting line fluxes in spectroscopy mode. The resolution is R= 8000. The wavelength range is only: 2.0-2.2 and 2.2-2.4 μm. The limit is computed for the 3 σ integrated flux of the line. A seeing of 0.5 arcsec is assumed. The CDS mode is used for the estimations.

4.5.5 Estimations for the galaxies in the LIRIS-GAL sample

In the same manner that the limiting magnitudes are estimated, the minimum exposure times can be determined for the objects in the LIRIS-GAL sample of galaxies with known magnitudes and fluxes. The estimations are performed in image and spectroscopy modes employing the continuum *J*-band magnitude. Table 4.13 show some examples of the brightest galaxies. It can be seen that, in image mode, 10σ level is easily achieved, while in spectroscopy mode (with R=1000), the continuum of some of the galaxies is not detected. Such was the case with the galaxy BD0840-0, observed with NICS (see section 3.4.2). The faint reference star used to align the slit in that observation, is also given in Table 4.13 to show that, ∼600 of single exposure times are required at least to identify the continuum of the spectrum and to establish the aperture profile (see the discussion in section 3.4.1).

Table 4.13: Required exposure times (s) for some galaxies of the LIRIS-GAL sample to reach the S/N specified in the image and spectroscopy (R=1000) modes. (Values for the continuum).

Object	Cont. *J*	Image		Spectroscopy[a]	
	(mag)	3σ	10σ	3σ	10σ
BD0474-0	19.2	1.0	5.4	270.9	1440
CS0472-0	21.8	35.0	361.2	10504.9	—
CS0520-0	21.5	21.3	210.7	6284.4	—
CS0555-0	20.0	2.6	16.7	687.3	4786
CS0561-0	20.7	6.4	52.0	1773.9	—
CS0586-0	21.3	15.5	147.5	4507.2	—
CS0608-0	20.5	4.9	37.2	1332.4	—
CS0681-0	22.4	99.3	1073.6	—	—
CS0682-0	21.4	18.2	176.3	5316.0	—
CS1010-0	21.8	35.0	361.2	10504.9	—
CS1020-0	21.9	41.5	432.7	—	—
Reference Star	18.5	0.5	2.3	130.2	585

Notes: *a*) No values are given for times grater than 3 h

As it was discussed in the previous section and in Chapter 3, the spectroscopic observations objective is to detect and measure the Hα emission line rather than the continuum. Therefore, the estimation for the required exposure time is based on the expected Hα emission line flux. In fact, the selection of the galaxies has a parameter that is the minimum line flux detected by LIRIS. Such, limiting flux was determined in the previous section (see Table 4.12). Now, the observation of the galaxy BD0840-0 (see section 3.4.2) gives a measurement of the flux of 15.4 $\pm 3 \times 10^{-17}$ ergs s^{-1} cm^{-2}. Then, the time required to detect such flux to a level of 10σ, estimated for LIRIS is 10650 s. This means that the observational program will require ∼3 h of exposure time for each field (i.e. with the multi-slit mask from 4 to 6 galaxies will be observed simultaneously, as described in section 6.6).

5

Near-infrared detector characterization

5.1 Introduction

The detector is the most important element in any astronomical instrument. Being a state-of-the art device, it defines the characteristics of the instrument such as the wavelength range and sensitivity. The size and number of pixels of the detector play an important role in the optical design at the moment of fitting the relation between the field of view and the resolution. However there is only a limited variety of detectors; in fact, for the near-infrared wavelengths (1 to 2.5 μm) there are only a couple of large-format devices (i.e. with more than a million of pixels): the Aladdin and the HAWAII families of detectors. In most of the cases, the selection of the detector is limited by the availability of the devices and the date at which the instrument will be commissioned. Such availability is related to the demand of detectors and to the technological development of the semiconductor companies.

Section 4.5 describes how the spectroscopic observations can be limited by detector parameters such as the readout noise and the dark current. The readout noise limits directly the signal to noise ratio (S/N) of short time exposures. The photon shot noise produced by the dark current limits the long time exposures. These parameters, when combined with those referred to the stability of the detector behavior (see below), require a detailed study in order to characterize and to improve the instrument performance.

The detectors have a series of characteristics given by their manufacturers. The published values are, generally the common ones to all the devices of the same family. They depend on two aspects: a) the detector itself and, b) the electronic circuits that are used to control and read the array. This chapter describes the tests to the detector of LIRIS that I performed in collaboration with Dr. Ezequiel Ballesteros and Dr. Jose Acosta. The chapter also includes the analysis of the detectors of NICS and Omega Prime, which are similar to that of LIRIS. Through all this chapter three types of arrays are referred: a scientific grade detector (hereafter, scientific detector), an engineering grade one (hereafter, engineering detector) and a bare multiplexer (hereafter, multiplexer). The difference between the scientific grade and the engineering grade detector is that, the latter one does not fulfill the requirements to be used for scientific purposes due to its elevated number of defects. The multiplexer is the electronic circuit of the detector without the sensitive layer to near-infrared emission, although it is slightly sensitive to optical wavelengths.

Table 5.1: Detectors in some near-infrared instruments

Instrument	Detector	comments
CGS4	NICMOS3	camera and spectrograph
MAGIC	NICMOS3	camera and spectrograph
SOFI	HAWAII	camera and spectrograph
Omega Cass	HAWAII	camera and spectrograph
Omega Prime	HAWAII	camera
ISAAC	HAWAII & Aladin	camera and spectrograph
NIRC	Aladin	camera
Nirspec	Aladin	spectrograph
INGRID	HAWAII	camera
NICS	HAWAII	camera and spectrograph
NOTCAM	HAWAII	camera and spectrograph
Flamingos	HAWAII2	camera and spectrograph
Omega2000	HAWAII2	camera
CONICA	Aladin	camera and spectrograph
LIRIS	HAWAII	camera and spectrograph
GNIRS	Aladin	spectrograph

5.1.1 Detectors for near-infrared spectrographs

The spectroscopic observations require large format detectors, primarily in the spectral-dispersion direction. The detector of LIRIS is the HAWAII array of 1024 x 1024 pixels, the same used in most of the modern near-infrared spectrographs (see Table 5.1). The large number of pixels in the spectral direction allows to obtain intermediate resolution spectra of a broad wavelength range. The large size in the spatial direction allows, on one hand, to combine the spectroscopic and imaging modes in a single detector/instrument and, on the other hand, it allows the instrument to be ideal for the multi-slit spectroscopy, such is the case of LIRIS. The HAWAII detector, manufactured by Rockwell Scientific Corporation (hereafter RSC), has the best characteristics for the wavelength range of 1 to 2.5 μm and it is the evolution of the NICMOS3 256 x 256 array and the predecessor of the HAWAII2, which has 2048 x 2048 pixels.

5.2 Detector description

HAWAII is the acronym of HgCdTe Astronomical Wide Area Infrared Imager. This detector was designed jointly between the University of Hawaii and the RSC. The tests on the first prototype were reported by Kozlowski et al. (1994) and the first scientific grade array was installed in the Quick Infrared Camera (QUIRC; Hodapp et al. 1996) on December 1995.

The array is made of multiple layers, each one with a specific function such as the photon detection and the electron storage and manipulation. The layers are made from different materials and, thus the detector is called a “hybrid” array. The layer sensitive to the near-infrared wavelengths (0.9 to 2.5 μm) is made of mercury cadmium telluride (HgCdTe), frequently called MCT. This layer is configured as a grid of square pixels of 18.5 μm per side. The HgCdTe is grown over a sapphire

layer, which forms the front part of the detector. Each pixel of the grid in the detection layer makes electrical contact to a pixel at a similar grid made of silicon (Si). The latter layer is called "the multiplexer" because it carries out the detector control and readout multiplexing all the pixels. The interconnection between the pixels in the detection layer and those in the multiplexer is made through an indium (In) "bump" at each pixel of the grid. The main reason that these layers are made of different materials is that, on one side, the HgCdTe has a band gap of lower energy than that of the Si, thus it is excited with longer (i.e. infrared) wavelengths. However, on the other side, the technological development to make circuits in Si is higher than that in any other material, so that Si the best option for the multiplexer. The drawback of the hybridization is that the first prototypes presented a degradation of the detector caused by the thermal cycling (i.e. the process to cool the detector to the operational temperature and to warm it, later to room temperature). Estimations on the first science detectors showed that, 10 to 20 pixels were lost each time the detector was cycled (Hodapp et al. 1996).

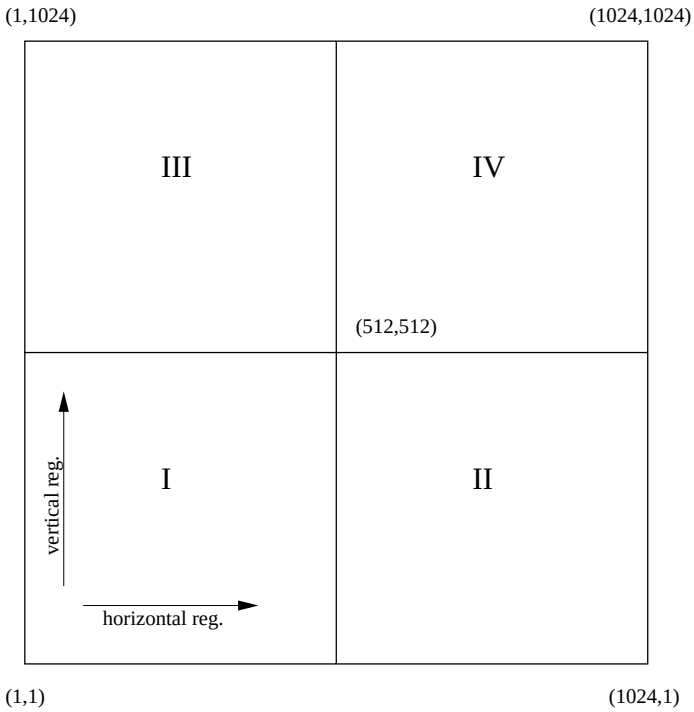

Figure 5.1: Nomenclature for the detector quadrants. The arrows represent the direction of the vertical and horizontal shift registers.

The principle of operation of the detector is based on that, when a photon reaches the detection layer, it produces an electron-hole pair at the pixel where it arrived. This pair is almost immediately separated by the electric field formed by the inverse-biased *pn* junction of the photodiode, which is the basic element of a pixel. A depletion region is formed in the junction when the reverse bias voltage is applied and it is discharged by the generation of electron-hole pairs; in this manner, the charge is stored on the pixel that forms a capacitor (called *well*). Some charge in the form of *dark current* (see section 5.5.7 is also generated by recombination of the electron-hole pairs as a function of the temperature. The voltage produced by the charge is applied to a metal oxide semiconductor

- field effect transistor (MOSFET) configured as a source follower amplifier, which is located in the multiplexer; there is one of these MOSFETs at each pixel. There is also, other FETs at each pixel, configured as logical switches for the connection of the reverse bias voltage (the *reset*) and to enable the readout of the pixel, when it is addressed.

The mode of operation of the detector allows to read the pixel while it is integrating charge (i.e. being exposed to a source of infrared illumination), because such read is non-destructive. In other words, the action of addressing the pixel to connect the output of the source follower amplifier to the subsequent electronics does not affect the charge stored in the capacitor of the pixel. This is a great difference respect to the CCDs, which operate transferring the charge from one pixel to other until it reaches the output amplifier. The destruction of the charge occurs only when the pixel is reset by the application of the reverse bias voltage and the photodiode becomes completely inverse-biased. It is interesting to note that, when the pixel saturates, the photodiode becomes completely de-biased, thus no bleeding occurs like in the case of CCDs.

The pixels are addressed one by one to read their charge, this process is carried out by the multiplexer, which is organized in 4 quadrants (see Figure 5.1). Each quadrant has two shift registers: vertical and horizontal. These registers address a determined pixel by its row and column coordinates. The registers are driven by two clock signals; the horizontal register is clocked faster than the vertical one; the result is that the detector readout is structured by rows. The clock signals for the horizontal register are “PIXEL” and “LSYNC” (line synchronization); the former drives the increments on the shift registers, while the latter selects the beginning of the line, as it can be seen in the oscilogram in Figure 5.2, where the “LSYNC” pulse indicates the change of row. The “PIXEL” clock determines the pixel data rate, incrementing the register on both edges of the pulse (i.e. the odd columns are selected on the positive edges and the even columns in the negative edge). The vertical register is driven in an analog manner by the clock “LINE” and frame synchronization “FSYNC”. Finally, the “READ” clock is active during all the readout process to allow the source follower amplifier output pass to the column bus, and the “RESET” clock, that is activated to reset an entire row selected by the vertical shift register. An example of a sequence of reset-read-read-reset is shown in Figure 5.4.

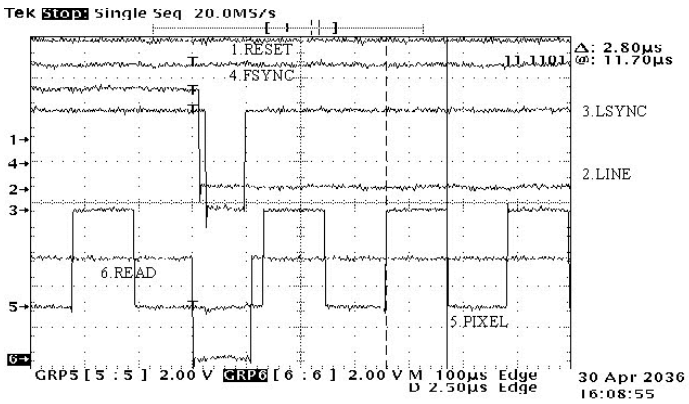

Figure 5.2: Clock profiles for the change of line (row) in a single read. Note the pulse on “LSYNC” at the end of 256 “PIXEL” cycles and the de-activation of “READ” during the time of row changing.

The array is read in 4 quadrants to minimize the work of the shift registers and to allow a faster

Table 5.2: HAWAII characteristics as given by RSC

Spectral range	0.85-2.5 μm
Pixel size	18.5 μm
Well capacity	1.0 $\times 10^5$ carriers
Well capacitance	18 to 35 fF
Gain	3.4 to 6.8 μV/e$^-$
Maximum data rate	$>$1 MHz
Maximum slew rate	400 ns
Readout noise (CDS)	$<$10 e$^-$
Readout noise (MNDR)	$<$3 e$^-$
Quantum efficiency	$>$60 %
Dark current at 78 K	$<$0.03 e$^-$/s

readout of the entire detector. Although the multiplexer is organized in these quadrants, there is no physical separation between the quadrants at the HgCdTe layer. Each quadrant contains 512 $\times$ 512 pixels of 18.5 μm per side. The pixel has capacity, or full well of 100,000 carriers (i.e. electron-hole pairs) as summarized in the detector characteristics[1] of Table 5.2.

5.2.1 Detector control and readout electronics

The control and readout of the detector is based on three components: a) the fanout board, b) the preamplifier and, c) the controller.

The "fanout" board is inside the cryostat, it is the physical support for the detector and it couples all the input and output signals of the array. The four channel outputs from the detector (i.e. the signal from the four quadrants) are amplified by a JFET, that is used to bypass the array internal pre-amplifiers. These JFETs have a very high input impedance, so that the current demand to the detector is a minimum. Due to the detector working temperature, the selection of these amplifications devices is extremely limited. This input signal coupling is formed by a zenner diode protection for all the signals and a high frequency capacitive filter for all the analogic inputs.

All the wiring from the fanout board to the external wall of the cryostat is divided in several sections to allow the mechanical assembling. The first of these sections goes from the fanout board to the "wiring ring". Twisted pair wiring is used for the analogic signals with an external shield and coaxial wiring is used for the digital signals. Another section runs from the "wiring ring" to the external wall of the cryostat, with the same wiring configuration then the prior section. The final section goes from the cryostat to the SDSU controller. The digital signals are connected directly using coaxial wiring. The analogic output signals go through the preamplifier board, that is located outside the cryostat at the exact point of the output connector (i.e. the connector is mounted on the board itself). This configuration reduces the noise that could be picked by the wiring outside the cryostat. Each preamplifier channel is formed by an operational amplifier that has an offset control to adjust the voltage to the controller input.

The controller carries out the synthesis of all the signals required to control the detector, it reads the outputs from the amplifier and converts them into a digital signal that is sent to the data acqui-

[1] As given by RSC in www.rockwellscientific.com

sition computer. For years, the only commercial controller has been the one developed by Leach, Beale, & Eriksen (1998) and called "San Diego State University controller" (hereafter, SDSU controller). This controller is a general-purpose unit for CCDs and infrared detectors. It has been used at several near-infrared instruments and its design has been improved (Leach & Low 2000). Moreover, right now it is the standard controller at the WHT. The SDSU controller can be configured in different manners; the one that is used for the detector of LIRIS has 4 channels for the readout, one for each quadrant. This configuration includes the following boards:

Video board.- This is the board that samples the preamplifier analogic output and converts it into Analog to Digital Units (ADU) which represent the pixel values. Each one of these boards has two 16 bit analog to digital converters (A/D) with a sample rate up to 1 MHz, so that, there are two video boards to read the four quadrants of the detector.

Clocks board.- This board synthesizes all the clock signals from the pulses of the "timing board". The clock signals are: "PIXEL", "LSYNC", "LINE", "FSYNC", "READ" and "RESET". The pixel sample rate is fixed to 358 KHz (one pixel each 2.85 μs as shown in Figure 5.3). The detector bias and reset voltages are also generated at this board, by a 12 bit digital to analog converter (D/A).

Timing board.- This board carries out the timing, synchronization, communication and control off all the other boards. It is based on a digital signal processor (DSP; Motorola 56002) and a program written in a EPROM memory. It also carries out the communication with the computer (a Sun Ultra Sparc 1) via a fiber optic link.

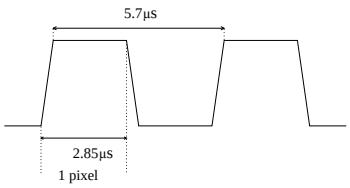

Figure 5.3: Pixel clock timing. One pixel is addressed on each edge of the pulse.

5.2.2 Noise in the detector readout

As it can be seen in Table 5.2, the HAWAII detector has a specified readout noise value higher than the typical for CCDs. There are different sources of noise intrinsic to the detector and its electronics: KTC, $1/f$ and white noise. Additional noise comes from external sources, for example: the digital clocks at the SDSU controller, the power supply unit, as well as from any other electronic device close to the detector: the temperature sensors, the temperature controller, the closed cycle cooler and the mechanism motors.

The KTC noise appears with the action of "reset" and can be described as the uncertainty in the reset charge given by $\sqrt{(kT/C)}$, where k is the Boltzman constant, T is the absolute temperature and C is the pixel capacitance. The other "internal" noise sources, the $1/f$ and the white noise, are induced in the source follower amplifier and the off-chip amplifiers. The generation of dark current and the photon incidence to the detector also have an associated noise, as described in section 4.4.

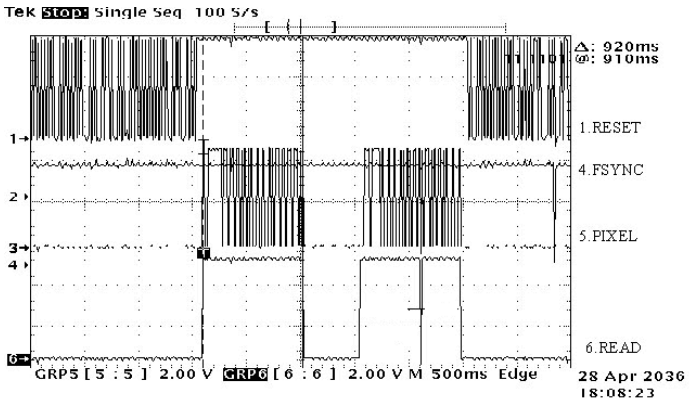

Figure 5.4: Clock profiles for a CDS read.

5.2.3 Detector readout modes

The problem with the high readout noise, have led to develop new readout modes, in order to reduce it. The most common modes, from the works of Chapman et al. (1990); White & Lampe (1974); Fowler & Gatley (1990,1991); Garnett & Forrest (1993), are:

Single read,- This is the basic readout mode, which consists in a reset of the complete array and a read after the integration time. In this mode the initial charge (bias) is added to the accumulated charge in the integration time. Thus, the read value has two contributions: the bias and the signal, as shown in Figure 5.5, where the bias is represented by the step after the reset. Due to the KCT noise, the bias can not be subtracted by a constant value. In this mode, the signal (S) is the read value (s) and the readout noise is equal to that of a single read (N).

CDS.- The Correlated Double Sampling method used commonly, is a variation from the original technique proposed by White & Lampe (1974). The main purpose of this mode is to eliminate the KTC noise and the bias level. As shown in Figure 5.5, it consist of a reset of the whole array, a readout immediately after that and a second read after the integration time. This method is sometimes related as the "Fowler mode", since Fowler & Gatley (1990) was the first to promote its use. The signal (S) is the result of the subtraction of both reads.

$$S = s_2 - s_1 \tag{5.1}$$

where s_1 is the image previous to the integration (also called *pre*) and s_2, the image after (called *post*).

The operation can be performed *on line* storing only the resultant image or, it can be computed any time latter if both images are saved. The former option presents a problem, because if a pixel saturates it would not be noticed. An example of the timing required for this mode is shown in Figure 5.4.

The noise of both reads are added in quadrature, giving the CDS noise (N_{cds}):

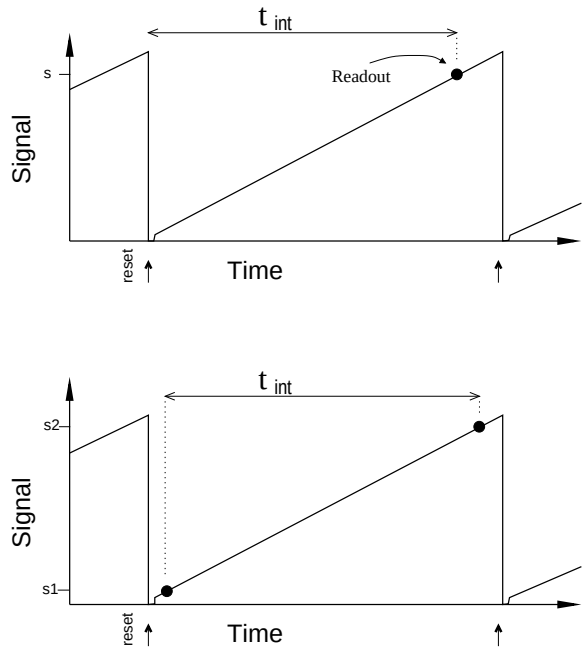

Figure 5.5: Representation of the signal integration in the *single* (top) and *CDS* (bottom) readout modes. The dark points represent one non-destructive readout and t_{int} the integration time. The reset pulse and the bias level (i.e. the step after reset) are also represented.

$$N_{cds} = \sqrt{N^2 + N^2} = N\sqrt{2} \tag{5.2}$$

MNDR.- The Multiple Non Destructive Reads mode was initially reported by Fowler & Gatley (1990). It is based on the same principle of CDS, with the difference of taking *m* reads at each point instead of one. Figure 5.6 illustrates the case for *m*=4. This method eliminates the KTC noise and reduces the readout noise statistically when the group of *m* reads at each point are averaged. Although this method requires more images, the implementation and computation of the final image is simple. The signal (*S*) is, therefore given by:

$$S = \frac{1}{m}\sum_{m} sa_i - \frac{1}{m}\sum_{m} sb_i \tag{5.3}$$

where *sa* and *sb* are the groups of reads before and after the integration time, respectively. The readout noise is reduced as a function of *m*, and it is given by:

$$N_{mndr} = \sqrt{\frac{2}{m}}N \tag{5.4}$$

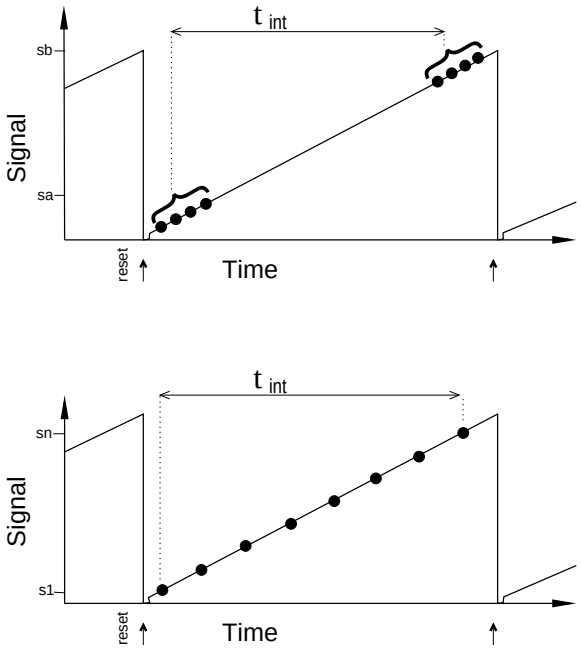

Figure 5.6: Representation of the signal integration in the *MNDR* mode (top), with *m*=4 and in the *ramp* mode (bottom) with 8 non-destructive reads. The symbols are the same than in Figure 5.5

Sample-the-ramp.- This mode consists on sampling the signal several times at a constant interval (Δt) during the integration time, as shown in Figure 5.6. A linear fit is adjusted to the n points (reads) and the signal (S), derived from the slope (Chapman et al. 1990; Garnett & Forrest 1993), is:

$$S = \frac{\sum_n sn_i \left(i - \frac{n-1}{2}\right)}{\frac{n}{12}(n^2-1)\Delta t} \tag{5.5}$$

This mode is very useful to take continuous reads (i.e. with no KTC noise contribution) as the required for dark current measurements. The readout noise is reduced as a function of the number of reads n:

$$N_{ramp} = \frac{N}{\sqrt{\frac{n(n+1)}{12(n-1)}}} \approx \frac{N}{\sqrt{\frac{n}{12}}} \tag{5.6}$$

The SDSU controller and image-acquisition computer of LIRIS are programmed to allow the selection of the detector readout mode from any of these modes.

5.3 Detector test setup

A test cryostat was designed at the IAC to test and to characterize the detector system. This cryostat allows to cold the detector close to liquid nitrogen (LN_2) temperature (78 K) and to test it using

different optical configurations. Inside the cryostat and behind the entrance window there is a removable cold mask with a *pin-hole* on its center. The optical set of the cryostat consists on a baffle and a small filter wheel with four possible selections (*J*, *H*, *Ks*-band filters and a cold dark slide). These mechanisms, allow to test the detector under different conditions of illumination: a) completely dark; b) uniform illumination (i.e. flat-field) through the *pin-hole* and, c) open, to create images placing a lens outside the cryostat. The tests *b* and *c* can be done at any of the near-infrared bands (*J*, *H*, *Ks*). For all the configurations, a temperature-controlled *black body* placed outside the cryostat, is used as the source of illumination.

There is a thermal link that joints the LN_2 tank to the fanout board and the detector; it is designed in such way that the detector cools down at a slower rate than the cryostat. As it can be seen in Figure 5.7, the detector reaches a minimum temperature of 82 K. At this value, the thermal stability is very high, as shown in Figure 5.8. The tests were performed at such temperature, although in LIRIS the detector will be cooled down to 65 K using the second stage of a Closed Cycle Cooler (hereafter CCC). In that case a temperature controller will be used because the temperature stabilization will not be as good as that of LN_2. At these series of tests, the temperature controller is also characterized, specially its noise contribution to the detector. The importance of the temperature stabilization comes from the variations observed in the *bias* behavior, as described in section 5.5.3.

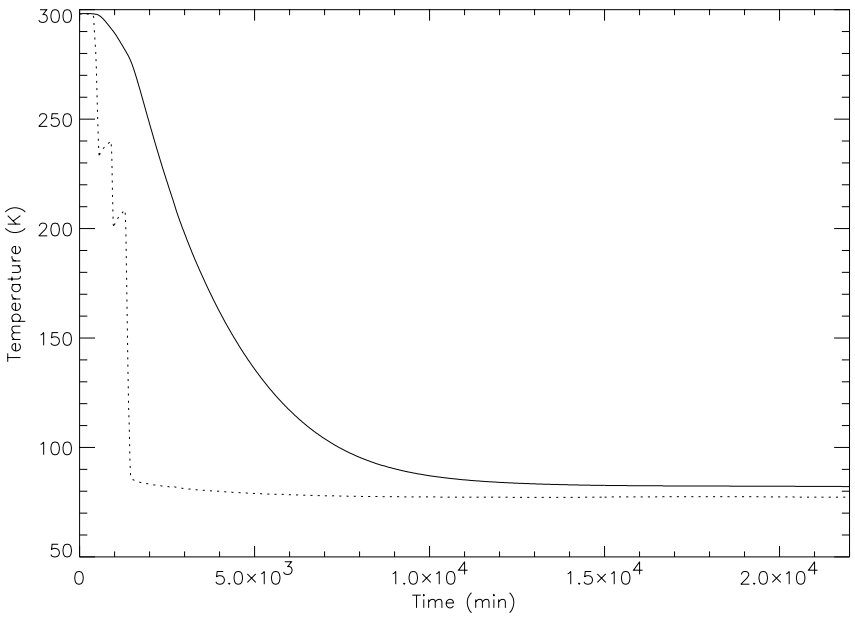

Figure 5.7: Detector temperature (solid line) in the test cryostat during the cooling down. The internal cool base is the dotted line.

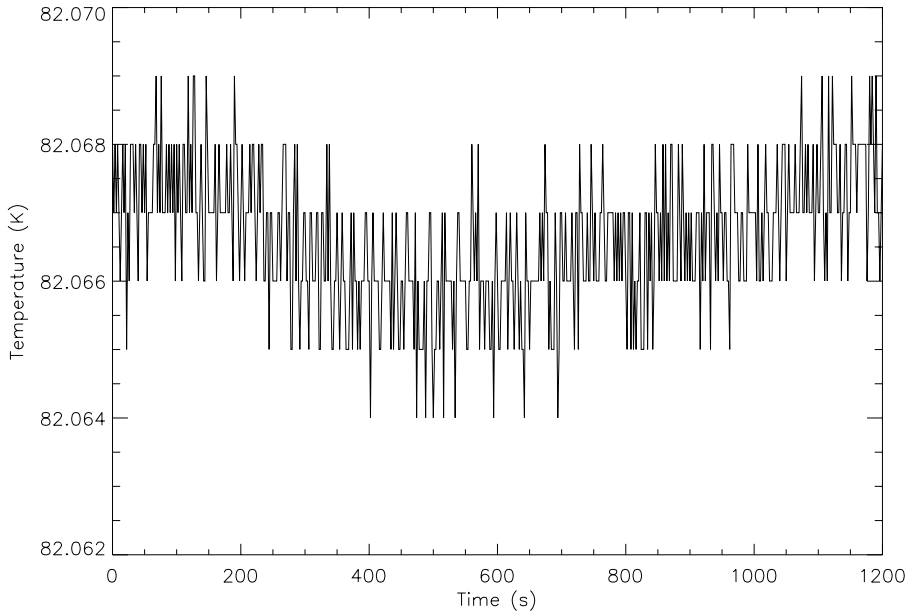

Figure 5.8: Detector temperature in the test cryostat at LN_2 temperature.

5.3.1 Data analysis

I carried out the test data analysis using IRAF[2] and IDL[3]. More than 3000 images were acquired during all the tests occupying some 25 GB of disk space. The test images were stored in two planes, the *pre* and the *post* images. The elevated number of images responds to the aim of maintaining the statistical errors as low as possible in the characterization of the noise and in the estimation of the bias stability; for these purposes, series from 50 to 100 images were acquired for each test. With these amount of data, I found it easier to analyze the series using IDL because of its possibility to store the images in RAM memory and compute the difference *post* - *pre* without saving the image to disk. I used IRAF to analyze the image structures, the image quality, and to use some of the packages as IMEXAMINE, FIXPIX, etc.

The analysis is done in several steps, including visual inspection and the test of different work-out techniques:

- The initial step of the analysis is to identify, at each quadrant, the *good* pixels (see section 5.5.8 for the definition of *bad* pixels) to work with them. This selection is to exclude the detector regions with high concentration of bad pixels, such as the top of the upper right quadrant in the engineering detector.

- A histogram of the number of pixels as a function of their individual values is constructed, as the one showed in Figure 5.9. This figure shows the difference among the good pixels (those that follows a Gaussian distribution), the dead pixels at zero, and the hot pixels (those

[2]IRAF: Image Reduction and Analysis Facility developed at NOAO
[3]IDL is the acronym of Interactive Data Language, by Research Systems, Inc

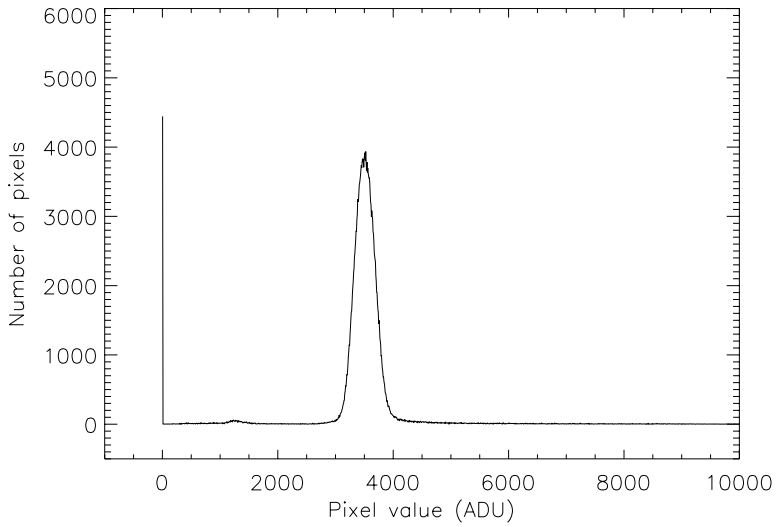

Figure 5.9: Data histogram for one quadrant. A huge amount of *bad* pixels with 0 ADU and a small number with 1200 ADU can be seen. The *good* pixels are concentrated in the gaussian distribution.

that have the highest values, even at saturation limit). From looking at the histogram figures, it is clear the importance of considering only the *good* pixels for the signal level and noise measurements.

- Different statistical tools are computed to estimate the central value of the *good* pixels and its dispersion. It can be seen in the figure that computing the *mean* of all the pixels in a quadrant would give an incorrect value of the main signal level of the pixels, because the estimation is affected by the hot and dead pixels; the *median*, instead, is the correct measurement, as it can be seen in Figure 5.10. To estimate the noise, the *standard deviation* method presents the same problem than the calculus of the *mean*. The main problem is that these statistical tools are intended to be used in "normal" distributions, and only the *good* pixels follow such distribution, therefore all the *bad* pixels have to be discarded. A threshold could be established to remove those *bad* pixels from the computations, however the problem of the discrimination between the *good* and *bad* pixels remains. The better method to do this is to fit a gaussian profile the histogram data as shown in Figure 5.10. With this method, the central signal level of the pixels is accurately determined. The noise value is obtained from the gaussian *sigma*; in fact, the *standard deviation* of a normal (i.e. gaussian) distribution gives an estimation of the *sigma*. The values given in the same figure show the difference of calculating the center of the gaussian fit, the *median* and the *mean*. It can be seen that the value given by the *mean* is incorrect, and in consequence the *standard deviation* is also affected, giving a wrong value.

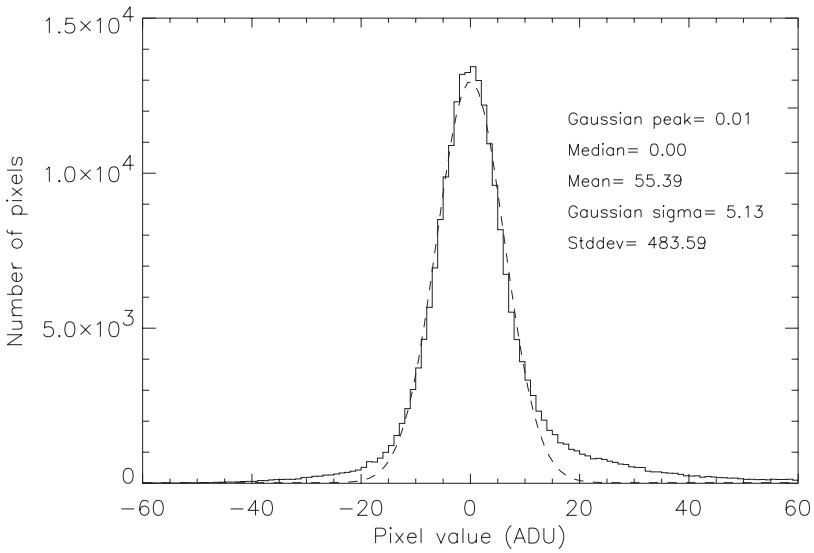

Figure 5.10: Data histogram for one quadrant and gaussian fit to the data. The center of the gaussian, the *median* and the *mean* are computed to estimate the center of the distribution of the data. The values of the *sigma* and *standard deviation* are computed to estimate the noise.

Table 5.3: Multiplexer readout noise (ADU) at LN_2 temperature as a function of the number of reads,*m* in *MNDR* mode. (20 s exposure time)

Date	Detector	Comments
Feb - Sep 2000	Multiplexer	electronic and software tests
Oct 2000	Multiplexer	1^{st} cooldown
Nov 2000	Multiplexer	2^{nd} cooldown
Nov 2000	Engineering	1^{st} cooldown
Feb 2001	Multiplexer	software tests
Jun 2001	Multiplexer	wiring tests
Jul 2001	Multiplexer	3^{rd} cooldown
Jul 2001	Multiplexer	noise workout
Jul 2001	Engineering	characterization

5.4 Multiplexer tests

The main utility of the multiplexer is to calibrate the complete detector system, including all the software and electronic components: the data acquisition computer, the controller, the fan-out board, the preamplifier and the wiring. As it is resumed in Table 5.3 the characterization of the detector system included several tests to the multiplexer and to the engineering detector. The multiplexer was tested in warm and cryogenic conditions, while the engineering detector was tested only in cryogenic conditions (i.e. due to the immediate saturation produced if tested at room temperature)

The multiplexer is blind to the near-infrared emission because it lacks the sensitive layer; however, it is slightly sensitive to optical wavelengths. So that, it constitutes an excellent tool to calibrate the image reconstruction software, the cryostat optical configuration, the preamplifier offsets, etc. In any case, the most important tests carried out with the multiplexer were those related to measure the readout noise and to work on its reduction.

One of the first multiplexer images of the USAFR reticle[4] is shown in Figure 5.11. This image, taken at room temperature, shows the defects of the array such as some bad columns. The quadrant misconfiguration can be seen from the displaced USAFR images. Such misconfiguration is originated in by the independent treatment of the quadrants until the image is reconstructed at the data acquisition computer.

The first tests to measure the readout noise gave extremely high values, as summarized in Table 5.4. It can be seen that even with the detector turned off (i.e. without the bias voltage nor clocks) and without the temperature sensors, the readout noise is over 20 ADU; which means that the higher noise contribution comes from noise sources external to the detector.

5.4.1 Readout noise reduction workout

In order to analyze each source of noise, several series of measurements were carried out, changing the configuration of the possible noise sources.

[4]The USAFR is a test slide with the 1951 US Air Force test pattern that is used to determine the spatial resolution of optical systems.

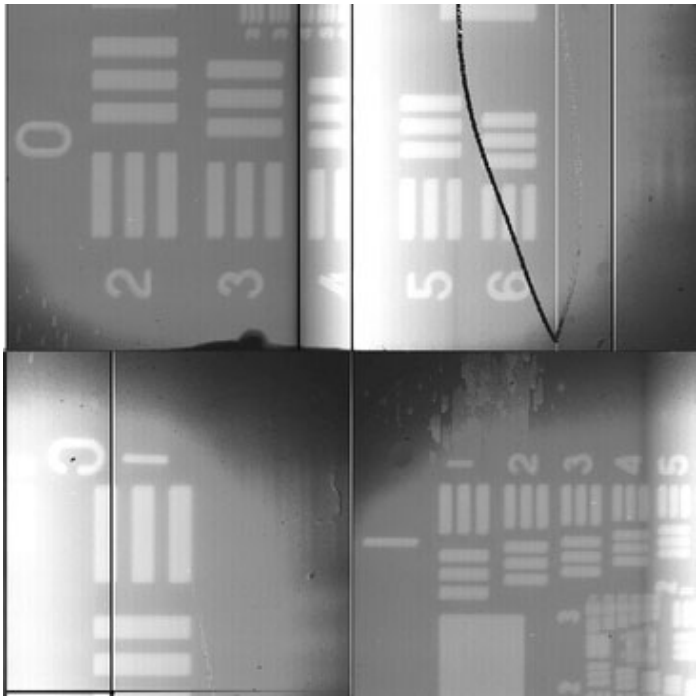

Figure 5.11: Multiplexer image of the USAFR reticle at room temperature. Note the defects of the array and the quadrant misconfiguration.

Table 5.4: Multiplexor readout noise (N) measurements in ADUs.

Configuration	I	II	III	IV
Detector with temperature sensors	39	40	40	35
Detector OFF with temperature sensors	22	23	22	17
Detector OFF and no temperature sensors	22	24	23	17

The first changes were done in the grounding scheme. The absolute "ground star" (i.e. connected to physical ground) established at the power supply was changed to a "floating" ground star at the SDSU controller. The connection of this *star* to the physical ground is made through the power board in the controller. Surprisingly, this change reduced the noise to $\sim$15 ADU, as shown in Table 5.5.

Two more changes were performed, the first was to double the shielding of all the wiring going from the fanout board to the preamplifier and, from this to the SDSU controller. The second change was to connect together the digital ground (DGND) to the analogic one (AGND) at the fanout board point. These grounds are connected to the ground star point at the SDSU, and the *star* configuration establishes that they must not be connected at any other point. However, private communication with Dr. Peter Moore (from the project INGRID at the Isaac Newton Group) and Dr. Gert Finger (from the projects SOFI and ISAAC at the European Southern Observatory), indicated that they have these grounds connected in the fanout board of their respective instruments to improve the readout noise. With these changes, the readout noise was reduced down to $\sim$3 ADU as shown in

Table 5.5: Multiplexor readout noise (N) measurements in ADUs.

Configuration	I	II	III	IV
SINGLE wire shielding				
ground star at power supply	39	40	40	35
ground star at SDSU and AGND≠DGND	15	14	16	15
DOUBLE wire shielding				
ground star at SDSU and AGND=DGND	∼4	∼3	∼3	∼3

Table 5.6: Multiplexer readout noise (N) in ADUs at room temperature.

Configuration	I	II	III	IV
OLD WIRING cryostat connected to ground	2.4	2.3	2.3	2.8
cryostat NOT connected to ground	4.0	3.0	3.4	3.1
cryostat & preamp. connected to ground	2.9	2.2	2.4	2.7
NEW WIRING (crimped)				
multiplexer outside the cryostat	2.7	2.4	2.7	2.9
open cryostat	2.4	2.3	2.4	3.0
closed cryostat	2.3	2.1	2.3	2.8
SDSU without shielding net	2.3	2.2	2.3	2.7
cryostat NOT connected to ground	3.5	2.7	3.6	3.1
cryostat connected to ground	2.2	2.2	2.3	2.7
moving farther the SDSU	2.3	2.3	2.4	2.9
moving closer the SDSU	2.4	2.3	2.4	2.7
rotating the SDSU	2.3	2.2	2.3	2.6

Table 5.5.

Additional work on the study of the noise sources was carried out. The first tests were done with the cryostat grounded. We found that noise is a strong function of the grounding of the cryostat, not only because it represents an electromagnetic shield to external sources, but as a ground plane for the internal noise sources. Table 5.6 summarizes the results of these tests. After these tests, it was evident that the detector wiring presented a false-contact problem, so that, it was decided to replace the complete wiring and the connectors and further tests were carried out as summarized in the same table. The false-contact problems were solved and a slight improvement in the noise was found.

The noise contribution of the temperature controller and its sensors was studied at the 3^{rd} cool-down of the multiplexer tests. It was carried out measuring the readout noise in three different conditions: a) with the controller fully operational, b) with the temperature sensors only and, c) with the temperature monitor turned off and the sensors connected to ground. As it can be seen in Table 5.6, the noise contribution from the sensors is approximately 1 ADU.

From visual inspection to the images in order to analyze the sources of noise, we found that there

Table 5.7: Multiplexer readout noise (N) in ADUs at LN_2 temperature as a function of the temperature monitor.

Connected sensors	I	II	III	IV
all	3.2	2.0	2.4	2.4
none	2.4	1.8	1.9	1.8
PC-on	2.8	1.8	2.0	1.9
diodes only	3.3	2.1	2.6	2.7
cernox only	3.3	2.1	2.4	2.5
none (again)	2.3	1.8	1.9	1.8

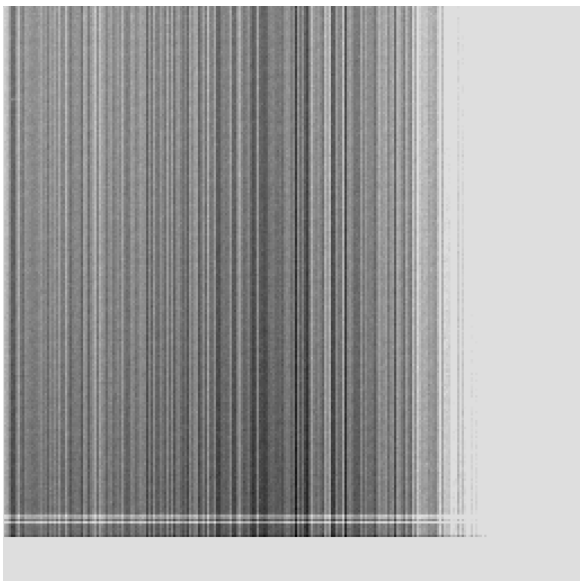

Figure 5.12: Fixed pattern noise in a *pre* image. Only a region of the image is shown. Note the vertical pattern associated with the columns of pixels.

were two fixed patterns at the multiplexer images. The first pattern, that can be seen in Figure 5.12, is a variation of the pixel bias synchronized with the columns. This pattern is very similar in both *pre* and *post* images thus, it is eliminated at the *post* – *pre* subtraction. We believe that the origin of this pattern is the two-edge principle of operation of the PIXEL clock.

The second noise pattern is found in the *post* – *pre* images, as a set of diagonal bands (see Figure 5.13). The level of this pattern is extremely low, so that its contribution to the readout noise is negligible, as it can be seen in Table 5.8. The frequency of this pattern was estimated from the Fast Fourier Transform (FFT) of a single row of one quadrant, considering the pixel sampling time of 2.85 μs (see section 5.2.1). The power spectrum of the FFT can be seen in Figure 5.14, where a frequency of $\sim$83 KHz is identified with the prescence of the pattern. The identification of the possible noise source that matched that frequency (or its harmonic values) became complex because the pattern was not always present, indicating that the source was external to the detector system. A final attempt to isolate the detector from any external noise source was to take the it, the SDSU

Table 5.8: Multiplexer readout noise (N) in ADUs at images with and without the noise pattern. The test at LN_2 temperature.

Pattern	I	II	III	IV
yes	2.44	2.67	2.34	2.59
no	2.59	2.77	2.26	2.41

Table 5.9: Multiplexer readout noise (N) in ADUs at room temperature in the electro-magnetic shielded room

Location of tests	I	II	III	IV
electronics laboratory	2.3	2.1	2.3	2.8
open shielded room	2.21	2.33	2.14	2.21
closed shielded room	2.23	2.30	2.14	2.21

controller and the test cryostat into the "electro-magnetic shielded room" at the IAC. The pattern was not found anymore.

The readout noise values were slightly better than those measured at the "electronics laboratory", as it is summarized in Table 5.9. No differences were found between having the shielded room open or closed, which stated that the possible noise source was located close to the electronics laboratory and that it was very weak. From these tests it was decided to carry out all the tests in the shielded room.

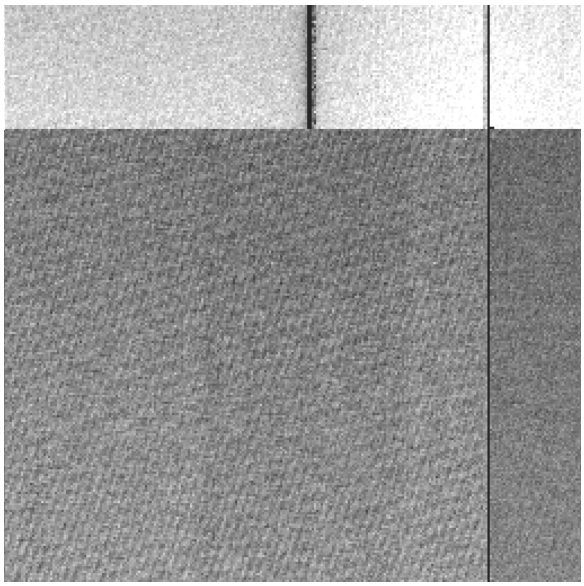

Figure 5.13: Fixed pattern noise in a *post-pre* image. Only a region of the image is shown. Note the diagonal pattern.

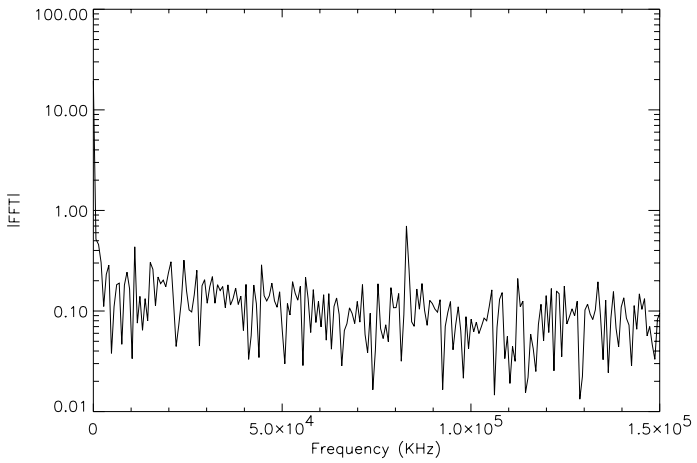

Figure 5.14: Fast Fourier transform of one row of the image with the diagonal pattern. Note the main frequency at 83 KHz.

5.5 Engineering detector tests

5.5.1 Initial tests

The first cool down of the engineering grade detector was carried out on October 2000, with the objective to test the performance of the complete detector system and to characterize the readout noise. Although the previous tests with the multiplexer had given the values of readout noise, this first approach to the engineering detector was essential because the bare multiplexer lacks of some important parameters such as: the signal integration (i.e. it gives only the measurement of the instantaneous photon flux), the sensitivity to infrared wavelengths and the dark current generation.

Three tests were planned: a) the follow-up of the bias behavior at the cool down, b) the measurement of the readout noise and c) the first estimation of the dark current. During the cool down, at 100 K, the quadrant III stopped giving signal. Therefore, only three quadrants were available for the tests. One week latter (after warming up and opening the cryostat) we discovered a false contact in the clock wires of the quadrant. The relationship of bias and temperature was established from the bias measurements at different temperatures during the warming up.

The readout noise was measured from a series of 15 images. These images were acquired with the cold black slide placed in front of the detector and 1 s exposure times. The result of this measurement was a readout noise $N \sim 16.8$ ADU, which was an extremely elevated value: 84 ± 8 e^- considering a gain of 5 ± 0.5 e^-/ADU (see section 5.5.4). The conclusion of this test was that further work on the reduction of the noise was required (Domínguez-Tagle & Acosta-Pulido 2001), as it is scheduled in Table 5.3

No further measurements were performed at this test run because three more problems appeared: a) a light leak in the cold black slide, b) a permanent offset of $\sim$ 800 ADU and, c) a non-uniform illumination in all the flats. The light leak was discovered when a lamp was used to illuminate through the cryostat window and an exposure was acquired. The image, that should have been dark, showed bright spots that changed as a function of the changes of the lamp; they were evidently related each other. The 800 ADU offset in the images was present in all the images of the first three days of the tests. The non uniformity was present in all the illuminated images in a form of a darker rectangle at the center of the image. These problems made that the analysis of the images became complex and that many of the results had no confidence. A further characterization was required.

5.5.2 Engineering detector characterization

We performed the characterization tests to the engineering detector during its second cool down from the last week of July to the first one of August 2001. The test objectives were to measure the most important properties of the detector: noise, linearity, gain, dark current and glow from the shift registers (see Domínguez-Tagle, Acosta-Pulido, & Ballesteros 2001).

A flat-field image from each filter was acquired illuminating the detector with the *black body* at temperatures of 300°C for *J*-band filter and 100°C for the *H* and *Ks*-band filters. The images can be seen in figures 5.16 to 5.18. *J* and *H*-band flats are in good conditions, however, *Ks*-band filter shows several spots, that we suspect are filter defects. Figure 5.15 shows the first light image of the engenieering grade detector, taken with an USAFR reticle and corrected from *bad* pixels (described in section 5.5.8).

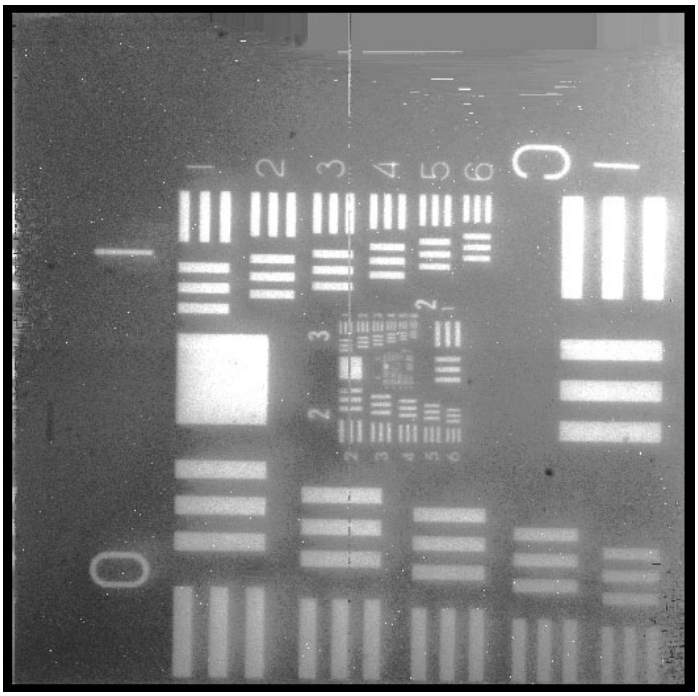

Figure 5.15: Engenieering grade detector image of the USAFR reticle. The image is corrected from *bad* pixels.

5.5.3 Bias

As reviewed in the detector description, the bias level is eliminated applying the readout modes: DCS, MNDR and *ramp*. However, all of these modes assume that, even if the bias level of the first read after reset is uncertain, it will be constant during the consecutive non-destructive reads (i.e. with no reset between them). However, if the bias level changes from one read to the next one the result of the readout will present a contribution of the bias change, thus any measure on it will be wrong.

While cooling down the detector from room temperature to 82 K, we maintained a periodic follow up of the bias and readout noise. Although the noise did not present any variation, the bias showed a clear relationship with temperature. The variation was so high that the preamplifier offsets needed to be adjusted at 115 K to avoid saturation. Further analysis was done using the temperature controller to take the detector from 82.5 to 85 K in a period of more than 30 minutes, during which, consecutive dark images of 1 s, were acquired. The result of this test is shown in Figure 5.19, where a linear relation of 134 ADU/K is determined. Such dependence of the bias on the temperature establishes a requirement of thermal stabilization according to the following reasoning: for long exposure times in the spectroscopy mode it is desired to keep the bias deviation under the 10% of the readout noise. If the CDS readout noise is less than 5 ADU (see section 5.5.6) then, the upper limit of the variation of bias should be 0.5 ADU; from the “ADU to Kelvin” relationship estimated, it represents a maximum temperature variation of ± 0.004 K.

We attempted to measure the bias stability, however it was not easy due to the *reset anomaly*. An indirect method to estimate the bias variation relies on the assumption that, the second read and

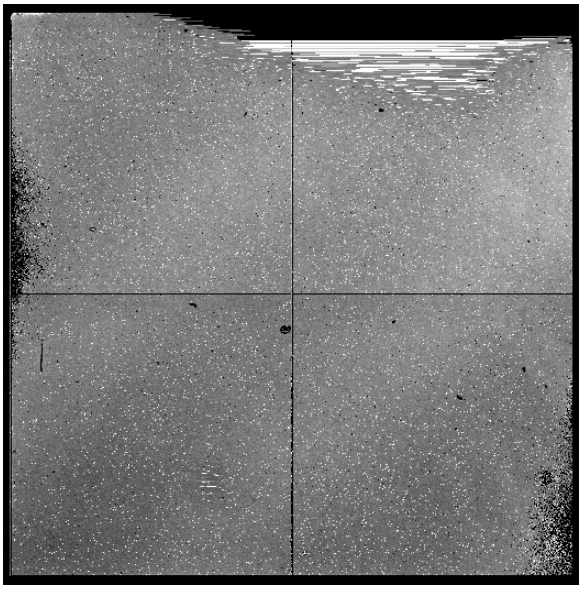

Figure 5.16: Raw flat-field image at *J*-band

the rest are not affected by the reset anomaly in the *ramp* mode. It also assumes that the deviation from the theoretical linear response is the combination of the readout noise and the variation of the bias. The dark images were used to apply this method; they were taken at LN_2 temperature. As can be seen in Figure 5.20 the residuals found are within ± 5 ADU, from which the highest contribution is the readout noise. Thus, the bias variation is almost negligible at the LN_2 temperature, where the thermal stabilization is about ± 0.003 K.

5.5.4 Gain

The determination of the detector gain establishes the relationship between the electrons generated at the detector and the signal measured in ADUs at the resultant image. The gain determination has greater importance for instrumental analysis rather than for scientific observations, because the latter are rarely calibrated in terms of the absolute conversion between the incident flux and the obtained ADUs; instead, they are calibrated relative to a standard star. Therefore, the gain is mainly important to determine, in electrons, the readout noise and the full well and, to use this value to compare with the values given by the detector manufacturer.

It is not easy to determine the gain in a consistent manner. I have tried several methods to measure and all of them change up to a 20% if the image region or the series of images are changed. I present here the two methods that are most commonly used: the first is the called "Photon transfer function" and, the second is the one from the IRAF package FINDGAIN.

A small region free of bad pixels (see section 5.5.8) was selected at each quadrant of the detector in order to compute both methods. These regions listed in Table 5.10.

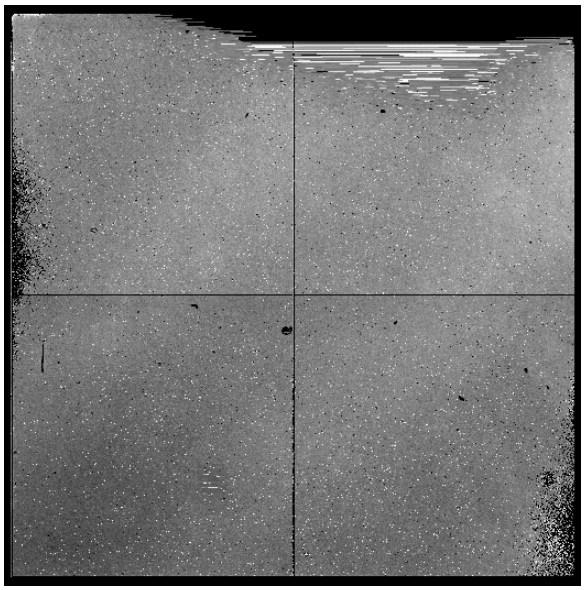

Figure 5.17: Raw flat-field image at *H*-band

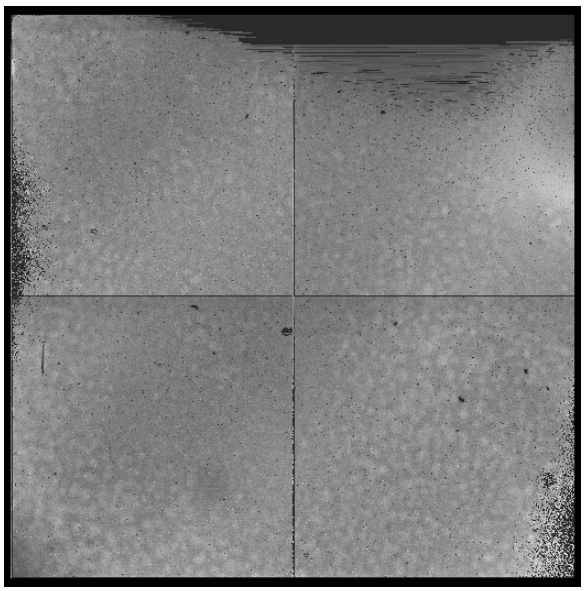

Figure 5.18: Raw flat-field image at *Ks*-band

Table 5.10: Regions free of bad pixels

Quadrant	Region [x_{ini}:x_{end}, y_{ini}:y_{end}]
I	[181:190,788:797]
II	[847:856,693:702]
III	[249:258,114:123]
IV	[730:739,149:158]

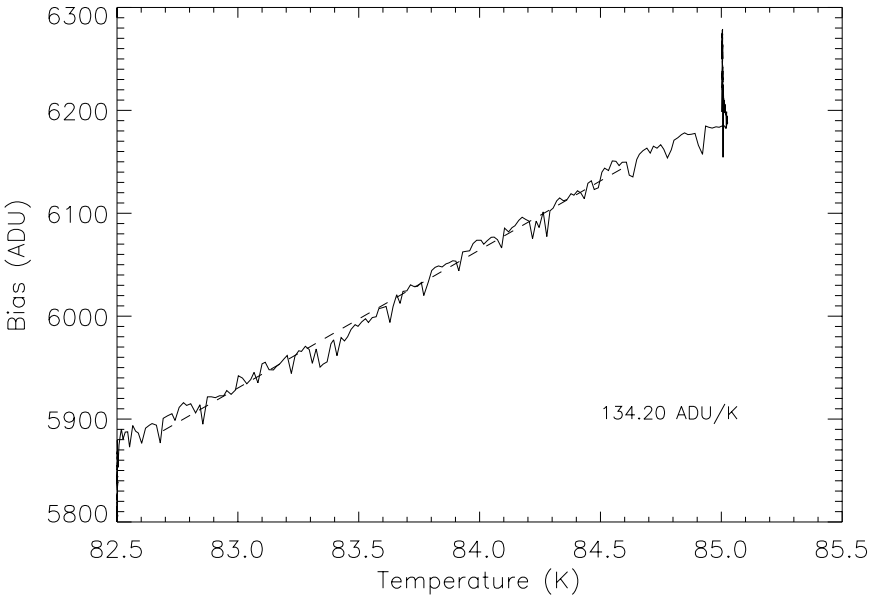

Figure 5.19: Bias as function of temperature. An increment of the detector temperature was controlled from 82.5 to 85 K.

Photon transfer function

The "Photon transfer function" method, as described in McLean (1989) is based on the idea that the two dominant noise sources in a flat-field image are the photon shot noise (P) and the readout noise (N). Therefore the total noise (N_{tot}), expressed in ADU can be approximated to:

$$\left(\frac{N_{tot}}{g}\right)^2 = \left(\frac{P}{g}\right)^2 + \left(\frac{N}{g}\right)^2 \tag{5.7}$$

where N_{tot}, P and N are given in electrons and g is the detector gain.

The left term in equation 5.7 can be computed as the *variance* (V) expressed in ADU. The photon shot noise is $P = \sqrt{gS}$, where S is the signal measured in ADU (i.e. it is scaled by the gain to obtain P in electrons). Therefore, equation 5.7 is reduced to:

$$V = \frac{1}{g}S + \left(\frac{N}{g}\right)^2 \tag{5.8}$$

which is a linear relation between the variance and the signal of the image: the "photon transfer curve". This curve is constructed with several images (i.e. flat-field exposures) of a constant source of illumination, while increasing the exposure time. These images have to be *flat-fielded* to remove the pixel to pixel variation, which would increase the value of the *variance*. The drawback of this method is that it is sensitive to the flat-field used.

To compute the "photon transfer curve" of the engineering detector we took series of 15 flat-field images at J-band, illuminating with the black body at 200°C. Several exposure times were

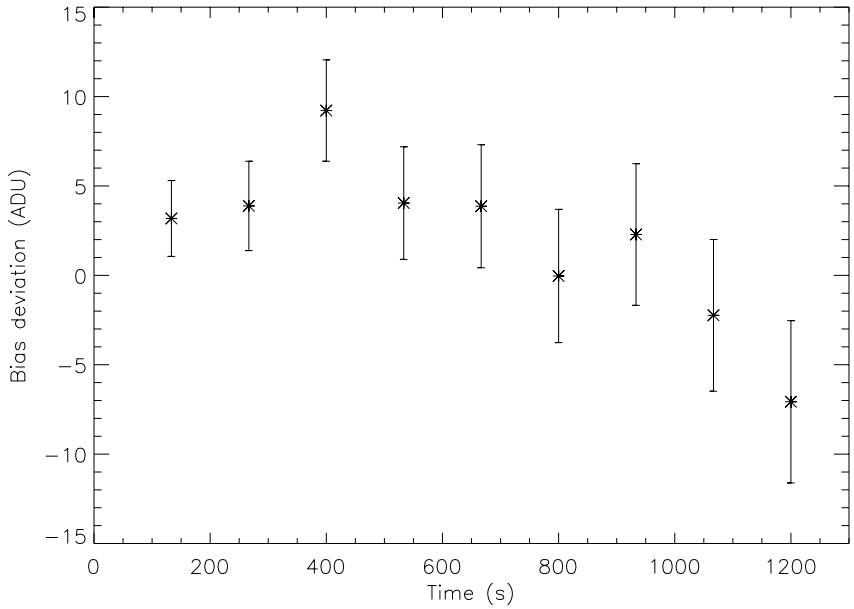

Figure 5.20: Bias variation at stable temperature conditions estimated from the residuals to the linear fit. The error bars represent the noise (readout and photon shot) at each read. The reads are taken from the fit to dark images in *ramp* mode, so that, the longer exposure reads have higher photon shot noise.

taken to increase the signal level. One of these series was used to construct a "flat" to flat-field the other series. The resultant curve for a small region of each quadrant of the engineering detector is shown in Figure 5.21; the estimated gain value is given from the slope of the line.

Findgain method

The method used in FINDGAIN[5] is based on an expression called the "Janesick's method" (Janesick, Evans, & Elliott 1987) developed for CCDs to determine the gain using a pair of flat-field and bias images (or image sections). The basic principle of the formulae is the noise in electrons:

$$N_{tot}(e^-) = g \times N_{tot}(ADU) \tag{5.9}$$

where g is the gain. Then, after an error propagation analysis, the expression for the gain, given in electrons per ADU, is:

$$g = \frac{(mean(flat1) + mean(flat2)) - (mean(bias1) + mean(bias2))}{(sigma(flat1 - flat2))^2 - (sigma(bias1 - bias2))^2} \tag{5.10}$$

where $flat1$ and $flat2$ are two flat-field images no-bias corrected, and $bias1$ and $bias2$ are two zero length dark exposures. For the the IR detectors, the bias frame is the first read in the shortest dark

[5]This IRAF package is included in NOAO.NPROTO

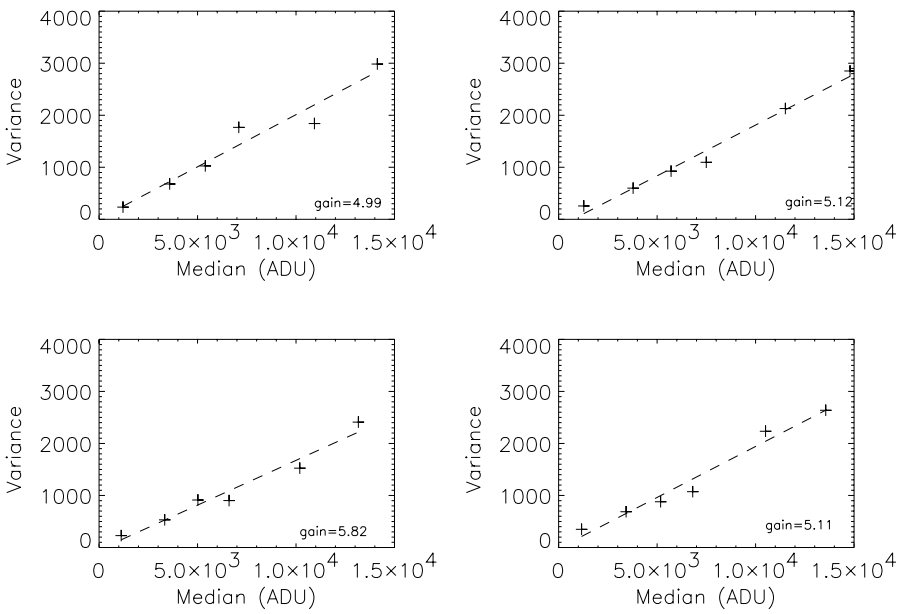

Figure 5.21: Photon transfer curve of the detector. The gain is estimated from the slope of the line, given in electrons per ADU

Table 5.11: Gain [e^-/ADU] at the four quadrants computed with the FINDGAIN method.

Region	I	II	III	IV
small 1	4.9	5.4	6.6	5.9
small 2	5.5	5.8	6.3	7.3
large 1	5.9	5.6	5.9	6.2
large 2	6.1	5.7	5.7	6.5

exposure in CDS mode and, the flat-field frame is the second read of an illuminated exposure. Both frames must be selected from the same region of the detector.

Being extremely simple to compute, this method however, presents high uncertainties if the image region is changed within the same quadrant. Table 5.11 shows a comparison of four different regions, two in small areas free of bad pixels (called *small*) and two including a large area in the quadrant (called *large*). The regions 1 and 2 are for different exposure times. It can be seen that the uncertainty is ~ 0.5 ADU between the two regions.

Being aware of these discrepancies in the gain determination, a value of 5 ± 0.5 e^-/ADU is assumed for the subsequent calculus such as the noise and dark current.

5.5.5 Linearity

The linearity curve gives a measure of what portion of the detector-well responses linear to the photon flux. The main nonlinearity cause is the change of capacitance produced by the discharge the

reverse biased of the photodiodes as a consequence of photon detection, an intrinsic characteristic of infrared arrays. We determined the linearity curve taking series of images with different exposure times. The images are flat fields at *J*-band, illuminating with the black body at 200°C.

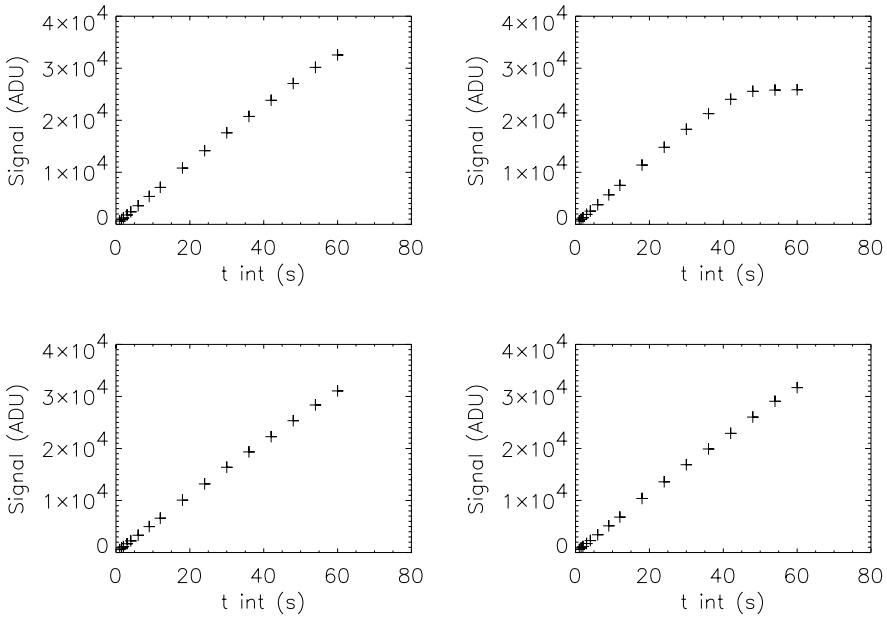

Figure 5.22: Linearity curve from CDS mode images.

As it can be seen in Figure 5.22, the quadrant III saturates at a lower level than the others. One possible reason for this, is the large defect of the quadrant itself. Other possibility is that this quadrant is behaving well and it saturates a few thousands of electrons above the detector-well specification of 100,000 e^-, and that the other three quadrants present exceptionally deep detector-wells (more than 150,000 e^-).

To estimate the linearity error, the residuals of the linear fit are represented as the percent of the fit value and plotted as a function of the signal. The plot is showed in Figure 5.23, from which it can be determined that three quadrants are linear within 2% from 1000 to 20,000 ADU (5000 to 100,000 $\pm$10,000 e^-); the quadrant III is limited to 15,000 ADU (75,000 $\pm$7,500 e^-). This curve is in agreement to the figure 8.12 in McLean (1989), that presents the typical nonlinearity of infrared arrays.

5.5.6 Readout noise

As it was seen with the multiplexer, the readout noise is the result of several noise sources. During the engineering detector tests, several readout noise measurements were performed to obtain a confident value. One of these measurements is shown in Figure 5.24, which involves the readout noise (N) estimation over 40 consecutive images acquired in CDS mode; the typical value is 3.05 ADU (15.2 $\pm$1.5 e^-, with the gain estimated in the previous section). To investigate why this value is greater than the obtained with the multiplexer, we measured the readout noise in several conditions.

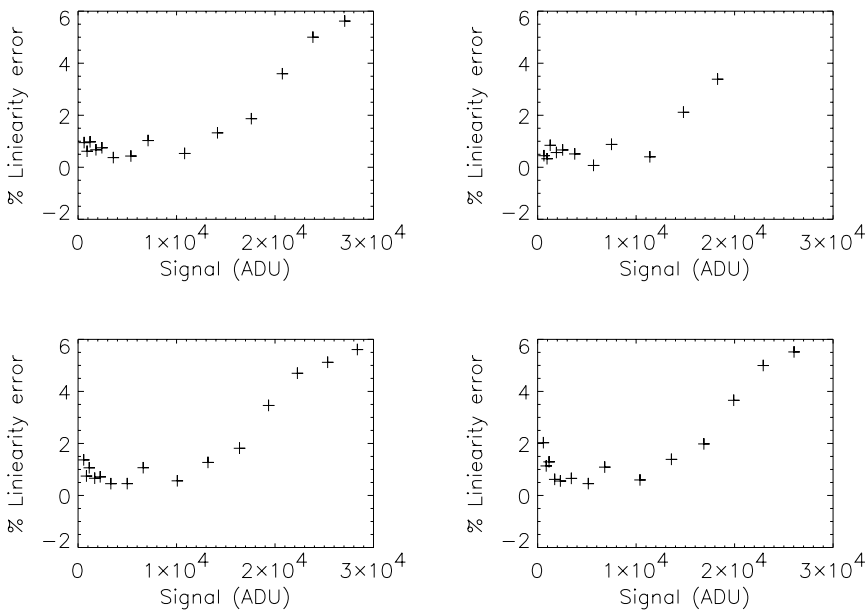

Figure 5.23: Linearity error from CDS mode images.

Table 5.12 summarizes the results of these tests. It can be seen that, either at LN_2 temperature or with the temperature controller set at different values, the readout noise keeps the typical value; however, a significant noise reduction is obtained when the temperature sensors are disconnected. We have confidence that this noise contribution can be eliminated shielding the sensor's wiring. Additional tests were done with the engineering detector turned off; the result of these measurements revealed that a great percentage of the noise was introduced by the detector, since the electronics showed less than 1.5 ADU (7.5 e^-) of readout noise.

The mean readout noise given by RSC is 0.07 mV, that would represent from 10.2 to 20.6 e^- (considering the specified gain range of 3.4 to 6.8 $\mu V/e^-$).

The use of multiple reads reduce the detector readout noise, as described in section 5.2.3. Several tests with the MNDR mode were performed for m values of 2, 4, 8, 12, 16 and total exposure times of 25 s. Figure 5.25 shows the results of how the readout noise can be reduced significantly. The crosses represent the noise in function of m and the dashed line is the theoretical noise reduction for this mode. The dark current noise is subtracted (i.e. the square root of the squares subtraction) from the data points. It can be seen that $N_{MNDR} \approx 5$ e^- is reached for $m = 16$. Although, the data for quadrant I follows the predicted behavior, there are small discrepancies at the other quadrants for high values of m.

I inspected the images searching for a noise pattern similar to that identified in the images of the multiplexer. No pattern was evident; however, it can be hidden by the readout noise, since the noise level was higher.

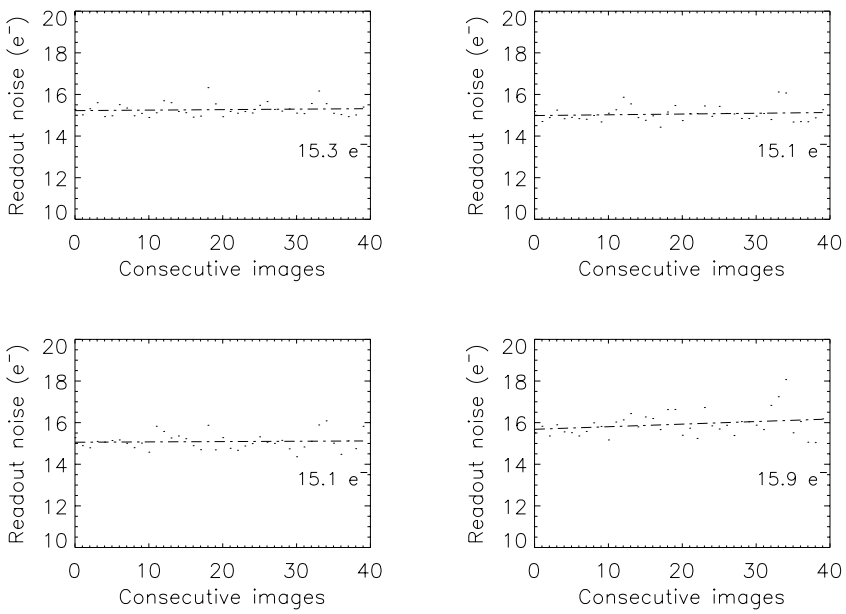

Figure 5.24: Readout noise estimated from 40 CDS mode images with the temperature sensors disconnected. The values are expressed as the readout noise of a single read, (N).

5.5.7 Dark Current

The dark current is the generation of electrons due to the recombination of electron-hole pairs at the semiconductor. This parameter is a function of the temperature and integration time. Since the expected value is lower than 1 e^-/s, the tests require long exposure times in order to be over the readout noise.

For the determination of the dark current in the engineering detector it was tested at a temperature of 82.0 K with the cold black slide placed in front of the detector. A series of 1200 s exposure time images were acquired in *ramp* mode with 10 sample points. The result from the dark tests is shown Figure 5.26. As it can be seen, the estimated value of the slope of the linear fit is around 0.74 e^-/s. This value of dark current is higher than that given in the RSC measurements (0.08 e^-/s). The RSC is determined at LN_2 temperature, and we believe that this difference in temperature is the main reason of the discrepancy of the values. The high dependence of the dark current on the temperature is reported by Finger & Nicolini (1998a).

5.5.8 Bad pixels

To identify the bad pixels in the detector a series of flat-field images were acquired. These images are quasi-uniformly illuminated with a signal at half dynamic range ($\gtrsim$10000 ADU) according to the linearity curve as determined in section 5.5.5. The **good pixels** are those that deviate less than 5σ from the typical value (i.e. the center of the gaussian fit to the distribution of the data) of the pixels at each quadrant.

The **bad pixels** are identified as those that deviate more than 5σ and are classified as: “hot” for

Table 5.12: Readout noise in electrons in the four quadrants at different configurations of the temperature controller. The values are expressed as the readout noise of a single read, (N).

	I	II	III	IV
LN_2 temperature	17.90	18.80	18.08	17.74
Controlled temperature at 82.5 K	17.30	17.89	17.39	17.08
Controlled temperature at 84.3 K	17.21	18.16	17.47	17.26
Controlled temperature at 84.4 K	17.12	18.18	17.55	17.37
Controlled temperature at 84.5 K	17.51	18.45	17.76	17.60
Temperature sensors disconnected	15.10	15.88	15.28	15.08
Detector OFF	10.07	9.44	9.69	9.79

Table 5.13: Bad pixel quantities and percentages for each quadrant.

	I	II	III	IV
Hot	2873 (1.1%)	4973 (1.9%)	3097 (1.2%)	3589 (1.4%)
Dead	4697 (1.8%)	11453 (4.4%)	17615 (6.7%)	35922 (13.7%)
Total	7570 (2.9%)	16426 (6.3%)	20712 (7.9%)	39511 (15.1%)

the pixels that deviate over the typical value, and “dead” for those that have no response or that are below the typical value. Table 5.13 lists the quantities and percentages of bad pixels hot, dead and total. Note that the quadrant III is the one that has the large value due to the dead pixels region at the top of the quadrant (see Figure 5.28). As it can be seen in the mask of bad pixels (hot and dead) in Figure 5.29 and in Table 5.13, dead pixels are the most common type of bad pixels.

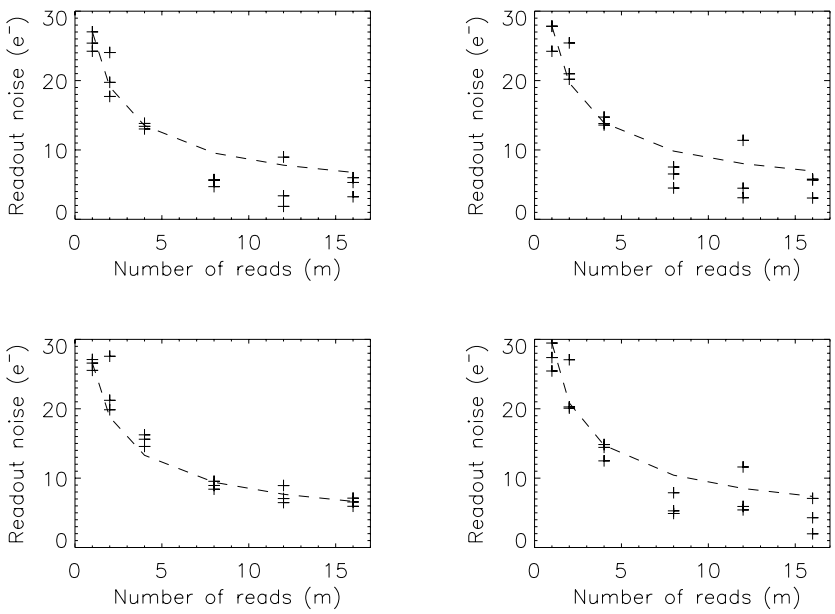

Figure 5.25: Readout noise as a function of the number of read in MNDR mode. The crosses represent the readout noise measured at each value of *m* and the dashed line is the theoretical readout noise as function of *m*.

5.5.9 Shift registers glow

The HAWAII detectors present a glowing produced by the electroluminiscence of the shift registers in the multiplexer. This effect is seen when the registers warm up as a consequence of continuous working, such as when the MNDR mode is used with a high value of *m*. A first approach to identify was carried out reading the detector three consecutive times with the lowest possible exposure time and employing the MNDR mode with *m*=16. The result, shown in Figure 5.27 has the glow effect at the lower-central corner of quadrants I and II. It is also seen at the lower-outer corner in quadrant II. According to the reports of Hodapp et al. (1996) and Finger et al. (2000), the glow should be also seen in the upper corners of quadrants III and IV, due to the physical location of the shift registers circuits. Unfortunately, the large bad pixel region in those quadrants hides the glow effect.

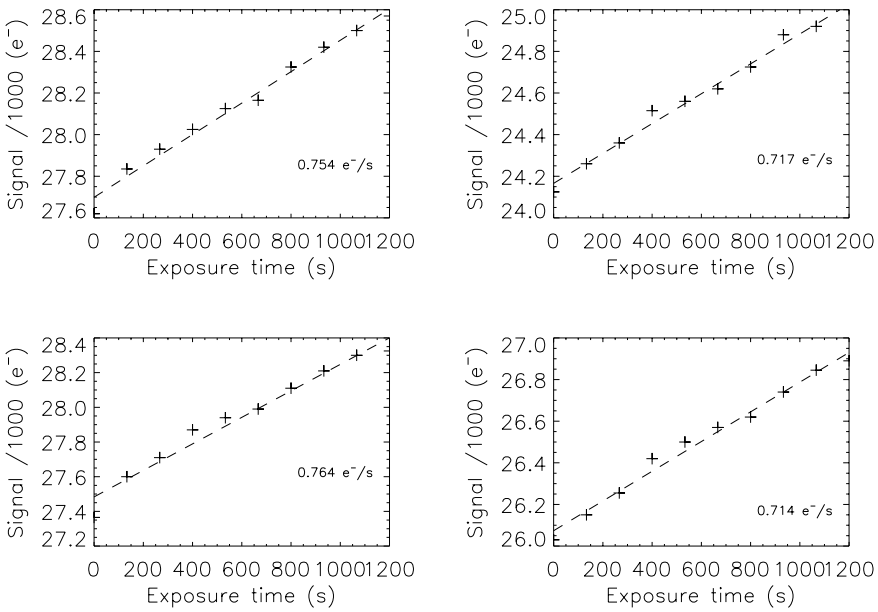

Figure 5.26: Dark current determination from 1200 s exposure time images in *ramp* mode

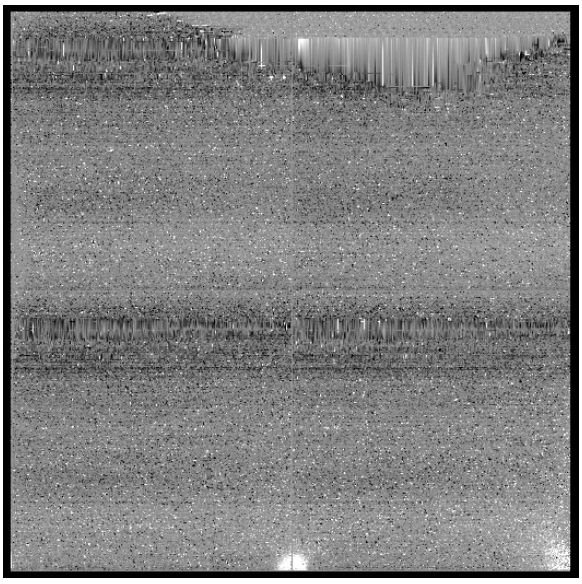

Figure 5.27: Glow from the shift registers observed in a MNDR mode image with m=16. The glow at the top can not be seen due to the bad pixels.

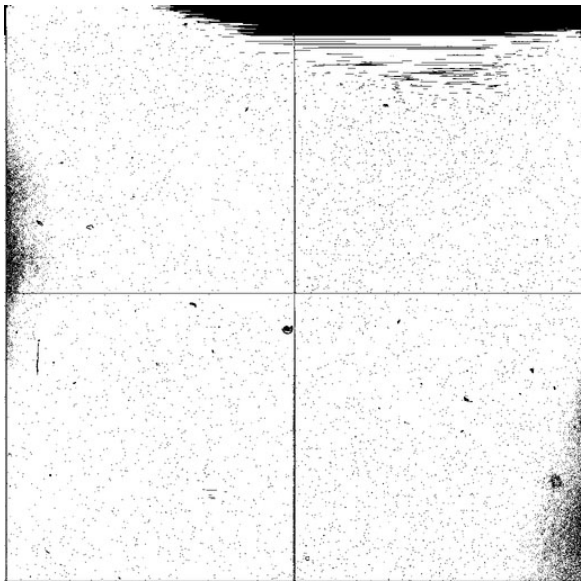

Figure 5.28: Bad pixel mask: dead pixels

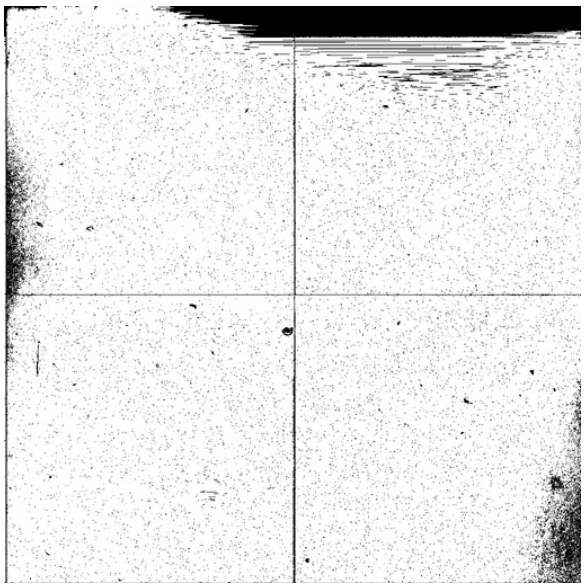

Figure 5.29: Bad pixel mask including dead and hot pixels

5.6 Scientific detector characterization

We cooled down the scientific detector for the first time in the beginning of November 2001. The characterization plan was essentially the same than that followed with the engineering grade detector. Besides to the standard properties measured to the engineering detector, some others were studied with the scientific one, such as the first read anomaly, the crosstalk and the persistence (see Domínguez-Tagle, Acosta-Pulido, & Ballesteros 2002). .

The first light image of the scientific grade detector, shown in Figure 5.30, was taken in *J*-band with an USAFR reticle and the *black body* at 400°C. A flat-field image from each filter was acquired illuminating the detector with the *black body* through the *pin-hole*. As seen on section 5.5.2, the filters presented some spots or filter defects. To avoid these spots, a series of flats were acquired moving the filter (similar to the *dithering* observational technique, but moving the filter instead of the telescope). The 14 images from the series were *median* combined to obtain the image (free of filter defects) that is shown in Figure 5.31. This image in *J*-band shows the main detector cosmetic defects: the border of the array, two small scratches on quadrant III and a series of spots going from quadrant I to III. Such defects will be discussed in section 5.6.5.

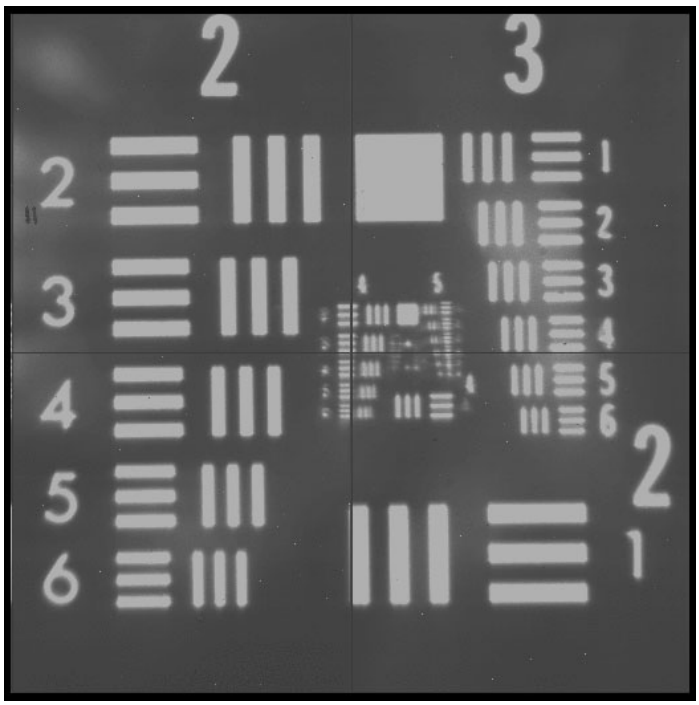

Figure 5.30: Scientific detector *J*-band raw image of the USAFR reticle.

5.6.1 Gain

As it was seen on section 5.5.4 there are two methods to compute the gain of the detector, the *findgain* and the "photon transfer curve". The main problem to overcome is to achieve a good and flat illumination. We acquired a series of "flats" by illuminating the array with the *black body* (at a temperature of 400°C) through the *pin-hole* to obtain an uniform illumination.

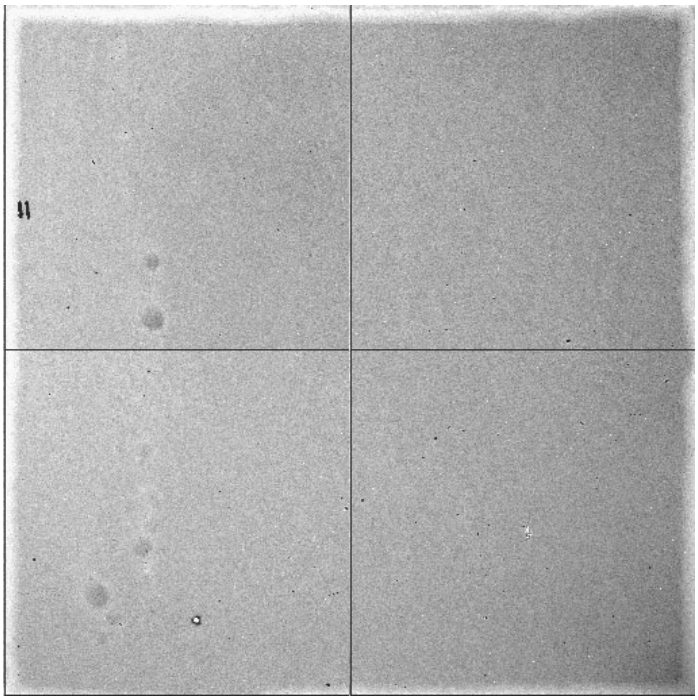

Figure 5.31: Scientific detector *median* combined flat image in *J*-band.

Table 5.14: Regions for the calculus of gain.

Quadrant	Region [x_{ini}:x_{end}, y_{ini}:y_{end}]
I	[200:250,200:250]
II	[600:650,200:250]
III	[200:250,800:850]
IV	[600:650,550:600]

I constructed a "photon transfer curve" for each quadrant using a region of 50 $\times$ 50 pixel (see Table 5.14), as shown in Figure 5.32. The images are *flat-fielded* to remove the pixel to pixel variation, as described in McLean (1989). The mean gain-value for the four quadrants is 4.5 $\pm$0.3 e^-/ADU. This value is, as expected, very similar to the determination in the engineering detector; the error represents the standard deviation of the measurements using different sets of images.

5.6.2 Linearity

The "linearity curve", shown in Figure 5.33, was constructed with flat field images at *J*-band, illuminating with the black body at 200 °C. As it can be seen in the figure, the four quadrants behave similarly, saturating over 35,000 ADU (157,000 $\pm$10,000 e^-).

The linearity error, is estimated as described in section 5.5.5. The linearity error plot is shown in Figure 5.34, from which it can be determined that the whole array is linear within 2% from 1000 to 25,000 ADU (4500 to 110,000 $\pm$10,000 e^-). The nonlinearities at low values migth be produced

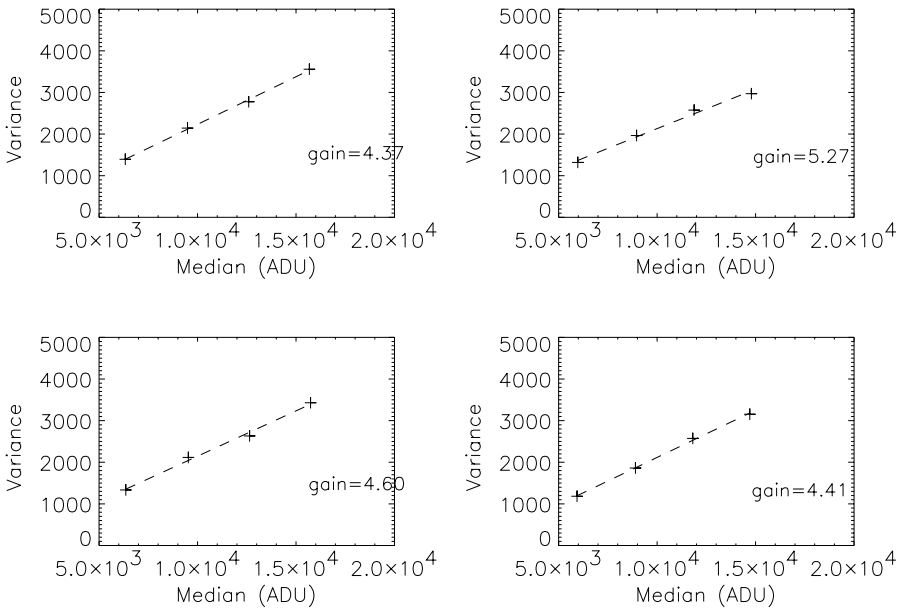

Figure 5.32: Photon transfer curve of the scientific detector. The gain is estimated from the slope of the line, given in electrons per ADU.

by the offset problem described in next section.

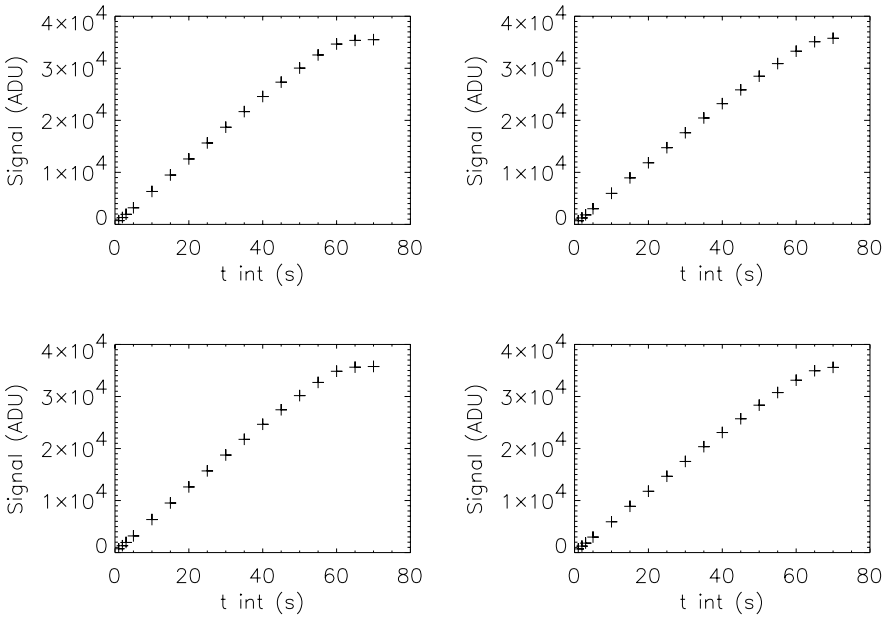

Figure 5.33: Linearity curve from CDS mode images.

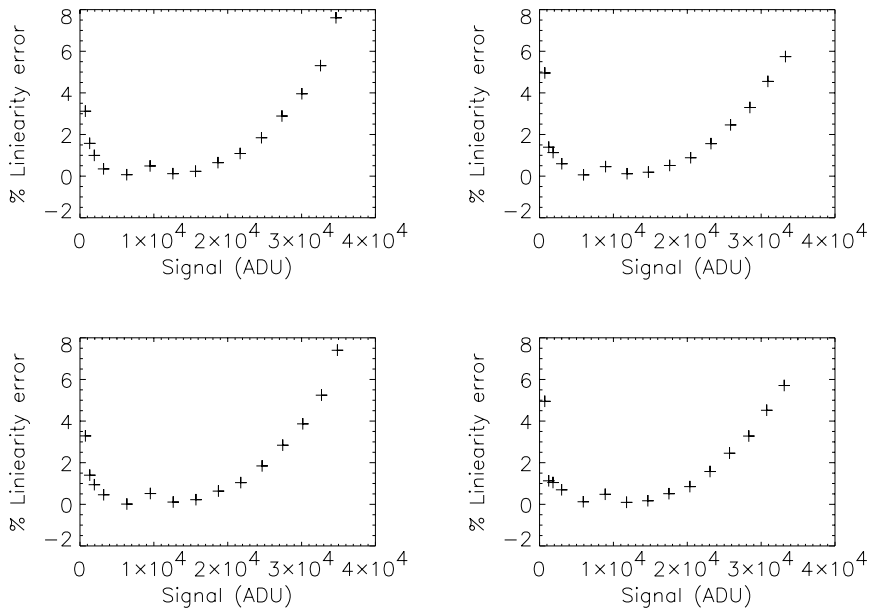

Figure 5.34: Linearity error from CDS mode images.

5.6.3 Readout noise

The readout noise measurement was performed in a similar manner than with the engineering detector. Figure 5.35 shows the noise (N) measured in CDS mode images with t_{int}=1 s. It was estimated from the image regions listed in Table 5.15 due the fact that the images presented a signal pattern with a level up to 50 ADU. From the high noise value it is evident that the images present some problem. One of these 1 s dark images is shown in Figure 5.36; the median signal level is around 100 ADU.

Table 5.15: Regions for the noise estimation.

Quadrant	Region [x_{ini}:x_{end}, y_{ini}:y_{end}]
I	[30:180, 30:180]
II	[800:950,130:280]
III	[30:180,800:950]
IV	[630:780,830:980]

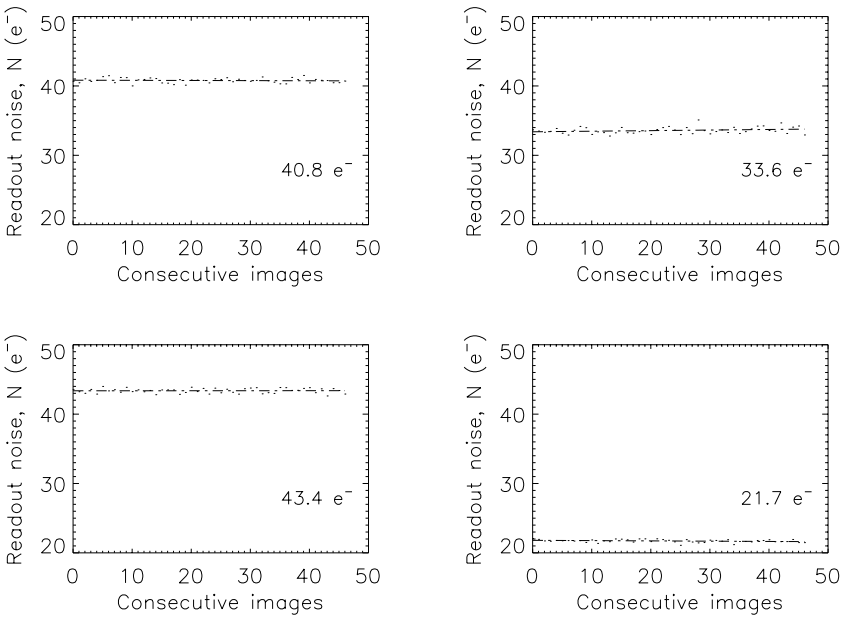

Figure 5.35: Readout noise estimated from 50 CDS mode images (t_{int}=1 s). The values are expressed as the readout noise of a single read, (N). The high noise value makes evident that the 1 s images present some problem (see text).

To study these offset and pattern effects, we acquired dark images with integration times from 1 to 50 s. First, the offset level diminishes as the integration time increases reaching a minimum around 15 s, as it can be seen in Figure 5.38. The noise behaves in the same manner reaching a minimum at integration times from 7 to 10 s (see Figure 5.39). The pattern disappears for integration

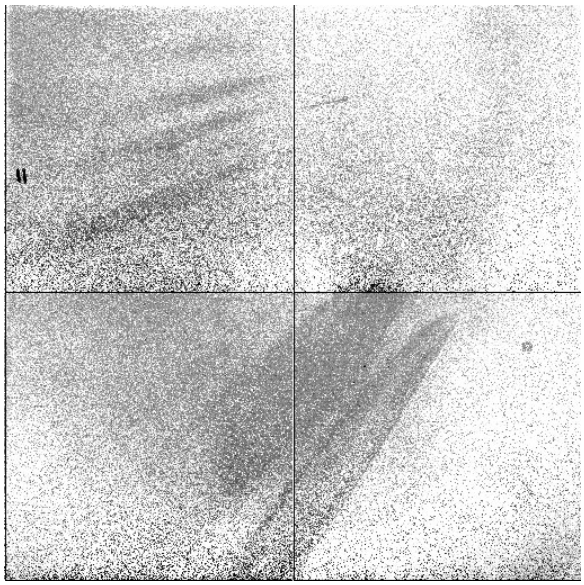

Figure 5.36: Scientific detector CDS mode Dark image with t_{int}=1 s

times greater than 7 s (e.g. the 10 s image in Figure 5.37). Although we think that this effect could be produced by the reset anomaly or by any perturbation introduced in the readout of the array, further studies will be required.

In order to estimate the readout noise without being affected by such “anomaly”, a series of 50 images with 10 s integration times was acquired. I measured the readout noise in these images following the criteria described in section 5.3.1. The result of the estimations can be seen in Figure 5.40. The readout noise, N is around 16 $\pm$1 e^-, that is a more reliable value and, as expected, similar to the value measured for the engineering detector, considering that the readout electronics are the same for both detectors.

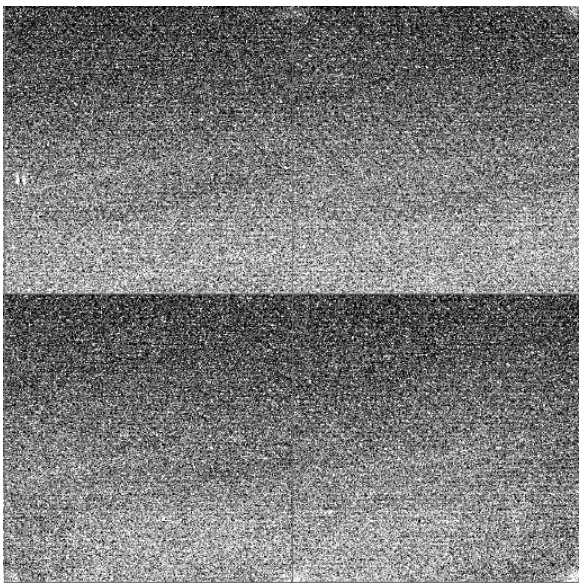

Figure 5.37: Scientific detector CDS mode Dark image with t_{int}=10 s

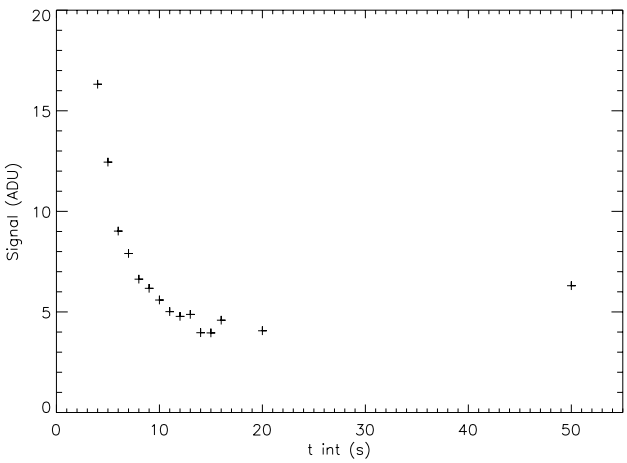

Figure 5.38: Offset as a function of the integration time (t_{int}) in CDS mode.

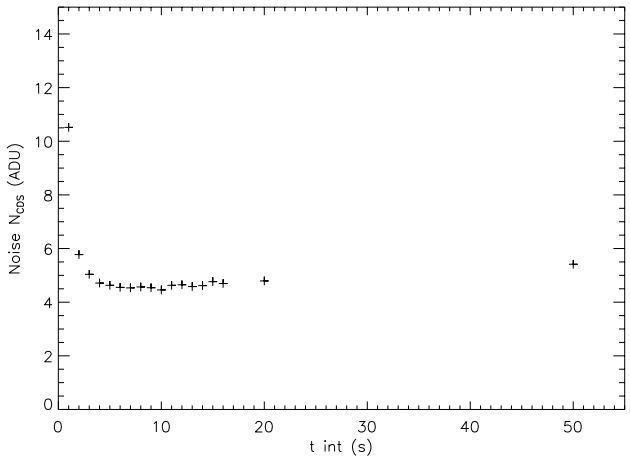

Figure 5.39: Readout noise as a function of the integration time (t_{int}) in CDS mode.

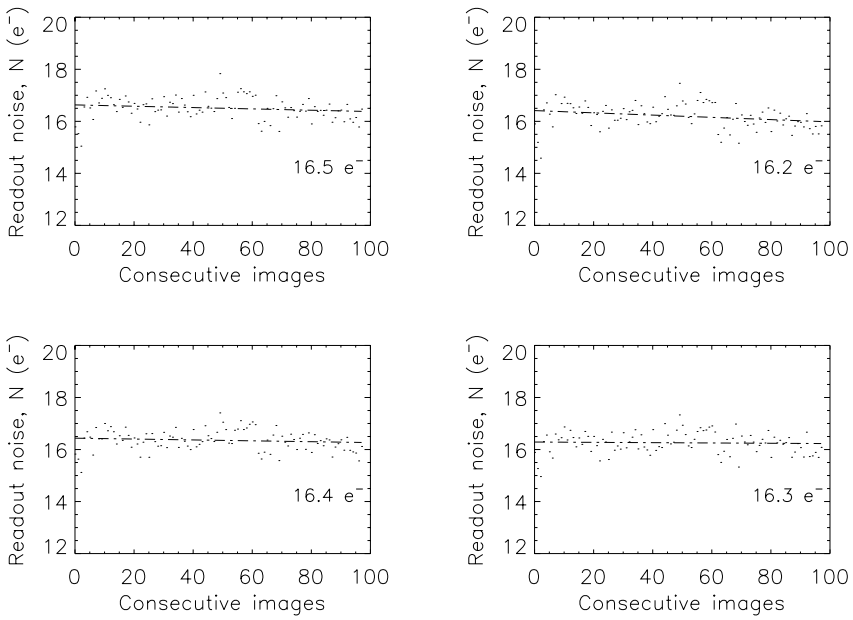

Figure 5.40: Readout noise estimated from 50 CDS mode images (t_{int}=10 s). The values are expressed as the readout noise of a single read, (N). This is a more reliable measurement than that in Figure 5.35

5.6.4 Dark Current

One of the most important requirements for the scientific detector is to have low dark current. For a first estimation, the detector was tested at a temperature of 83.0 K with the cold black slide placed in front of the detector. A series of 1200 s exposure time images were acquired in *ramp* mode with 10 sample points. The result from the dark tests is shown Figure 5.41. These graphs represent the median value of a 10×10 pixel region of the image. It can be seen that there are some uncertainties in the measurements. Other representation[6] of the detector dark current is an histogram with the dark-current-values of all the pixels in the array. Such representation is shown in Figure 5.42, where it can be seen that the central value is 0.065 e^-/s.

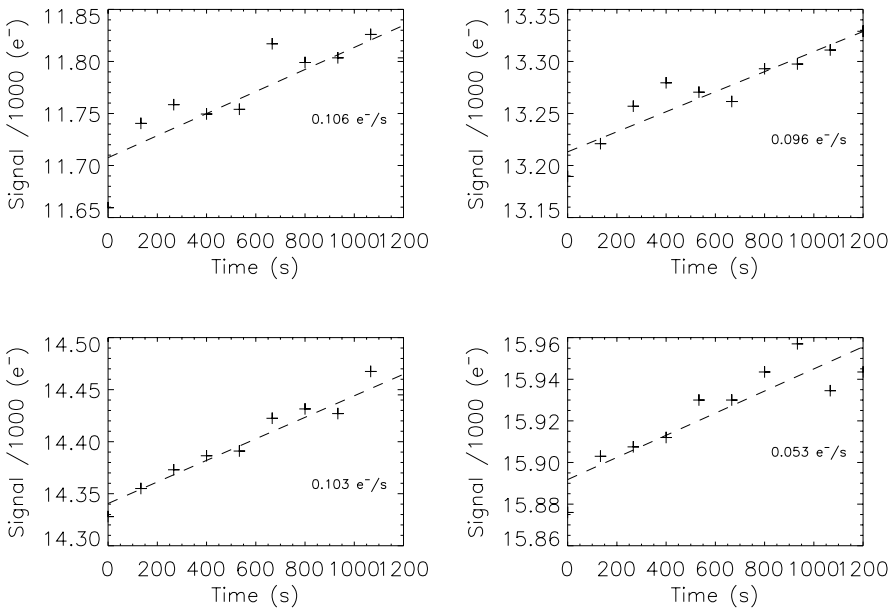

Figure 5.41: Dark current determination from 1200 s exposure time images in *ramp* mode.

5.6.5 Bad pixels

The identification of the bad pixels in the detector was carried out from two series of flat-field images, one series with low illumination and the other with high. The identification of the bad pixels is based on obtaining a linear fit to the low and high values of each pixel. The **good pixels** are considered as those that deviate less than 5σ from the typical fit value (i.e., those that are linear). Table 5.16 lists the quantities and percentages of bad pixels: hot, dead and total. Note that the quadrant III has the largest value; it is due to the hot pixels region at the border of the quadrant (see Figure 5.43). The complete bad pixel mask including dead and hot pixels is shown in Figure 5.44.

[6]The representation that RSC uses in the detector data sheets

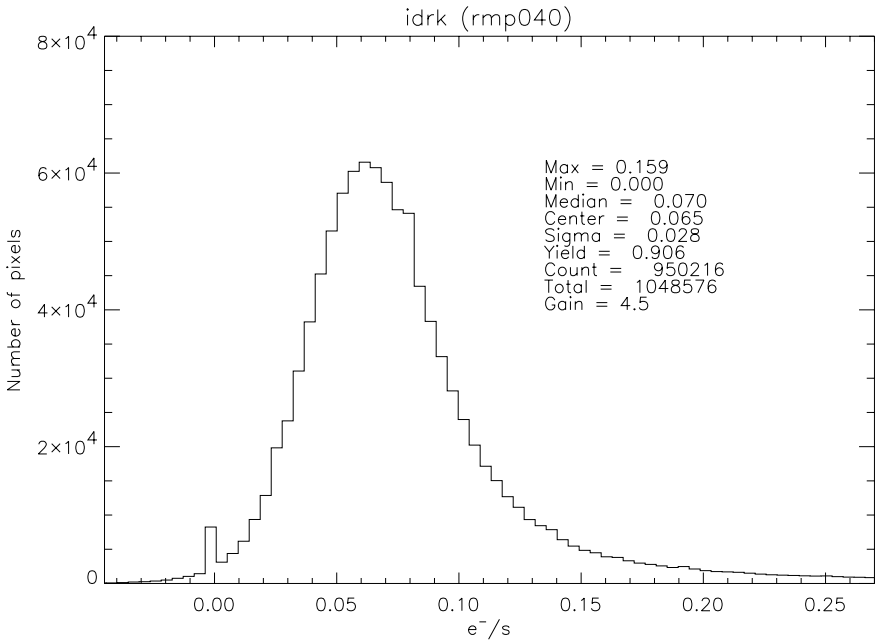

Figure 5.42: Dark current histogram

Table 5.16: 5σ bad pixel quantities and percentages for each quadrant.

	I	II	III	IV
Dead	1871 (0.7%)	2481 (0.9%)	2053 (0.8%)	1727 (0.7%)
Hot	2148 (0.8%)	691 (0.3%)	6504 (2.5%)	2134 (0.8%)
Total	4019 (1.5%)	3172 (1.2%)	8557 (3.3%)	3861 (1.5%)

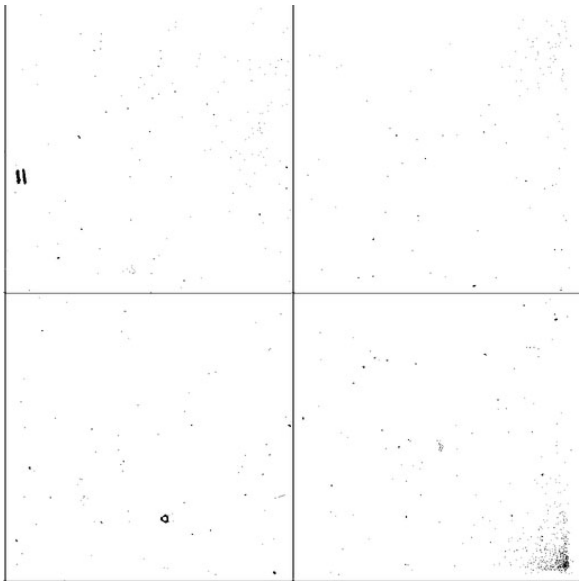

Figure 5.43: Bad pixel mask: dead pixels only.

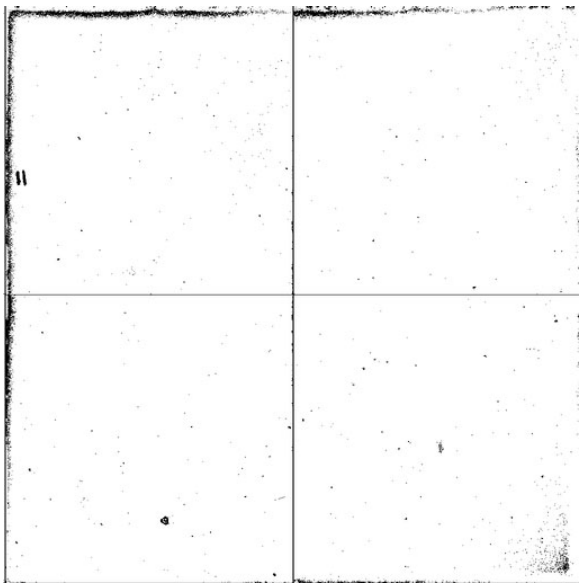

Figure 5.44: Bad pixel mask including dead and hot pixels.

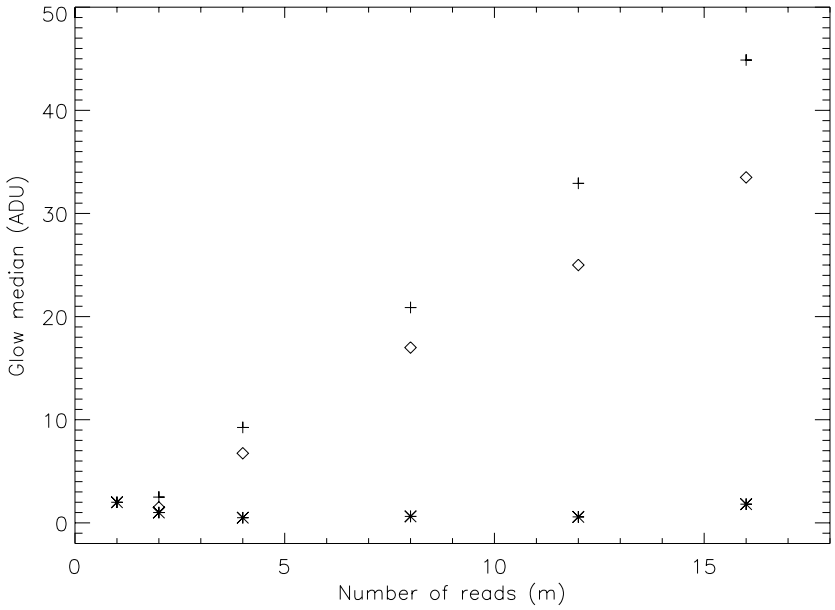

Figure 5.45: Shift registers glow in the scientific detector. The asterisks represent the nonglow-regions value, the diamonds represent the glow at the corners and the crosses, the glow at the central junction of quadrants.

5.6.6 Shift registers glow

The shift registers glow, described in section 5.5.9, is present in the scientific detector for images with a number of reads as low as m=2. A comparison between two 25 s images with different number of reads can be seen in Figure 5.46. The images were acquired with the cold black slide placed in front of the detector. The measured values of the glow as a function of m are shown in Figure 5.45. The asterisks represent the median value of a 100 pixel box in a nonglow-central region of the array, the diamonds are the glow at the corners and the crosses are the glow at the junction of quadrants I-II and III-IV. It is noticeable that the later type of glow is higher than that at the corners.

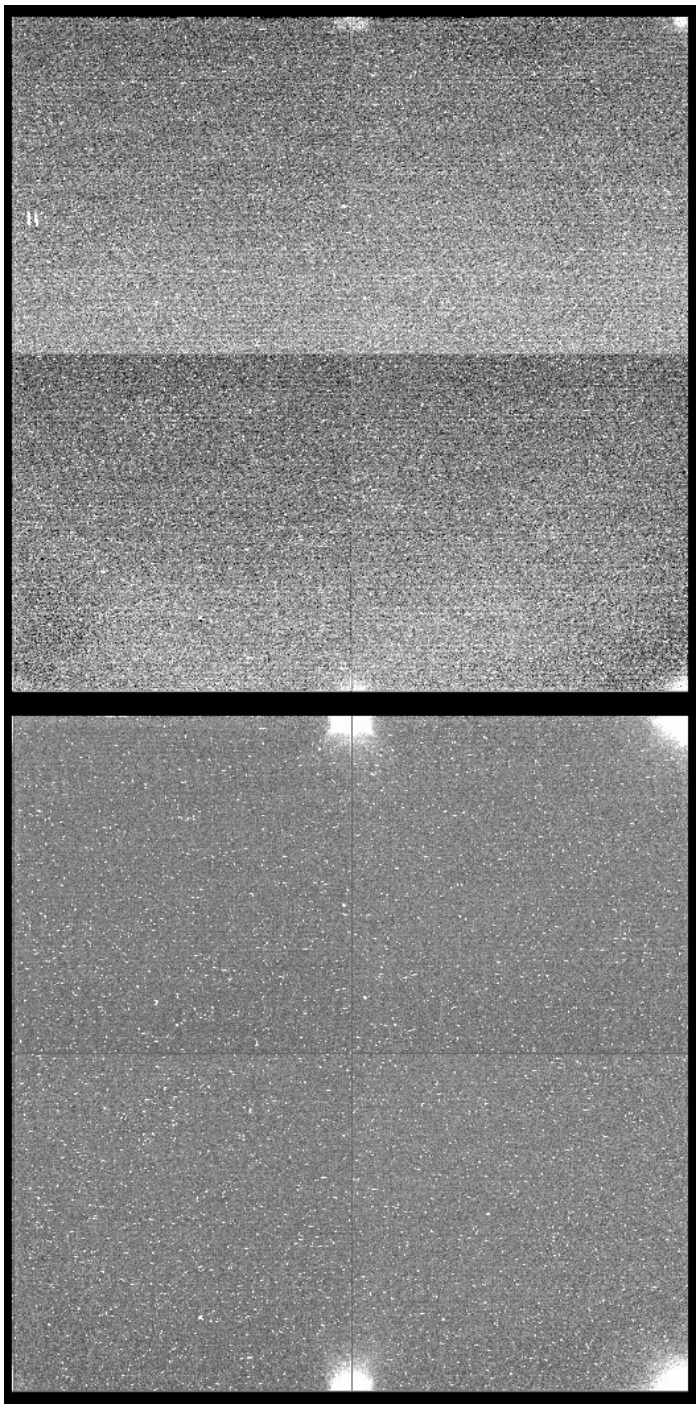

Figure 5.46: Glow effect in m=2 (top) and m=16 (bottom).

5.6.7 Crosstalk

The crosstalk mechanism is poorly understood within the scientific community, although it is assumed that it occurs in the multiplexer (Finger & Nicolini 1998b). This effect has two components, the interquadrant and the intraquadrant crosstalk. Both are produced when a region of the detector is exposed to bright illumination, then two "virtual images" appears in the detector, one in the same row of the vertically adjacent quadrants (interquadrant) and the other, dispersed along the same row (intraquadrant). As described by Finger & Nicolini, the intensity of a pixel (i,j) produced by row crosstalk can be modeled in the following manner:

$$I'_{i,j} = I_{i,j} + C_i + C_{i\pm 512} \tag{5.11}$$

where, $I_{i,j}$ is the real intensity, C_i is the intraquadrant crosstalk and $C_{i\pm 512}$ is the interquadrant crosstalk. The "$\pm$" applies according to the quadrant that has the real intensity. The crosstalk is given by:

$$C_i = \alpha \sum_{k=1}^{1024} I_{i,k} \tag{5.12}$$

where α is a coefficient that depends on the integrated intensity of all the pixels in the row i. The value estimated by Finger & Nicolini is $\alpha = 1.3 \times 10^{-5}$.

To characterize the crosstalk in the scientific detector, the image of a slit was created on it. Such image can be seen in Figure 5.47. The interquadrant effect is the series of brigth rows in quadrants III and IV. Since the slit orientation goes along the rows, the crosstalk has the maximum effect (i.e. there are a huge number of illuminated pixels in the row that are added together according to equation 5.12). The coefficient in such equation was determined from a series of images (similar to Figure 5.47) for the interquadrant and for the intraquadrant crosstalk effects. The derived values are:

$$\begin{aligned} \alpha_{inter} &= (1.34 \pm 0.4) \times 10^{-5} \\ \alpha_{intra} &= (8.05 \pm 0.4) \times 10^{-6} \end{aligned} \tag{5.13}$$

If the slit orientation goes along the columns, the crosstalk coefficients are the same, although the effect seems to be less evident due to the smaller number of illuminated pixels along the row. It, however, appears another effect that has not been reported. The image of the slit produces a "negative" crosstalk along the columns. This effect can be seen in Figure 5.48, and the coefficient is:

$$\begin{aligned} I'_{i,j} &= I_{i,j} - C_j \\ \alpha_{negative} &= 1.69 \times 10^{-6} \end{aligned} \tag{5.14}$$

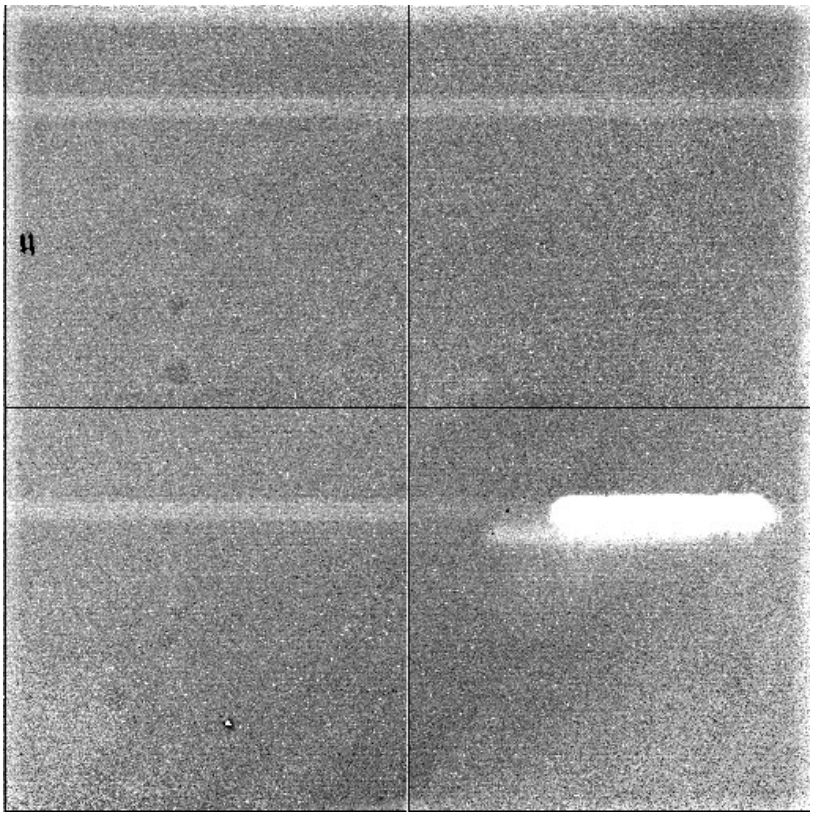

Figure 5.47: Slit image on the detector to characterize the crosstalk. The interquadrant effect is the series of bright rows in quadrants III and IV. There is also a ghost image of the slit (at the bottom-left of the slit) produced by the optics.

5.6.8 Persistence

The persistence is a "memory" effect that is present in the pixels whenever they are highly exposed (Finger et al. 1998). This memory is approximately 1% of the original intensity. The NICS manual recommends as many as 10 readouts to eliminate this effect, while Finger et al. (1998) reports that, when a pixel saturates, it takes up to 4 min for the effect to decay.

The initial tests with the scientific detector shows that this effect is very low and that it is only present in the first dark image after the one exposured. To perform this test, a bright image was created on the detector, a couple of images were acquired, then the cryostat entrance window was covered and a series of ten dark images was acqured. The illuminated regions of the image show a persistence only in the first dark image; none of the subsequent dark images shows persistence effects. The quantization of the persistence was performed over one line in the quadrants I and III, where the horizontal bars of the USAFR pattern are present (see Figure 5.30). The cut along the image column is shown in Figure 5.49, where the dotted line is the signal of the first dark image and the dash-dot line is the second dark. The solid line is the signal of the illuminated scaled to match the persistence signal. The scaled image is:

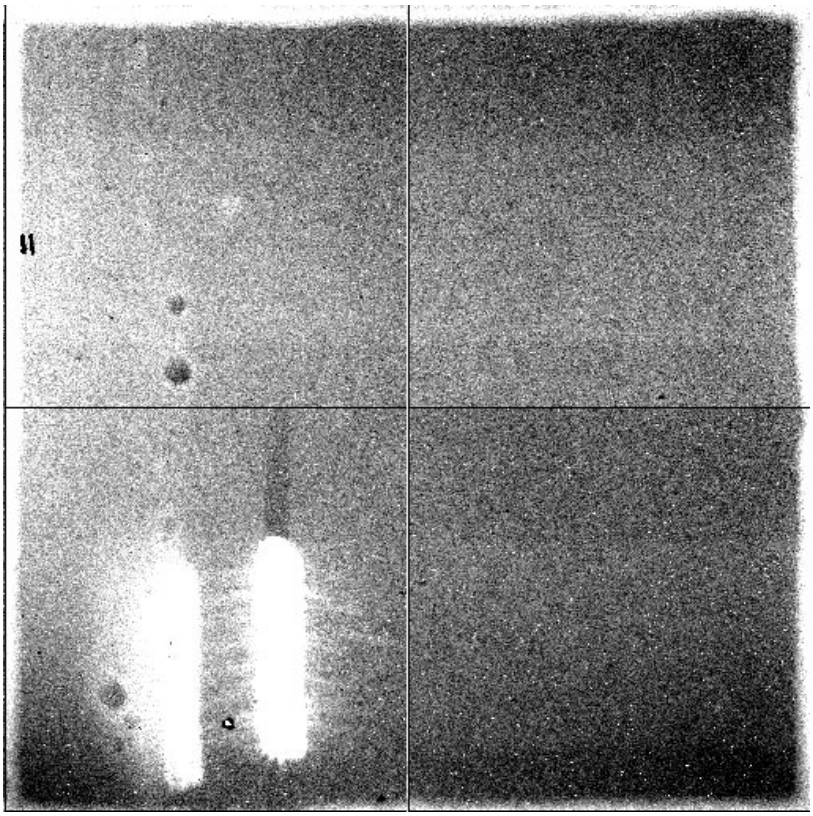

Figure 5.48: Slit image on the detector to characterize the negative intraquadrant crosstalk. There is also a bright ghost image of the slit (at the left) produced by the optics.

$$\text{scaled image} = \sqrt{\text{original image} + (75 * col)} \tag{5.15}$$

where *col* is the column number from 1 to 512. In general, the persistence does not represent more than the 1.3% of the original signal.

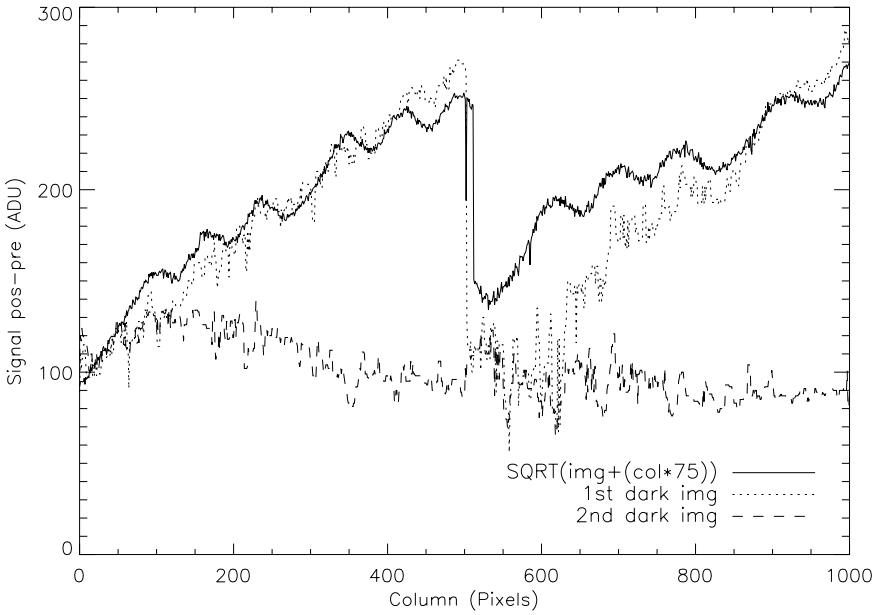

Figure 5.49: Measurement of the persistence including the original signal (scaled solid line) the first and the second dark image. Notice that only the 1^{st} dark image present a signal that follows the original profile.

5.7 Scientific detectors in other NIR instruments

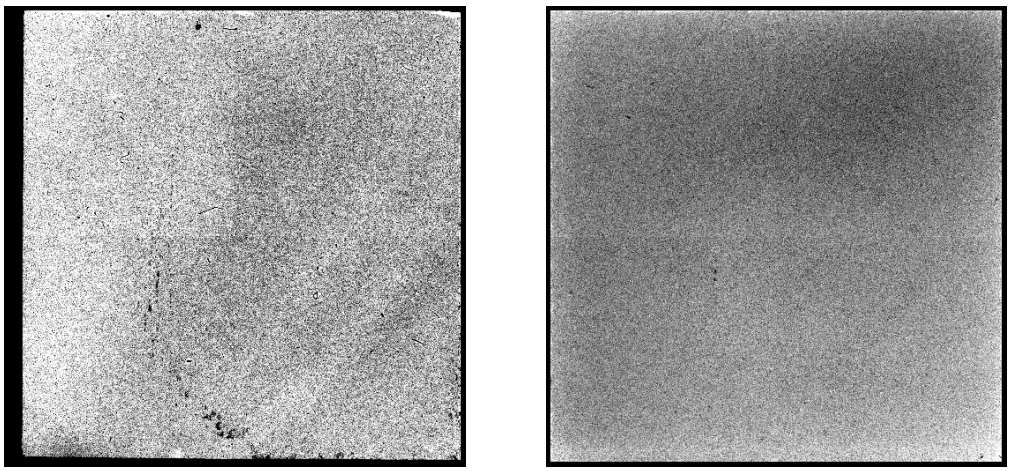

Figure 5.50: NICS (left) and Omega Prime (right) flat-field full images at *J*-band. Note that the NICS image is vignetted on left and bottom sides.

In order to illustrate the behavior of other scientific grade detectors, I present here a brief analysis of the HAWAII arrays in NICS and Omega Prime (see Chapter 1). The latter instrument is a near-infrared camera that was built by the same group than Omega Cass (i.e. the Max Planck Institute for Astronomy), so that the detector electronics are the same for both. The images for this review of detector properties were acquired at their respective telescopes, during daytime observing runs.

The parameters analyzed for these detectors are the quality of the flat images, the gain, the readout noise and the bad pixel mask. The bias stability, linearity, dark current, and readout noise in other modes are not determined due to the lack of appropriated images for these tests.

Flat-field. The flat-field *J*-band images of the two detectors can be seen in Figure 5.50, where is notorious the high "cosmetic" quality of the scientific grade detectors. Some of the marks of the NICS flat-field could be caused by some dirt on the filter.

Gain. The gain of the detectors was computed with the two methods described in section 5.5.4. For the detector of NICS, the gain computed with FINDGAIN goes from 8.0 to 8.4 e^-/ADU and the "photon transfer curve" are shown in Figure 5.51. The value given at the NICS' manual[7] is approximately 8 e^-/ADU.

The detector of Omega prime has a gain estimated in 3.3-3.7 e^-/ADU employing the FINDGAIN method. The "photon transfer curve", shown in Figure 5.51, gives a value of 4.1-4.3 e^-/ADU, which is almost the same that the one specified in the header of the images (i.e. the information added to the image by the observatory).

Readout noise. To determine the readout noise in the detector of NICS, a series of 50 images was acquired in CDS mode. A resultant readout noise $N \sim$ 10.1-14.6 e^- is estimated from the graphs shown in Figure 5.53.

[7] www.tng.iac.es/instruments/nics/nics.html

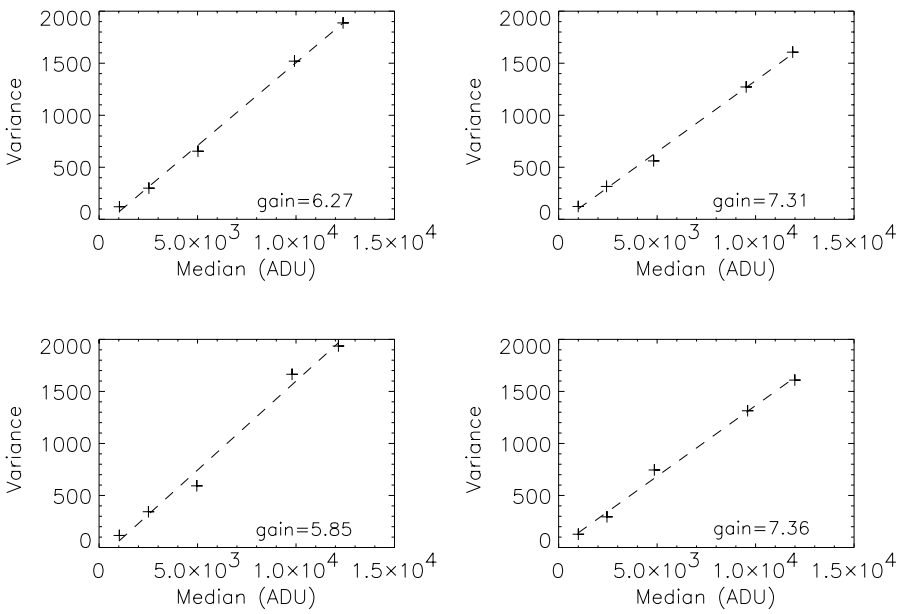

Figure 5.51: NICS detector photon transfer curve. The gain is estimated from the slope of the line, given in electrons per ADU.

The detector of Omega Prime has two different readout modes: the CDS mode and the "Full MPIA". The former is the common mode described in section 5.2.3, and the latter mode is an implementation of the *reset* to improve the observing efficiency reducing the overhead time[8]. In the "Full MPIA" mode, one line of the detector is read, then it is reset and read again. With this line-oriented technique the short consecutive images save up to 50% of the time wasted in the *reset* of the full frame. The drawback of this mode is the increase of the readout noise form $N \sim 10$ to 19 e^-, as shown in figures 5.54 and 5.55 for the CDS and "Full MPIA" modes respectively.

Dark current. As described in section 5.5.7, the determination of the dark current requires long exposure time images. From the set of images that I used for the analysis, only those of NICS are longer enough to make any estimation. The NICS detector is cooled to 78 K and, from the linear fit to a series of images with exposure times up to 150 s, a mean dark current can be estimated in 0.58 e^-/s, as shown in Figure 5.56.

Bad pixels. The bad pixel masks allows to estimate the "cosmetics" of the detector. As it was seen in section 5.5.8, the engineering detector has a large quantity of bad pixels (i.e. this problem took it out from being a scientific grade detector). The analysis of the detectors of NICS and Omega Prime brings the opportunity to review the "cosmetics" of the scientific grade detectors. The method to discriminate from *good*, hot and dead pixels is the same than that described in section 5.5.8. Figure 5.57 shows the bad pixels (dead and hot) masks for both detectors and tables 5.17 and 5.18 summarizes the values.

[8] this mode is explained at the Omega Prime manual: www.caha.es/instruments/oprime

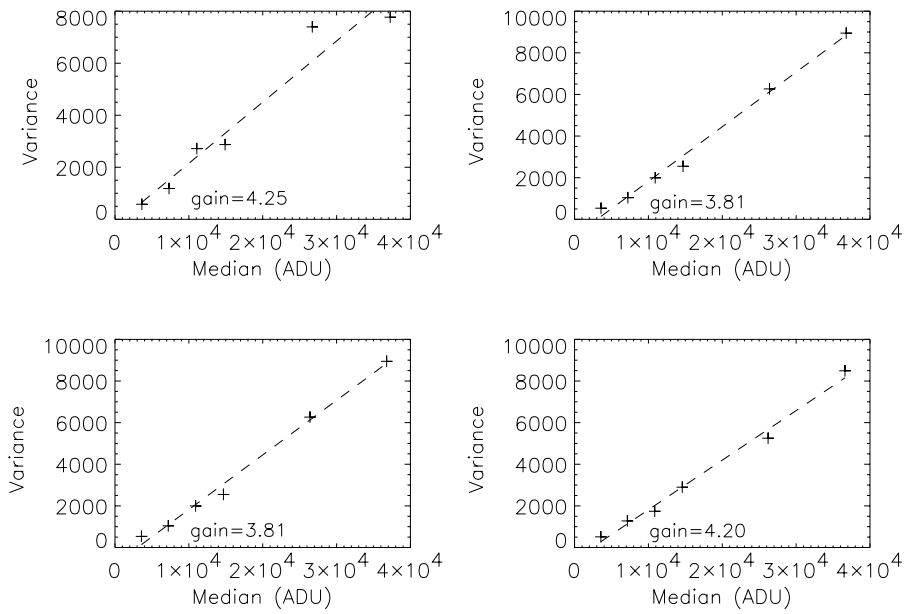

Figure 5.52: Omega Prime detector photon transfer curve. The gain is estimated from the slope of the line, given in electrons per ADU

Table 5.17: NICS bad pixel quantities and percentages for each quadrant.

	I	II	III	IV
Hot	42 (0.0%)	112 (0.0%)	526 (0.2%)	807 (0.3%)
Dead	1134 (0.4%)	837 (0.3%)	909 (0.3%)	614 (0.2%)
Total	1176 (0.4%)	949 (0.4%)	1435 (0.5%)	1421 (0.5%)

5.8 Discussion

As it has been seeing through this chapter, the detector system "tune up" requires a hard work, with progressive improvements. Since the first tests to the multiplexer to the second cool-down of the engineering detector, the readout noise was reduced more than 10 times. The system employed in the last tests (SDSU, preamplifier location, wiring length, etc.) is the same than the one that will be used at LIRIS, so that, no large differences in the behavior are expected.

From the comparison among the characteristics of the LIRIS, Omega Prime and NICS detectors, it is evident that the readout noise measurements are in the same order for all the arrays with slight higher values for our detectors. The reduction of the temperature to that, at which the scientific detector will work (60 K), will benefit the characteristics in the form of reducing the KTC noise (i.e. that depends on the temperature; see section 5.2.2), the dark current and, hence, the dark current noise.

It was seen that the MNDR mode can reduce the readout noise below than the specified value,

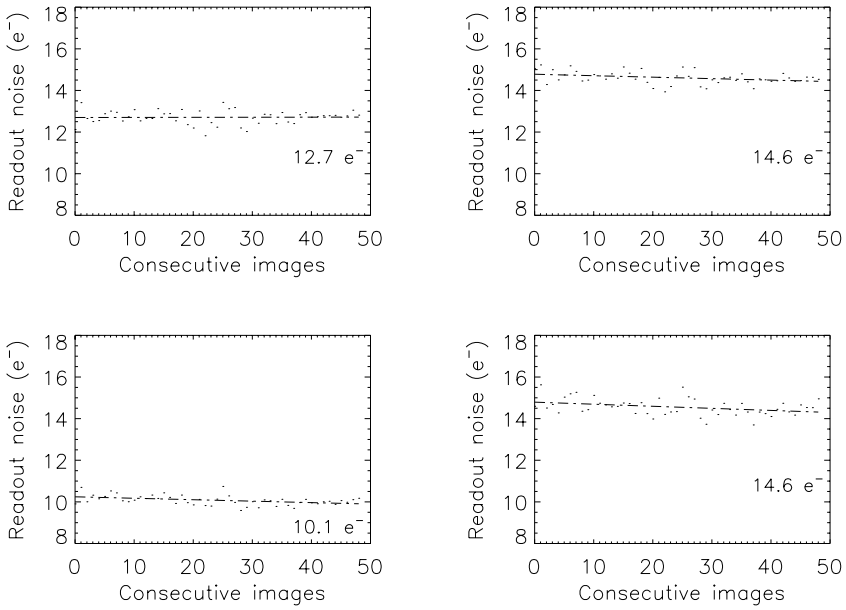

Figure 5.53: NICS readout noise estimated from 50 CDS mode images. The values are expressed as the readout noise of a single read, (N).

Table 5.18: Omega Prime bad pixel quantities and percentages for each quadrant.

	I	II	III	IV
Hot	215 (0.1%)	446 (0.2%)	1376 (0.5%)	419 (0.2%)
Dead	133 (0.1%)	127 (0.0%)	152 (0.1%)	106 (0.0%)
Total	348 (0.1%)	573 (0.2%)	1528 (0.6%)	525 (0.2%)

therefore an improvement of the signal to noise ratios computed in chapter 4, is expected.

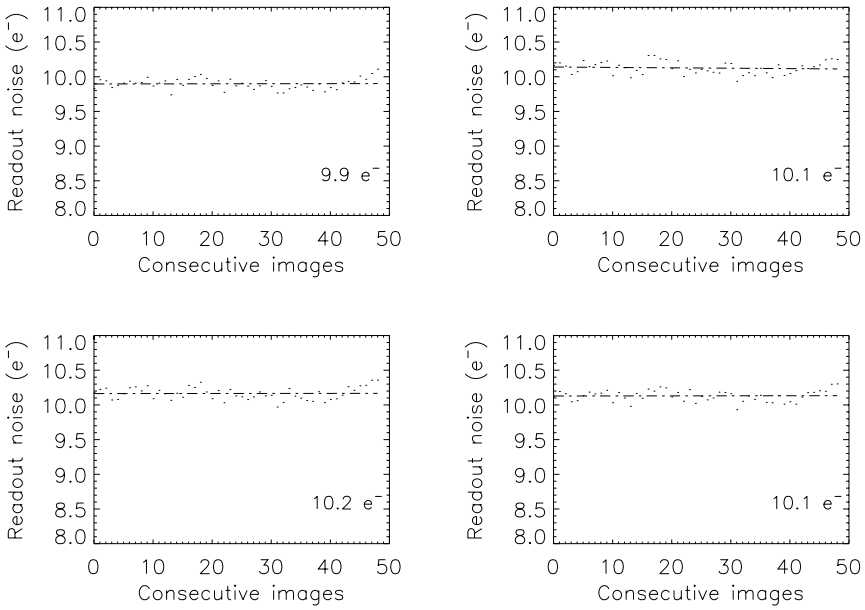

Figure 5.54: Omega Prime readout noise estimated from 50 CDS mode images. The values are expressed as the readout noise of a single read, (N).

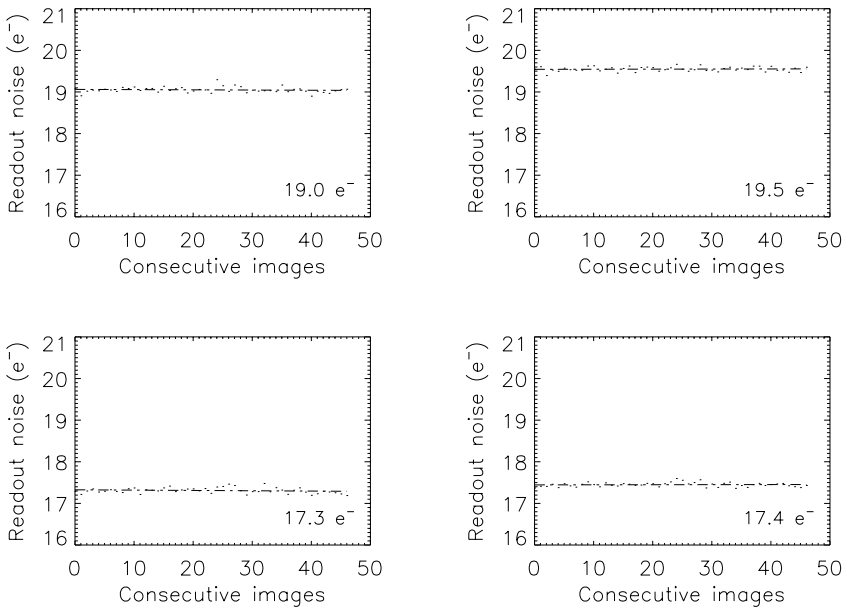

Figure 5.55: Omega Prime readout noise estimated from 50 “Full MPIA” mode images. The values are expressed as the readout noise of a single read, (N).

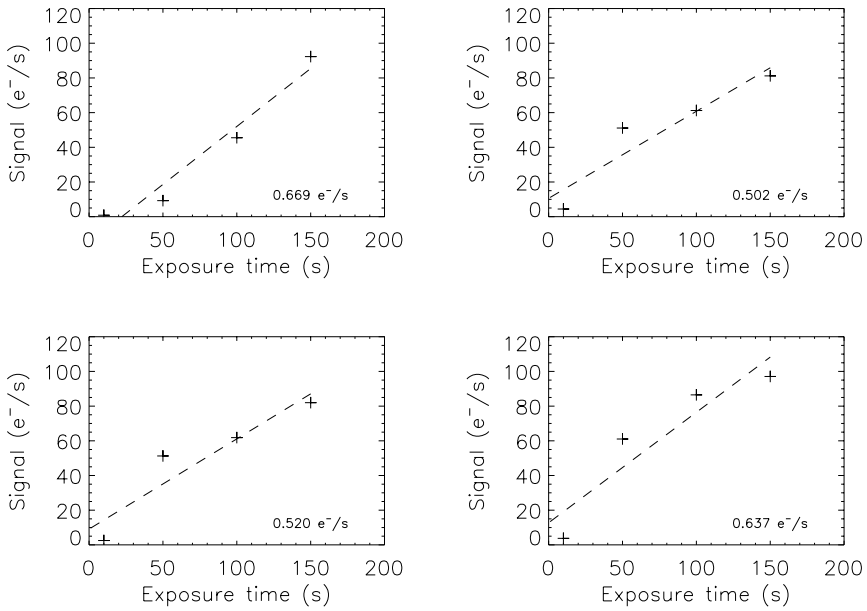

Figure 5.56: NICS detector dark current determination from 150 s exposure time images

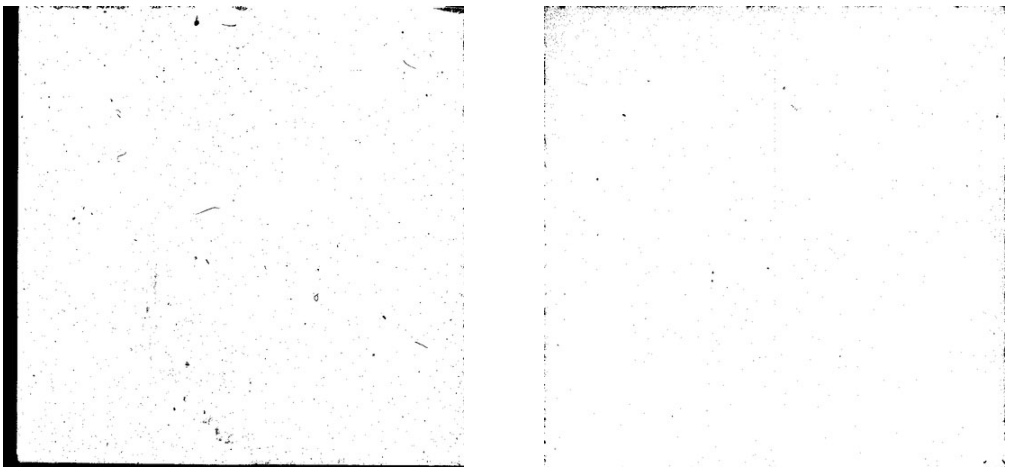

Figure 5.57: NICS (left) and Omega Prime (right) bad pixel masks.

6

Multi-slit mask design

6.1 Introduction

The observation of the galaxies from the LIRIS-GAL sample (described in Chapters 2 and 3) will take advantage of the multi-slit spectroscopy mode of LIRIS. The preparation of these observations includes the multi-slit masks design and manufacture. These tasks are quite complex due to the special requirements for the slits used in near-infrared spectroscopy. Such requirements are mainly related to the mask material and to the slit profile. The former restriction has to take into account the cooling of the instrument, as well as the thermal stability. The latter is related to the quality of the spectra. The instrumental parameters, on which the quality of the spectra depends on, are: 1) the position accuracy of the slit at the focal plane and its repeatability, 2) the position accuracy and repeatability of the grisms (i.e. the dispersion element), 3) the slit profile and 4) the slit-to-slit position error in the multi-slit masks. The slit position accuracy is crucial at the observations in order to center different objects in the slit and do not loose the centering for slit width changes. The slit profile affects the reduction of the data, particularly the sky subtraction (see below).

6.2 Slit masks

At spectroscopy mode, LIRIS has 15 slit options: 5 long-slit masks and 10 multi-slit masks. The masks are fully cryogenic (i.e. cooled to 65 K) to work in all near-infrared bands, including *K*-band. They are mounted on the slit wheel (also called the entrance wheel), inside the cryostat. The slits are oriented tangential to the wheel in order to reduce the slit positioning error due to the wheel angular position uncertainty.

The mask exchange is performed through a special door at the cryostat. This exchange is carried out at the beginning of each observing period (i.e. 3 to 6 months), because such procedure requires warming up and pressurizing the whole instrument. Consequently, the mask design and manufacture are carried out several weeks before the observation run.

The slit masks are square with 74 mm per side covering the LIRIS field of view of 4.2×4.2 arcmin^2 at the WHT focal plane scale of 4.507 arcsec per mm. The long-slit masks are permanently mounted on the entrance wheel with 5 slit widths: 0.5, 0.75, 1.0, 2.5 and 5.0 arcsec (0.111, 0.166, 0.222, 0.554 and 1.109 mm, respectively). The length of these slits is 4.2 arcmin or 55 mm.

The multi-slit masks are specific for each observation. They can hold up to 30 small slits with a minimum length of 1.66 mm (see section 6.2.3).

6.2.1 Requirements to the slit profile

6.2.2 Slit width error

For the long-slit masks, the edge roughness and the slit-edge parallelism are the critical requirements. They are essential for an efficient sky subtraction when applying the *nodding* technique (see section 3.4.1). With this mode, the object and the sky spectra are acquired at the same time in a first exposure. Then, an offset is applied to the telescope and a second exposure is acquired. This process is repeated for 2 to 4 positions along the slit. The signal from all of these positions is sky-subtracted and integrated together at the data reduction process. Any change in the slit width along these positions will produce an error in the sky subtraction. Thus, to keep the sky subtraction error to 1%, the slit profile errors must also be within 1% (Domínguez-Tagle 1999). The slit profile is determined by the slit edges parallelism and roughness of the edge, as it can be seen in Figure 6.1. The parallelism is defined as the ratio between the variation of the slit width ($a - b$) and its length (L), thus this requirement is set for the full length of the long-slit masks. The long-slits are 55 mm in length, thus the ratio $(a - b)/L$ must be lower than 2×10^{-5} to keep the errors below 1%.

The roughness is considered at a scale that goes from the pixel size to the length of the slit; in other words, the variations in the slit edge at distances smaller than the pixels size can be neglected since they are not resolved by the detector. For the case of LIRIS, the pixel size represented at the focal plane is 55.5 μm. Considering that the minimum slit width is 0.5 arcsec (equivalent to 111 μm), the 1% error represents a maximum roughness of r $\leq$ 1.1 μm r.m.s.

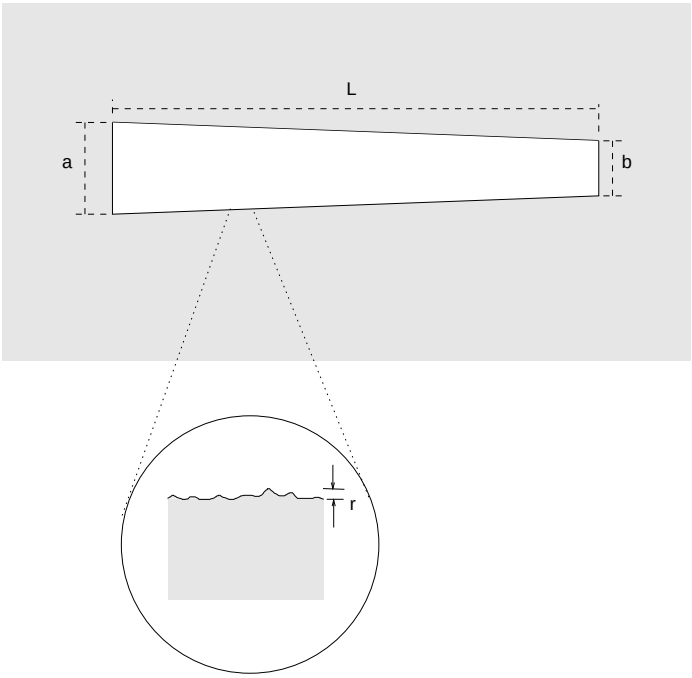

Figure 6.1: Slit profile representation.

6.2.3 Slit length

The long slits can have any length, only limited by the field of view (4.2 arcmin or 55 mm). The multi-slit masks can hold up to 30 small slits. This maximum number of slits is set by their minimum length, which is 30 pixels (1.66 mm at the slit mask, considering a detector scale of 0.25 arcsec per pixel). The criteria used to set the minimum slit length at 30 pixel is based on the idea to apply the *nodding* technique along the slit and to be able to identify the aperture. The aperture FWHM depends on the seeing and goes from 2 to 4 pixels (for a seeing from 0.5 to 1.0 arcsec, respectively). Therefore, 5 pixels can be assigned to the aperture. Other 5 pixels are required at each side of the aperture. Then, 15 pixels are required for each position along the slit. If the *nodding* technique is performed with two positions, then the slit length goes to 30 pixels.

6.2.4 Slit-to-slit position error

For the multi-slit masks, the relative slit-to-slit position has to be guaranteed in order to achieve high multi-object observing efficiency. This means that all the objects must fall on the center of their respective slits at the time of centering the mask on the field. The masks usually include 2 or 3 holes for the reference stars. These holes are used to image the stars and to center the mask on the field.

The manufacturing error should not contribute more than 10% of the astrometric error. The latter error is measured in the relative position between the objects (i.e. galaxies for the case of this work) and the reference stars. Good standard astrometric error is on the order of 0.2 arcsec. Since these stars are used to center the mask to the field the absolute astrometry is not necessary. The astrometric errors are included in the multi-slit mask design.

The manufacturing error requirement concerns mainly to the spectral dispersion direction. It can be relaxed by a factor of ten in the spatial direction, because of the length of the slits will be much larger than any error. The slit-to-slit precision is also affected by the thermal expansion of the mask due to variations on the working temperature. The mask material must have a low "coefficient of thermal expansion" (hereafter CTE) because the mask temperature could have variations of ± 10 K. Table 6.1 summarizes the CTE for different materials (Rogatto 1993).

Table 6.1: Coefficient of thermal expansion (CTE) for different materials at 65 K

Material	CTE ($\times 10^{-6}$ m/m/K)
copper	6.766
copper (OFHC)	5.837
stainless steel (AISI-302)	5.028
Invar	< 1
Aluminum (6061)	6.562

Two materials were Initially considered to manufacture the masks: Invar and stainless steel. The former has lower CTE than stainless steel; however, the manufacture of Invar masks is harder because of its strength. Therefore, the Invar edge roughness is not as good as that obtained with stainless steel. Then, the latter material (with the 2^{nd} lowest CTE; see Table 6.1), was selected. For masks made in stainless steel, a 10 K temperature variation produces a change of $\pm$ 3.7 μm in

the size of the whole mask and, a variation of 0.006 arcsec in the distance of two slits separated 2 arcmin from each other. Then, it fulfills the positioning requirements.

The requirements for the mask manufacturing are summarized as follows:

- Slit edge roughness ≤ 1.1 μm r.m.s.
- Slit edges parallelism $< 2 \times 10^{-5}$
- Slit–to–slit position error: ≤ 0.02 arcsec (4.4 μm) in the dispersion direction

6.3 Mask design

The multi-slit mask design includes the following processes: a) select the objects whose spectra is desired, b) determine the field center, c) compute the astrometry and, d) design the mask.

The spatial distribution of the objects determines the number of masks required to observe them. There is also a trade between the spectral range required for each object and the limits in the spectral range when the slit is not at the center of the field. The objects must have a priority number because, as it will be seen below, some of them may have to be discarded if they are extremely close to another with higher priority. It is also indispensable to identify two or three stars in the field to be used as a reference for the mask centering. The astrometry of the objects has to be computed in reference to these stars.

If the multi-slit observations are being prepared from previous images on the same field, the astrometry has to be derived from such images. Here, there are two cases: if the images were acquired with the same instrument (i.e. LIRIS) or from any other. In the former case, no astrometry calculus would be required if the images have the same field-size and orientation for the spectroscopy. Some optical spectrograph-imagers employ this mode (e.g. VIMOS, DOLORES). In the case that the images are from different instruments, three steps must be followed: a) select all the stars with known astrometric coordinates on the image, b) determine the image pixel-scale with these stars and, c) apply the scale solution to the selected objects. The result from this process shall be a list with the coordinates of the reference stars and the objects that will be observed. It is recommended to have astrometric errors less than 0.2 arcsec. The next step is the design of the slits in the mask. From the object selection and their priority, it must be clear the center of the mask and the spatial direction (i.e. the image orientation).

The spectral range of each object over the detector has to be reviewed because it depends on the position of the slit respect to the midpoint (in the spectral direction) of the mask. When any feature of the spectrum (e.g., the Hα emission line) falls close to the borders of the range, any change in the slit position from the midpoint of the mask, would produce the lost of such feature in the spectrum imaged by the detector. In consequence, it is possible to accommodate more objects at the spatial direction than at the spectral one. Then, the objects will be added to the mask according their priority. The slit dimensions are restricted by the minimum slit length (described before) and by the free space (at the spatial direction) between two objects.

If more than three reference stars are available at the field of view, they are selected according to their magnitude and their interference with other object's spectrum. Although, these reference stars do not require a slit, the hole used to view the stars and center the mask will produce a spectrum of the star.

6.4 Mask manufacturing

Different options for mask manufacturing have been considered. The slit masks requirements were sent to some companies that have manufactured slit masks for optical spectrographs. From the companies contacted, none of them answered positively. The given reason in the answer was that they were not able to fulfill the requirements presented.

Following the reported results on Szeto et al. (1997) and Conti et al. (1999), the idea to acquire a laser-cutting machine was pursued. These machines consists on high power laser beam (typically 60 W), mounted on a sevrvo-mechanism computer controlled (see Figure 6.2). Several stencil-laser machine manufacturers were contacted to investigate the precision of their equipments. One of the manufacturers answered and sent us a slit-mask sample. The characterization of this sample is described on the next section.

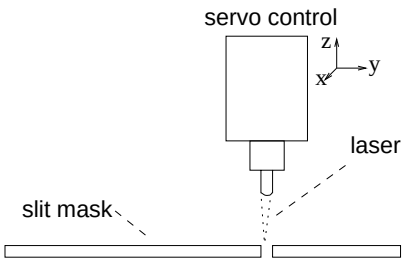

Figure 6.2: Representation of a laser-cutting machine

An alternative approach to laser cutting, suggested by Eng. Vicente Sánchez, was followed with Electric Discharge Machining (hereafter EDM). In this process, the cutting element is the erosion produced by the electric sparks between the electrode, a brass wire, and the mask when a potential of some tens of volts is applied. Both the mask and the electrode are immersed in a dielectric fluid (see Figure 6.3). This fluid recirculates through a filter to clean the debris from the removed material.

This method requires the mask material to be electrically conductive. An initial hole has to be drilled on the mask to place the electrode. A high speed Computer Numerical Control (hereafter CNC) machine is used for this purpose, which makes a hole with a diameter smaller than the slit width.

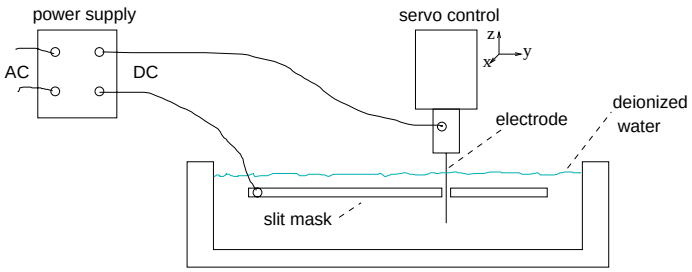

Figure 6.3: Representation of the EDM process

6.5 Prototype slit-mask testing

The setup for the measurements is based on a coordinate-measuring machine. This equipment is a Mitutoyo FJ805 with a microscope and a CCD camera. The profile along the slit in the prototype masks was measured with a $\pm 1\mu$m error, the instrument precision with the specified setup. Due to the uncertainty in the measurements, this setup was limited to determine the slit-to-slit positioning error and the slit edge parallelism error.

The edge roughness is a difficult parameter to be directly measured at the slits. Although an indirect method consisting on aligning the mask edge to the measurement instrument, such as the one described in (Conti et al. 2001) is also possible, the analysis with electronic microscope imaging was preferred. The measurements were performed from these images and the roughness was estimated in r.m.s. values (in a pixel-scale), as if it would be measured by a mechanical roughness meter.

6.5.1 Laser-cut slit mask

The prototype mask sent by the stencil-laser machine manufacturer was measured and imaged on the electronic microscope (see Figure 6.4). The material of the mask was black-anodized stainless steel. As it can be seen in the figure, there are some defects in the profile. As well, the measurement results listed on Table 6.2 show that this prototype did not fulfill the parallelism and roughness requirements. Conti et al. (2001) report similar experience with stencil-laser machines and conclude that, to obtain the required quality, a fine tuning of the machine was necessary. The option of acquiring one stencil-laser was still considered to perform the fine tuning; however, the cost of the machine exceeded enormously the budget assigned for the slit masks. And, since mask production is limited to 10 masks per observing period, this option was finally discarded.

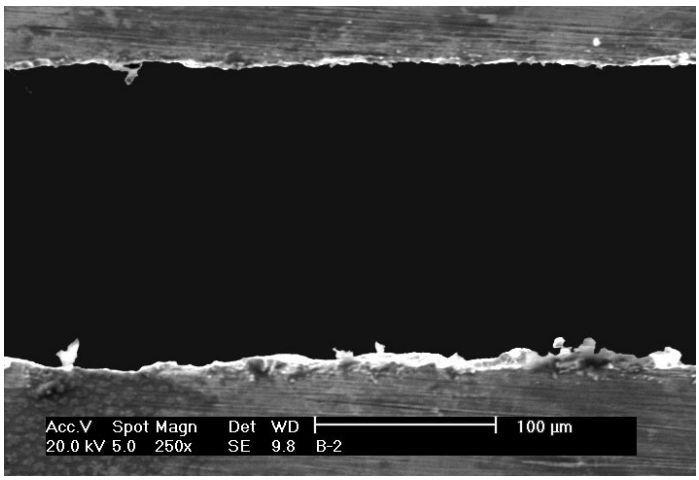

Figure 6.4: Electronic microscope inspection of the steel slit-mask manufactured by laser.

6.5.2 EDM-cut slit mask

The high-precision-manufacturing company, "Mecanizados Gines S.A."[1] sent us different slit-mask samples EDM-manufactured in stainless steel to verify the accuracy of the cutting process. These samples have different slit widths. The slit edges parallelism and the slit-to-slit position error were measured and the microscope inspection was carried out to estimate the edge roughness. A sample of a slit of 0.5 arcsec width imaged by the electronic microscope is shown in figure 6.5.

Table 6.2: Results from measurements.

Parameter	Required	Measured	
		laser	EDM
Parallelism	$< 2 \times 10^{-5}$	$88 \pm 11 \times 10^{-5}$	$7 \pm 4 \times 10^{-5}$
Roughness (μm)	≤ 1.1	1.6±0.2	1.15±0.15
Waviness (μm)	—	—	1.4±0.2
Slit-to-slit (μm)	≤ 4.4	—	3.2 ±2.2

Roughness and slit–to–slit positioning error requirements are satisfied. Parallelism is not satisfied at the full length of the slit; however, for most observing cases (not very extended objects) *nodding* is done using less than half of the slit length. In that case, the parallelism error would produce a maximum of 2% error in sky subtraction.

The *waviness* parameter as defined in Conti et al. (2001) was measured although it was not originally defined at the requirements. Table 6.2 summarizes the results obtained with the prototype masks.

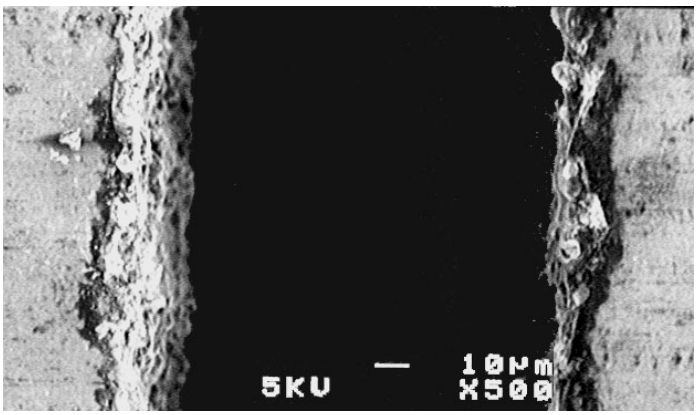

Figure 6.5: Electronic microscope inspection of a 0.7 arcsec slit manufactured by EDM.

The results on the tests of the prototype masks show that the approach to multi-slit manufacturing based on Electric Discharge Machining (EDM) satisfies the scientific requirements for the instrument spectroscopic mode (Domínguez-Tagle et al. 2001).

[1] www.gines.es

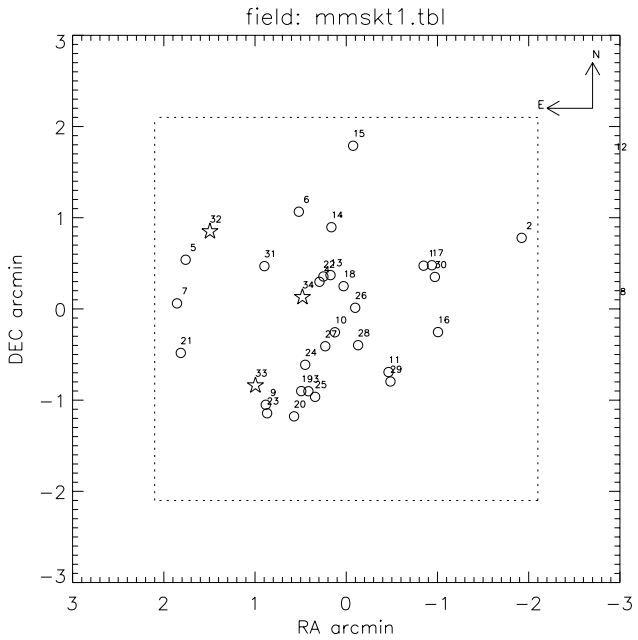

Figure 6.6: Selected field for the multi-slit mask. The dotted box indicates the LIRIS 4.2×4.2 arcsec field of view. The galaxies in the field are represented by circles and the reference stars by star symbols.

Table 6.3: Priority table with the objects included in the mask design.

Object No.	Name	Priority
1	CS0472-0	1
2	BD0474-0	3
3	BD0475-1	1
4	BD0476-0	3
5	BD0480-0	10
6	CS0484-0	3
7	BD0487-0	1
8	CS0520-0	1
9	CS0525-0	4
10	CS0557-0	5
11	BD0560-0	1
12	CS0561-0	1
13	BD0594-1	4
14	BD0654-1	3
15	CS0672-0	10
16	CS0681-1	10
17	CS0682-0	4
18	BD0693-1	3
19	BD0747-0	5
20	CS0778-0	3
21	BD0784-0	5
22	BD0788-0	3
23	BD0821-0	2
24	CS0841-0	1
25	CS0858-0	5
26	BD0904-0	5
27	BD0907-0	3
28	CS1001-0	1
29	CS1014-0	3
30	CS1020-0	3
31	BD1084-0	5
32	Reference star	99
33	Reference star	99
34	Reference star	99

6.6 Mask design for the LIRIS-GAL sample of galaxies

As it was described in section 6.1, the observation of the LIRIS-GAL sample of galaxies will employ the instrument multi-slit capability in order to take advantage of their high surface density (see section 2.3). Here I present a multi-slit mask design example performed with my own IDL program written for that purpose.

A 4.2×4.2 arcsec field within the HDF-N+FF is shown in Figure 6.6. The dotted box indicates the LIRIS field of view. The galaxies are represented by circles and the reference stars by star symbols. The numbers indicate the reference according to Table 6.3, which enumerates the reference stars and the galaxies (from LIRIS-GAL) that are found in the field. It can be seen that the field is plenty of galaxies; however, some of them are quite close to each other. As well, others are very close to the field border. This field and table are all the input data for the mask design with the procedure described in section 6.3.

Table 6.4: Approximate spectral range for the selected objects.

Object No.	Spectral range [Å]
1	9908 - 14271
11	9437 - 14742
28	9028 - 15151
23	7807 - 16372
4	8510 - 15669
6	8233 - 15946
17	10051 - 14128
10	8717 - 15462
25	8451 - 15728
26	8989 - 15190
15	8961 - 15218

Each object in Table 6.3 has a given priority according to the resolving power required for Hα detection and the following criteria: 1 for R$<$1000, 2 for the same resolution but with a noisy spectrum of the Hα emission line (see section 3.2.2), 3 for 1000 $\geq$ R $<$ 2000, 4 for 2000 $\geq$ R $<$ 3000, 5 for 3000 $\geq$ R $<$ 5000 and 10 for R $\geq$ 5000. The number 99 is given to the reference stars.

The multi-slit program computes the center of the field from the coordinates of the higher priority galaxies. Then it places the reference stars and it starts to select the galaxies according to their priority. The selected objects and their spectral ranges are given in Table 6.4. According to this table, the object number 1 has a useless spectral range to detect Hα because this emission line falls out of range. The galaxy number 17 is selected instead. All the other galaxies have appropriate spectral ranges.

The program draws the multi-slit mask, as it must be manufactured with slits for the galaxies and small holes for the reference stars. The mask, shown in Figure 6.7, includes slits for 10 galaxies. Finally, a coordinates table is generated for the mask manufacture with the four slit corners and the center of the small holes (see Table 6.5).

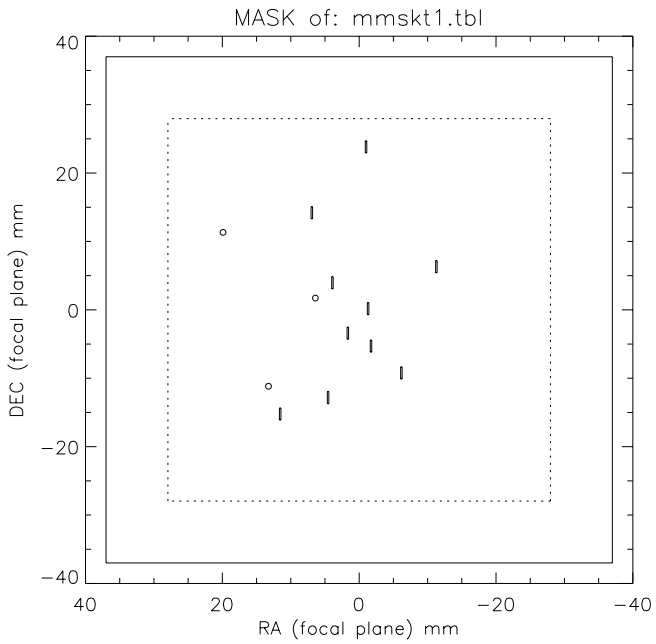

Figure 6.7: Multi-slit mask in millimeters for manufacture reference. The dotted box indicates the LIRIS 4.2×4.2 arcsec field of view and the solid box represents the physical size of the mask.

Table 6.5: Output table from the mask design program. The values are given in millimeters, referred to the center of the mask.

Object No.	X_{init}	X_{end}	Y_{init}	Y_{end}
32[a]	19.5557	19.5557	11.5208	11.5208
33[a]	12.9071	12.9071	-10.9753	-10.9753
34[a]	6.0514	6.0514	1.9135	1.9135
11	-6.6194	-6.3975	-9.9128	-8.1377
28	-2.1829	-1.9610	-5.9852	-4.2101
23	11.0960	11.3179	-15.9245	-14.1495
4	3.4602	3.6820	3.2686	5.0436
6	6.4645	6.6864	13.4974	15.2725
17	-12.9510	-12.7292	5.6849	7.4599
10	1.1993	1.4212	-4.0991	-2.3240
25	4.0878	4.3097	-13.5265	-11.7515
26	-1.7624	-1.5405	-0.5249	1.2501
15	-1.4516	-1.2297	23.1260	24.9010

Notes: *a*) These coordinates (i.e. for the reference stars) are the circle center.

7

Conclusions

The work presented in this thesis has been devoted with the scientific exploitation of the multi-slit spectroscopy mode of LIRIS. A sample of intermediate-redshift galaxies has been constructed and analyzed in detail, in order to study the cosmic star formation in the universe. The LIRIS multi-slit masks and scientific detector system have been designed and characterized to improve its spectroscopy mode performance, which giving the estimations also presented in this thesis, is very competitive for the observations of intermediate-redshift galaxies. The main results of the thesis are summarized as follows:

- I have constructed the LIRIS-GAL sample with 88 galaxies in the redshift range $0.46 \leq z < 1.1$ from the HDF-N+FF data. These galaxies have spectroscopically measured redshifts and are expected to be undergoing star forming episodes, according to the selection criteria. Theoretical color-color diagrams have been constructed from population synthesis and stelar evolution models in order to identify the prominent colors of star forming galaxies. The selection has been centered on HII region-like galaxies taking into account the limiting fluxes estimated for LIRIS. Different colors, metalicities and redshift ranges have been considered for the color-color diagrams, taking advantage of the multicolor *B*, *G*, *V*, *R*, *I*-band data and employing those bandpasses that better represent the continuum distribution. The color properties of the selected HDF-N+FF galaxies agree with the model predictions and the observed evidence of star formation. Optical spectroscopy data has been employed to analyze the spectral classification of the galaxies from the sample. According to diagnostic methods designed for intermediate redshift galaxies, possible objects having ionization from star formation (i.e. HII region-like galaxies) have been identified. Taking advantage of the sample database, a spatial distribution analysis has been performed identifying certain galaxies within high density environments.

- A pilot series of observations has been performed to assess the selection and the observation strategies: OH emission lines proximity, atmospheric transmission, required resolving power and instrumental setup. These observations were carried out with the long-slit near-infrared spectrographs Omega Cass and NICS. With the latter instrument, I obtained the NIR spectra of the galaxy BD0840-0, at redshift z=0.84. The Hα emission line was detected with a S/N$>$4 in a 5400 s exposure time spectrum. The estimated luminosity of this line ($L_{H\alpha}$=

3.98 $\pm$0.7 $\times 10^{41}$ ergs s^{-1}), when compared to the stelar evolution models, suggest that an instantaneous burst of 10^{11} solar masses could be the star forming scenario for this galaxy. The SFR of BD0840-0 is estimated in 3.1$\pm$0.6 M$_{\odot}$ yr^{-1}. This result is comparable with the typical values for local starburst galaxies (i.e. M82, "Antennae", etc), whereas other SFR-estimating methods, such as that one based in [OII](5007 Å), gives results which are 3 to 4 times higher.

- Theoretical estimations of the limiting fluxes and magnitudes for LIRIS have been obtained from a broad analysis of the instrumental parameters. A study between the most important sources of noise (background emission and detector readout noise) has shown that the "background limited observations" are always reached for J, H, Ks-bands in imaging mode using *MNDR* readout mode. The 3 σ image mode limiting magnitudes (for 1 h and 0.5 arcsec seeing) are: J=24.3, H=22.8 and Ks=21.5 mag. For R=1000 spectroscopy, the continuum limiting magnitudes are: J=22.1, H=19.6 and Ks=18.5 mag. Furthermore, the 3 σ liming flux for J-band R=1000 spectroscopy, estimated in 4.4×10^{-17} ergs s^{-1} cm^{-2}, show that the LIRIS is sensitive enough for the intermediate-redshift galaxies project and other faint object programs.

- Both the engineering and scientific grade detectors were successfully tested in a special test-cryostat. The noise-reduction workout performed to the electronics readout enabled us to identify the major noise sources and concluded with its reduction to the minimum level. The engineering grade detector characterization showed that, although it presents a large bad-pixel region in quadrant IV, good performance is obtained with the other quadrants. A readout noise N = 15 $\pm$1 e$^-$ is obtained for CDS mode and a dark current of 0.7 e$^-$/s for the test temperature of 82 K. Moreover, the engineering grade detector showed to be linear within 2% from 5000 to 100,000 $\pm$10,000 e$^-$. Once the tests had been successfully completed on the engineering grade detector, the scientific grade detector was characterized. The detector showed that low readout noise is obtained: N = 16 $\pm$1 e$^-$ for correlated double sampling and, as low as $N_{MNDR} \approx 5$ e$^-$ is reached for $m = 16$. The linearity within 2% goes from 4500 to 110,000 $\pm$10,000 e$^-$. The very low dark current value (0.07 e$^-$/s at 83 K) proves that the observations are not limited by the dark current noise. The bad-pixel number along the detector is below 2%. Glow, cross-talk and persistence effects are a minimum. These parameters show that the scientific grade detector is very competitive and that it improves the instrument performance.

- The observation of faint objects has defined strict requirements in the spectroscopy mode for adequate background subtraction. In order to fulfill the requirements, a novel slit-mask manufacturing technique called "Electric Discharge Machining" was tested. The profile measurements performed to the multi-slit masks show that this technique produce excellent results. The slit edge roughness $\leq$ 1.1 μm r.m.s. and the slit–to–slit position error: $\leq$ 0.02 arcsec (4.4 μm) in the dispersion direction measured values makes the manufacturing process as competitive as the best in other observatories. The masks for the intermediate-redshift galaxies project have been designed and are under manufacturing, ready for the scientific operation of LIRIS.

Future work.

The scientific work on this thesis is focused on the selection of the sample of galaxies. The successful results encourages future observations, which depend on the LIRIS scientific operation commissioning date. Once LIRIS has been commissioned, the whole program may be completed in a few nights of observation. For example, the spectra of BD0840-0 may be obtained with the detection of Hα to a level of 10 σ, in a total exposure time of 10650 s. This is quite fast and is due to the advantages of observing several galaxies simultaneously with the multi-slit mode. The SFR in intermediate-redshift galaxies project will not end here as the sample of galaxies will be extended to other surveys employing the same selection criteria. Furthermore, with the advent of multi-object NIR spectrographs in 10 m class telescopes, the sample could be enlarged to galaxies at redshifts z = 2.6 (*K*-band). In this case, a complete "cosmic star formation history" at $0 < z < 2.6$ might be obtained from Hα luminosities. On the instrumental area, we expect that LIRIS on the WHT will be a highly competitive NIR spectrograph. The multi-slit mode will ensure that the best results will be obtained from the WHT on nights with good seeing and weather conditions.

Bibliography

Atad-Ettedgui E., 1999, LIRIS Historical record, L07E0HR1, 1

Barger A. J., Cowie L. L., Trentham N., Fulton E., Hu E. M., Songaila A., Hall D., 1999, AJ, 117, 102

Bates D. R., Nicolet M., 1950, PASP, 62, 106

Baugh C. M., Cole S., Frenk C. S., 1996, MNRAS, 282, L27

Baugh C. M., Cole S., Frenk C. S., Lacey C. G., 1998, ApJ, 498, 504

Bruzual A. G., Charlot S., 1993, ApJ, 405, 538

Buat V., Xu C., 1996, A&A, 306, 61

Calzetti D., Kinney A. L., Storchi-Bergmann T., 1994, ApJ, 429, 582

Chapman R., Beard S., Mountain M., Pettie D., Pickup A., 1990, in Instrumentation in astronomy VII; Proceedings of the Meeting, Tucson, AZ, Feb. 13-17, 1990 (A91-29601 11-35). Bellingham, WA, Society of Photo-Optical Instrumentation Engineers, 1990, p. 34-42., Vol. 1235, p. 34

Cohen J. G., 2001, AJ, 121, 2895

Cohen J. G., Hogg D. W., Blandford R., Cowie L. L., Hu E., Songaila A., Shopbell P., Richberg K., 2000, ApJ, 538, 29

Cohen J. G., Hogg D. W., Pahre M. A., Blandford R., Shopbell P. L., Richberg K., 1999, ApJS, 120, 171

Cole S., Aragon-Salamanca A., Frenk C. S., Navarro J. F., Zepf S. E., 1994, MNRAS, 271, 781

Connolly A. J., Szalay A. S., Dickinson M., Subbarao M. U., Brunner R. J., 1997, ApJ, 486, L11

Content R., 1996, ApJ, 464, 412

Conti G., Chiappetti L., Mattaini E., Maccagni D., Le Fèvre O., Saisse M., Vettolani G., 1999, Astro Tech Journal, 2, 2

Conti G. et al., 2001, PASP, 113, 452

Cowie L. L., Hu E. M., Songaila A., Egami E., 1997, ApJ, 481, L9

Dessauges-Zavadsky M., Pindao M., Maeder A., Kunth D., 2000, aap, 355, 89

Domínguez-Tagle C., 1999, LIRIS Engineering note, L02B0EN1, 1

Domínguez-Tagle C., Acosta-Pulido J., 2001, LIRIS Engineering note, L07E0EN1, 1

Domínguez-Tagle C., Acosta-Pulido J., Ballesteros E., 2001, LIRIS Engineering note, L07E0EN4, 1

Domínguez-Tagle C., Acosta-Pulido J., Ballesteros E., 2002, LIRIS Engineering note, L07E0EN10, 1

Domínguez-Tagle C., Sánchez V., Acosta-Pulido J., López R., Barreto M., Manchado A., 2001, Astro Tech Journal, 4, 1

Dressler A., 1984, araa, 22, 185

Eggen O. J., Lynden-Bell D., Sandage A. R., 1962, ApJ, 136, 748

Elias J. H. et al., 1998, in Proc. SPIE Vol. 3354, p. 555-565, Infrared Astronomical Instrumentation, Albert M. Fowler; Ed., Vol. 3354, p. 555

Elston R., 1998, in Proc. SPIE Vol. 3354, p. 404-413, Infrared Astronomical Instrumentation, Albert M. Fowler; Ed., Vol. 3354, p. 404

Fernández-Soto A., Lanzetta K. M., Yahil A., 1999, ApJ, 513, 34

Filippenko A. V., 1982, PASP, 94, 715

Filippenko A. V., Terlevich R., 1992, apjl, 397, L79

Finger G., Biereichel P., Mehrgan H., Meyer M., Moorwood A. F., Nicolini G., Stegmeier J., 1998, in Proc. SPIE Vol. 3354, p. 87-98, Infrared Astronomical Instrumentation, Albert M. Fowler; Ed., Vol. 3354, p. 87

Finger G., Mehrgan H., Meyer M., Moorwood A. F., Nicolini G., Stegmeier J., 2000, in Proc. SPIE Vol. 4008, p. 1280-1297, Optical and IR Telescope Instrumentation and Detectors, Masanori Iye; Alan F. Moorwood; Eds., Vol. 4008, p. 1280

Finger G., Nicolini G., 1998a, ESO report, 3, 1

Finger G., Nicolini G., 1998b, ESO report, 1, 1

Fowler A. M., Gatley I., 1990, ApJ, 353, L33

Fowler A. M., Gatley I., 1991, in Proc. SPIE Vol. 1541, p. 127-133, Infrared Sensors: Detectors, Electronics, and Signal Processing, T. S. Jayadev; Ed., Vol. 1541, p. 127

Gallego J., Zamorano J., Aragon-Salamanca A., Rego M., 1995, ApJ, 455, L1

Gallego J., Zamorano J., Rego M., Vitores A. G., 1997, ApJ, 475, 502

Garnett J. D., Forrest W. J., 1993, in Proc. SPIE Vol. 1946, p. 395-404, Infrared Detectors and Instrumentation, Albert M. Fowler; Ed., Vol. 1946, p. 395

Girardi M., Giuricin G., Mardirossian F., Mezzetti M., Boschin W., 1998, ApJ, 505, 74

Glazebrook K., Blake C., Economou F., Lilly S., Colless M., 1999, MNRAS, 306, 843

Guzman R., Gallego J., Koo D. C., Phillips A. C., Lowenthal J. D., Faber S. M., Illingworth G. D., Vogt N. P., 1997, ApJ, 489, 559

Hammersley P. L., 1998, New Astronomy Review, 42, 533

Herbst T. M., Beckwith S. V., Birk C., Hippler S., McCaughrean M. J., Mannucci F., Wolf J., 1993, in Proc. SPIE Vol. 1946, p. 605-609, Infrared Detectors and Instrumentation, Albert M. Fowler; Ed., Vol. 1946, p. 605

Hodapp K., Hora J., Graves E., Irwin E. M., Yamada H., Douglass J. W., Young T. T., Robertson L., 2000, in Proc. SPIE Vol. 4008, p. 1334-1341, Optical and IR Telescope Instrumentation and Detectors, Masanori Iye; Alan F. Moorwood; Eds., Vol. 4008, p. 1334

Hodapp K.-W. et al., 1996, New Astronomy, 1, 177

Hogg D. W. et al., 2000, ApJS, 127, 1

Hopkins A. M., Connolly A. J., Szalay A. S., 2000, AJ, 120, 2843

Hutley M. C., 1982, Diffraction gratings. Techniques of Physics, London: Academic Press, 1982

Iglesias-Páramo J., Vilchez J. M., 1999, apj, 518, 94

Iwamuro F. et al., 2000, PASJ, 52, 73

Janesick J. R., Evans K., Elliott T., 1987, Optical Engineering, 26, 972

Kauffmann G., White S. D. M., Guiderdoni B., 1993, MNRAS, 264, 201

Kells W., Dressler A., Sivaramakrishnan A., Carr D., Koch E., Epps H., Hilyard D., Pardeilhan G., 1998, PASP, 110, 1487

Kennicutt R. C., 1992, ApJ, 388, 310

Kennicutt R. C., 1998, ARA&A, 36, 189

Kennicutt R. C., Tamblyn P., Congdon C. E., 1994, ApJ, 435, 22

Koo D. C., 1995, in The Light Element Abundances, Proceedings of an ESO/EIPC Workshop Held in Marciana Marina, Isola d'Elba, 21 - 26 May 1994. Edited by Phillippe Crane. Springer-Verlag Berlin Heidelberg New York. Also ESO Astrophysics Symposia (European Southern Observatory), 1995, p.133, p. 133

Kozlowski L. J., Vural K., Cabelli S. A., Chen A. C., Cooper D. E., Bruce C. F., Hodapp K., Hall D. N., 1994, in Proc. SPIE Vol. 2268, p. 353-364, Infrared Detectors: State of the Art II, Randolph E. Longshore; Ed., Vol. 2268, p. 353

Kurucz R. L., 1992, in IAU Symp. 149: The Stellar Populations of Galaxies, Vol. 149, p. 225

Le Fevre O. et al., 2000, in Proc. SPIE Vol. 4008, p. 546-557, Optical and IR Telescope Instrumentation and Detectors, Masanori Iye; Alan F. Moorwood; Eds., Vol. 4008, p. 546

Leach R. W., Beale F. L., Eriksen J. E., 1998, in Proc. SPIE Vol. 3355, p. 512-519, Optical Astronomical Instrumentation, Sandro D'Odorico; Ed., Vol. 3355, p. 512

Leach R. W., Low F. J., 2000, in Proc. SPIE Vol. 4008, p. 337-343, Optical and IR Telescope Instrumentation and Detectors, Masanori Iye; Alan F. Moorwood; Eds., Vol. 4008, p. 337

Leitherer C. et al., 1999, ApJS, 123, 3

Lenzen R., Bizenberger P., Salm N., Storz C., 1998, in Proc. SPIE Vol. 3354, p. 493-499, Infrared Astronomical Instrumentation, Albert M. Fowler; Ed., Vol. 3354, p. 493

Lilly S. J., Le Fevre O., Hammer F., Crampton D., 1996, ApJ, 460, L1

Lilly S. J., Tresse L., Hammer F., Crampton D., Le Fevre O., 1995, ApJ, 455, 108

Lisi F., Baffa C., Gennari S., Oliva E., 1999, Astro Tech Journal, 2, 1

Llewellyn E. J., Long B. H., Solheim B. H., 1978, Planetary and Space Science, 26, 525

Llewellyn E. J., Solheim B. H., 1978, Planetary and Space Science, 26, 533

Lubin L. M., Postman M., 1996, AJ, 111, 1795

Madau P., Ferguson H. C., Dickinson M. E., Giavalisco M., Steidel C. C., Fruchter A., 1996, MNRAS, 283, 1388

Madau P., Pozzetti L., Dickinson M., 1998, ApJ, 498, 106

Maihara T., Iwamuro F., Yamashita T., Hall D. N. B., Cowie L. L., Tokunaga A. T., Pickles A., 1993, PASP, 105, 940

Manchado A. et al., 2000, in Proc. SPIE Vol. 4008, p. 1162-1171, Optical and IR Telescope Instrumentation and Detectors, Masanori Iye; Alan F. Moorwood; Eds., Vol. 4008, p. 1162

Manchado A. et al., 1998, in Proc. SPIE Vol. 3354, p. 448-455, Infrared Astronomical Instrumentation, Albert M. Fowler; Ed., Vol. 3354, p. 448

Mayya Y. D., 1994, PASP, 106, 424

McLean I. S., 1989, Electronic and computer-aided astronomy: From eyes to electronic sensors. Chichester, England/Englewood Cliffs, NJ, Ellis Horwood, Ltd./Prentice Hall, 1989, 305 p.

McLean I. S., ed, 1994, McLean I. S., ed, Infrared Astronomy with Arrays, The Next Generation

McLean I. S. et al., 1998, in Proc. SPIE Vol. 3354, p. 566-578, Infrared Astronomical Instrumentation, Albert M. Fowler; Ed., Vol. 3354, p. 566

Mihos J. C., Bothun G. D., Richstone D. O., 1993, ApJ, 418, 82

Moorwood A. et al., 1998, The ESO Messenger, 94, 7

Moorwood A., Cuby J.-G., Lidman C., 1998, The ESO Messenger, 91, 9

Moorwood A. F. M., van der Werf P. P., Cuby J. G., Oliva E., 2000, A&A, 362, 9

Moss C., Whittle M., 1993, apjl, 407, L17

Niklas S., Klein U., Wielebinski R., 1997, aap, 322, 19

Noeske K. G., Iglesias-Páramo J., Vílchez J. M., Papaderos P., Fricke K. J., 2001, aap, 371, 806

Oconnell R. W., Mangano J. J., 1978, ApJ, 221, 62

Oke J. B. et al., 1995, PASP, 107, 375

Oke J. B., Gunn J. E., 1983, ApJ, 266, 713

Oliva E. et al., 2001, A&A, 369, L5

Oliva E., Origlia L., 1992, A&A, 254, 466

Osterbrock D. E., 1974, Astrophysics of gaseous nebulae. Research supported by the Research Corp., Wisconsin Alumni Research Foundation, John Simon Guggenheim Memorial Foundation, Institute for Advanced Studies, and National Science Foundation. San Francisco, W. H. Freeman and Co., 1974. 263 p.

Pettini M., Kellogg M., Steidel C. C., Dickinson M., Adelberger K. L., Giavalisco M., 1998, ApJ, 508, 539

Phillips A. C., Guzman R., Gallego J., Koo D. C., Lowenthal J. D., Vogt N. P., Faber S. M., Illingworth G. D., 1997, ApJ, 489, 543

Ramsay S. K., 1993, Ph.D. Thesis, 200

Ramsay S. K., Mountain C. M., Geballe T. R., 1992, MNRAS, 259, 751

Rieke G. H., Lebofsky M. J., 1985, ApJ, 288, 618

Rogatto W. D., 1993, Electro-optical components. The infrared and electro-optical systems handbook - IR/EO systems handbook, Bellingham: SPIE-The International Society for Optical Engineering and Ann Arbor, Michigan: ERIM-Infrared Information Analysis Center, —c1993, edited by Rogatto, William D.

Rola C. S., Terlevich E., Terlevich R. J., 1997, mnras, 289, 419

Rousselot P., Lidman C., Cuby J.-G., Moreels G., Monnet G., 2000, A&A, 354, 1134

Sandage A., 1961, ApJ, 134, 916

Schroeder D. J., 1987, Astronomical Optics. San Diego: Academic Press, 1987

Shuder J. M., Osterbrock D. E., 1981, apj, 250, 55

Steed A. J., Baker D. J., 1979, Appl. Opt., 18, 3386

Steidel C. C., Giavalisco M., Pettini M., Dickinson M., Adelberger K. L., 1996, ApJ, 462, L17

Steidel C. C., Hamilton D., 1993, AJ, 105, 2017

Szeto K., Stilburn J. R., Bond T., Roberts S., Sebesta J., Saddlemyer L. K., 1997, Proceedings of SPIE, 2871, 1262

Taylor M. J., Espy P. J., Baker D. J., Pendleton W. R., Sica R. J., Neal P. C., 1991, Planetary and Space Science, 39, 1171

Thompson R. I., Weymann R. J., Storrie-Lombardi L. J., 1999, in American Astronomical Society Meeting, Vol. 195, p. 12904

Tresse L., Maddox S. J., 1998, ApJ, 495, 691

Tresse L., Maddox S. J., Fevre L., Cuby J. G., 2002, (astro-ph/0111390)

Treyer M. A., Ellis R. S., Milliard B., Donas J., Bridges T. J., 1998, MNRAS, 300, 303

Veilleux S., Osterbrock D. E., 1987, apjs, 63, 295

Vincent J. D., 1989, Fundamentals of infrared detector operation and testing. New York : Wiley, c1990.

White M., Lampe D., 1974, in Proc. IEEE Vol. SC9, p. 1-12, Solid State Circuits, Vol. 9, p. 1

White S. D. M., Frenk C. S., 1991, ApJ, 379, 52

Williams R. E. et al., 1996, AJ, 112, 1335

Yan L., McCarthy P. J., Freudling W., Teplitz H. I., Malumuth E. M., Weymann R. J., Malkan M. A., 1999, ApJ, 519, L47